MODELING BIOSYNTHESIS AND TRANSPORT OF VOLATILE ORGANIC COMPOUNDS IN PLANTS

by

Shaunak Ray

A Dissertation

Submitted to the Faculty of Purdue University

In Partial Fulfillment of the Requirements for the degree of

Doctor of Philosophy

Davidson School of Chemical Engineering

West Lafayette, Indiana

May 2020

THE PURDUE UNIVERSITY GRADUATE SCHOOL
STATEMENT OF COMMITTEE APPROVAL

Dr. John A. Morgan, Chair
Davidson School of Chemical Engineering

Dr. Natalia Dudareva
Department of Biochemistry

Dr. Sangtae Kim
Davidson School of Chemical Engineering

Dr. Nien-Hwa Linda Wang
Davidson School of Chemical Engineering

Approved by:
Dr. John A. Morgan

This dissertation is dedicated to my beloved parents,
my first teachers.

ACKNOWLEDGMENTS

I wish to express my sincere gratitude towards my advisor, Dr. John Morgan, for his continued guidance and mentorship throughout my graduate studies. His creativity and curiosity as a researcher, motivated me to excel. His continuous and unwavering support over the course of my research made difficult days comprised of challenging experiments easier to manage. I would also like to extend my deep appreciation to Dr. Natalia Dudareva for being an exception co-advisor. Her dedication for excellence, attention to detail, and passion for science are infinitely inspiring. Working under their advisement has provided me with an exemplary illustration of the importance of collaboration and friendship in life. I would also like to thank the members of my advisory committee, Dr. Linda Wang and Dr. Sangtae Kim, who are both among my favorite professors at Purdue and have been instrumental in my learning experience and education.

I want to thank Joe Lynch, Longyun Guo, Rohit Jaini, Peng Wang, and Ben Boachon who have all contributed towards the technical knowledge and skills I have developed over the years. In their honor, I have strived to better myself as a mentor towards others. I am grateful to Dr. Brett Savoie, who has taught me so much in such a short period of time. Many thanks also go to my fellow lab members, Robin, Jeremiah, Joel, Arnav, and Meng-Ling for their creative input, support, and help fostering a magnificent work environment. I would also like to thank my friends for their unwavering emotional support despite my prolonged absence in their lives. I also want to thank Ryan Bing and Sam Heath, two exemplary undergraduate researchers who demonstrated remarkable diligence and sincerity in the lab. In truth, I have learned more by working with them, and I know that they will find tremendous success in their future.

Lastly, I would like to thank my family. My parents, aunt, and uncle have been a source of utmost knowledge, support and love. In particular, I would like to thank my mother, Dr. Madhumita Ray, for her aid in editing this dissertation, and my father, Dr. Ajay Ray, for handy tips on formatting. Finally, I wish to express love and appreciation for Krina Jhala, who has been a source of happiness and calming influence during my time at Purdue. She is the reason I take the time to smell the roses along the way.

TABLE OF CONTENTS

LIST OF TABLES

LIST OF FIGURES

ABSTRACT

To compensate for their sessile existence, plants synthesize and emit a wide diversity of volatile organic compounds (VOCs) that serve important biological functions pertaining to defense, reproduction, and plant-plant signaling. In addition to their importance in plant secondary metabolism, VOCs are used as fragrances, flavoring agents, and therapeutics. Plant metabolic engineering has successfully been implemented towards the design of value-added plants with enhanced defense, improved aroma and flavor, and increased production of specialty chemicals. However, rational design requires rigorous characterization of the mechanisms controlling metabolic fluxes in a network. Thus, the major aims of this dissertation are to study biological and physical mechanisms controlling the synthesis and emission of plant VOCs. This dissertation focuses on (*i*) modeling 2-phenylethanol biosynthesis in *Arabidopsis* and (*ii*) characterization of the biophysical properties of flower cuticles with respect to the emission of VOCs.

2-Phenylethanol (2-PE) is a naturally-occurring aromatic volatile with properties that make it a candidate oxygenate for petroleum-derived gasoline. In plants, 2-PE biosynthesis competes with the phenylpropanoid pathway for the common precursor L-phenylalanine (Phe). The phenylpropanoid pathway directs up to 30% of fixed carbon towards the production of lignin, a major constituent of plant cell walls that renders biomass recalcitrant to pretreatment techniques impeding the economical production of biofuels. An initial genetic engineering approach was proposed, whereby a portion of the carbon flux towards lignin production is diverted towards the biosynthesis 2-PE. Transgenic *Arabidopsis thaliana* expressing enzymes catalyzing the biosynthetic steps from Phe to 2-PE were generated. Excised stems from transgenic Arabidopsis were supplied $^{13}C_6$-ring labeled Phe, and isotopic enrichment of downstream metabolites were quantified to calculate fluxes. By combining flux measurements with predictions from a kinetic model of the Phe metabolic network, we hypothesized that 2-PE biosynthesis in transgenic Arabidopsis was limited by endogenous pools of cytosolic Phe. Multiple independent genetic strategies were proposed based on model-guided predictions, such as inducing Phe hyper-accumulation, reduction of the activity of the competing phenylpropanoid pathway, and sequestering the 2-PE biosynthesis pathway in plastids. Combining kinetic modeling with time-course *in vivo* metabolomics led to successful rational engineering of 2-PE accumulating plants.

The plant cuticle is the physical interface between the flower and its surrounding environment. Passage of VOCs through the cuticle is driven solely by diffusion and is thus dependent on the cuticle physicochemical properties. Wax compounds in the cuticular matrix self-assemble into a multiphase system of crystalline and amorphous regions, where their relative amounts and arrangements govern VOC diffusion. To investigate the effect of wax composition on the crystallinity and permeability of the cuticle, we characterized the cuticular waxes of *Petunia hybrida* petals using GC-MS, FTIR, DSC, and XRD. Petal waxes were found to be enriched with long-chain hydrocarbons forming semi-crystalline waxes localized on petal surfaces. A ternary system of wax compounds was proposed as a model for petal cuticles to investigate the effect of wax composition on cuticle crystallinity and permeability. Atomistic simulations of VOC displacement in waxes of varying chemical composition were performed at 298 K and 1 bar under NPT conditions to estimate diffusivities. Wax anisotropy was found to be highly dependent on the elongation of methylene chains, restricting the molecular diffusion path. Changes in crystalline symmetry were found to have measurable effects on VOC diffusion. Simulations of compositional variants of the model cuticle shows that changes in relative crystallinity exert differential control on the dynamics of VOC emissions.

To directly determine the effect of the cuticle on VOC emissions in petunia flowers, the wax exporter PhABCG12 was silenced using RNA interference, resulting in flowers with thinner cuticles. However, VOC emissions were found to have significantly decreased in transgenic flowers relative to the wild-type control. Dewaxing wild-type and transgenic petunia revealed that the cuticle serves as a site of VOC build-up during emission, and deficient coverage limits the extent to which compounds can accumulate. In addition, the cuticle was found to impart differing levels of mass transfer resistance for certain VOCs, suggesting that the cuticle controls the dynamics of VOC emissions. Taken together, petal cuticles provide an additional layer of regulation in emission of VOCs from plants

CHAPTER 1. INTRODUCTION

1.1 Plant volatiles

Plants synthesize and release a bouquet of secondary metabolites classified as volatile organic compounds (VOCs) (Peñuelas & Llusià, 2004). Upwards of 36% of assimilated carbon can be directed towards the production of VOCs (Kesselmeier et al., 2002), accounting for 4-8×10^{11} kg carbon emitted annually, amounts that exceed anthropogenic methane emissions (Smith and Mueller, 2010). VOCs are extremely reactive and have short life-times in the troposphere, and can have ecological effects at the global scale and influence atmosphere chemistry (Lerdau et al., 1997; Pinto et al., 2010). Plant volatiles represent a structurally diverse group of metabolites that are categorized by their biosynthetic origin. Despite this diversity, compounds are classified as volatile based on shared physicochemical properties; they are generally (*i*) low molecular weight (30-300 Da), (*ii*) generally lipophilic (octanol-water partition coefficient > 1), and (*iii*) have relatively high vapor pressures at ambient conditions. The production of individual classes of VOCs is significantly distributed over the plant kingdom, where the assortment and quantity of VOCs released can vary between species and organs (Knudsen et al., 2006).

The advent and improvement of analytical methods such as gas chromatography (GC), mass spectrometry (MS), and nuclear magnetic resonance (NMR) have enabled scientists to profile and characterize the individual compounds found in the headspace of plants. Over the past few decades, headspace profiling has improved substantially with numerous trapping methods that have allowed for the identification and detection of VOCs with great sensitivity (Bicchi and Joulain, 1990; Knudsen et al., 1993). Thus far, over 1700 unique scent compounds have been identified in approximately 1000 flowering species and gymnosperms (Knudsen et al., 2006). While progress in detecting and identifying VOCs is relatively recent, humans have utilized floral scent compounds since antiquity (Maffei, 2010). For humans, VOCs have been a source of olfactory indulgence, and have successfully extracted and implemented floral compounds as flavoring agents, preservatives, natural remedies, floriculture, and as cosmetics (Pichersky and Gershenzon, 2002).

1.2 The integrative role of volatiles in plant secondary metabolism and ecosystems

The primary biological functions of aerial VOCs are related to secondary metabolic process including plant defense, reproduction, and signaling (Dudareva and Pichersky, 2008). As plants are sessile organisms, defense of the plant is relegated to the emissions of VOCs in response to abiotic and biotic stresses (Dudareva et al., 2006). Responses to biotic stresses include herbivory (McCall and Irwin, 2006) and pathogenic infection (Junker et al., 2011). Induced production of VOCs for plant defense is commonly characterized as direct, where plants reduce their susceptibility to attack, or indirect, where plant volatiles attract the natural predators to the attacking insect (Kessler and Baldwin, 2001). The emissions of certain volatiles have been shown to serve as airborne signals that can prime the defense of other organs of the same plant or in neighboring plants (Heil and Silva Bueno, 2007; Ton et al., 2007). Plants also release volatiles in response to abiotic stresses including flooding (Kreuzwieser et al., 2000), drought (Ebel et al., 1995), and light and temperature changes (Gouinguene and Turlings, 2002). Changes in growth and environmental conditions such as availability of nitrogen and phosphorous (Schmelz et al., 2003), soil salinity and pH, and relative humidity (Vallat et al., 2005) have also been shown to elicit changes in plant volatile metabolomes. Elevated levels of atmospheric carbon and changing global climates have also been linked to greater levels of plant volatile emissions (Scholefield et al., 2004). Other abiotic stresses such as the accumulation of reactive oxygen species (ROS) leading to degradation of macromolecules have been shown to be met with enhanced plant biosynthesis of isoprenoids (Sauer et al., 1999; Vickers et al., 2009). The photosynthetic capacity and rates of gas exchange in leaves are also associated with modulation of VOC emissions, revealing that plant volatile production is greatly linked to seasonal and day/night changes (Kuhn et al., 2004).

Plant volatile emissions are critical for plant reproduction and are released in a controlled and timely manner to attract pollinators and seed dispersers (Bolen and Green, 1997). While pollinator attraction can occur by flower color, VOC emissions are beneficial at night when visual cues are inadequate (Majetic et al., 2007). The ability for flowers to attract pollinators from a distance is speculated to be the major reason why volatile biosynthetic pathways have been conserved through natural selection (Parachnowitsch et al., 2013). Genetic manipulation of floral scent biosynthetic pathways has led to increased understanding of the specific compounds that attract certain pollinators (Pichersky and Gershenzon, 2002).

Outside of their functions in plant secondary metabolism, volatiles have notable influences on atmospheric chemistry and global climate. Oxidized volatiles released over the Amazon and other forests can react with anthropogenic aerosols to form secondary aerosols, which can influence precipitation, formations of smog, reduce atmospheric quality, and even effect the global radiative balance (Shrivastava et al., 2019). The accumulation of certain plant-emitted VOCs is known to be precursors to phytotoxic compounds that can accumulate in the local atmosphere, leading to health implications in the local populace (Padhy and Varshney, 2005). Oxidation of VOCs in the troposphere can result in the harmful production of ozone (Blande et al., 2014). While plant secondary metabolism has been shown to have significant flexibility when responding to a plethora of stresses and external signals, rapid changes in global climate may outpace this adaptability (Yuan et al., 2009). Thus, the study of plant VOC emissions and their integrated role in secondary metabolism and other ecological functions will need to account for changes in global climates and human activity.

1.3 Volatile biosynthesis

The above- and belowground surfaces of plants have an intact layer of cells that form the plant epidermis, and it is in these cells that VOCs are primarily synthesized (Effmert et al., 2006). Volatiles are released from the epidermal cells of stems, fruits, leaves, and petals into the atmosphere, and from the roots into the rhizosphere (Chen et al., 2004). As discussed earlier, compounds designated as VOCs are classified as such due to shared physical properties but can vary significantly in their molecular structure and can have significantly different biosynthetic routes. The major classes of plant VOCs include the terpenoids (moni-, di-, sesquiterpenes), phenylpropanoid/benzenoids, fatty acid-derived, amino acid-derived, as well as aliphatic hydrocarbons such as aldehydes, alcohols, alkanes, esters, and ketones (Pichersky and Gershenzon, 2002; Dudareva et al., 2006; Dudareva et al., 2013). A schematic of the major biosynthetic pathways leading to VOC production is shown in Fig. 1.1.

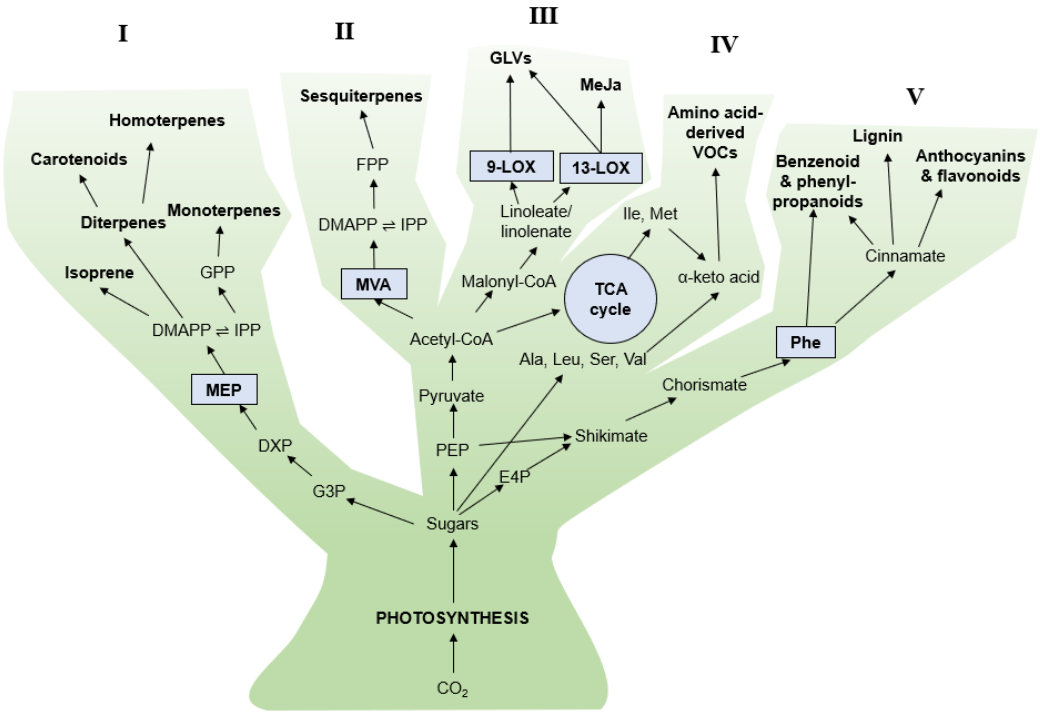

Fig. 1.1 Plant volatile biosynthetic pathways. Branches of tree represents VOCs produced by different biosynthetic pathways. Branch I represents the MEP pathway for the production of mono-, di-, and homoterpenes. Branch II represents the MVA pathway to produce sesquiterpenes. Branch III represents the production of fatty acid-derived VOCs. Branch IV represents the production of amino acid-derived VOCs. Branch V represents the production of phenylalanine derived benzenoid and phenylpropanoids. Abbreviations: DMAPP – dimethylallyl diphosphate, DXP – 1-deoxy-D-xylulose 5-phosphate, E4P – erythrose 4-phosphate, FPP – farnesyl diphosphate, G3P – D-glyceraldehyde 3-phosphate, GPP – geranyl pyrophosphate, GLV – green leaf volatiles, IPP – isopentenyl diphosphate, LOX – lipoxygenase pathway, MeJa – methyl jasmonate, PEP – phosphoenolpyruvate. Figure adapted and modified from Maffei, (2010), Dudareva et al., (2013), Villamar-Torres et al., (2018).

Terpenoids/isoprenoids represent the largest and most diverse class of secondary metabolites produced in nature (Pichersky and Raguso, 2018). Terpenoids are derived from the precursors dimethylallyl diphosphate (DMAPP) and its isomer isopentenyl diphosphate (IPP), which are synthesized by two routes: the mevalonic acid (MVA) and methylerythritol phosphate (MEP) pathways (branches I and II of Fig. 1.1). The MVA pathway is localized in the cytosol, peroxisomes, and the endoplasmic reticulum (ER), and produces the precursors involved in sesquiterpene biosynthesis (Dudareva et al., 2013). The MEP pathway is exclusively localized in the chloroplast, and synthesizes the precursors for the production of hemi-, mono-, and diterpene and some volatile carotenoid derivatives (Dudareva et al., 2013). Isotopic-labeling of MVA and MEP pathway metabolites in cotton (*Gosspium hirsutum* L.) plants revealed that the two pathways

are not completely autonomous, with subunits and precursors possibly being translocated between pathways by metabolic transporters (Opitz et al., 2014). The nature of the cross-talk between pathways is still somewhat elusive, with certain mechanisms not yet uncovered.

Another major class of volatiles is derived from the aromatic amino acid phenylalanine (Phe), a major product from the shikimate and aromatic amino acid pathway (branch III of Fig. 1.1). While biosynthesis of Phe takes place in the plastids, Phe-derived benzenoid and phenylpropanoid compounds are synthesized in the cytoplasm. Identification and characterization of the plastidial Phe exporter PhpCAT in *Petunia hybrida* flowers revealed that Phe is exported from the plastid into the cytosol (Widhalm et al., 2015a). Phe is the major precursor towards the production of the monomeric units of the biopolymer lignin, a major component of the secondary cell walls of plants. Production of Phe-derived volatiles begins with the deamination of Phe to *trans*-cinnamic acid by phenylalanine ammonia lyase (PAL). Benzenoid volatiles (C_6-C_1 backbone) are synthesized by a β-oxidative or non β-oxidative pathway, or by some combination of both (Orlova et al., 2006). Routing of metabolites through the non β-oxidative pathway is not yet fully characterized (Boatright et al., 2004). Phenylpropanoid volatiles possess a C_6-C_2 backbone, and compete with PAL for Phe availability (Kaminaga et al., 2006). In petunia flowers, Phe is directly converted into phenylacetaldehyde (PhAld) by the functional phenylacetaldehyde synthase (PAAS) catalyzing the subsequent deamination and decarboxylation of Phe (Sakai et al., 2007). The formation of the phenylpropenes (C_6-C_3 backbone) eugenol (Eug) and isoeugenol (IEug) shares common enzymatic steps with lignin biosynthesis and are derived from the phenylpropanoid pathway intermediate *p*-coumaric acid.

Oxylipins, or fatty acid-derived volatiles, are derived from polyunsaturated fatty acids (branch IV of Fig. 1.1). Precursors enter the lipoxygenase (LOX) pathway and are converted into alcohols (such as 3-hexenol) and aldehydes (such as hexenal and nonanal), esters (methyl jasmonate) (Matsui, 2006). Production of structurally different oxylipins occurs by the two independent 9-LOX and 13-LOX pathways (Howe and Schilmiller, 2002), numbered as such based on the position of the oxygenation position on the substrate carbon chain. Jasmonic acid (JA), methyl jasmonate (MeJA) and other green leaf volatiles (GLVs) are derived from α-linolenic acid via the 13-LOX pathway. Just as with the MEP and MVA isoprenoid pathways, evidence of cross-talk between the two lipoxygenase pathways exists (Zhou et al., 2014).

The synthesis of branched-chain volatiles derived from amino acids such as alanine (ALA), leucine (Leu), isoleucine (Ile), methionine (Met), and valine (Val) is found prominently in fruits (Surburg and Panten, 2005; Schwab et al., 2008). VOCs derived from these amino acids are either decarboxylated into an amine or are converted into a 2-ketoacid via an aminotransferase reaction. Amines and 2-ketoacids are subsequently converted by decarboxylation, reduction, oxidation, or esterification reactions to produce VOCs (Reineccius, 2007). Amino acid derived compounds such as isoamyl acetate, 2-methylbutyl acetate, and methyl (S)-2-methylbutanoate are volatile esters that contribute to the distinct flavors found in bananas (Surburg and Panten, 2005), apples (Dixon and Hewett, 2000), and pears (Weckerle et al., 2001), respectively. Volatiles with nitrogen- and sulfur-moieties such as indole, methanethiol, and *S*-methyl thioacetate are derived from amino acids such as tryptophan, cysteine, and methionine (Jones et al., 2004).

1.4 Volatile emission

Synthesized VOCs are emitted or secreted by specialized organs such as osmophores (Vogel, 1990) and trichomes (Levin, 1973) into the surrounding plant environment to fulfill their functions in plant secondary metabolism. In vegetables such as tomato and basil, VOCs are synthesized in glandular trichomes (Glas et al., 2012), are secreted from mechanical disruption. In leaves, controlled release of VOCs occur by the opening of the stomata (Niinemets et al., 2004). However, many plants are able to sustain high emission rates in the absence of specialized organs such as osmophores, glandular trachomes, or during limited stomatal conductance, thus requiring them to diffuse through a composite layer known as the plant cuticle. The rate of volatile emission is determined by both their rate of biosynthesis and their rate of export out of epidermal cells. VOCs are predominantly synthesized in the cytosol of epidermal cells, and must traverse the cytosol, lipid bilayer, aqueous cell wall, and in many cases, the waxy cuticle (Jetter, 2006). As VOCs are generally small molecules and can readily volatilize into the gas phase, it was assumed that the compounds would freely diffuse through individual subcellular layers. Thus, the rate of emissions are dictated by the diffusive resistance imparted by the plasma membrane, cell wall and cuticle. To test this assumption, a Fick's law model for VOC diffusion was applied to observed floral scent emissions (Widhalm et al., 2015b). It was determined that for flowers to sustain their apparent emission rates, VOCs would need to accumulate to levels that would be considered toxic to their internal membranes. It was therefore hypothesized that VOC emissions are reliant on more

than just simple diffusion to sustain emission rates; biological mechanisms such as active and facilitated transport would be needed to supplement diffusive mass transfer. In addition to VOCs, epidermal cells synthesize a diverse array of aliphatic compounds that comprised the composite layers of the plant cuticle. Due to their hydrophobic properties, cuticular components are suspected to be trafficked through the cytoplasm (Pulsifer et al., 2012), exported through the plasma membrane by adenosine triphosphate (ATP)-binding cassette (ABC) transporters (Pighin et al., 2004; Bird et al., 2007), and then shuttled through the aqueous cell wall via lipid-transfer proteins (LTPs) (Debono et al., 2009; Kim et al., 2012) before they self-assemble to form the cuticle. As both cuticle compounds and VOCs have low aqueous partitioning, the alternative modes of VOC mass transfer were proposed (Fig. 1.2).

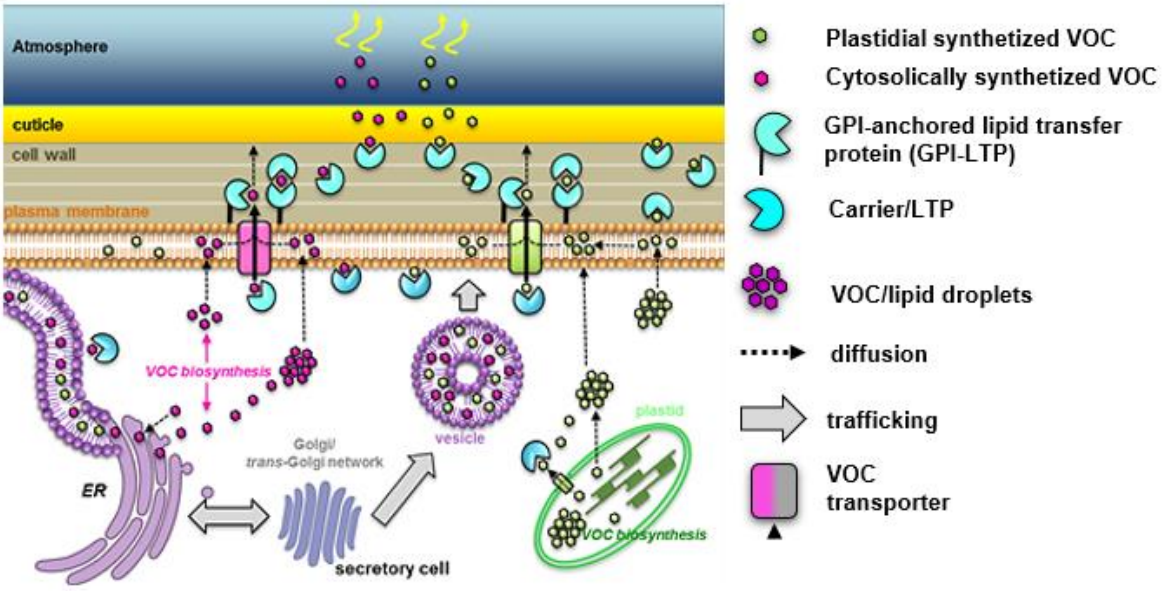

Fig. 1.2 Proposed modes for VOC subcellular translocation in plant cells. VOCs can diffuse (dashed arrows) in subcellular compartments or be trafficked via facilitated protein carriers or by vesicle trafficking (block arrows). Membrane-bound transporters export VOCs through the plasma membrane. Lipid transfer proteins (LTPs) can aid in the transport of VOCs in aqueous regimes such as the cytosol and cell wall. VOCs must diffuse through the cuticle prior to release into the atmosphere. Figure adapted from Widhalm et al. (2015b).

Upon synthesis in the cytoplasm (or plastids), VOCs must first reach the plasma membrane. The possibility of vesicle trafficking has been proposed for other compounds that are known to be secreted such as hormones (Geldner et al., 2001), pigments (Zhao and Dixon, 2010), and cuticular waxes (McFarlane et al., 2014). However, these compounds are generally large molecules and

likely have lower aqueous diffusivity than the much smaller VOCs. Nonetheless, if ER and *trans*-Golgi network vesicle trafficking exists for other compounds, it is possible for VOCs to be trafficked to the plasma membrane. VOCs, in particular those containing aromatic groups, are known to disrupt and eventually rupture lipid bilayers if they are allowed to accumulate to certain levels (Sikkema et al., 1995). Due to their lipophilicity, VOCs will readily partition into lipids and other organic phases. To alleviate potential toxic-levels of accumulation, candidate ABC transporters in petunia flowers were characterized (Adebesin et al., 2017). Down-regulation of PhABCG1 was found to significantly reduce VOC emission rates and damage to the plasma membrane was noted, providing evidence that active transport contributes to the VOC export network.

Upon export from the plasma membrane, VOCs must cross the aqueous cell wall. Although the diffusive resistance is relatively low for VOCs in this region, their preference towards organic layers could result in back-partitioning towards the plasma membrane. Thus, the possibility of LTPs facilitating the diffusion of VOCs towards the surface was proposed. LTPs are relatively low molecular weight proteins (7-30 Da) that possess a large hydrophobic cavity capable of accommodating long-chain hydrocarbons (Finkina et al., 2016). Most plant LTPs are non-specific with respect to their binding with ligands, as the binding is purely based on hydrophobic interactions. Thus, if LTPs are active during scent emission, it is conceivable that VOCs can bind to these hydrophobic cavities.

Finally, VOCs must diffuse through the cuticle covering the surfaces of the epidermis. As the cuticle is almost purely organic, biological components such as proteins cannot be involved in the transport through this layer. Thus, the diffusion of VOCs is dependent on the properties of the cuticle. The structure of the cuticle is highly heterogeneous; the majority is made up of the biopolymer cutin, which is interspersed and embedded with wax compounds. Many of these wax compounds form highly crystalline rafts that are believed to exclude diffusion altogether, and thus, the cuticle is suspected to impart significant mass transfer resistance (Jeffree, 1996). As the extent to which this cuticle is crystalline is dependent on the relative mixture and distribution of wax compounds, it is suspected that the composition of the cuticle is a greater determinant into the diffusivity of compounds than the actual thickness of the cuticle (Riederer and Schreiber, 2001).

1.5 Engineering floral scent

While the emissions of plants have no immediate impact on human activities, growing demand for natural products have led to significant advancements towards the engineering of other metabolic processes of organisms. Improved genomic, transcriptomic and metabolomics techniques have provided significant information relating to VOC biosynthetic pathways and their regulation. VOC biosynthetic pathways in plants have been engineered for a variety of purposes such as enhancing scent (Zuker et al., 2002), improving resistance to pathogens (Wang et al., 2004), attraction of pollinators (Kessler et al., 2008), improvement of flavor (Davidovich-Rikanati et al., 2007), or the production of valuable chemicals (Gigot et al., 2010).

The successful genetic manipulation of VOC metabolic pathways requires significant understanding into the regulation and mechanisms governing these pathways. The effective transformation of plants is thus reliant on rational metabolic engineering approaches, where the results from genetic perturbations can be predicted by mechanistic models of metabolism. To parameterize predictive mathematical models, physiologically relevant parameters such as kinetic rate constants, protein turnover rates, transcriptional regulation, and mass transfer coefficients need to be measured. The integrative approach of predictive modeling with –omics techniques will allow for the generation of more novel transformations with increased ability to fine-tune the production of desired bio-chemicals. Future efforts to meet the demand for natural plant-derived products will necessitate the concerted efforts of scientists across all disciplines.

1.6 Motivation and research objectives

This dissertation seeks to use mechanistic models for the purposes of harnessing plant metabolism towards the production of economically viable compounds and to understand physical phenomena in the plant epidermis relating to the emissions of VOCs. Using a combination of analytical chemistry, computational chemistry, and physical characterization methods we seek to parameterize models for (*i*) increasing VOC biosynthesis and (*ii*) understand the barrier properties of the cuticle as it relates to VOC emissions.

The objectives can be summarily described by the following:

(1) To combine a kinetic modeling approach with *in vivo* metabolomics to implement rational engineering strategies leading towards the increased production of a valuable VOC, 2-phenylethanol, in *Arabidopsis thaliana*.
(2) To characterize the physical and chemical properties of the cuticles of *Petunia hybrida* flowers.
(3) To calculate the diffusion coefficients of petunia VOCs in atomistic simulations to determine the factors that control VOC emissions.
(4) To evaluate the effect of genetically modified petunia cuticles on the emissions of VOCs.

1.7 Organization of dissertation

This dissertation entitled "Modeling Biosynthesis and Transport of Volatile Organic Compounds in Plants" is structured in the following manner. Chapter 2, titled "Model-guided metabolic engineering of increased 2-phentylethanol production in plants" details the introduction of a pathway towards 2-phenylethanol in Arabidopsis and its effect on lignin production. Chapters 3-5, titled "Physical and structural characterization of flower cuticles", "Molecular dynamics of volatile organic compounds in the epicuticle of plant epidermal cells", and "Thermotropic polymorphism of plant cuticles", respectively, cover the experiments performed to characterize the chemical and physical properties of petunia petal cuticles, formulate a model system representing the molecular arrangements of the cuticle, and molecular dynamics (MD) simulations performed to measure the diffusion of VOCs. Analysis of cuticle phase behavior and crystallinity are discussed in detail. Chapters 6 and 7 titled "Cuticle thickness affects the dynamics of volatile emission from petunia flowers into the atmosphere" and "Characterizing the phenotypes of genetically modified plant cuticles", respectively, detail the analysis of petunia flowers with genetically altered cuticles. Chapter 7 also includes a perspective on the effects of genetically modified cuticles in relation to plant secondary metabolism.

1.8 References

Adebesin F., Widhalm JH., Boachon B., Lefèvre F., Pierman B., Lynch JH., Alam I., Junqueira B., Benke R., Ray S., Porter JA., Yanagisawa M., Wetzstein HY., Morgan JA., Boutry M., Schuurink RC., Dudareva N. (2017) Emission of volatile organic compounds from petunia flowers is facilitated by an ABC transporter. *Science, 356* (6345), 1386-88

Bicchi C., Joulain D. (1990) Headspace gas chromatographic analysis of medicinal and aromatic plants and flowers. *Flavour and Fragrance Journal, 5*, 131-45

Bird D., Beisson F., Brigham A., Shin J., Greer S., Jetter R., Kunst L., Wu X., Yephremov A., Samuels L. (2007) Characterization of Arabidopsis ABCG11/WBC11, an ATP binding cassette (ABC) transporter that is required for cuticular lipid secretion. *Plant Journal, 52,* 485-98

Blande JD., Tiiva P., Oksanen E., Holopainen JK. (2007) Emission of herbivore-induced volatile terpenoids from two hybrid aspen (*Populus tremula* × *tremuloides*) clones under ambient and elevated ozone concentrations in the field. *Global Change Biology, 13*, 2538-50

Boatright J., Negre F., Chen XL., Kish CM., Wood B., Peel G., Orlova I., Gang D., Rhodes D., Dudareva N. (2004) Understanding in vivo benzenoid metabolism in petunia petal tissue. *Plant Physiology, 135*, 1993–2011

Bolen RH., Green SM. (1997) Use of olfactory cues in foraging by owl monkeys (*Aotus nancymai*) and capuchin monkeys (*Cebus paella*). *Journal of Comparative Psychology, 111* (2), 152-8

Chen F. (2004) Characterization of a Root-Specific Arabidopsis Terpene Synthase Responsible for the Formation of the Volatile Monoterpene 1,8-Cineole. *Plant Physiology, 135* (4), 1956-66

Davidovich-Rikanati R., Sitrit Y., Tadmor Y., Iijima Y., Bilenko N., Bar E., Carmona B., Fallik E., Dudai N., Simon JE., Pichersky E., Lewinsohn E. (2007) Enrichment of tomato flavor by diversion of the early plastidial terpenoid pathway. *Nature Biotechnology, 25* (8), 899–901

DeBono A., Yeats TH., Rose JK., Bird DA., Jetter R., Kunst L., Samuels L. (2009) Arabidopsis LTPG is a glycosylphosphatidylinositol-anchored lipid transfer protein required for export of lipids to the plant surface. *Plant Cell, 21*, 1230-38

Dudareva N., Klempien A., Muhlemann JK., Kaplan I. (2013) Biosynthesis, function and metabolic engineering of plant volatile organic compounds. *New Phytologist, 198* (1), 16-32

Dudareva N., Negre F., Nagegowda DA., Orlova I. (2006) Plant volatiles: Recent advances and future perspectives. *Critical Reviews in Plant Sciences, 25*, 417-40

Dudareva N., Pichersky E. (2008) Metabolic engineering of plant volatiles. *Current Opinion in Biotechnology, 19* (2), 181-9

Ebel RC., Mattheis JP., Buchanan DA. (1995) Drought stress of apple-trees alters leaf emissions of volatile compounds. *Physiologia Plantarum, 93*, 709-12

Effmert U., Buss D., Rohrbeck D., Piechula B. (2006) Localization of the Synthesis and Emission of Scent Compounds within the Flower. In: N Dudareva, E Pichersky, eds, Biology of Floral Scent. London: Taylor & Francis Group, 105–24

Finkina EI., Melnikova DN., Bogdanov IV., Ovchinnikova TV. (2016) Lipid Transfer Proteins As Components of the Plant Innate Immune System: Structure, Functions, and Applications. *ActaNaturae*, *8* (2), 47-61

Geldner N., Friml J., Stierhof YD., Jürgens G., Palme K. (2001) Auxin transport inhibitors block PIN1 cycling and vesicle trafficking. *Nature*, *413*, 6854

Gigot C., Ongena M., Fauconnier ML., Wathelet JP., du Jardin P., Thonart P. (2010) The lipoxygenase metabolic pathway in plants: potential for industrial production of natural green leaf volatiles. *Biotechnologie, Agronomie, Société et Environnement*, *14* (3), 451-60

Glas JJ., Schimmel BCJ., Alba JM., Escobar-Bravo R., Schuurink RC., Kant MR. (2012) Plant Glandular Trichomes as Targets for Breeding or Engineering of Resistance to Herbivores. *International Journal of Molecular Sciences*, *13* (12), 17077-103

Gouinguene SP., Turlings TCJ. (2002) The effects of abiotic factors on induced volatile emissions in corn plants. *Plant Physiology*, *129*, 1296-1307

Heil M., Silva Bueno JC. (2007) Within-plant signaling by volatiles leads to induction and priming of an indirect plant defense in nature. *Proceedings of the National Academy of Sciences of the United States of America*, *104*, 5467-72

Howe GA., Schilmiller AL. (2002) Oxylipin metabolism in response to stress. *Current Opinion in Plant Biology*, *5* (3), 230-6

Jeffree CE. (1996) Structure and ontogeny of plant cuticles. In Kerstiens G ed; Plant cuticle: an integrated functional approach. BIOS Scientific publishers, Oxford. pp. 33–82

Jetter R., Kunst L., Samuels AL. (2006) Composition of plant cuticular waxes. In M Riederer, C Müller, eds, Biology of the Plant Cuticle. Blackwell, Oxford, pp 145–181

Jones MG., Hughes J., Tregova A., Milne J., Tomsett AB., Collin HA. (2004) Biosynthesis of the flavor precursors of onion and garlic. *Journal of Experimental Botany*, *55*, 1903-18

Junker RR., Loewel C., Gross R., Dötterl S., Keller A., Blüthgen N. (2011) Composition of epiphytic bacterial communities differs on petals and leaves. *Plant Biology*, *13*, 918-24

Kaminaga Y, Schnepp J, Peel G, Kish CM, Ben-Nissan G, Weiss D, Orlova I, Lavie O, Rhodes D, Wood K., Porterfield DM., Cooper AJ., Schloss JV., Pichersky E., Vainstein A., Dudareva N. (2006) Plant phenylacetaldehyde synthase is a bifunctional homotetrameric enzyme that catalyzes phenylalanine decarboxylation and oxidation. *Journal of Biological Chemistry*, *281*, 23357–66

Kesselmeier J., Ciccioli P., Kuhn U., Stefani P., Biesenthal T., Rottenberger S., Wolf A., Vitullo M., Valentini R., Nobre A., Kabat P., Andreae MO. (2002) Volatile organic compound emissions in relation to plant carbon fixation and the terrestrial carbon budget. *Global Biogeochemical Cycles*, *16* (4), 1126

Kessler A., Baldwin IT. (2001) Defensive function of herbivore-induced plant volatile emissions in nature. *Science*, *291* (5511), 2141-4

Kim H., Lee SB., Kim HJ., Min MK., Hwang I., Suh MC. (2012) Characterization of glycosylphosphatidylinositol-anchored lipid transfer protein 2 (LTPG2) and overlapping function between LTPG/LTPG1 and LTPG2 in cuticular wax export or accumulation in Arabidopsis thaliana. *Plant Cell and Physiology*, *53*, 1391-1403

Knudsen JT, Tollsten L., Bergström G. Floral scent: a checklist of volatile compounds isolated by headspace techniques. *Phytochemistry*, *33* (2), 253-80

Knudsen JT., Eriksson R., Gershenzon J., Ståhl B. (2006) Diversity and distribution of floral scent. *The Botanical Review*, *72* (1), 1-120

Kreuzwieser J., Kuhnemann F., Martis A., Rennenberg H., Urban W. (2000) Diurnal pattern of acetaldehyde emission by flooded poplar trees. *Physiologia Plantarum*, *108*, 79-86

Kuhn U., Rottenberger S., Biesenthal T., Wolf A., Schebeske G., Ciccioli P., Kesselmeier J. (2004) Strong correlation between isoprene emission and gross photosynthetic capacity during leaf phenology of the tropical tree species *Hymenaea courbaril* with fundamental changes in volatile organic compounds emission composition during early leaf development. *Plant Cell and Environment*, *27*, 1469-85

Lerdau M., Guenther A., Monson R. (1997) Plant production and emission of volatile organic compounds: Plant-produced hydrocarbons influence not only the plant itself but the atmosphere a well. *BioScience*, *47* (6), 373-83

Levin RA., McDade LA., Raguso RA. (2003) The Systematic Utility of Floral and Vegetative Fragrance in Two Genera of Nyctaginaceae, *Systematic Biology*, *52* (3), 334-51

Maffei ME. (2010) Sites of synthesis, biochemistry and functional role of plant volatiles. South African Journal of Botany, *76* (4), 612-31

Majetic CJ., Raguso RA., Tonsor SJ., Ashman TL. (2007) Flower color-flower scent associations in polymorphic *Hesperis matronalis* (Brassicaceae), *Phytochemistry*, 68, 865-74

Matsui K (2006) Green leaf volatiles: hydroperoxide lyase pathway of oxylipin metabolism. *Current Opinion in Plant Biology*, *9* (3), 374-80

McCall AC., Irwin RE. (2006) Florivory: the intersection of pollination and herbivory. *Ecology Letters*, *9* (12), 1351-65

McFarlane HE., Watanabe Y., Yang W., Huang Y., Ohlrogge J., Samuels AL. (2014) Golgi- and trans-Golgi network-mediated vesicle trafficking is required for wax secretion from epidermal cells. *Plant Physiology*, *164* (3), 1250-60

Niinemets U., Loreto F., Reichstein M. (2004) Physiological and physicochemical controls on foliar volatile organic compound emissions. *Trends in Plant Science*, *9* (4), 180-6

Opitz S., Nes WD., Gershenzon J. (2014) Both methylerythritol phosphate and mevalonate pathways contribute to biosynthesis of each of the major isoprenoid classes in young cotton seedlings. *Phytochemistry*, *98*, 110-19

Orlova I., Marshall-Colon A., Schnepp J., Wood B., Varbanova M., Fridman E., Blakeslee JJ., Peer WA., Murphy AS., Rhodes D., Pichersky E., Dudareva N. (2006) Reduction of benzenoid synthesis in petunia flowers reveals multiple pathways to benzoic acid and enhancement in auxin transport. *Plant Cell*, *18*, 3458–75

Padhy PK., Varshney CK. (2005) Emission of volatile organic compounds (VOC) from tropical plant species in India. *Chemosphere, 59*, 1643-53

Parachnowitsch AL., Burdon RCF., Raguso RA., Kessler A. (2013) Natural selection on floral volatile production in Penstemon digitalis. *Plant Signaling and Behavior, 8* (1), 137-40

Peñuelas J., Llusià J. (2004) Plant VOC emissions: making use of the unavoidable. *Trends in Ecology & Evolution*, *19* (8), 402-4

Pichersky E., Gershenzon J. (2002) The formation and function of plant volatiles: perfumes for pollinator attraction and defense. *Current Opinion in Plant Biology*, *5* (3), 237-43

Pichersky E., Raguso RA. (2018) Why do plants produce so many terpenoids compounds? *New Phytologist, 220* (3), 692-702

Pighin JA., Zheng H., Balakshin LJ., Goodman IP., Western TL., Jetter R., Kunst L., Samuels AL. (2004) Plant cuticular lipid export requires an ABC transporter. *Science, 306*, 702-4

Pinto DM., Blande JD., Souza SR., Nerg AM., Holopainen JK. (2010) Plant volatile organic compounds (VOCs) in ozone (O3) polluted atmospheres: the ecological effects. *Journal of Chemical Ecology, 36* (1), 22-34

Pulsifer IP., Kluge S., Rowland O. (2012) Arabidopsis long-chain acyl-CoA synthetase 1 (LACS1), LACS2, and LACS3 facilitate fatty acid uptake in yeast. *Plant Physiology and Biochemistry, 51*, 31–9

Reineccius GA. (2006) Flavour-Isolation Techniques. In: Berger RG., eds, Flavours and Fragrances. Springer, Berlin, Heidelberg

Riederer M., Schreiber L. (2001). Protecting against water loss: analysis of the barrier properties of plant cuticles. *Journal of Experimental Botany, 52* (363), 2023–2032

Sakai M., Hirata H., Sayama H., Sekiguchi K., Itano H., Asai T., Dohra H., Hara M., Watanabe N. (2007) Production of 2-phenylethanol in roses as the dominant floral scent compound from L-phenylalanine by two key enzymes, a PLP-dependent decarboxylase and a phenylacetaldehyde reductase. *Bioscience, Biotechnology, and Biochemistry, 71* (10), 2408-19

Sauer F, Schafer C, Neeb P, Horie O, Moortgat GK. (1999) Formation of hydrogen peroxide in the ozonolysis of isoprene and simple alkenes under humid conditions. *Atmospheric Environment, 33*, 229-41

Schmelz EA., Alborn HT., Engelberth J., Tumlinson JH. (2003) Nitrogen deficiency increases volicitin-induced volatile emission, jasmonic acid accumulation, and ethylene sensitivity in maize. *Plant Physiology, 133*, 295-306

Scholefield PA., Doick KJ., Herbert BMJ., Hewitt CNS., Schnitzler JP., Pinelli P., Loreto F. (2004) Impact of rising CO_2 on emissions of volatile organic compounds: isoprene emission from *Phragmites australis* growing at elevated CO_2 in a natural carbon dioxide spring. *Plant Cell and Environment, 27*, 393-401

Shrivastava M., Andreae MO., Artaxo P., Barbosa HMJ., Berg LK, Brito J., Ching J., Easter RC., Fan J., Fast JD., Feng Z., Fuentes JD., Glasius M., Goldstein AH., Alves EG., Gomes H., Gu D., Guenther A., Jathar SH., Kim S., Liu Y., Lou S., Martin ST., McNeill VF., Medeiros A., de Sá SS., Shilling JE., Springston SR., Souza RAF., Thornton JA., Isaacman-VanWertz G., Yee LD., Ynoue R., Zaveri RA., Zelenyuk A., Zhao C. (2019) Urban pollution greatly enhances formation of natural aerosols over the Amazon rainforest. *Nature Communications, 10*

Sikkema J., de Bont JA., Poolman B. (1995) Mechanisms of membrane toxicity of hydrocarbons. *Microbiology Reviews, 59* (2), 201-22

Smith SN., Mueller SF. (2010) Modeling natural emissions in the Community Multiscale Air Quality (CMAQ) Model–I: building an emissions data base. *Atmospheric Chemistry and Physics, 10,* 4931-52

Surburg H., Panten J., eds, (2005) Common Fragrance and Flavor Materials: Preparation, Properties and Uses. Wiley-VCH: Weinheim, Germany

Ton J., D'Alessandro M., Jourdie V., Jakab G., Karlen D., Held M., Mauch-Mani B.,Turlings TCJ (2007) Priming by airborne signals boosts direct and indirect resistance in maize. *Plant Journal, 49,* 16-26

Vallat A., Gu HN., Dorn S. (2005) How rainfall, relative humidity and temperature influence volatile emissions from apple trees in situ. *Phytochemistry, 66,* 1540-1550

Vickers CE., Gershenzon J., Lerdau MT., Loreto F. (2009) A unified mechanism of action for volatile isoprenoids in plant abiotic stress. *Nature Chemical Biology, 5,* 283-91

Villamar-Torres R., Jazayeri SM., Liuba-Delfini G., Cruzaty LCG., Viot C-R. (2018) Volatile organic compounds: plant natural defense mechanisms against herbivorous arthropods and an opportunity for plant breeding of cotton. *Scientie Agropecuaria, 9* (2), 287-97

Vogel S. (1990) The role of scent glands in pollination: on the structure and function of osmophores. Amerind, New Delhi

Weckerle B., Bastl-Borrmann R., Richling E., Hör K., Ruff C., Schreier P. (2001) Cactus pear (*Opuntia ficus indica*) flavor constituents: Chiral evaluation (MDGC-MS) and isotope ratio (HRGC-IRMS) analysis. *Flavour and Fragrance Journal, 16,* 360-63

Widhalm JR., Gutensohn M., Yoo H., Adebesin F., Qian Y., Guo L., Jaini R., Lynch JH., McCoy RM., Shreve JT., Thimmapuram J., Rhodes D., Morgan JA., Dudareva N. (2015a) Identification of a plastidial phenylalanine exporter that influences flux distribution through the phenylalanine biosynthetic network. *Nature Communications, 6,* 8142

Widhalm JR., Jaini R., Morgan JA., Dudareva N. (2015b) Rethinking how volatiles are released from plant cells. *Trends in Plant Science, 20* (9), 545-50

Yuan JS., Himanen SJ., Holopainen JK., Chen F., Stewart CN Jr. (2009) Smelling global climate change: mitigation of function for plant volatile organic compounds. *Trends in Ecology & Evolution, 24* (6), 323-31

Zhao Q., Dixon RA. (2011) Transcriptional networks for lignin biosynthesis: more complex than we thought? *Trends in Plant Science, 16* (4), 227-33

Zuker A., Tzfira T., Ben-Meir H., Ovadis M., Shklarman E., Itzhaki H., Forkmann G., Martens S., Neta-Sharir I., Weiss D., Vainstein A. (2002) Modification of flower color and fragrance by antisense suppression of the flavanone 3-hydroxylase gene. *Molecular Breeding*, *9*, 33–41

CHAPTER 2. MODEL-GUIDED METABOLIC ENGINEERING OF INCREASED 2-PHENYLETHANOL PRODUCTION IN PLANTS

2.1 Abstract

2-Phenyletahnol (2-PE) is a natural aromatic with properties that make it a candidate oxygenate for petroleum-derived gasoline. In plants, 2-PE biosynthesis competes with the phenylpropanoid pathway for the common precursor phenylalanine. The plant phenylpropanoid pathway directs significant carbon flux towards the production of lignin, a major biopolymer in plant cell walls that impedes the process of biofuel production. We therefore proposed a genetic engineering strategy at the phenylalanine branch point, whereby a portion of the carbon flux towards lignin biosynthesis is diverted towards the production of an economically viable product, 2-PE. Transgenic *Arabidopsis thaliana* were generated that overexpress aromatic aldehyde synthase (AAS) in tandem with tomato phenylacetaldehyde reductase (PAR) introducing a pathway to produce 2-PE. To analyze the competition between lignin and 2-PE biosynthesis, excised stems and leaves were exogenously fed with $^{13}C_6$-ring labeled phenylalanine, and isotopic enrichment of downstream metabolites were quantified in time-course to calculate fluxes. Combining metabolic flux analysis with the kinetics of pathway enzymes revealed that endogenous phenylalanine limits 2-PE production. This prediction was tested by combining the overexpression of PAR/AAS with: (1) the overexpression of a feedback-insensitive 3-deoxy-D-arabino-heptulosonate 7-phosphate (DAHP) synthase known to have hyper-induced phenylalanine biosynthesis, and (2) with the double mutant *pal1 pal2* known to have reduced activity of the competing enzyme, phenylalanine ammonia lyase (PAL). Furthermore, to evaluate the effect of subcellular partitioning on the extent of competition between PAL and AAS, the PAR/AAS tandem overexpression construct was fused to chloroplast transit peptides to localize 2-PE biosynthesis in plastids. The high accumulation of plastidial phenylalanine combined with the lack of competition from cytosolic PAL resulted in significantly elevated 2-PE levels validating the predictions derived from kinetic modeling. Combining kinetic modeling with time-course *in vivo* metabolomics led to successful rational engineering of 2-PE accumulating plants.

2.2 Introduction

2.2.1 2-Phenylethanol from lignocellulosic feedstock

2-Phenylethanol (2-PE) is a naturally occurring aromatic compound with a distinctive "rose-like" odor used as in cosmetics, fragrances, flavoring, and as an anti-microbial agent (Etschmann et al., 2002; Stark et al., 2002; Masuo et al., 2015). 2-PE is also readily converted into styrene, ethyl benzene and 2-phenylethyl acetate, compounds that are typically derived as byproducts of crude oil refining (Hua et al., 2011; Shen et al., 2016). Additionally, 2-PE is considered an alternative to ethanol as an oxygenate for petroleum-derived gasoline due to its higher energy density, lower volatility, and lower hygroscopicity (Atsumi et al., 2008). While the uses of 2-PE are broad and diverse, most of the >10,000 tons produced per year globally (Hua and Xu, 2011) is synthetically derived, produced primarily from compounds downstream of petroleum refinery. Since its discovery in 1876, numerous organic synthesis reactions have been developed for the economic production of 2-PE (Bedoukian, 1986). Presently, most 2-PE synthesized chemically comes from the Friedel-Crafts reaction of ethylene oxide and benzene in the presence of aluminum chloride (Etschmann et al., 2002). Although inexpensive, the low selectivity, accumulation of toxic byproducts, high temperature and pressure, as well as the use of strong acids, make the chemical production of 2-PE less attractive. A major concern during chemical synthesis of 2-PE is purification; poor separation from byproducts can result in a final product with off-odors that are undesirable for fragrance and flavoring industries (Clark, 1990). As a result, synthetic 2-PE is significantly cheaper than naturally derived 2-PE (USD $5/kg vs. $1000/kg, Wang et al., 2019), making the economic production of natural 2-PE enticing. With the natural flavors and fragrance industries set to reach $700 million by 2020 (Pandal, 2014), harnessing metabolism for the enhanced production of 2-PE is an attractive option.

Various microorganisms including bacteria (Zhang et al., 2014), filamentous fungi (Wani et al., 2010; Celinska et al., 2013; Etschmann et al., 2015) and yeast (Gethins et al., 2015) possess some of the pre-requisite genes necessary for 2-PE biosynthesis. Among the reported 2-PE producers, yeast such as *Saccharomyces cerevisiae* and *Yarrowia lipolytica* are the most efficient strains (Etschmann et al., 2004). Previous studies have shown that yeast can convert L-phenylalanine (Phe) into 2-PE via the linear Ehrlich pathway which converts amino acids into alcohols via sequential trans-amination, decarboxylation, and dehydrogenation (Hazelwood et al.,

2008). Various genetic engineering methods such as the alleviation of feedback inhibition, improvement of precursor transport, enhancing enzyme activity, and reduction of competing pathways have led to significant improvement in the yield and productivity of 2-PE in microbes (Wang et al., 2019). Methods such as high-throughput screening of high-performance strains, random mutagenesis, and bioprocess optimization have also led to significant improvement in 2-PE production using microorganisms (Martinez-Avila et al., 2018; Wang et al., 2019).

While many microbial 2-PE producing strains have resulted in high yields, there are certain limitations such as the need for complex culture techniques that can render the process economically unfavorable. Additionally, 2-PE is inherently anti-microbial, resulting in toxicity to the culture after a certain accumulation (Etschmann et al., 2002). In contrast, plants can synthesize 2-PE without the need of any exogenously supplied precursors, limiting the feed cost necessary for production. Plants have also been shown to sequester 2-PE in a non-toxic form by *in planta* derivatization allowing for continued production and storage of the desired compound (Hayashi et al., 2004). However, our interest in engineering a 2-PE pathway into plants is to introduce a metabolic sink to divert carbon flux away from the biosynthesis of the hetero-aromatic biopolymer lignin. Lignin is the second most abundant biopolymer on the planet and is found in the secondary cell wall of plants. Lignin plays important roles in the reinforcement of the plant cell wall, water transport, and defense against abiotic and biotic stresses (Douglas, 1996; Boerjan et al., 2003). However, its abundance in the cell wall renders lignocellulosic feedstock recalcitrant to enzymatic hydrolysis, greatly limiting the production of biofuels (Chapple et al., 2007; Vanholme et al., 2008). In order to achieve effective hydrolysis, lignocellulosic biomass is subjected to pretreatment techniques to reduce the binding between lignin and the polysaccharides needed for ethanol production. Pretreatment techniques can be mechanical, physicochemical, chemical or biological, and accounts for up to 20% of the total cost of ethanol production, reducing the economic viability of biofuels (Loqué et al., 2015). Research into cost-effective pretreatment strategies and other steps have been shown to improve the productivity of the process (Mosier et al., 2005; da Costa Sousa et al., 2009), however, genetic engineering of plant cell walls to obtain feedstock more amenable to saccharification is another viable strategy (Li et al., 2008). Genetic manipulation of lignin amount and composition has been shown to be a promising strategy for increasing biomass saccharification (Bonawitz and Chapple, 2013). Previous studies have shown that downregulation or knockout of lignin biosynthetic genes in tobacco (Sewalt et al., 1997), poplar (Jouanin et al.,

2000), switchgrass (Fu et al., 2011) and alfalfa (Reddy et al., 2005) have led to improvements in pulping efficiency, forage digestibility, and ethanol production.

Lignin is a cross-linked polymer of phenolic alcohols synthesized from the phenylpropanoid pathway (Fig. A1) which starts with the deamination of the aromatic amino acid Phe, a common precursor needed for 2-PE biosynthesis. 2-PE synthesis must thus compete with the lignin biosynthesis pathway for Phe availability, limiting the amount that can be synthesized. However, plants can direct up to 30% of fixed carbon towards the production of lignin (Chapple et al., 2007), making it conceivable that some of that high carbon flux can be re-directed towards the production of 2-PE. Diverting carbon flux away from lignin and towards 2-PE can lead to lignocellulosic biomass with increased saccharification efficiency and increased accumulation of a valuable biochemical enhancing the value of the biomass. There is no deficit in the energetic cost to re-direct carbon flux away from lignin towards 2-PE (Table 2.1), so in theory, the biomass amount should remain the same. Under light or carbon limited conditions, for every percent of total lignin mass decreased between 0.65-0.70 g of 2-PE may be produced (Fig. 2.1). One concern to this strategy is that plants with deficit lignin content can express dwarfism or a stunted phenotype, due to reduced mechanical support, increased risk of disease, and poor control on the plant water balance (Pederson et al., 2005). However, there is no significant correlation between lignin content and biomass (Novaes et al., 2009), and there are many instances of transgenic plants with reduced lignin content with limited or negligible sacrifice in biomass yield (Rohde et al., 2004).

Table 2.1 – Substrate and energetic (in moles) cost to make a mole of 2-PE or lignin (full substrate balance available in Appendix A)

Substrate	CO_2	ATP	NADPH + NADH	O_2	H_2O
Lignin	10.118	35.29	27.472	2.118	15.354
2-Phenylethanol	8	29	21	1	14

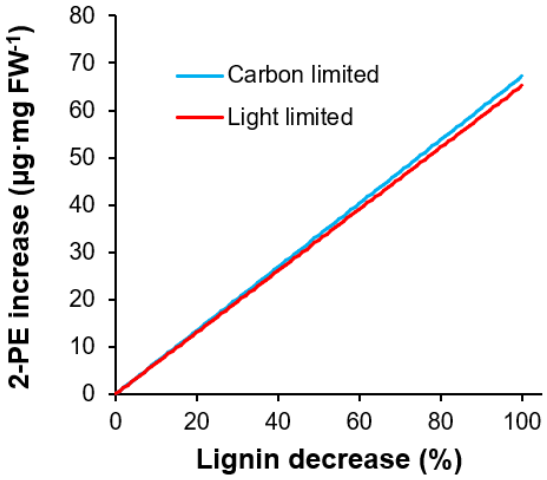

Fig. 2.1 - 2-PE accumulation as a function of total lignin (weight %) decrease under light and carbon limiting conditions. Slopes of the lines are calculated from ratio of carbon fixed (carbon limited) and ratio of ATP spent (light limited).

2.2.2 Engineering 2-PE pathways in plants

2-PE is found in the headspace or natural oils of many flowering species such as rose, carnation, hyacinth, orange blossom, geranium, and champaca (Kaminaga et al., 2006). While the biosynthetic routes and genes vary between species, 2-PE is always derived from the aromatic amino acid Phe. Few of the different biosynthetic pathways towards 2-PE have been identified in plants (Fig. 2.2). One pathway consists of an enzyme of the CYP79 family responsible for the oxidative decarboxylation of Phe to phenylacetaldoxime, which may then be hydrolyzed to the intermediate phenylacetaldehyde (PhAld), and subsequently reduced by an alcohol dehydrogenase into 2-PE (Irmisch et al., 2013). Identification of an aromatic amino acid transaminase (AAAT) in melon suggests that a native Ehrlich pathway may exist in some plants (Gonda et al., 2010). In tomatoes, an aromatic amino acid decarboxylase (AADC) which converts Phe into 2-phenylethylamine was identified, which is then converted into PhAld by a monoamine oxidase (MAO), and then reduced into 2-PE by a phenylacetaldehyde reductase (PAR) (Tieman et al., 2006). The major known pathway in rose and petunia is via the bifunctional enzyme aromatic aldehyde synthase (AAS, or more specifically, phenylacetaldehyde synthase, PAAS) (Kaminaga et al., 2006; Sakai et al., 2007). AAS is a PLP-dependent enzyme that catalyzes the sequential deamination and decarboxylation of Phe into the intermediate PhAld, thus bypassing the need to go through an intermediate such as phenylpyruvate or 2-phenylethylamine. PhAld is then reduced

to 2-PE by a native dehydrogenase (Kaminaga et al., 2006). This pathway has been utilized in existing work to produce 2-PE in higher plants such as *Arabidopsis thaliana* (Qi et al., 2015) and hybrid poplar (Costa et al., 2013).

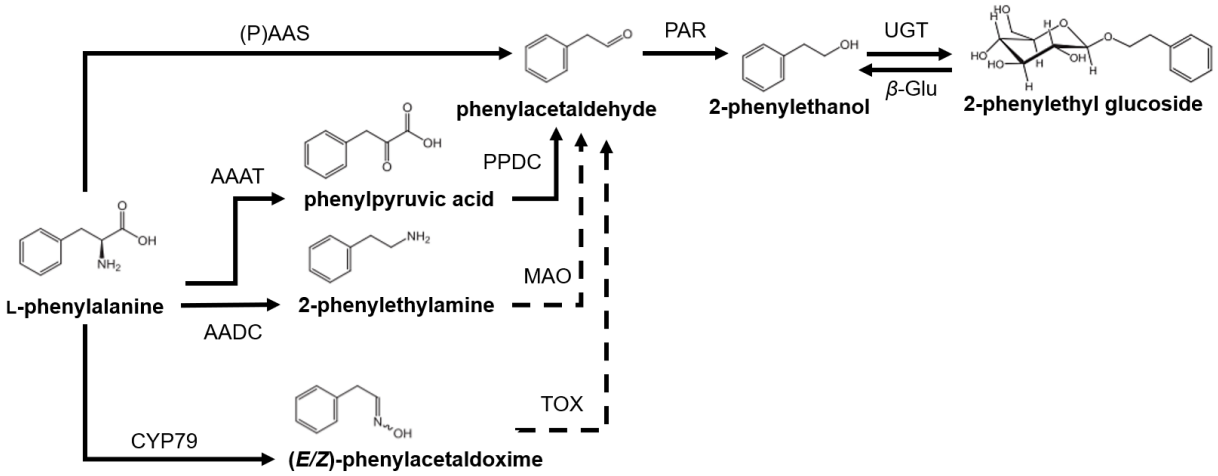

Fig. 2.2 – Proposed and known 2-PE biosynthesis routes in plants. Solid lines represent known mechanisms; dashed lines represent proposed mechanisms. AAAT – aromatic amino acid transaminase; AADC – aromatic amino acid decarboxylase; CYP79 – cytochrome P450 family 79 enzyme; *β*-Glu – *β*-glucosidase; (P)AAS – aromatic (phenylacet)aldehyde synthase; PAR – phenylacetaldehyde reductase; PPDC – phenylpyruvic acid decarboxylase; MAO – monoamine oxidase; TOX – transoximase; UGT – UDP glycosyltransferase. Figure adapted pathways identified from (Kaminaga et al., 2006; Sakai et al., 2007; Gonda et al., 2010; Irmisch et al., 2013; Günther et al., 2019).

Upon synthesis in the cytosol, 2-PE is either emitted into the atmosphere, or is stored within the cell. 2-PE has been detected in plant tissue in its free form, or as a glycosylated product. Volatile compounds are often acetylated or glycosylated to prevent over-accumulation leading to degradation of cellular membranes (Costa et al., 2013). Studies in rose flower diurnal cycles observed the change in 2-phenylethyl glucoside levels and free 2-PE levels occur rhythmically, implying there is a mechanism by which 2-PE and its corresponding glucoside are regulated, though it was concluded that the interconversion of 2-PE and its glucoside is not necessarily due to diurnal patterns (Watanabe et al., 2002; Hayashi et al., 2004).

Introduction of 2-PE biosynthetic pathways in plants have been successfully achieved by different transgenic approaches. A study on *Populus tremula×Populus alba* (hybrid poplar) utilized petunia PAAS (*PhPAAS*) and rose PAAS (*RhPAAS*) genes in conjunction with tomato PAR (*LePAR1*) resulted in accumulation of derivatized 2-phenylethanol in leaf tissue up to 4% by dry weight (Costa et al., 2013). More recently, a group of researchers were able to reduce lignin

content with increasing yields of 2-PE in *Arabidopsis thaliana* (Qi et al., 2015). Two separate mutant lines were produced, a *PAAS/LePAR1* line encoding PAAS from petunia leaves and PAR from tomato, and an *ARO9*/*ARO10*/*ADH2* line which uses key enzymes of the Ehrlich pathway from *S. cerevisiae*. The authors reported that the transgenic lines accumulated 2-PE up to 0.04% of fresh weight tissue, and reduction of lignin content by 12-14%, with no visible defect in growth, but reported no detection of glycosylated 2-PE. These studies provide the initial roadmap for the economic production of 2-PE in crops, however, due to limited information on the metabolic network these studies do not provide significant context towards increasing yield. Further improvement in 2-PE yield requires a rational engineering approach. Rational metabolic engineering employs mechanistic models of metabolism that can be used to predict which genetic manipulations lead to desirable outcomes. We therefore seek to use a kinetic model of phenylalanine metabolism as a guide for the rational design of plants producing increased amounts of 2-PE.

2.2.3 Kinetic modeling of plant secondary metabolism

Kinetic models are an important type of mechanistic metabolic models that can be used to understand plant metabolism (Zhu et al., 2007; Beauvoit et al., 2014). As kinetic models account for the enzymatic kinetic parameters, metabolic control analysis can be applied to determine which enzymatic steps within the studied metabolic network exert the greatest control on the flux (Colón et al., 2010). A parameterized kinetic model can be used to simulate pathway perturbations to predict new metabolic steady states (Fell, 2005). These predictions are invaluable to the metabolic engineer as it reduces the number of trial-and-error genetic manipulations and can contextualize observed cell behavior (Zhu et al., 2007; Colón et al., 2010).

To date there are a few models of Phe and lignin biosynthesis in plants (Faraji et al., 2015; Wang et al., 2014; Guo et al., 2018). Faraji et al. (2015) constructed a general mass action kinetic model of lignin biosynthesis in switchgrass, with their model suggesting possible feedback regulation and enzyme competition mechanisms previously undiscovered for their model system. Implementation of metabolic channels resulted in agreement between simulated and measured *in vivo* fluxes, suggesting that channeling is necessary to overcome allosteric regulation and enzyme competition. Wang et al. (2014) formulated a kinetic model for the phenylpropanoid pathway in poplar using both proteomic data and kinetic assays to obtain Michaelis-Menten kinetic parameters.

The parameterized kinetic model was validated against experimental data obtained from transgenic poplar and was able to successfully predict lignin content and composition. Guo et al. (2018) used isotopic labeling studies of the phenylpropanoid pathway in *Arabidopsis thaliana* to obtain measurements of carbon flux under different tracer feeding conditions. Using the multiple *in vivo* flux datasets for model training and validation, kinetic parameters and their confidence intervals were calculated using rigorous statistical analysis and an information theory approach. The trained kinetic model considered multiple subcellular compartments and the best-fit solutions indicated that certain metabolites are sequestered in the vacuole. While these three studies all lead to the construction of kinetic models, the approaches to obtaining parameters can differ significantly.

A major feature that can be extracted from kinetic models is the elucidation of the parameters responsible for the control of flux. Metabolic control analysis (MCA) is a method for quantifying how the control of flux and metabolite concentrations in a metabolic network is distributed among each enzymatic step (Kascer and Burns, 1973; Fell et al., 2005). Instead of considering the existence of a single rate-limiting step, MCA assumes that the finite amount of flux control is distributed among all enzymes in the pathway. Implementation of MCA allows for the calculation of flux control coefficients that specify the relative change in the metabolic steady state resulting from infinitesimal changes in enzyme activities. In essence, MCA is a form of linear perturbation theory and is useful for determining which enzymes in the metabolic network are important targets for metabolic engineering strategies.

2.2.4 Motivations and objectives

2-PE has been identified as a commodity chemical of high value with growing demand for natural production. Our major aim was to redirect carbon flux away from lignin biosynthesis towards the increased production of 2-PE. To achieve this, we selected *Arabidopsis thaliana* as the model organism to transform. Arabidopsis was selected due to its relative ease of transformation, rapid growth times when compared to lignocellulosic feedstock (switchgrass, poplar, etc.), and having a large genomic toolbox. Additionally, kinetic parameters for many of the relevant enzymes have already been characterized *in vitro* in the BRENDA enzyme database (www.brenda-enzymes.org) or been estimated *in silico* by kinetic models (Guo et al., 2018). Arabidopsis is an established model system for the study of lignin biosynthesis and biofuel production (Vanholme et al., 2012; Van Acker et al., 2013; Bonawitz et al., 2014).

We proposed a genetic engineering strategy at the phenylalanine branch point, whereby a portion of the carbon flux towards lignin biosynthesis is diverted towards the production of an economically viable product, 2-PE. Using a parameterized kinetic model at the phenylalanine branchpoint, we predict and test several metabolic engineering strategies to maximize the flux diverted towards 2-PE biosynthesis. We use a combined experimental and computational approach to iteratively improve 2-PE accumulation in transgenic Arabidopsis.

2.3 Materials and methods

2.3.1 Plant material

Arabidopsis thaliana ecotype Columbia (Col-0) was used in the experiments outlined. Arabidopsis plants were grown in greenhouses at 16h light/8 h dark at 22°C with 65% relative humidity. Seeds were sterilized before sown on half-strength MS medium. After stratification at 4°C for 2 days, Arabidopsis seeds were germinated at 22°C. A CaMV 35S promoter was used for constitutive overexpression of the native aromatic aldehyde synthase (*AtAAS*). Tomato phenylacetaldehyde reductase (*LePAR1*) was linked using a viral self-cleaving 2A linker for co-expression of distinct peptides (Ha et al., 2010), as shown in Fig. 2.3. The gene cassette was inserted into the pB2GW7 binary vector for stable integration into the Arabidopsis genome via agro-mediated transformation. Resultant progeny was selected for resistance to glufosinate and screened for transgene expression. Four lines were self-pollinated to generate homozygous lines. Independently, constructs for $AroG_{175}$ (point mutation at position 524; Leu175Gln; Tzin et al., 2013) and *pal1 pal2* (Rohde et al., 2004) were obtained and planted. These plants were cross-pollinated with *AtAAS/PAR1* plants and individual progeny were screened for Phe and 2-PE accumulation.

Fig. 2.3 – Gene cassette inserted into the pB2GW7 binary vector for stable integration in the *Arabidopsis thaliana* genome. 35s denotes the CaMV 35S promoter, used for constitutive overexpression. PAR1 denotes phenylacetaldehyde reductase obtained from *S. lycopersicum.* AtAAS denotes aromatic aldehyde synthase from *A. thaliana*. 2A denotes the viral self-cleaving 2A-linker, used for co-expression of distinct peptides.

2.3.2 GC-MS analysis of volatile compounds

Stems were collected from 5-6 week old *Arabidopsis* in triplicate biological replicates were flash frozen and ground in a mortar and pestle under liquid nitrogen. For free volatile analysis (2-phenylethanol and phenylacetaldehyde), samples were extracted in dichloromethane containing naphthalene as an internal standard (overnight at room temperature in a tightly capped vial). Aliquots of the extraction solvent were then concentrated under a gentle stream of nitrogen gas and analyzed on an Agilent 7890A gas chromatograph coupled with a 5975C inert MSD quadrupole mass spectrometer using a HP5-MS column (0.25 mm x 30m x 0.25µm, Agilent, Santa Clara, CA). The temperature program used was as follows: 40°C maintained for 2 min and raised from 40 to 150°C at 10°C/min, then from 150 to 250°C at 20°C/min with a final holding time of 2 min. Injector and detector temperatures were set at 250 and 230°C, respectively, 2-PE and PhAld were quantified based on known m/z values, and quantified based on calculated response factors relative to the internal standard naphthalene.

2.3.3 LC-MS/MS analysis of soluble phenolic compounds

For lignin precursor compounds and glycosylated 2-PE analysis, separate stem tissue was ground in the same fashion described above. Samples were then extracted using methanol:water (7:3, v/v) containing *para*-fluoro phenylalanine as an internal standard. Extraction was conducted at 65°C for 2 hours with induced mixing on a thermal shaker (Benchmark Multi-Therm). Post vortexing, samples were centrifuged at 18000 rpm for 15 minutes, and supernatants were collected and dried under vacuum at 30°C using a centrifugal evaporator (LABCONCO Centrivap). The residues were collected after 12 hours of drying and re-suspended in 60 µL of 50% (v/v) methanol:water and transferred to standard HPLC vials. Soluble phenolic compounds were analyzed using LC-MS/MS. Chromatographic separation was achieved using a Shimadzu HPLC-20AD system equipped with a Zorbax Eclipse C8 column (150 mm × 4.6 mm, 5 µm, Agilent Technologies, Santa Clara, CA) and metabolite profiling was performed using an AB Sciex QTRAP 5500 triple quadrupole mass spectrometer operating in the negative ion mode. The linear gradient for HPLC and MS tuning parameters were obtained from Jaini et al., (2017).

2.3.4 Analysis of total lignin content

Arabidopsis stems were analyzed for lignin content using the established acetal bromide (AcBr) method (Chang et al., 2005) with minor changes (Wang et al., 2018). Harvested stems (n = 3 biological replicates) were ground in liquid nitrogen and washed in 0.1 M sodium phosphate buffer (pH 7.2) at 50°C for 30 min followed by five washes with 10 mL 70% ethanol (v/v) at 80°C and once with 2 mL acetone. Dried cell wall residue (CWR) was weighed and dissolved in 2.5 mL of acetal bromide/glacial acetic acid (25:75 v/v) overnight at room temperature. As a control, tubes without CWR were also incubated with the AcBr/glacial acetic acid solution. Dissolved samples were transferred into 50 mL volumetric flasks containing 2.5 mL 2 M NaOH and 12 mL acetic acid. 500 µL of freshly prepared 7.5 M hydroxylamine hydrochloride was added into each sample followed by 35 mL acetic acid. The sample was mixed and allowed to settle before the volume was brough to 50 mL with the gradual addition of acetic acid. To obtain total lignin content, absorbance at 280 nm was measured on a spectrophotometer using the control as a blank. Beer's law was used to calculate the concentration of lignin, with a value of 23.20 $L \cdot g^{-1} \cdot cm^{-1}$ for the extinction coefficient.

2.3.5 Exogenous isotopic labeling studies

Arabidopsis plants used for feeding studies obtained from a single batch, grown under controlled greenhouse conditions (16/8 h light/dark cycle) or in growth chambers (23°C, light intensity of 150 µE m^{-2} s^{-2}, 16/8 h light/dark cycle). 5-8 week old primary stems and rosette leaves were excised from the plant and dipped in 1.5 mL centrifuge tubes containing a liquid MS medium with varying concentrations of the isotopically labeled substrate ($^{13}C_6$)-phenylalanine (1, 10, 100 M). Plants were incubated for up to 6 hrs and harvested for metabolic analysis. All labeling experiments were performed in triplicate (n = 3 biological replicates).

2.3.6 Kinetic modeling

The metabolic model stoichiometry, subcellular compartmentation, and enzymatic steps are shown in Fig. 2.4. Both 2-PE and lignin biosynthesis occurs in the cytoplasm of lignifying cells, while Phe synthesis occurs exclusively in plastids. Widhalm et al. (2015) characterized a plastidial phenylalanine exporter PhpCAT in petunia flowers, and Guo et al. (2018) estimated

kinetic parameters based *in vivo* fluxes obtained from time-course isotopic labeling studies. Upon export into the cytosol, Phe is converted into phenylacetaldehyde by aromatic aldehyde synthase (AAS) or into *trans*-cinnamic acid by phenylalanine ammonia lyase (PAL). PAL is considered the first step in the lignin biosynthesis pathway, and we are primarily interested in the split in carbon flux at the cytosolic Phe branchpoint. For the model, mass balances on each metabolite are written:

$$\frac{\mathrm{d}[\mathrm{Phe}_p]}{\mathrm{d}t} = v_{\mathrm{ADT}} - v_{\mathrm{CAT}} \tag{2.1}$$

$$\frac{\mathrm{d}[\mathrm{Phe}_c]}{\mathrm{d}t} = v_{\mathrm{CAT}} - v_{\mathrm{AAS}} - v_{\mathrm{PAL}} \tag{2.2}$$

$$\frac{\mathrm{d}[\mathrm{PhAld}]}{\mathrm{d}t} = v_{\mathrm{AAS}} - v_{\mathrm{PAR}} \tag{2.3}$$

$$\frac{d[\text{2-PE}]}{dt} = v_{\mathrm{PAR}} \tag{2.4}$$

$$\frac{\mathrm{d}[\mathrm{CA}]}{\mathrm{d}t} = v_{\mathrm{PAL}} \tag{2.5}$$

Where each flux v_i corresponds to i^{th} enzymatic step. The flux is determined by kinetic parameters and substrate amount and is given by the classic Michaelis-Menten equation. For the five enzymes in the metabolic network, the kinetic equations are as follows:

$$v_{\mathrm{ADT}} = \frac{v_{\mathrm{ADT}}^{\mathrm{app}}}{1 + \frac{[\mathrm{Phe}_p]}{K_{i,\mathrm{Phe}}^{\mathrm{ADT}}}} \tag{2.6}$$

$$v_{\mathrm{CAT}} = \frac{V_{\mathrm{max,CAT}}[\mathrm{Phe}_p]}{K_{M,\mathrm{Phe}}^{\mathrm{CAT}}\left(1 + \frac{[\mathrm{Phe}_c]}{K_{i,\mathrm{Phe}}^{\mathrm{CAT}}}\right) + [\mathrm{Phe}_p]} \tag{2.7}$$

$$v_{\mathrm{AAS}} = \frac{V_{\mathrm{max,AAS}}[\mathrm{Phe}_c]}{K_{M,\mathrm{Phe}}^{\mathrm{AAS}} + [\mathrm{Phe}_c]} \tag{2.8}$$

$$v_{\mathrm{PAR}} = \frac{V_{\mathrm{max,PAR}}[\mathrm{PhAld}]}{K_{M,\mathrm{PhAld}}^{\mathrm{PAR}} + [\mathrm{PhAld}]} \tag{2.9}$$

$$v_{\mathrm{PAL}} = \frac{V_{\mathrm{max,PAL}}[\mathrm{Phe}_c]}{K_{M,\mathrm{Phe}}^{\mathrm{PAL}} + [\mathrm{Phe}_c]} \tag{2.10}$$

Where $V_{\max,i}$, $K^i_{M,j}$, and $K^i_{i,j}$ are the maximal rate, the Michaelis-Menten constant (substrate affinity), and inhibition constant, respectively, for the i^{th} enzyme and j^{th} substrate. ADT and CAT take on the forms of uncompetitive and competitive inhibition, respectively (Guo et al., 2018). All kinetic parameters used are tabulated in **Table S2.1**.

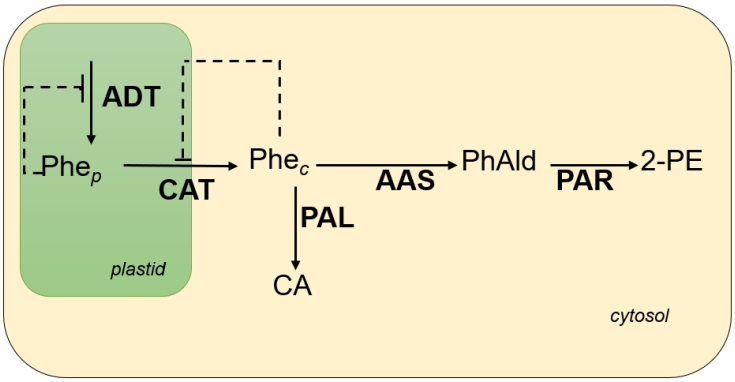

Fig. 2.4 – Cellular model depicting metabolite-enzyme interactions, reaction stoichiometry, and subcellular compartmentalization. Enzymes are shown in bold: AAS – aromatic aldehyde synthase; ADT – arogenate dehydratse; CAT – cationic amino acid transporter; PAL – phenylalanine ammonia lyase; PAR – phenylacetaldehyde reductase. Metabolites: CA – *trans*-cinnamic acid; 2-PE – 2-phenylethanol; PhAld – phenylacetaldehyde; Phe$_c$ – cytosolic phenylalanine; Phe$_p$. Solid arrows indicate direction of reaction, dashed arrows indicate feedback inhibition.

Experimentally we can resolve the fluxes at the Phe branch point by time course measurements of the isotopic enrichment of downstream metabolites upon feeding. As we are interested in maximizing flux through AAS by diverting flux away from PAL, we are interested in the ratio between the two fluxes, v_R:

$$v_R = \frac{v_{\mathrm{AAS}}}{v_{\mathrm{PAL}}} \tag{2.11}$$

2.3.7 Metabolic control analysis

Metabolic control analysis (MCA) provides a framework for quantitative assessment of the small perturbations in enzyme activity on the metabolic steady state J (Fell, 2005). This is accomplished by the evaluation of flux control coefficients, C_i^J, for each enzyme i in the network:

$$C_i^J = \frac{\partial J}{J} \cdot \frac{[e_i]}{\partial [e_i]} = \frac{\mathrm{d} \ln J}{\mathrm{d} \ln [e_i]} \tag{2.12}$$

Where $[e_i]$ is the abundance of enzyme i. The greater the value of the flux control coefficient (FCC), the greater the control on the flux J. The flux-control summation theorem states that due to the normalization of the coefficients to the total flux, the FCCs must sum to unity (Stephanopoulos et al., 1988):

$$\sum_{i=1}^{N \text{ enzymes}} C_i^J = 1 \tag{2.13}$$

This theorem holds true for linear pathways but can deviate from unity with large branched networks. In large metabolic networks, individual FCCs can have very low values due to highly distributed control. Upon calculation of FCCs, MCA provides the means to estimate new values of flux based on large perturbations in enzyme activity. From equation 2.12, large perturbations in enzyme activity can be used to predict large deviations in flux:

$$\frac{\partial J}{J^r} = C_i^J \frac{\Delta [e_i]}{\Delta [e_i^r]} \tag{2.14}$$

Where r describes the extent to which enzyme activity has been altered. This dimensionless number can also be referred to as the activity amplification factor (AAF) defined as the ratio between the new enzyme activity $[e_i^r]$ and the original activity $[e_i^0]$:

$$\mathrm{AAF}_i = \frac{[e_i^r]}{[e_i^0]} \tag{2.15}$$

Similarly, a flux amplification factor (FAF) can be defined as the ratio of the new flux and original flux:

$$\mathrm{FAF}_i = \frac{J^r}{J^0} \tag{2.16}$$

Combining equations 2.14-2.16, we obtain a relationship between the FAF and the AAF:

$$\mathrm{FAF}_i = \frac{1}{1 - C_i^J \left(\frac{\mathrm{AAF}_i - 1}{\mathrm{AAF}_i}\right)} \tag{2.17}$$

Utilization of large perturbations in enzyme activity to estimate fluxes is known as the theory of large perturbations. As genetic manipulations often target several order of magnitude changes in enzyme activities, it is beneficial to use large-perturbation theory to provide insight into the possible outcomes from transformations. Additionally, large-perturbation theory can be helpful in comparing different genetic modification strategies.

2.4 Results and Discussion

2.4.1 Selection and screening of 2-PE accumulating lines

2-PE biosynthesis in Arabidopsis is achieved by two enzymatic steps (Fig. 2.3); first Phe is converted into phenylacetaldehyde (PhAld) by AAS, which is then reduced to 2-PE by PAR. While Arabidopsis has a native AAS gene, accumulation of PhAld in wild-type plants is below the limit of detection, suggesting very low activity. Additionally, a specific phenylacetaldehyde dehydrogenase or reductase has not been characterized for Arabidopsis, and it is unknown if the specificity of native alcohol dehydrogenases (ADH) can catabolize the reduction of PhAld. Therefore, the initial transformation strategy was the overexpression of Arabidopsis aromatic aldehyde synthase (AtAAS) in tandem with tomato (*Solanum lycopersicum*) phenylacetaldehyde reductase (LePAR1) (Fig. 2.2). This transformation resulted in progeny screened for glufosinate resistance and screened for transgene expression by qRT-PCR. Four independent lines were self-pollinated to generate homozygous lines that were used for analysis (Fig. 2.5a).

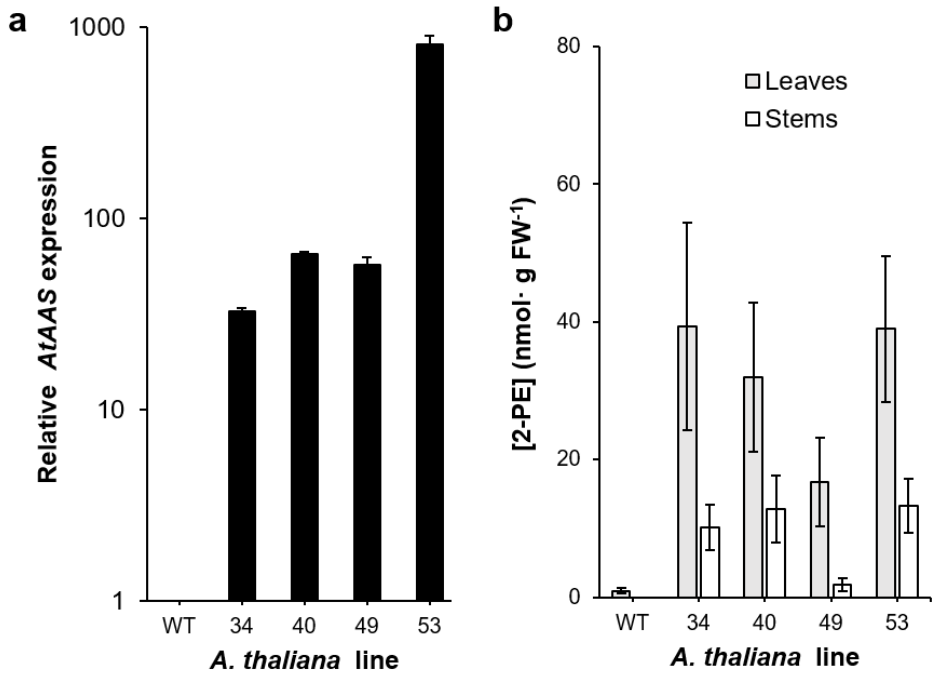

Fig 2.5 – Initial transformation of *Arabidopsis thaliana* generated four independent homozygous lines. (a) Relative AAS expression obtained by qRT-PCR in rosette leaves of *A. thaliana* plants. Values are relative to endogenous AAS expression in wild-type leaves. (b) 2-PE accumulation in transformants. Analysis was performed on rosette leaves and primary stems. Data are means ± S.E. (n = 3 biological replicates). * $P < 0.001$ using Student's *t*-test for comparison of means against wild-type.

Total pools of 2-PE were quantified in wild-type and transformed Arabidopsis rosette leaves and primary stems (Fig. 2.5b). Overall, significant accumulation was observed in the initial transformation, however, the level of accumulation did not correlate with transgene expression across the four lines, indicating possible limitation in further accumulation of 2-PE. The line with the greatest measured AAS transcript, *AtAAS/PAR1*-53, did not accumulate 2-PE to a statistically different quantity when compared to the other homozygous lines.

Accumulation of the intermediate PhAld was below the limit of detection, suggesting that PhAld pools turn over rapidly. To determine if product was being lost to the environment in the form of volatile emissions, overnight headspace collections were conducted for *AtAAS*/*PAR1*-53 and the wild-type control (Fig. 2.6a). The combined emissions of 2-PE and PhAld were below 8 pmol g FW^{-1} hr^{-1}, a quantity that is almost negligible compared to the total internal pools. As 2-PE is known to be glycosylated in many plant species (Jacobsen and Christensen, 2002; Costa et al., 2013), transgenic Arabidopsis was screened for phenylethyl glucoside. Analysis of plant tissue

revealed that glycosylated 2-PE pools accumulated in amounts 3-5 fold greater than that of free 2-PE pools (Fig. 2.6b). However, the pools of glycosylated 2-PE did not increase with transgene expression, indicating that the inability to further accumulate free 2-PE was not due to sequestration.

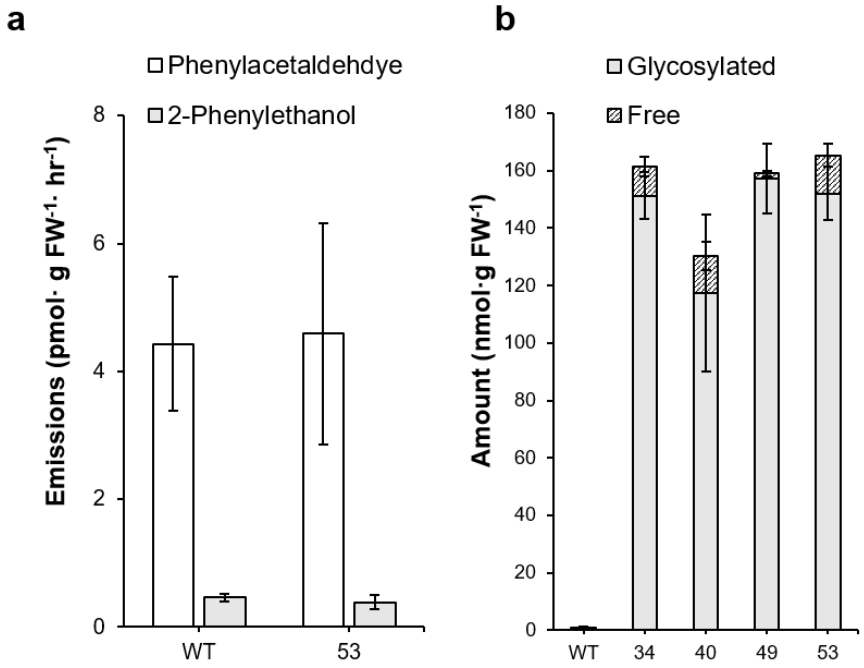

Fig. 2.6 – Metabolic fate of synthesized 2-PE in *Arabidopsis thaliana*. (a) Volatile emission rates of PhAld and 2-PE in wild-type and *AtAAS*/*PAR1* – 53. (b) Phenylethyl glucoside accumulation in transgenic and wild-type *A. thaliana*. Data are means ± S.E. (n = 3 biological replicates).

2.4.2 Simulation of metabolic flux

To gain insight into the flux split at the phenylalanine branchpoint, simulated flux through AAS was compared to the flux through PAL (Fig 2.7). From the initial screening of the transgenic lines, we hypothesized that the inability of *AtAAS/PAR1*-53 to produce more 2-PE compared to other transgenic lines was due to limited substrate (Phe) availability. Only at high ratios of AAS to PAL abundance and high Phe availability would the flux split at the Phe branchpoint become favorable towards enhanced production of 2-PE ($v_R > 1$). Endogenous pools of Phe in Arabidopsis stems are typically about 2-3 μM (Jaini et al., 2017), indicating that limited substrate availability is a major bottleneck in increasing biosynthetic flux towards 2-PE biosynthesis.

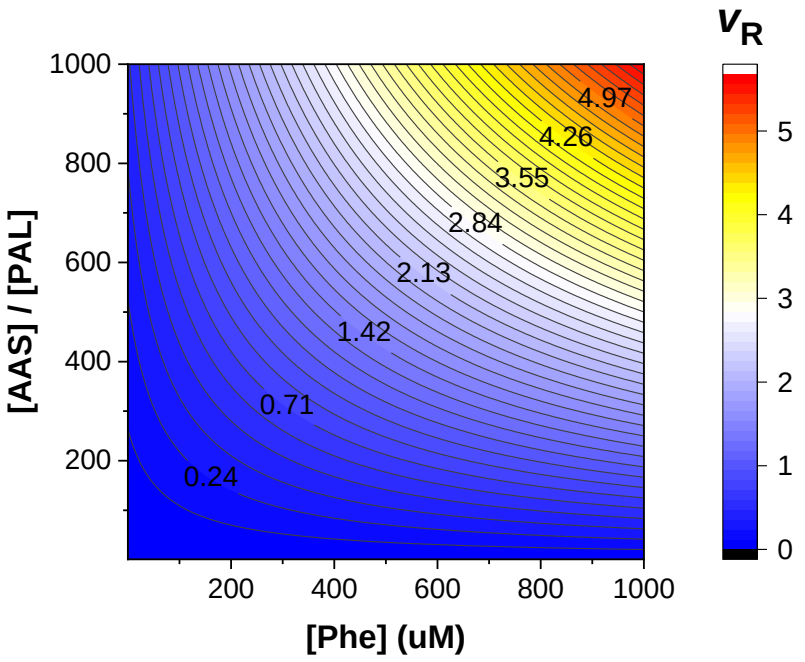

Fig. 2.7 – Flux ratio of AAS to PAL with respect to substrate (Phe) availability and the ratio of enzyme activity ([AAS]/[PAL]). Flux was estimated using parameterized kinetic model (Section 2.2.6 – Kinetic modeling) with Phe and enzyme concentration treated as continuous variables.

To test whether 2-PE biosynthesis can be enhanced with increased Phe levels, wild-type and transgenic Arabidopsis stems were supplied with 1, 10, and 100 mM of ring labeled ($^{13}C_6$)-Phe exogenously for 6 hr (Fig. 2.8). Flux through AAS and PAL were calculated based on downstream ^{13}C enrichment of 2-PE and *para*-coumaric acid (the first measured intermediate in the phenylpropanoid pathway). Feeding with enhanced concentrations of Phe was able to substantially increase the accumulation of 2-PE in transgenic plants, while wild-type Arabidopsis did not accumulate the product. Between 10 and 100 mM there appears to be a concentration of Phe that leads to saturation of the enzymes, an observation that is also observed in the simulated flux. Comparison of the measured flux ratio with simulated data further suggest that transgenic Arabidopsis is substrate limited, and increasing Phe levels in transgenic lines with high AAS expression can feasibly improve 2-PE accumulation.

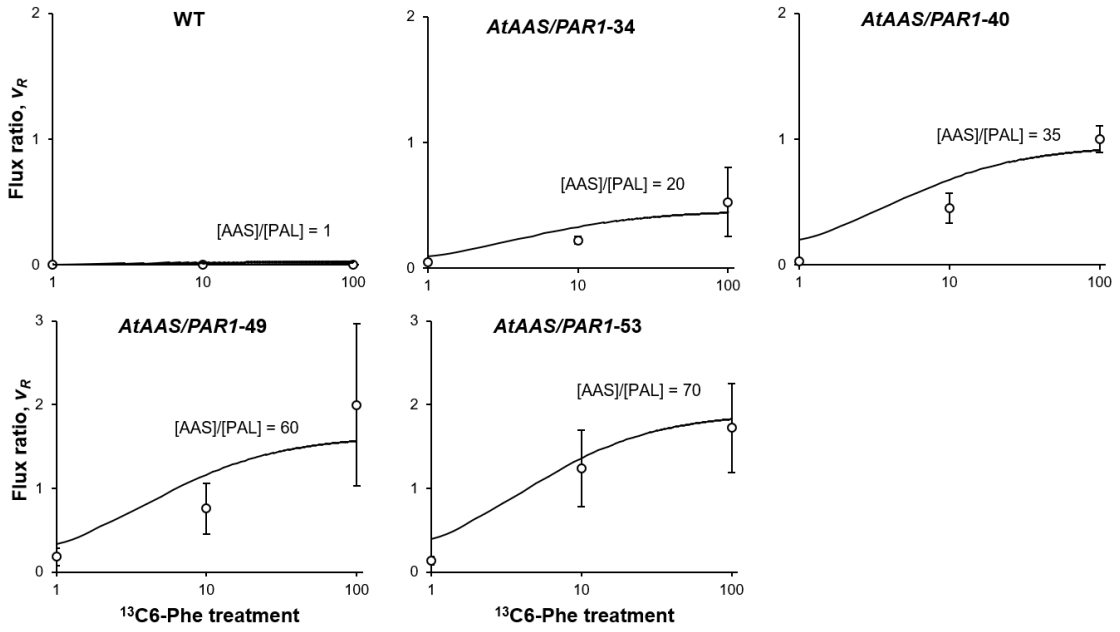

Fig. 2.8 – Feeding of transgenic and wild-type *Arabidopsis thaliana* with exogenous $^{13}C_6$-phenylalnine for 6 hours. Flux through AAS and PAL are expressed as a ratio, v_R (equation 2.11). Data are means ± S.E. (n = 3 biological replicates). Lines are the simulated flux ratio at specified ratio AAS to PAL enzyme abundance.

FCCs determined by MCA provide insight into the distribution of control that individual enzymes impose on flux towards 2-PE biosynthesis (Fig. 2.9). The step with the highest control coefficient was the plastidial Phe transporter, further evidence of the limitation of cytosolic Phe in the production of 2-PE. In petunia flowers, ~80% downregulation of *PhpCAT* expression leads to ~40% reduction in phenylpropanoid pathway flux, confirming the high level of flux control the Phe exporter exerts on the biosynthesis of cytosolic Phe-derived metabolites (Widhalm et al., 2015). Kinetic modeling of the phenylpropanoid pathway confirmed this observation by MCA and found that over 70% of the flux control was exerted by the Phe exporter (Guo et al., 2018). Thus, it becomes evident that cytosolic Phe pools are limiting the enhanced production of 2-PE.

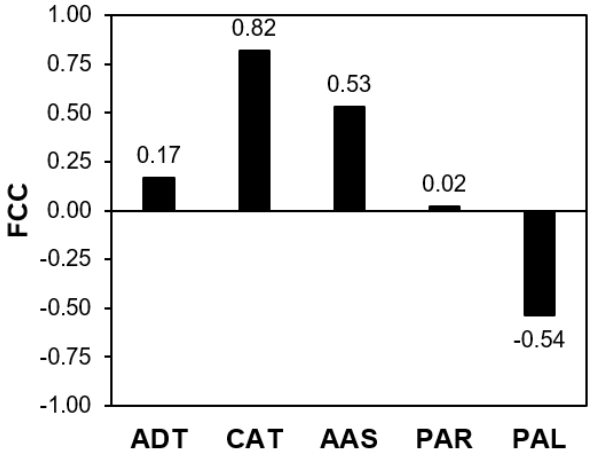

Fig. 2.9 – Flux control coefficients (FCCs) of pathway enzymes. FCCs are estimated by perturbation of ± 5% perturbation of individual enzyme activity and observing the change in flux towards 2-PE.

At the Phe branchpoint, the FCCs for AAS and PAL are essentially identical in magnitude, suggesting that the competition between the two enzymes greatly affects flux towards 2-PE. Targeting the competition at the branch point is another suitable point of modulation for the subsequent metabolic engineering strategies. In contrast, PAR has negligible control on the metabolic network suggesting that there is sufficient activity to rapidly turn over PhAld into 2-PE, an observation validated by the low pools of PhAld observed in transgenic Arabidopsis.

2.4.3 Model-guided engineering of transgenic Arabidopsis

Combining flux analysis and the measurement of flux control from the kinetic model revealed that endogenous cytosolic Phe is limiting the further accumulation of 2-PE (Fig. 2.8, 2.9). Plants synthesize Phe via the shikimate and aromatic amino acid pathways (Fig. A2) (Gilchrist and Kosuge, 1980). The first step in the shikimate pathway is 3-Deoxy-D-arabinoheptulosonate 7-phosphate (DAHP) synthase which converts phosphoenolpyruvate and erythrose 4-phosphate into DAHP. Flux through these pathways is known to be regulated by allosteric inhibition at several points, including the feedback inhibition of Phe on DAHP synthase (Brown, 1968). Indeed, overexpression of a mutated feedback-insensitive DAHP synthase (*AroG*$_{175}$) in tomato resulted in up to 50-fold increase in Phe levels (Xie et al., 2016). Additionally, *AroG*$_{175}$ plants were noted to have increased flux through Phe, as several Phe-derived metabolites were found to increase up to

200-fold relative to the wild-type control (Tzin et al., 2012). Introducing the 2-PE biosynthesis pathway in *AroG*$_{175}$ background Arabidopsis provides a route for increasing 2-PE accumulation.

Furthermore, the flux split at the Phe branch point is unfavorable at low concentrations of Phe and high expression of PAL relative to AAS (Fig. 2.7, 2.9). Arabidopsis have four PAL isoforms of which knock-down of PAL1 and PAL2 resulted in 75% decrease in total PAL activity and only 30% residual lignin, with no major decrease in growth (Rohde et al., 2004). The *pal1 pal2* double mutants are also known to hyper-accumulate Phe, which we hypothesized would enable greater flux to be diverted towards the production of 2-PE.

To test these predictions, *AtAAS*/*PAR1* plants were separately cross-pollinated with (*i*) lines overexpressing a feedback-insensitive *E. coli* (DAHP) synthase known to have hyper-induced Phe biosynthesis (Tzin et al., 2012), and (*ii*) the double mutant *pal1 pal2* known to have reduced activity of the competing enzyme PAL (Rohde et al., 2004). Progeny from the cross-pollination were screened for 2-PE content (Fig. 2.10). Lignin biosynthetic activity is not uniform over the length of the Arabidopsis stem, with highest activity found in the basal segment (< 2 cm). To discriminate between cells of varying lignin biosynthetic activity and its effect on 2-PE biosynthesis, individual stem segments (0-2, 2-4 and > 4 cm) and rosette leaves were profiled separately.

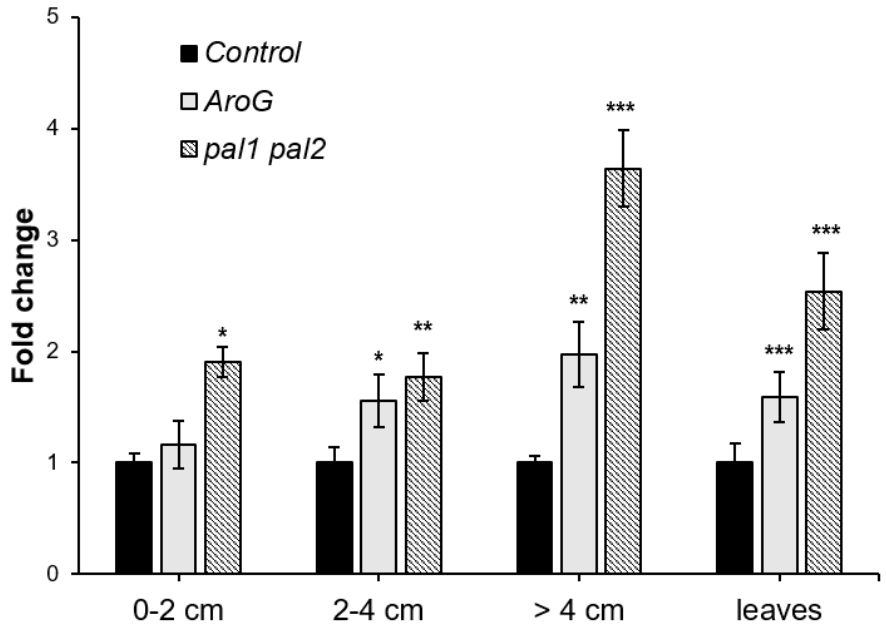

Fig. 2.10 – Fold change of 2-PE pools upon subsequent genetic modification. 8-week-old transgenic Arabidopsis were harvested by segments (0-2 cm stem, 2-4 cm stem, > 4 cm stem, rosette leaves) and profiled for free and glycosylated 2-PE pools. All fold changes are reported with respect to the control, *AtAAS*/*PAR1*-53. AroG – *AroG* × *AtAAS*/*PAR1*-53; *pal1 pal2* - *pal1 pal2* × *AtAAS*/*PAR1*-53. Data are means ± S.E. (n = 4 biological replicates). * $P < 0.05$, ** $P < 0.01$, *** $P < 0.001$ by Student's *t*-test.

With the exception of the basal stem segment (0-2 cm), 2-PE accumulation increased in both *AroG* and *pal1 pal2* backgrounds relative to the initial transformation, *AtAAS*/*PAR1*-53. The greatest increase in 2-PE accumulation was found in the upper stem segment (> 4 cm) and rosette leaves, the segments of Arabidopsis plants that express the lowest lignification rate (Wang et al., 2018). In the basal stem segment, there was no measurable increase in 2-PE accumulation in the *AroG* background compared to the transgenic control. Tzin et al. (2012) reported a significant increase in Phe-derived metabolites including lignin precursor compounds. Due to high PAL activity in the basal stem segment, it is likely that increasing substrate amount may not alleviate the competition at the Phe branch point. To determine if the introduction of the 2-PE metabolic sink has an effect on the steady state pools of lignin precursors, transgenic Arabidopsis was analyzed for phenylpropanoids (Fig. 2.11, Fig.A3).

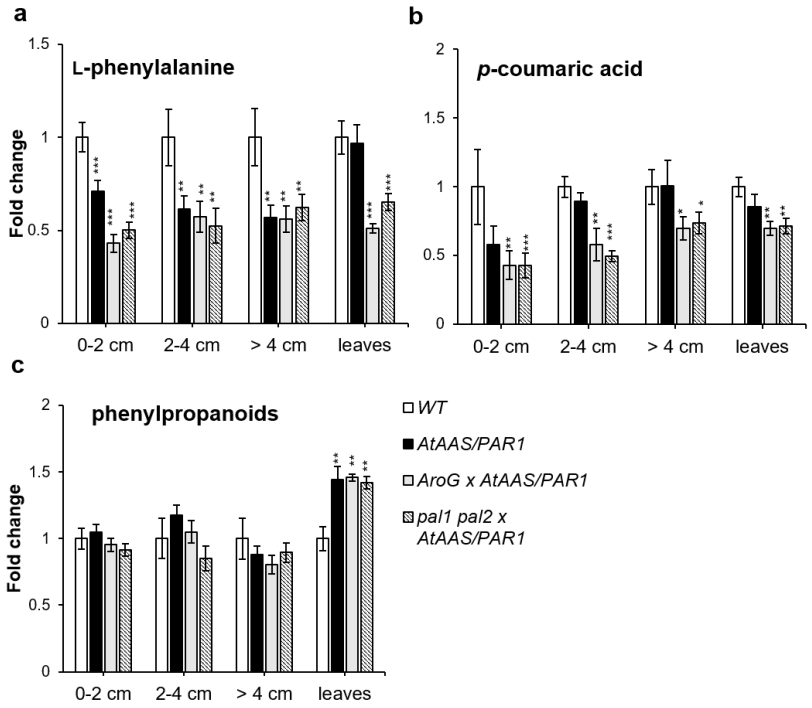

Fig. 2.11 – Fold change of Phe and Phe-derived phenolic compound pools upon subsequent genetic modification. (a) Fold change in phenylalanine pools. (b) Fold change in *para*-coumaric acid pools. (c) Fold change in the sum of phenylpropanoid pools (all metabolites profiled listed in Appendix A). 8-week-old wild-type transgenic Arabidopsis were harvested by segments (0-2 cm stem, 2-4 cm stem, > 4 cm stem, rosette leaves) and profiled for free and glycosylated 2-PE pools. All fold changes are reported with respect to the wild-type control, *AtAAS*/*PAR1*-53. WT – wild-type; AroG – *AroG* × *AtAAS*/*PAR1*-53; *pal1 pal2* - *pal1 pal2* × *AtAAS*/*PAR1*-53. Data are means ± S.E. (n = 4 biological replicates). * $P < 0.05$, ** $P < 0.01$, *** $P < 0.001$ by Student's *t*-test.

Unexpectedly, Phe levels were decreased significantly across transgenic lines compared to wild-type plants (Fig. 2.11a). Previous characterization of the *AroG* and *pal1 pal2* backgrounds in Arabidopsis resulted in 1-3 order of magnitude increases in total Phe levels (Rohde et al., 2004; Tzin et al., 2012). Depleted Phe levels in transgenic plants may be due to re-direction of carbon flux towards 2-PE biosynthesis. To test whether flux was diverted away from lignin metabolism, the pool sizes of phenylpropanoid pathway intermediates were measured in transgenic and wild-type lines. The first metabolite in the phenylpropanoid pathway that can be detected by LC-MS/MS analysis is *p*-coumaric acid. In all segments of transgenic Arabidopsis in the *AroG* and *pal1 pal2* backgrounds, there was an observed decrease in *para*-coumaric acid pools (Fig. 2.11b). The decrease in *p*-coumaric acid pools corresponds to the decrease in total Phe pools, indicating that flux is re-distributed towards the production of 2-PE. However, this trend was not observed for the sum of all phenylpropanoid metabolites (Fig. 2.11c). A possible explanation for lower Phe levels

in *AroG* and *pal1 pal2* backgrounds may be that the increased flux across AAS does not perturb lignin biosynthesis, but simply consumes the endogenous cytosolic Phe pool. Using the kinetic model, AAS abundance was varied to observe the effect on the steady state metabolite pools (**Fig. 2.12**). At high concentrations of AAS relative to PAL, cytosolic Phe pools can substantially deplete to sustain flux towards 2-PE biosynthesis. Phenylpropanoid metabolism has a corresponding decrease with Phe pools, a trend that was only observed for *para*-coumaric acid. Nonetheless, based on the model, introduction of a 2-PE pathway can result in Phe depletion with increasing flux over AAS.

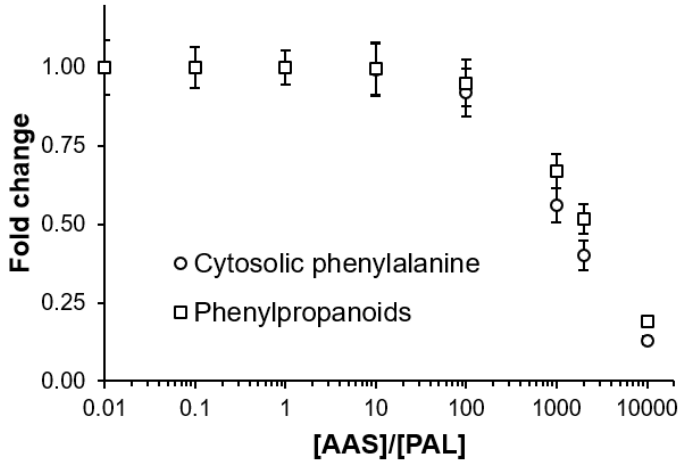

Fig. 2.12 – Model predicted fold change in metabolite pools with increasing AAS activity. Error bars denote standard error propagated from model parameter uncertainty values.

To study the effect of an introduced 2-PE pathway on lignin biosynthesis, total lignin content was measured in wild-type and transgenic Arabidopsis (Fig. 2.13). An overall decrease in total lignin content was observed with respect to increasing 2-PE accumulation. However, only *pal1 pal2* ×*AtAAS*/*PAR1* had measurable decrease in total lignin. These plants experienced a slower growth rate (1-1.5 week delay in bolting), but were able to achieve similar size and height, resulting in a higher value crop overall. The minimal penalty in growth suggests that 2-PE accumulating crops with decreased lignin content is viable.

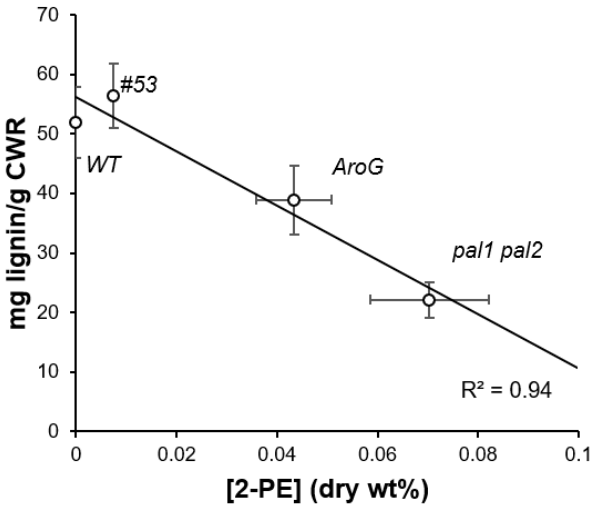

Fig. 2.13 – Effect of 2-PE accumulation on total lignin content. Total lignin measured in wild-type (*WT*), *AtAAS*/*PAR1*-53 (*#53*), *AroG* × *AtAAS*/*PAR1*-53 (*AroG*), and *pal1 pal2* × *AtAAS*/*PAR1*-53 (*pal1 pal2*). Cell wall residue (CWR) was obtained from harvested stems from 8-week-old plants and analyzed for AcBr lignin. Data are means ± S.E. (n = 4 biological replicates). *** $P < 0.001$ by Student's *t*-test.

2.4.4 Plastid-localized compartmentalization of 2-PE biosynthesis

As discussed in Section 2.1.2, two previous studies have introduced 2-PE biosynthetic pathways in plants. Qi et al. (2015) transformed Arabidopsis and achieved a maximum accumulation of 0.037 dry wt% 2-PE. Costa et al. (2013) transformed hybrid poplar and achieved a maximum accumulation of 0.06 dry wt% 2-PE in seven-week-old poplar plants. However, they observed accumulation of glycosylated 2-PE in four-month-old poplar leaves approaching 4% by dry weight, a substantially high quantity with respect to plant metabolic engineering. Thus far, the highest achieving line, *pal1 pal2* × *AtAAS*/*PAR1*-53, was able to reach an accumulation of 0.07 dry wt%, a quantity comparable to previous studies. However, our approach combined two strategies to overcome metabolic bottlenecks, but only led to marginal improvement. A point of consideration was our choice to overexpress *AtAAS*, which has significantly lower affinity for Phe compared to AAS genes found in rose and petunia (Kaminaga et al., 2006). Thus, our original approach was already limited in the extent to which it can compete with PAL activity. Only after down-regulation of PAL activity did we observe 2-PE accumulation comparable with that of previous studies. Thus, instead of competing with PAL, we considered an alternative approach to reducing the competition for Phe availability. Due to high plastidial partitioning of Phe, we

hypothesized that a plastidial 2-PE biosynthetic pathway would greatly improve 2-PE accumulation. In the plastid, 2-PE biosynthesis has access to a higher concentration of Phe as well as no competition from PAL. The branch now occurs at plastidial pools of Phe, with 2-PE biosynthesis competing with the plastidial exporter instead (Fig. 2.14a).

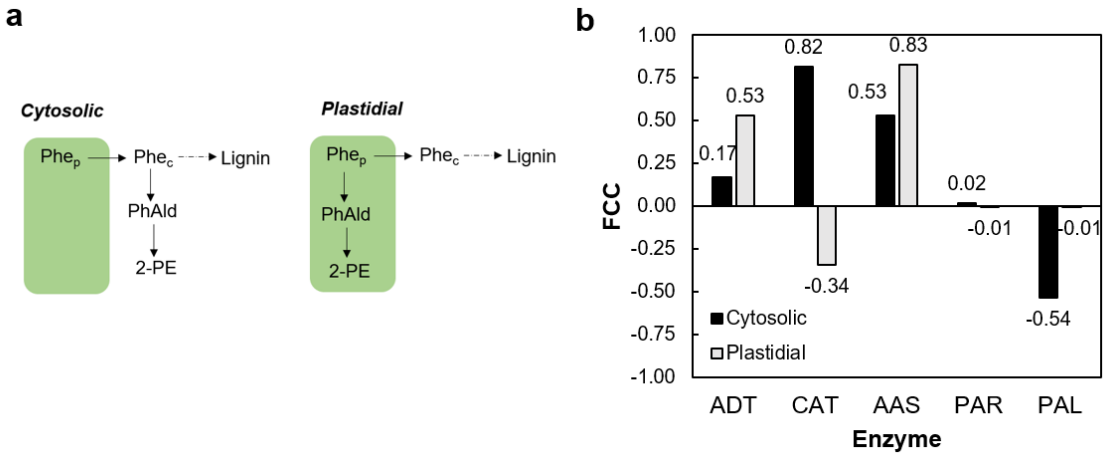

Fig. 2.14 – Plastidial compartmentalization of 2-PE biosynthetic genes. (a) Illustration of the shift in reaction network stoichiometry when sequestering the 2-PE biosynthesis pathway in plastids. (b) Re-distribution in flux control measured by MCA. FCCs are obtained using ± 5% perturbations of enzyme activity and estimating the new metabolic steady state flux.

To determine if sequestering 2-PE biosynthesis in the plastids can lead to increased 2-PE production, we performed MCA on the re-structured kinetic model to quantify the shift in flux control (Fig. 2.14b). Previously, the plastidial Phe exporter was found to exert the greatest control on flux towards 2-PE. Due to its competition for plastidial Phe pools, the exporter control coefficient becomes negative as it diverts flux away from 2-PE biosynthesis with increasing expression. Additionally, Phe biosynthesis has increasingly greater control on flux towards 2-PE. However, in the case of the plastidial pathway, the greatest control is exerted by AAS. While in the cytosolic pathway, AAS and PAL exhibited a similar extent of flux control, AAS out-competes the plastidial exporter for Phe. Using large-perturbation theory to test the effect of large variations in enzyme activity on flux through AAS, we can further illustrate the differences in flux control between the two pathway constructions (Fig. 2.15). AAS flux increases substantially more with increased Phe biosynthesis flux when the pathway is localized in the plastids, emphasizing the effect of Phe plastidial compartmentalization on 2-PE biosynthesis. Furthermore, a plastidial 2-PE biosynthetic pathway is more sensitive to AAS overexpression, achieving higher flux at the same

expression level when compared to the cytosolic pathway. While the exporter does compete with AAS for substrate availability, AAS flux is quite insensitive to variations in exporter expression, suggesting that AAS can adequately compete for plastidial Phe. Finally, lignin biosynthesis has negligible effect on plastidial 2-PE production, allowing for the design of plants dedicated to 2-PE production, in contrast to the earlier posed strategy of diverting carbon flux away from lignin and towards 2-PE. Using model-guided predictions, introduction of the pathway into plastids was posited as an alternative strategy to further increase 2-PE yield.

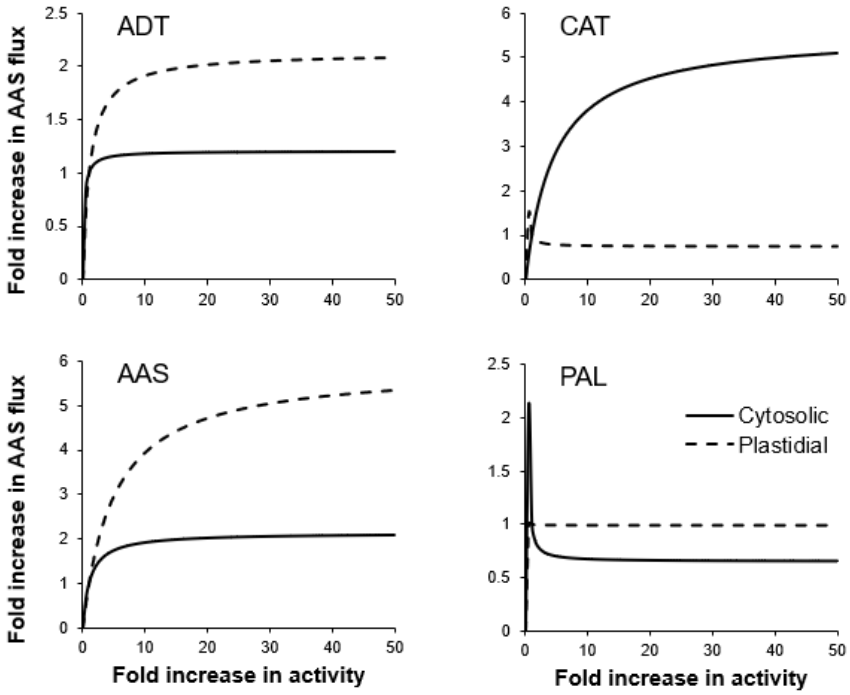

Fig. 2.15 – Effect of large perturbations of enzyme activity on flux through AAS. The vertical axis represents the flux amplification factor which is calculated from equation 2.17.

We tested this hypothesis by overexpressing *AtAAS*/*PAR1* with transit peptides to ensure plastidial targeting of the resultant proteins (Fig. 2.16a). Four transformed lines were screened for AAS expression (Fig. 2.16b) and 2-PE accumulation (Fig. 2.16c). Despite only marginal AAS overexpression compared to the original constructs (Fig. 2.5a), *tpAtAAS*/*PAR1* lines were found to have substantially greater accumulation of 2-PE. Indeed, 2-PE accumulation exceeded that *pal1 pal2* × *AtAAS*/*PAR1*-53, our previous highest accumulating line. By dry weight %, the highest accumulation in *tpAtAAS*/*PAR1* lines was found to be 0.123%, which is 1.7-fold greater than the amount detected in *pal1 pal2* × *AtAAS*/*PAR1*-53 (Table 2.2).

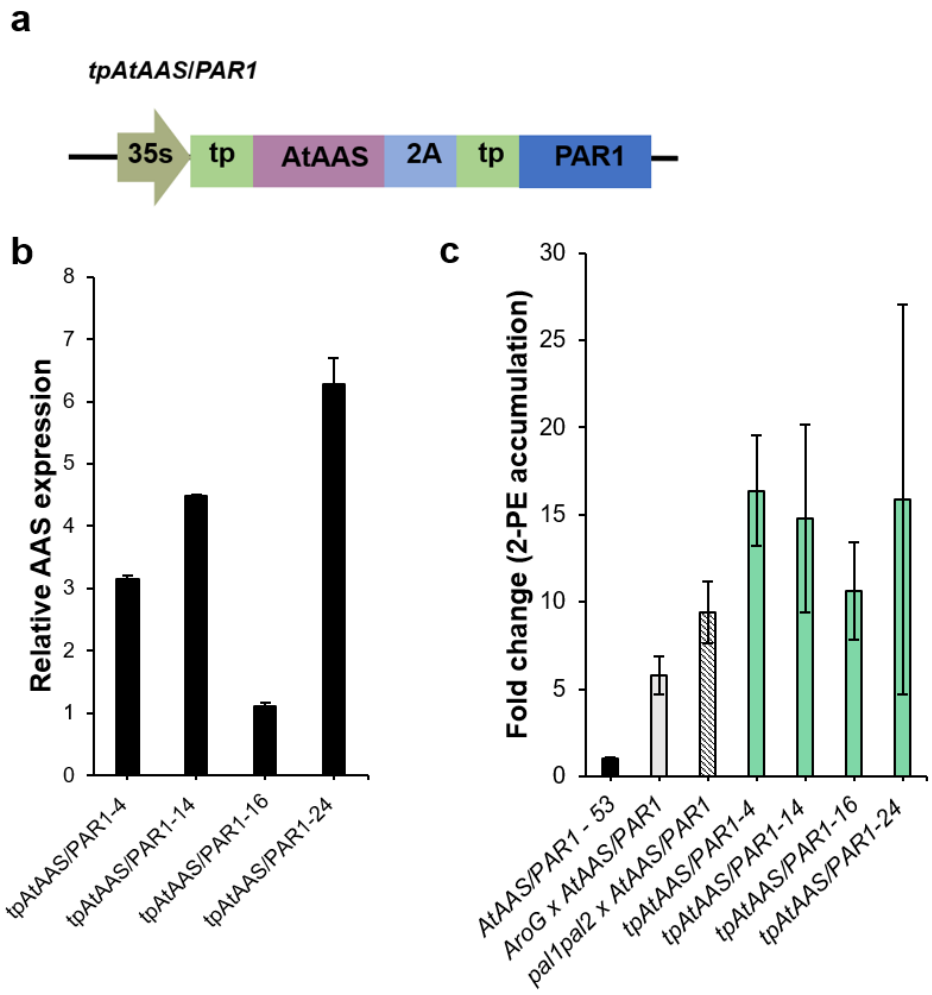

Fig. 2.16 – Plastid-localized compartmentalization of 2-PE biosynthesis in *Arabidopsis thaliana*. (a) Gene cassette depicting fusion of *PAR1/AtAAS* construct to chloroplast transit peptides (tp) to localize 2-PE biosynthetic genes in plastids. (b) Relative AAS expression obtained by qRT-PCR in rosette leaves of *A. thaliana* plants. Values are relative to endogenous AAS expression in wild-type leaves. (c) 2-PE accumulation in 8-week-old plants. Data are means ± S.E. (n = 3 biological replicates).

Table 2.2 - 2-PE accumulation in different genetic backgrounds.

Line	*AtAAS*/*PAR*-53	*AroG* ×*AtAAS*/*PAR1*	*pal1 pal2* ×*AtAAS*/*PAR1*	*tpAtAAS*/*PAR*-4
[2-PE] 10^{-2} dry wt. %	0.75 ± 0.06	4.34 ± 0.75	7.03 ± 1.18	12.28 ± 2.15

2.5 Conclusions

Using metabolic modeling we were able to identify limitations in the biosynthesis of 2-PE in plants. This modeling led us to propose several metabolic engineering strategies to increase 2-PE production in Arabidopsis. Kinetic models revealed that 2-PE biosynthesis is substrate limited and out-competed by PAL activity. We tested these predictions by introducing the 2-PE biosynthetic pathway into transgenic Arabidopsis overexpressing the feedback-insensitive DAHP synthase and the double mutant *pal1 pal2*. Screening the transformed lines demonstrated significant improvement in 2-PE yield. High accumulation of 2-PE was also correlated with a measurable decrease in lignin content, suggesting that the high carbon flux through the Phe branch point can be re-directed towards the introduced metabolic sink. Furthermore, we evaluated the effect of subcellular Phe partitioning by fusing the tandem PAR/AAS overexpression construct to transit peptides to localize the 2-PE biosynthetic pathway in plastids. The net result was even greater increase in 2-PE yield than previous metabolic engineering strategies.

One limitation in the approach is that Arabidopsis AAS has a higher K_M for the substrate Phe than either petunia or rose AAS (Kaminaga et al., 2006; Sakai et al., 2007; Gutensohn et al., 2011). Currently, we are working on introducing the pathway into poplar to determine if further improvement in 2-PE production can occur with an alternative AAS. Another improvement in 2-PE production can be possible with introduction of the plastid-localized 2-PE pathway in plants (Arabidopsis and poplar) overexpressing *AroG* to induce increased Phe biosynthesis. Flux control analysis predicts that Phe biosynthesis exerts the greatest control on plastidial 2-PE biosynthesis, making a transformation in the *AroG* background an attractive option.

2.6 Acknowledgements

This work was supported by the US Department of Energy, Office of Science, Office of Biological and Environmental Research (DOE-BER), Genomic Science program, under the Award Number DE-SC0008628 awarded to Dr. Clint C.S. Chapple, Dr. Natalia Dudareva, and Dr. John A. Morgan. I would like to thank Dr. Joseph Lynch for his work in transforming and growing the *Arabidopsis* lines, transcript screening, and assisting with metabolite profiling experiments (Figs. 2.3, 2.5, 2.6, 2.16). In addition, I would like to thank Dr. Peng Wang for her assistance in quantifying lignin using the acetal bromide procedure (Fig. 2.13).

2.7 References

Atsumi S., Hanai T., Liao, J. (2008) Non-fermentative pathways for synthesis of branched-chain higher alcohols as biofuels. *Nature*, *451*, 86–9

Beauvoit BP., Colombie S., Monier A., Andrieu MH., Biais B., Benard C., Chéniclet C., Dieuaide-Noubhani M., Nazaret C., Mazat J-P., Gibon Y. (2014) Model-assisted analysis of sugar metabolism throughout tomato fruit development reveals enzyme and carrier properties in relation to vacuole expansion. *Plant Cell*, *26* (8), 3224-42

Bedoukian PZ. (1986) Phenyl ethyl alcohol. In: Perfumery and flavoring synthetics. Allured, Wheaton, pp 370-83

Boerjan W., Ralph J., Baucher M. (2003) Lignin biosynthesis. *Annual Review of Plant Biology*, *54*, 519-46

Bonawitz ND., Kim J-I., Tobimatsu Y., Ciesielski PN., Anderson NA., Ximenes E., Maeda J., Ralph J., Donohoe BS., Ladisch M., Chapple C. (2014) Disruption of Mediator rescues the stunted growth of a lignin-deficient Arabidopsis mutant. *Nature*, *509*, 276-80

Brown K. (1968) Regulation of aromatic amino acid biosynthesis in *Escherichia coli* K12. *Genetics*, *60*, 31-48

Celinska E., Kubiak P., Bialas W., Dziadas M., Grajek W. (2013) *Yarrowia lipolytica*: the novel and promising 2-phenylethanol producer. *Journal of Industrial Microbiology and Biotechnology*, *40*, 389-92

Chapple C, Ladisch M, Meilan R. (2007) Loosening lignin's grip on biofuel production. *Nature Biotechnology*, *25*, 746-8

Clark GS. (1990) Phenethyl alcohol. *Perfum Flavor*, *15*, 37-44

Colón AM., Sengupta N., Rhodes D., Dudareva N., Morgan JA. (2010) A kinetic model describes metabolic response to perturbations and distribution of flux control in the benzenoid network of *Petunia hybrida*. *Plant Journal*, *62* (1), 64-76

Costa MA., Marques JV., Dalisay DS., Herman B., Bedgar DL., Davin LB., et al. (2013) Transgenic Hybrid Poplar for Sustainable and Scalable Production of the Commodity/Specialty Chemical, 2-Phenylethanol. *PLoS ONE, 8* (12), e83169

da Costa Sousa L., Chundawat SP., Balan V., Dale BE. (2009) "Cradle-to-grave" assessment of existing lignocellulose pretreatment technologies. *Current Opinion in Biotechnology*; *20*, 339-47

Douglas CJ. (1996) Phenylpropanoid metabolism and lignin biosynthesis: from weeds to trees. *Trends in Plant Science*, *1* (6), 171-78

Etschmann M., Bluemke W., Sell D., Schrader J. (2002) Biotechnological production of 2-phenylethanol. *Applied Microbiology and Biotechnology*, *59*,1-8

Etschmann MM., Huth I., Walisko R., Schuster J., Krull R., Holtmann D., et al. (2015) Improving 2-phenylethanol and 6-pentyl-alpha-pyrone production with fungi by microparticle-enhanced cultivation (MPEC). *Yeast*, *32*, 145-57

Etschmann MM., Sell D., Schrader J. (2004) Medium optimization for the production of the aroma compound 2-phenylethanol using a genetic algorithm. *Journal of Molecular Catalysis B: Enzymatic*, *29*, 187-93

Fell DA. (2005) Metabolic control analysis. *Systematic Biology*, *13* (5), 69-80

Fu C., Mielenz JR., Xiao X., Ge Y., Hamilton CY., Rodriguez M. Jr, Chen F., Foston M., Ragauskas A., Bouton J., Dixon RA., Wang ZY. (2011) Genetic manipulation of lignin reduces recalcitrance and improves ethanol production from switchgrass. *Proceedings in the National Academy of Science USA*, *108*, 3803-08

Gethins L., Guneser O., Demirkol A., Rea MC., Stanton C., Ross R P., et al. (2015) Influence of carbon and nitrogen source on production of volatile fragrance and flavour metabolites by the yeast *Kluyveromyces marxianus*. *Yeast*, *32*, 67-76

Gilchrist D., Kosuge T. (1980) Aromatic amino acid biosynthesis and its regulation. In: Miflin BN, ed. The biochemistry of plants. New York, NY, USA: Academic Press. New York 5: 507–531

Gonda I., Bar E., Portnoy V., Lev S., Burger J., Schaffer AA., Tadmor Y., Gepstein S., Giovannoni JJ., Katzir N., Lewinsohn E. (2010) Branched-chain and aromatic amino acid catabolism into aroma volatiles in *Cucumis melo* L. fruit. *Journal of Experimental Botany*, *61* (4), 1111-23

Günther J., Lackus ND., Schmidt A., Huber M., Stödtler H-J., Riechelt M., Gershenzon J., Köllner TG. (2019) Separate Pathways Contribute to the Herbivore-Induced Formation of 2-Phenylethanol in Poplar. *Plant Physiology*, *180*, 767-82

Guo L., Wang P., Jaini R., Dudareva N., Chapple C., Morgan JA. (2018) Dynamic modeling of subcellular phenylpropanoid metabolism in Arabidopsis lignifying cells. *Metabolic Engineering*, *49*, 36-46

Gutensohn M., Klempien A., Kaminaga Y., Nagegowda DA., Negre-Zakharov F., Huh J-H., Luo H., Weizbauer R., Mengiste T., Tholl D., Dudareva N. (2011) Role of aromatic aldehyde synthase in wounding/herbivory response and flower scent production in different Arabidopsis ecotypes. *The Plant Journal*, *66* (4), 591-602

Ha SH., Liang YS., Jung H., Ahn MJ., Suh SC., Kweon SJ., Kim DH., Kim YM., Kim JK. (2010) Application of two bicistronic systems involving 2A and IRES sequences to the biosynthesis of carotenoids in rice endosperm. *Plant Biotechnology Journal, 8* (8), 928-38

Hayashi S., Yagi K., Ishikawa T., Kawasaki M., Asai T., Picone J., Turnbull C., Hiratake J., Sakata K., Takada M., Ogawa K., Watanabe N. (2004) Emission of 2-phenylethanol from its *β*-D-glucopyranoside and the biogenesis of these compounds from [$^2H_8$] l-phenylalanine in rose flowers. *Tetrahedron, 60* (33), 7005-13

Hazelwood LA., Daran J-A., van Maris AJA., Pronk JT., Dickinson JR. (2008) The Ehrlich pathway for fusel alcohol production: a century of research on *Saccharomyces cerevisiae* metabolism. *Applied and Environmental Microbiology, 74*, 2259-66

Hua D., Xu P. Recent advances in biotechnological production of 2-phenylethanol. *Biotechnology Advances, 29* (6), 654-60

Irmisch S., McCormick AC., Boeckler GA., Schmidt A., Reichelt M., Schneider B., Block K., Schnitzler J-P., Gershenzon J., Unsicker SB., Köllner TG. (2013) Two herbivore-induced cytochrome P450 enzymes CYP79D6 and CYP79D7 catalyze the formation of volatile aldoximes involved in poplar defense. *Plant Cell*, 25, 4737-54

Jaini R., Wang P., Dudareva N., Chapple C., Morgan JA. (2017) Targeted metabolomics of the phenylpropanoid pathway in Arabidopsis thaliana using reversed phase liquid chromatography coupled with tandem mass spectrometry. *Phytochemical. Analysis, 28* (4), 267-276

Jakobsen HB., Christensen HB. (2002) Diurnal changes in the concentrations of 2-phenylethyl β-D-glucopyranoside and the corresponding volatile aglycone in the tissue and headspace of *Trifolium repens* L. florets. *Plant, Cell & Environment, 25*, 773-81

Jouanin L., Goujon T., de Nadaï V., Martin MT., Mila I., Vallet C., Pollet B., Yoshinaga A., Chabbert B., Petit-Conil M., Lapierre C. (2000) Lignification in transgenic poplars with extremely reduced caffeic acid O-methyltransferase activity. *Plant Physiology, 123*, 1363-74

Kaminaga Y., Schnepp J., Peel G., Kish CM., Ben-Nissan G., Weiss D., Orlova I., Lavie O., Rhodes D., Wood K., Porterfield DM., Cooper AJ., Schloss JV., Pichersky E., Vainstein A., Dudareva N. (2006) Plant phenylacetaldehyde synthase is a bifunctional homotetrameric enzyme that catalyzes phenylalanine decarboxylation and oxidation. *Journal of Biological Chemisty, 281* (33), 23357-66

Kascer H., Burns JA. (1973) The control of flux. *Symposia of the Society for Experimental Botany, 27*, 65-104

Li X., Weng JK., Chapple C. (2008) Improvement of biomass through lignin modification. *Plant Journal, 54*, 569-81

Loqué D., Scheller HV., Pauly M. (2015) Engineering of plant cell walls for enhanced biofuel production. *Current Opinion in Plant Biology, 25*, 151-61

Martinez-Avila O., Sanchez A., Font X., Barrena R. (2018) Bioprocesses for 2-phenylethanol and 2-phenylethyl acetate production: current state and perspectives. *Applied Microbiology and Biotechnology, 102* (23), 9991-10004

Masuo S., Osada L., Zhou S., Fujita T., Takaya N. (2015) *Aspergillus oryzae* pathways that convert phenylalanine into the flavor volatile 2-phenylethanol. *Fungal Genetics and. Biology*, *77*, 22-30

Mosier N., Wyman C., Dale B., Elander R., Lee YY., Holtzapple M., et al. (2005) Features of promising technologies for pretreatment of lignocellulosic biomass. *Bioresource Technology, 96*, 673-86

Novaes E., Osorio L., Drost DR., Miles BL., Boaventura-Novaes CR., Benedict C., Dervinis C., Yu Q., Sykes R., Davis M., Martin TA., Peter GF., Kirst M. (2009) Quantitative genetic analysis of biomass and wood chemistry of Populus under different nitrogen levels. *New Phytologist*, *182*, 878-90

Pedersen JF., Vogel KP., Funnell DL. (2005) Impact of reduced lignin on plant fitness. *Crop Science*, *45*, 812-19

Qi, G., Wang, D., Yu, L. Tang X., Chai G., He G., Ma W., Li S., Kong Y., Fu C., Zhou G. (2015) Metabolic engineering of 2-phenylethanol pathway producing fragrance chemical and reducing lignin in Arabidopsis. *Plant Cell Reports*, *34*, 1331-42

Reddy MS., Chen F., Shadle G., Jackson L., Aljoe H., Dixon RA. (2005) Targeted down-regulation of cytochrome P450 enzymes for forage quality improvement in alfalfa (*Medicago sativa L.*). *Proceedings in the National Academy of Science USA, 102*, 16573-78

Rohde A., Morreel K., Ralph J., Goeminne G., Hostyn V., De Rycke R., Kushnir S., Van Doorsselaere J., Joseleau J-P., Vuylsteke M., Van Driessche G., Van Beeumen J., Messens E., Boerjan W. (2004) Molecular Phenotyping of the pal1 and pal2 Mutants of Arabidopsis thaliana Reveals Far-Reaching Consequences on Phenylpropanoid, Amino Acid, and Carbohydrate Metabolism. *The Plant Cell*, *16* (10), 2749-71

Sakai M., Hirata H., Sayama H., Sekiguchi K., Itano H., Asai T., Dohra H., Hara M., Watanabe N. (2007) Production of 2-phenylethanol in roses as the dominant floral scent compound from L-phenylalanine by two key enzymes, a PLP-dependent decarboxylase and a phenylacetaldehyde reductase. *Bioscience, Biotechnology, and Biochemistry, 71*, 2408-19

Sewalt VJH., Ni WT., Jung HG., Dixon RA. (1997) Lignin impact on fiber degradation: increased enzymatic digestibility of genetically engineered tobacco (*Nicotiana tabacum*) stems reduced in lignin content. *Journal of Agricultural and Food Chemistry*, *45*, 1977-83

Shen L., Nishimura Y., Matsuda F., Ishii J., Kondo A. (2016) Overexpressing enzymes of the Ehrlich pathway and deleting genes of the competing pathway in Saccharomyces cerevisiae for increasing 2-phenylethanol production from glucose. *Journal of Bioscience and Bioengineering*, *122* (1), 34-9

Stark D., Münch T., Sonnleitner B., Marison I., von Stockar U. (2002) Extractive bioconversion of 2-phenylethanol from L-phenylalanine by Saccharomyces cerevisiae. *Biotechnology Progress*, *18* (3), 514-23

Stephanopoulos G., Aristidou AA., Nielsen JH. (1998). Metabolic engineering: Principles and methodologies. San Diego: Academic Press.

Tieman DM., Loucas HM., Kim JY., Clark DG., Klee HJ. (2007) Tomato phenylacetaldehyde reductases catalyze the last step in the synthesis of the aroma volatile 2-phenylethanol. *Phytochemistry, 68* (21), 2660-69

Tzin V., Malitsky S., Ben Zvi MM., Bedair M., Sumner L., Aharoni A., Galili G. (2012) Expression of a bacterial feedback-insensitive 3-deoxy-D-arabino-heptulosonate 7-phosphate synthase of the shikimate pathway in Arabidopsis elucidates potential metabolic bottlenecks between primary and secondary metabolism. *New Phytologist, 194* (2), 430-9

Van Acker R., Vanholme R., Storme V., Mortimer JC., Dupree P., Boerjan W. (2013) Lignin biosynthesis perturbations affect secondary cell wall composition and saccharification yield in Arabidopsis thaliana. *Biotechnology for Biofuels, 6*, 46

Vanholme R., Morreel K., Ralph J., Boerjan W. (2008) Lignin engineering. *Current Opinion in Plant Biology, 11*, 278-85

Vanholme R., Storme S., Vanholme B., Sundin L., Christensen JH., Goeminne G., Halpin C., Rohde A., Morreel K., Boerjan W. (2012) A Systems Biology View of Responses to Lignin Biosynthesis Perturbations in *Arabidopsis*. *The Plant Cell, 24* (9), 3506-29

Wang JP., Naik PP., Chen H-C., Shi R., Lin C-Y., Liu J., Shuford CM., Li Q., Sun Y-H., Tunlaya-Anukit S., Williams CM., Muddiman DC., Ducoste JJ., Sederoff RR., Chiang VL. (2014) Complete proteomic-based enzyme reaction and inhibitionkinetics reveal how monolignol biosynthetic enzyme families affect metabolicfluxand lignin in *Populus trichocarpa*. *Plant Cell, 26* (3), 894-914

Wang P., Guo L., Jaini R., Klempien A., McCoy RM., Morgan JA., Dudareva N., Chapple C. (2018) A ^{13}C isotope labeling method for the measurement of lignin metabolic flux in Arabidopsis stems. *Plant Methods, 14* (51)

Wani MA., Sanjana K., Kumar DM., Lal DK. (2010) GC-MS analysis reveals production of 2-phenylethanol from *Aspergillus niger* endophytic in rose. *Journal of Basic Microbiology, 50*, 110-4

Watanabe S., Hayashi K., Yagi K., Asai T., MacTavish H., Picone J., Turnbull C., Watanabe N. (2002) Biogenesis of 2-phenylethanol in rose flowers: Incorporation of [$^2H_8$] L-phenylalanine into 2-phenylethanol and its *β*-D-glucopyranoside during the flower opening of *Rosa 'Hoh-Jun'* and *Rosa damascena* Mill. *Bioscience, Biotechnology, and Biochemistry, 66*, 943-47

Xie Q., Liu Z., Meir S., Rogachev I., Aharoni A., Klee HJ., Galili G. (2016) Altered metabolite accumulation in tomato fruits by coexpressing a feedback-insensitive *AroG* and the *PhODO1 MYB-type* transcription factor. *Plant Biotechnology Journal, 14* (12), 2300-9

Zhang H., Cao M., Jiang X., Zou H., Wang C., Xu X., Xian M. (2014) De-novo synthesis of 2-phenylethanol by *Enterobacter* sp CGMCC 5087. *BMC Biotechnology, 14*, 1-7

Zhu X.-G., de Sturler E., Long S.P. (2007) Optimizing the distribution of resources be-tween enzymes of carbon metabolism can dramatically increase photosynthetic rate: A numerical simulation using an evolutionary algorithm. *Plant Physiology, 145* (2), 513-26

CHAPTER 3. CHEMICAL AND PHYSICAL CHARACTERIZATION OF FLOWER CUTICLES

3.1 Abstract

As an interface, the cuticle plays significant roles in protecting the plant against desiccation and external environmental stresses. In addition, volatile organic compounds (VOCs) are emitted into the surrounding environment of the plant via diffusion through the cuticle and is thus dependent on the cuticle physicochemical properties. Numerous characterization studies on plant cuticles across nature have facilitated better understanding on the relationship between cuticle composition and structure. The prevailing model for plant cuticles describes a composite matrix consisting of the biopolymer cutin and cuticular waxes that assemble into a multiphase system of crystalline and amorphous regions. The mass transfer resistance across the cuticle is speculated to be the result of crystalline waxes, where the relative amounts and arrangements govern the diffusivity of VOCs. To assess the relationship between cuticle wax composition and crystallinity, the waxes of *Petunia hybrida* flowers were investigated using gas chromatography - mass spectrometry, infrared spectroscopy, and X-ray diffraction. Composition analysis shows that petunia petal waxes are largely comprised of linear long-chain hydrocarbons with chain-lengths ranging from 14 to 44 carbon atoms with an average chain-length of 24 carbon atoms. X-ray diffraction results show that the isolated petal waxes are a mixture of amorphous domains and non-cubic crystalline subcells. Using spectroscopy to compare the structural features of petal cuticles and model waxes, we proposed a model cuticle that replicates the physicochemical properties of petunia petal cuticles. The model cuticle is a ternary system composed of *n*-tetracosane ($C_{24}H_{50}$), 1-docosanol ($C_{22}H_{45}OH$), and 3-methylbutyl dodecanoate ($C_{17}H_{34}O_2$), representing the relative aliphatic chain length, functional groups, molecular arrangements, and crystallinity of the natural waxes of petunia petals. X-ray diffraction analysis of varying compositions of the ternary wax system was used to measure differences in crystalline symmetry and abundance, showing that wax composition directly dictates the structure of the cuticle. VOC diffusion across cuticles of varying chemical composition also varied, showing that perturbations in cuticle composition can affect cuticle permeability.

3.2 The plant epidermis

Starting from over *c*. 400 million years ago, plants successfully integrated themselves into terrestrial habitats (Knauth and Kennedy, 2009). The adaption necessary for this expansion from aquatic to terrestrial domains necessitated the outermost cell layer (epidermis) to fulfil two major roles; protection against biotic and abiotic stresses, and the exchange of molecules with the environment (Javelle et al., 2010). To fulfil these multiple roles, the epidermis of higher plants such as gymnosperms and angiosperms developed a range of characteristics, including the development of specialized cell types such as stomatal guard cells, conical cells, and trichomes. The functional roles of these specialized cells with relation to VOC emissions were discussed briefly in Chapter 1, but many of these cell types serve purposes relating to maintaining the structural integrity and mechanical support of plant organs and tissue (Bemis and Torii, 2007). Over the diversity of plant species, the types of epidermal cells can vary significantly, but in general these cells are organized in a continuous and uniform monolayer surrounding plant organs (Glover, 2000). The adherence of epidermal cells is achieved by means of a rigid secondary cell wall, which is often thicker for the external surface of the cell (Javelle et al., 2010). The development of complex cell walls can be traced to Charophycean green algae (Sørensen et al., 2011) using fossil records and plant lineages, where divergence in radiation necessitated architectural changes in the cell wall. However, a more critical adaptive trait necessary for terrestrial expansion is the ability to retain water, particularly in increasingly dehydrating environments. Thus, over the course of plant evolution, the ability of epidermal cells to synthesize, export, deposit and maintain a hydrophobic layer known as the plant cuticle became an important characteristic necessary for survival (Waters, 2003). While plant cuticles vary significantly in composition and physical description across species and tissue-types, they are generally hydrophobic layers rich in long-chain aliphatic compounds. As the cuticle is the outermost layer of the plant epidermis, the aforementioned epidermal cell functions of protection and molecular exchange occur in the cuticle.

The epidermal cells of flower petals are generally conical in shape, which accumulate pigments and release scent compounds necessary for reproduction and defense (Bergougnoux et al., 2007). Many flower petals, such as those of *Petunia hybrida* flowers, lack specialized epidermal cell types such as stomatal guard cells and trichomes (Van der Krol and Chua, 1993), and thus the exchange of matter between the plant and its environment occurs solely via passive

diffusion through the cuticle. Therefore, our understanding of the dynamics of scent emission is dependent on the physicochemical properties of flower cuticles.

3.2.1 Structure of the plant cuticle

The outermost surface of terrestrial plants is covered by the cuticle, a composite structure comprised of the biopolymer cutin embedded with intra- and epicuticular waxes (Jeffree, 2006; Taiz et al., 2015). Cutin serves as a scaffold for the cuticular membrane, and is often referred to as the "cuticle proper" comprising between 40-80% of the total cuticle by thickness (Heredia, 2003). Cutin is a cross-linked polymeric network of esterified hydroxy C_{16} and C_{18} fatty acids, with trace amounts of glycerol, dicarboxylic acids, and phenolic compounds found coupled by transesterification or by peroxidation (Kolattukudy, 2001; Pfündel et al., 2006). On the inner side of the cutin layer is an intermediate layer rich in polysaccharides and intracuticular waxes, forming a heterogeneous interface with the aqueous cell wall. The outer surface of the cuticle proper is a layer abundant in wax compounds, forming the epicuticular layer. The epicuticle is the outermost layer of the cuticle, forming the distinctive "waxy feel" of plant surfaces. Due to the inhomogeneity of plant cuticles and the structural and functional differences of cuticular components, it is important to distinguish the various components of the cuticle from one another. As the waxes are regarded to impose significantly greater mass transfer resistance compared to that of cutin, (Schönherr and Riederer, 1989), the research highlighted in this thesis focuses primarily on the natural plant waxes.

3.2.2 Cuticle biosynthesis and export pathways

The biosynthesis of cutin monomers begins with *de novo* fatty acid synthesis in the plastids of epidermal cells (Fig. 3.1, Yeats and Rose, 2013). Free fatty acids are exported into the endoplasmic reticulum (ER) via an unknown mechanism, after which they are converted into acyl-CoA intermediates by ω- and midchain hydroxylation reactions, the sequence of which is also undetermined. Acyl-CoA intermediates are synthesized by acyltransferases encoded by the LACS family of enzymes, as characterized in *Arabidopsis thaliana* (Lü et al. 2009). Synthesis of glycerol intermediates occurs via a glycerol 3-phosphate acyltransferase (GPAT) (Yang et al., 2010), which are actively exported from the epidermal cell using ATP-binding cassette (ABC) transporters.

ABCG32 transporters identified in Arabidopsis (Bessire et al., 2011), wild barley and rice (*Hordeum spontaneum* and *Oryza sativa*; Chen et al., 2011) were characterized as cutin monomer precursor exporters. Once in the periclinal cell wall space, cutin monomers are polymerized using a putative cutin synthase, the mechanism of which is poorly understood. The multitude of linkages in the cutin polymeric matrix results in structures ranging from branched to cross-linked (Pollard et al., 2008), however, the specificity and abundance of these linkages are unknown. Additionally, the effect of cutin polymeric linkages on its overall structure and function remains relatively unclear.

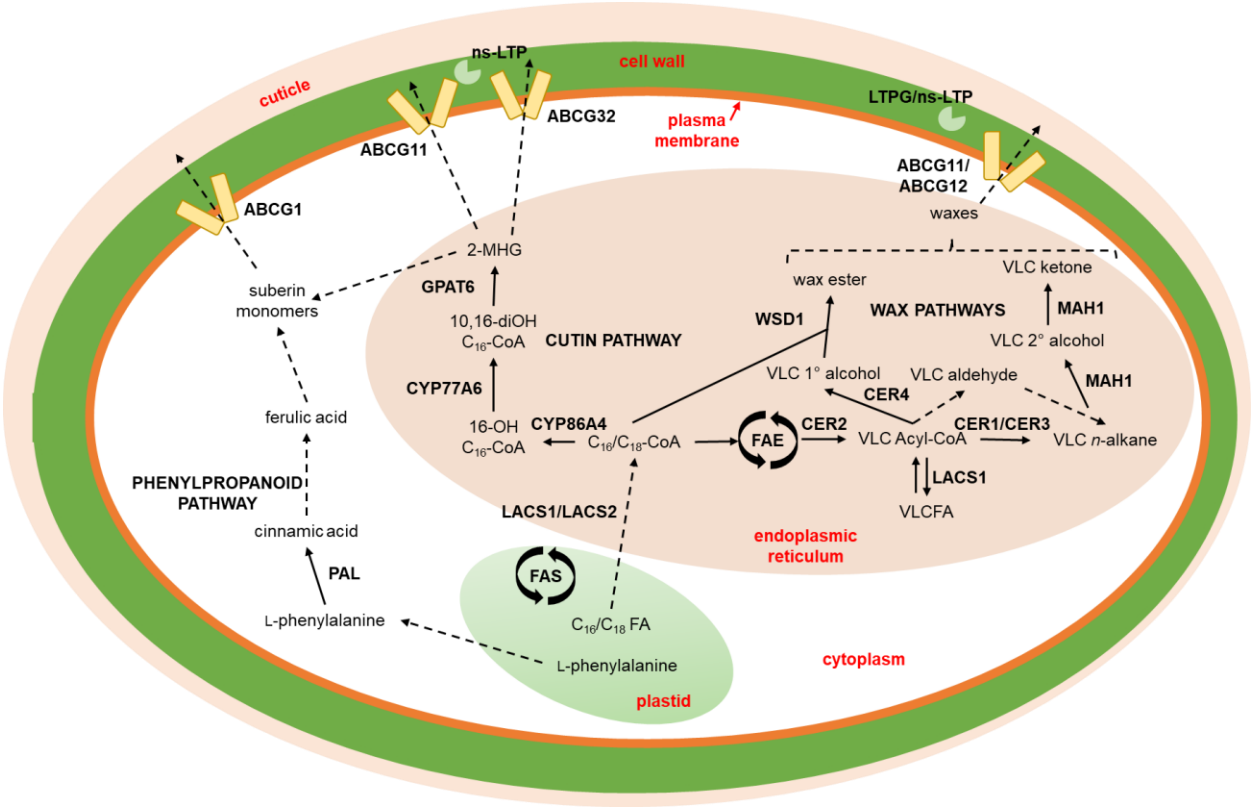

Fig. 3.1 – Major plant cuticle biosynthetic pathways. Subcellular compartments are shown in red, genes are in bold text. ABCG – ATP-binding cassette transporters; CER – eceriferum; CYP – cytochrome P450; FAE – fatty acid elongase; FAS – fatty acid synthase; GPAT6 – glycerol-3-phosphate acyltransferase; LACS – long-chain acyl-CoA synthetase; LTP(G) – (glycosylphosphatidylinositol-anchored) lipid transfer protein, (ns) – non-specific; MAH1 – midchain alkane hydroxylase; PAL – phenylalanine ammonia lyase; WSD1 – wax ester synthase. Figure adapted from Yeats and Rose (2013), Petit et al. (2017), Shanmugarajah et al. (2019).

In the majority of plant species, wax compounds such as acids, aldehydes, alcohols (primary and secondary), *n*-alkanes, branched alkanes, esters, and ketones, are derived from very-

long-chain fatty acids (VLCFAs) (Bernard and Joubès, 2013). Like cutin monomers, wax compounds are synthesized from C_{16} and C_{18} fatty acids produced in the plastid of the epidermal cell. Fatty acids are converted into CoA thioesters by a LACS enzyme and transported to the ER via vesicle trafficking (Pulsifer et al., 2012). These very-long-chain CoA-thioesters (VLC Acyl-CoA) undergo chain elongation by fatty acid elongases (FAE), forming VLCFAs. Characterization of the multitude of VLCFA catabolic pathways has been achieved by known-downs or knockouts of putative wax synthesis genes resulting in a series of "eceriferum" (lacking wax) mutants (Koornneef et al., 1989). Using Arabidopsis as the model system to study eceriferum plants, the enzymes used to convert VLCFAs into waxes with different functional groups have been identified and classified as the eceriferum (CER) family, with over 21 CER genes found (Yeats and Rose, 2013). Wax compounds are subsequently exported from the epidermal cells by the ABC transporters ABCG11 and ABCG12, first identified in Arabidopsis plants (Pighin et al., 2004; Bird et al., 2007). Export of wax compounds through the aqueous cell wall is facilitated by glycosylphosphatidylinositol (GPI)-anchored lipid-transfer proteins (LTPs) (Debono et al., 2009) and unbounded non-specific (ns-) LTPs (Salminen et al., 2018).

While the synthesis of the cuticle and its individual constituents vary with species, tissue, and environmental growth conditions, it is generally agreed that much of the formation of the cuticle occurs in early development (Jenks and Ashworth, 1999). In addition to the cutin scaffold and the interspersed waxes, plant cuticles can contain lipophilic secondary metabolites such as flavonoids and triterpenoids (Jetter et al., 2006). Due to improvements in sensitivity of analytical methods such as mass spectrometry and NMR, there has been substantial progress in the detection and quantification of wax metabolites intermediates in their metabolic pathways. However, many mechanisms such as intracellular trafficking, compartmentation, and regulation of cuticle development remain unexplored or poorly understood, thus limiting the ability to engineer plants with significant variations in cuticular phenotypes.

3.2.3 Functions of the plant cuticle

The major function of the plant cuticle is protection against desiccation, or the uncontrolled non-stomatal diffusion of water into the plants surroundings (Kerstiens, 1996a; Burghardt and Riederer, 2006). Additionally, the cuticle protects plant vasculature from a variety of abiotic and biotic stresses. In particular, the cuticle is a known barrier against pests and pathogens, preventing them from breaching into the epidermis. Subsets of fungal pathogens have been shown to form fissures in the cuticle by means of enzymatic degradation of cuticle components or by mechanical rupture (Deising et al., 2000). Fungal pathogens secreting cutinases are able to hydrolyze the cutin polymer and release free cutin monomers (Longhi and Cambillau, 1999), which in turn can elicit plant defense responses (Kraus et al., 1997). Epicuticular waxes may have known functions in plant-pest interactions, where the wax crystals may form unsteady surfaces that prevent insect locomotion or attachment to the epidermis (Borodich et al., 2010). The cuticle also plays important functions in defining developing organ boundaries, preventing the fusion of organs during plant growth, or organogenesis (España et al., 2014). The cuticle has also been shown to attenuate harmful UV irradiation that can damage DNA (Kraus et al., 1997; Waters, 2003).

In addition to its functions as a protective coating, the cuticle is the interface between the plant and its environment (Schönherr, 1976). Due to its structure and physicochemical properties, the cuticle is known to restrict the diffusion of large and polar molecules (Kerstiens, 1996b, Jeffree, 2006). Measurements of water permeability in isolated cutin and waxes demonstrate that the waxes impart 10-1000-fold greater mass transfer resistance than the cutin (Schönherr and Riederer, 1989). The difference in mass transfer resistance is attributed to the differences in crystalline arrangements between the waxes and the cutin polymer, where wax compounds synthesized by the epidermis self-assemble into highly crystalline domains (Goodwin and Jenks, 2005). The extent of these crystalline domains is speculated to limit, or altogether restrict, diffusion of molecules through the cuticle (Riederer and Schneider, 1990; Schreiber et al., 1997; Merk et al., 1998). While increased wax coverage has been shown to directly decrease cuticle permeability (Sieber et al., 2000; Martin and Rose, 2014), no link between changing wax composition and permeability has been fully established. Measurement of water permeability in the isolated waxes of 23 plant species with varying wax coverage revealed that there was no correlation between cuticle permeability and thickness (Riederer and Schreiber, 2001), suggesting that the chemical composition and arrangement of the waxes are the primary determinants of cuticular permeability.

The relationship between the cuticle composition and scent emissions is not well understood. In astomatous flower petals, VOCs must be released through the cuticle, suggesting that the cuticle may have some regulatory role in scent emissions. Analysis of scent emission in snapdragon flowers (*Antirrhinum majus*; Goodwin et al., 2003) and cuticle development demonstrated that the cuticle imparted little to no resistance with respect to methylbenzoate emission. VOC emissions are known to be regulated, at least in part by biosynthesis, which is partly controlled at the transcriptional level (Dudareva and Pichersky, 2000; Kolosova et al., 2001). To date, there is no evidence that VOC emissions are controlled by the physicochemical properties of cuticles.

3.2.4 Characterization of plant cuticles

Much of the plant cuticles composition, structure, and phase behavior has been characterized by a wide array of characterization methods such as mass spectrometry (Walton and Kolattukudy, 1972; Jetter et al., 2006), NMR (Lyons et al., 1995), calorimetry (Luque and Heredia, 1997; Matas et al., 2004), infrared spectroscopy (Chamel and Maréchal, 1992; Ramírez et al., 1992; Villena et al., 2000; Herredia-Guerrero et al., 2014), microscopy (TEM, SEM, AFM, etc.) (Benítez et al., 2004; Domínguez et al., 2011), and (X-ray and electron) diffraction (Baker, 1982; Ensikat et al., 2000; Koch et al., 2006).

As mentioned in the previous section, the structure and phase of the cuticle is dependent on the chemical composition of the waxes. The identification and quantification of natural wax compounds have been achieved primarily using different mass spectrometry methods coupled to gas chromatographs (GC-MS). Waxes are typically extracted from plant tissue by immersion in a nonpolar solvent (chloroform or hexane) (Still et al., 1970). Rapid dips in nonpolar solvents have been shown to readily solubilize aliphatic compounds without perturbation of the aqueous cell wall layer (Athukorala and Mazza, 2010). Many organic soluble waxes are readily analyzed by GC-injection, however; non-volatile waxes such as acids and alcohols require derivatization via silylation in order for detection (Osorio et al., 2012). Wax profiling in plants is generally regarded as non-targeted metabolomics, where the collection of molecular features such as chromatographic retention time, mass-to-charge (m/z) ratios, and fragmentation patterns are used to identify unique compounds (Aretz and Meierhofer, 2016). Non-targeted metabolomics methods involve data

processing algorithms that can align large datasets and compare the fragmentation patterns with databases. In addition to mass spectrometry based approaches, solid-state NMR has been shown to be a viable method for characterization of the linkages found in enzymatically-isolated cutin polymers (Chatterjee et al., 2015). NMR can be used to obtain the functional groups (aldehydes, alcohols, ketones, etc.) present in the wax chains, however, is often limited by overlapping broad spectral lines, and for quantitative analysis, typically requires long acquisition times (Serra et al., 2012). Infrared (IR) and Raman spectroscopic techniques offer a rapid and even non-destructive approach towards the analysis of the functional groups, conformations, and intra- and intermolecular interaction of cuticle components and exogenous molecules (Heredia-Guerrero et al., 2014). Spectroscopies are based on the excitation of molecular vibrations of chemical bonds by the absorption of light (IR spectroscopy) or scattering of photons (Raman spectroscopy). IR spectroscopy offers rapid analysis, with sample scans lasting less than 1 minute. However, IR spectra is significantly diminished by presence of water in samples, which limits the ability for *in situ* analysis for plant surfaces. Raman spectroscopy is less affected by sample aqueous content, however, it can have longer acquisition times compared to IR spectroscopy. IR spectroscopy acquisition is often performed using attenuated total-reflectance (ATR) mode, allowing for full surface analysis. ATR-Fourier-transform infrared spectroscopy (ATR-FTIR) is a common method for the analysis of the molecular arrangement and relative composition of plant cuticles. In general, analysis of composition is necessary for understanding the phase and crystallinity of the cuticle.

Differential scanning calorimetry (DSC) is a widely used method that measures heat flow to and from a sample, upon heating or cooling ramps. DSC is primarily used to identify phase transitions and has been used widely in the analysis of cuticular waxes. Endo- and exothermic effects are recorded to quantify temperatures and enthalpies of transition, as well as the heat capacity of the sample. Crystallization behavior is highly dependent on the phase transition (glass transition temperature, T_g), and thus the measurement of phase behavior is critical for the analysis of cuticle crystallinity (Luque and Heredia, 1994). DSC analysis of natural plant waxes demonstrate defined melting points between 60-95 °C, suggesting crystalline order similar to that of petroleum-derived paraffin waxes.

Microscopic analysis of wax morphology demonstrates that waxes can crystallize in differing ways resulting in different micromorphological descriptions. Using scanning electron microscopy (SEM), upwards of 23 unique descriptions for wax morphology were defined such as

platelets, tubules, films, and rodlets (Barthlott et al., 1998). Analyses of crystalline structure and symmetry have been conducted previously using electron (Baker, 1982) and X-ray (Ensikat et al., 2000) diffraction. Electron diffraction (ED) is beneficial for obtaining single-crystal diffraction patterns, and is effective for measurement of crystallite size. However, X-ray diffraction (XRD) provides detailed information on the lattice parameters, chain-length, and position of oxygen-containing groups, making it the preferred characterization tool. Most diffraction studies are performed on solvent-extraction, recrystallized waxes due to difficulties in the intact mechanical removal of the cuticle (Meusel et al., 2000). Comparison of recrystallized and mechanically isolated waxes for multiple plant species revealed no significant differences in the diffraction patterns, demonstrating that solvent extraction of plant cuticles is a viable method for analysis of cuticle crystallinity (Ensikat et al., 2006).

3.2.5 Motivations and research objectives

In order to determine if the structure and crystallinity of cuticles influence the emissions of volatile scent compounds, we will focus first on the chemical and physical characterization of petunia petal cuticles. As the wax compounds in plant cuticles are highly distributed, we seek to reduce the chemical complexity of the cuticle into a simplified model system. Our primary hypothesis is that greater wax crystallinity will result in decreased volatile emissions. Reduction of the plant cuticle into a representative model system with only a few wax components will allow us to control the extent to which the waxes form crystalline structures. Using spin-coated wax films, we can test the VOC permeability of varying mixtures of waxes, and quantify the effects of wax composition on the permeability of VOCs.

3.3 Chemical characterization of plant cuticles

Using GC-MS, the individual wax constituents comprising the epicuticular waxes of *Petunia hybrida* flower petals will be identified and quantified

3.3.1 Materials and methods

3.3.2 Plant materials and growth conditions

Wild-type *Petunia hybrida* cv. Mitchell diploid (W115; Ball Seed Co., West Chicago, IL) were grown under standard greenhouse conditions with a light period from 6:00 h to 21:00 h. Petunia buds were tagged the day prior to opening (anthesis), and all analyses were performed on petunia flowers two-days post-anthesis harvested at 18:00 h, the day and time when scent emission is the highest (Kolosova et al., 2002).

3.3.3 Wax extraction and GC-MS analysis

To extract waxes, petunia flower petals were submerged in 10 mL of GC-grade hexane for 20-30 sec. The solvent was decanted into fresh glass vial and dried completely under a gentle stream of N_2. The dried wax residue was derivatized using 200 µL of *N*,*O*-bis(trimethylsilyl)trifluoroacetamide (BSTFA Derivatization Grade, Sigma-Aldrich, St Louis, MO, USA) and pyridine (1:1 BSTFA:pyridine, v/v) for 15 min at 100°C, and excess BSTFA and pyridine were evaporated under N_2. Derivatized waxes were solubilized in hexane containing a known quantity of the internal standard *n*-tetracosane (99%, Sigma-Aldrich, St Louis, MO, USA) and samples were analyzed on an Agilent 6890 gas chromatograph equipped with a HP5-MS column (0.25mm x 30m x 0.25µm, Agilent, Santa Clara, CA, USA) and coupled to a 5975B inert MSD quadrupole mass spectrometer. The GC separation conditions were: an initial 2 min hold at 50°C, followed by a 40°C/min temperature ramp to 200°C and held for 10 min, then increased at 3°C/min to 280°C, and held for 10 min. Compounds were identified based on retention times and fragmentation patterns, and quantified by peak areas relative to the internal standard. Specific correction (response) factors and calibration curves were developed from external standards of fatty acids, primary alcohols, and *n*-alkanes of varying chain length and composition. Total wax quantity was obtained by pooling the wax extracts from 20 to 30 flowers in independent replicates, and measuring the weight of the dried residue. Wax quantity is expressed per petal dry weight, and all values represent the average of five biological replicates per petal sample.

3.3.4 Results and discussion

The waxes of *Petunia hybrida* were isolated by solvent-extraction from the petals of day 2 flowers after opening (post-anthesis), the developmental stage when benzenoid and phenylpropanoid VOC emissions are the highest (Kolosova et al., 2002). Over 35 cuticle metabolites were identified on the chromatograms of wax extracts (Fig. 3.2, Table 3.1). The majority of these wax compounds could be classified as fatty acids (23.1 ± 3.4% by total wt. %), primary alcohols (35.2 ± 7.2%), *n*-alkanes (18.9 ± 2.9%), and aliphatic esters (2.0 ± 0.2%). These compounds varied in their chain-length distribution, with fatty acids ranging from C_{14}-C_{26}, primary alcohols ranging from C_{16}-C_{28}, *n*-alkanes ranging from C_{15}-C_{33}, and esters ranging from C_{17}-C_{44} (Fig. 3.3a and b).

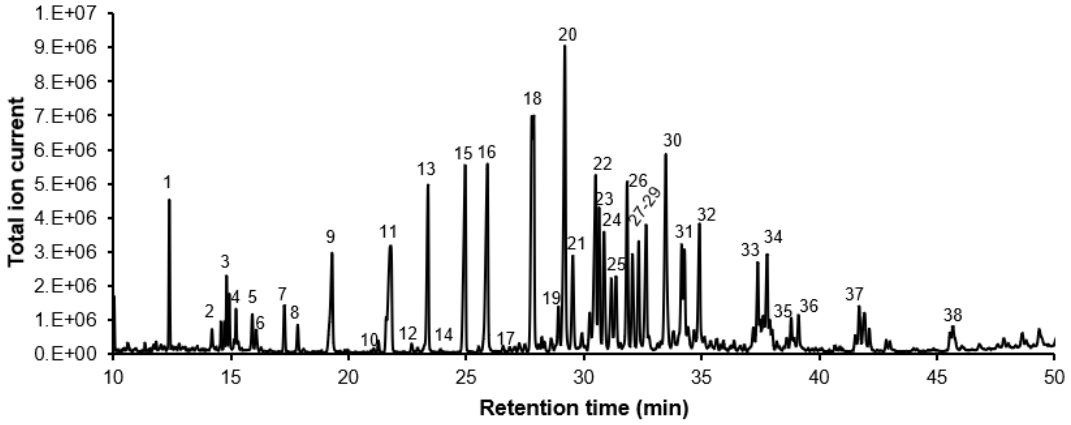

Fig. 3.2 – Representative chromatogram of derivatized wax extract from two day post-anthesis *Petunia hybrida* petals. Cuticular waxes were extracted from four flowers. Peak intensities do not correspond to relative abundance between compounds, due to differing response factors between compound types and biological variability. Annotated peaks correspond to compound identity (Table 3.1)

Table 3.1 – Wax constituents identified by GC-MS analysis of BSTFA-derivatized cuticle extracts from two-day post-anthesis flowers.

Peak No.†	RT (min)	Compound	Formula	Peak No.	RT (min)	Compound	Formula
1	12.37	*n*-pentadecane	$C_{15}H_{32}$	20	29.17	1-docosanol, TMS ester	$C_{25}H_{54}OSi$
2	14.16	*n*-nonadecane	$C_{19}H_{40}$	21	29.49	1-tetracosanol, TMS ester	$C_{27}H_{58}OSi$
3	14.80	*n*-tetradecanoic acid, TMS‡ ester	$C_{17}H_{36}O_2Si$	22	30.47	*n*-hentriacontane	$C_{31}H_{64}$
4	15.19	*n*-tricosane	$C_{23}H_{48}$	23	30.61	*n*-hexacosanoic acid, TMS ester	$C_{29}H_{60}O_2Si$
5	15.88	*n*-pentadecanoic acid, TMS ester	$C_{18}H_{38}O_2Si$	24	30.82	1-hexacosanol, TMS ester	$C_{29}H_{62}OSi$
6	16.00	1-hexadecanol, TMS ester	$C_{19}H_{42}OSi$	25	31.14	(1,1-dimethylpropyl)cyclohexane	$C_{11}H_{22}$
7	17.23	1-octadecanol, TMS ester	$C_{21}H_{46}OSi$	26	31.80	1-octacosanol, TMS ester	$C_{31}H_{66}OSi$
8	17.80	*n*-hexadecanoic acid, TMS ester	$C_{19}H_{40}O_2Si$	27	32.20	2-methyloctacosane	$C_{29}H_{60}$
9	19.28	oleic acid, TMS ester	$C_{21}H_{42}O_2Si$	28	32.29	2-methylnonacosane	$C_{30}H_{62}$
10	21.21	*n*-pentadecane	$C_{25}H_{52}$	29	32.61	3-methylbutyl dodecanoate	$C_{17}H_{34}O_2$
11	21.73	*n*-octadecanoic acid, TMS ester	$C_{21}H_{44}O_2Si$	30	33.46	*n*-tritriacontane	$C_{33}H_{68}$
12	22.64	*n*-heptacosane	$C_{27}H_{56}$	31	34.13	heptadecyl pentanoate	$C_{22}H_{44}O_2$
13	23.35	α-linolenic acid, TMS ester	$C_{21}H_{38}O_2Si$	32	34.88	2-methyltriacontane	$C_{31}H_{64}$
14	23.80	1-eicosanol, TMS ester	$C_{23}H_{50}OSi$	33	37.36	hexyl octadecenoate	$C_{24}H_{48}O_2$
15	24.93	Internal standard (*n*-tetracosane)	$C_{24}H_{50}$	34	37.75	octyl octadecenoate	$C_{26}H_{52}O_2$
16	25.87	*n*-eicosanoic acid, TMS ester	$C_{23}H_{48}O_2Si$	35	38.80	dodecanoic acid, phenylmethylester	$C_{19}H_{30}O_2$
17	26.45	*n*-nonacosane	$C_{29}H_{60}$	36	39.07	octadecyl eicosanoate	$C_{38}H_{76}O_2$
18	27.80	*n*-docosanoic acid, TMS ester	$C_{25}H_{52}O_2Si$	37	41.66	2-methyldotriacontane	$C_{33}H_{68}$
19	28.88	*n*-tetracosanoic acid, TMS ester	$C_{27}H_{56}O_2Si$	38	45.53	docosyl docosanoate	$C_{44}H_{88}O_2$

†Peak numbers correspond to annotated chromatogram (Fig. 3.2)

‡Trimethylsilyl (TMS) ester of compound after chemical derivatization

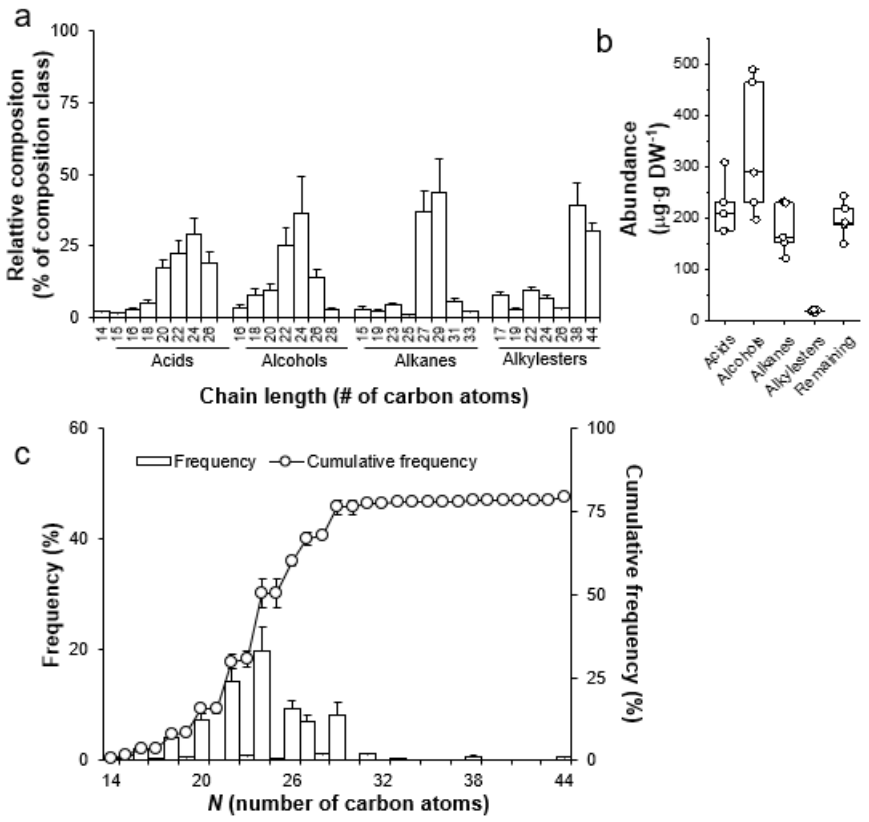

Fig. 3.3 – Cuticular wax composition of two-day post-anthesis *Petunia hybrida* flower petals. (a) Relative composition of wax compounds grouped by compounds class. (b) Abundance of wax constituent classes. (c) Chain-length distribution of wax compounds. Data is given by mean ± S.E. (n = 4 biological replicates).

Both acids and alcohols were identified as trimethylsilyl (TMS)-derivatives; fatty acids were predominantly saturated, with only trace α-linolenic acid detected, while most alcohols had primary hydroxyl groups, with trace secondary alcohols detected in the chromatogram. All alkanes detected in wax extracts were odd-numbered, as they are synthesized by decarboxylation of even-numbered fatty acids (Baker, 1982). Of the major wax constituent classes, only the alkyl esters branching usually in the form of iso-methyl terminal groups were identified. These compounds have generally low boiling points and low abundance, and thus it is important to have gradual temperature ramps in order to distinguish them. Unsaturated fatty acids, secondary alcohols, branched alkanes, ketones, and phenolic compounds comprise the ~20% of remaining wax compounds, however, each compound has low abundance and little to no distribution in carbon chain-length. The majority of wax constituents (> 65%) had a carbon chain-length between 20 and 30 atoms (Fig. 3.3c), and the mean of the chain-length distribution was approximately 24 carbon

atoms. Most of these major wax constituents identified are linear hydrocarbons, of which 61 ± 4% contain one or more oxygen-containing functional groups. Remarkably, the cuticle comprises only 0.095 ± 0.01% of the total dry mass of petunia corollas, with an average thickness 34.6 ± 0.3 nm (Fig. 6.6).

3.4 Physical characterization of plant cuticles

Chemical analysis of petunia petal waxes reveal an abundance of linear long-chain hydrocarbons, with a significant fraction of wax compounds containing polar functional groups. However, the composition of the petal cuticle is highly distributed, with compounds having a broad range of molecular weights and melting points, likely contributing to a highly polymorphic structure. To elucidate the cuticle morphology, physical characterization methods need to be employed if we are to establish a composition-structure relationship. Due to the distributed composition of the cuticle, it is unlikely that small perturbations in chemical composition will result in measurable changes in the structural features. To address this, we require a simplified model system that can both represent the structure of real cuticles and have a wax composition that is readily manipulated. To discriminate the structural features relevant to petunia cuticles, we use ATR-FTIR and XRD on reconstituted petal cuticles.

3.4.1 Materials and methods

3.4.2 Sample preparation

Petunia petal waxes were extracted according to the procedure (Section 3.3.1.2) and extracts were dried to completion under a gentle stream of nitrogen gas. Dried cuticle residue was weighed into fresh glass scintillation vials. The general wax yield is 0.8-1.0 mg/flower, thus for physical characterization analysis, the waxes from 30-50 flowers must be harvested. Reconstituted wax samples were heated to 80°C, and then gradually cooled to room temperature prior to FTIR and XRD analysis.

3.4.3 Fourier-transform infrared spectroscopy

Attenuated total internal reflectance – Fourier transform infrared spectroscopy (ATR-FTIR) spectra was measured using a Thermo Nicolet Nexus FTIR spectrophotometer (Waltham, MA, USA). Data was collected over 36 scans over the range of 700-4000 cm^{-1} under a nitrogen purge. Measurements were acquired on a diamond substrate using a KBr detector and a KBr beam splitter. Analysis was performed directly on harvested petunia petals, dewaxed petunia petals, reconstituted petunia petal waxes, and the prepared model cuticle waxes. Derivatives of the absorbance spectra ($dA/d\lambda$) was obtained using a forward difference method over 2 cm^{-1} increments.

3.4.4 X-ray diffraction

Powder diffraction (XRD) data were recorded on a Panalytical Empyrean X-ray diffractometer (Malvern Panalytical, Malvern, UK) at 45 kV, 40 mA with Bragg-Brentano mode using Cu Kα radiation ($\lambda = 1.5418$ Å). The diffraction patterns were collected from 2-45° over five calsides, and a PixCel3D Medipix detector. Isolated and blended waxes were dried, ground and annealed from 80°C to room temperature prior to XRD analysis, with wax sample quantity varying between 6-10 mg. XRD patterns were analyzed for peak geometry and background correction using the HighScore (Almelo, the Netherlands, 2015) software.

3.4.5 Results and discussion

Spectroscopic features of plant cuticles

Attenuated total reflectance – Fourier transform infrared spectroscopy (ATR-FTIR) has previously been used for *in situ* characterization of cuticle phase behavior and molecular structure (Chamel & Maréchal, 1992; Merk et al., 1998). While the infrared spectra of freshly harvested flowers did possess absorbance bands associated with plant cuticles, the abundance of water and complex macromolecules (polysaccharides) resulted in diminished absorbance bands associated with long-chain hydrocarbons (Fig. 3.4). The FTIR spectra of freshly harvested flowers and reconstituted epicuticular waxes exhibit absorbance bands common to the cuticles of other plants (Herredia-Guerrero et al., 2014): (i) a broad band at 3350 cm^{-1} assigned to the stretching of interacting hydroxyl groups by hydrogen-bonding, (ii, iii) doublet peaks at 2919 and 2850 cm^{-1}

associated with the asymmetric and symmetric stretching of methylene groups, (iv) a sharp peak 1730 cm^{-1} assigned to ester stretching, (v) a sharp peak at 1464 cm^{-1} corresponding to the methylene group scissoring, (vi, vii) peaks at 1170 and 1060 cm^{-1} assigned to the asymmetric and symmetric bending of ester groups, and (viii) a low intensity peak at 719 cm^{-1} assigned to the rocking of methylene groups. The peak assignments and cuticle component contribution are summarized in Table 3.2. The high intensity peaks associated with methylene stretching vibrations reveal waxes with elongated structures, a common spectroscopic feature for linear hydrocarbons. The occurrence of peaks between 600-1800 cm^{-1} are attributed primarily to vibrations from the stretching of carbon-oxygen groups, suggesting that a significant fraction of the aliphatic compounds are oxygenated. This observation is supported by the chemical analysis of the cuticle, where over 60% of wax metabolites were classified as alcohols, acids, and esters.

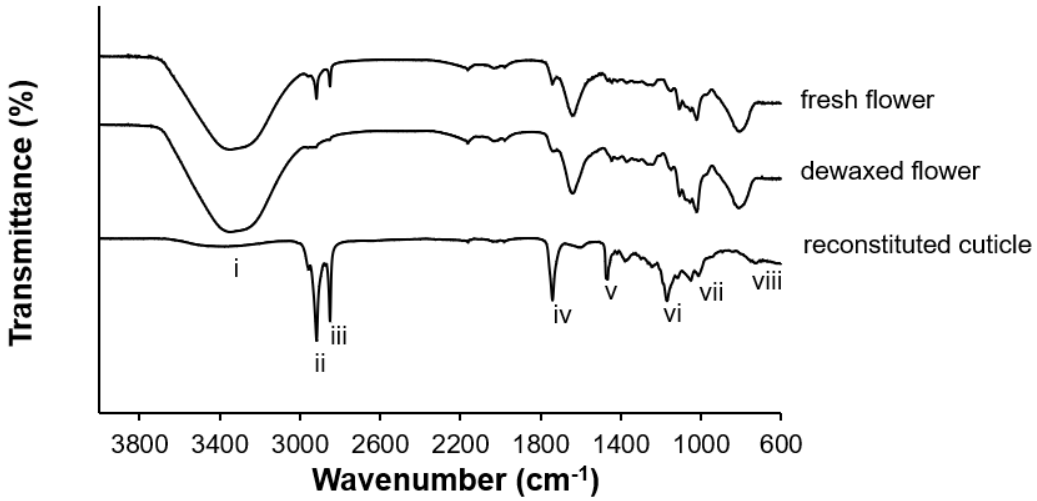

Fig. 3.4 – Transmission spectra of two-day post-anthesis *Petunia hybrida* flower petals. Spectra correspond to flowers that are freshly harvested, dewaxed, and cuticles that are reconstituted upon extraction. IR spectra is collected using ATR-FTIR mode on a diamond substrate using a KBr detector and a KBr beam splitter. Peak annotations correspond to molecular vibrations identified in Table 3.2 and in-text.

Table 3.2 – Main functional groups assigned to different vibrations present in the transmission spectra of reconstituted petunia petal cuticles. Peaks correspond to annotated peaks in Fig. 3.4.

Peak	Assignment †	Wavenumber (cm^{-1}) ‡	Cuticle component
i	ν(OH···O)	3350 (m,b)	Cutin, polysaccharides
ii	$\nu_a(CH_2)$	2919 (vs)	Cutin, epicuticular waxes
iii	$\nu_s(CH_2)$	2850 (s)	Cutin, epicuticular waxes
iv	ν(C=O) ester	1730 (m, sh)	Cutin
v	$\delta(CH_2)$ scissoring	1464 (m)	Cutin, epicuticular waxes
vi	ν_a(C-O-C) glycosydic bond	1170 (m)	Polysaccharides, waxes
vii	ν_s(C-O-C) glycosydic bond	1060 (w)	Polysaccharides, waxes
viii	$\delta(CH_2)$ rocking	719 (w)	Cutin, epicuticular waxes

†*ν* – stretching, *δ* – bending, *a* – asymmetric, *s* - symmetric

‡vs – very strong, s -strong, m – medium, b – broad, sh – shoulder, w – weak

Crystallinity of isolated flower cuticles

Crystallinity of petunia petal waxes was obtained using powder X-ray diffraction (XRD) on the dried wax residues from solvent-isolated cuticle extracts (Fig. 3.5). The XRD pattern of the isolated cuticle exhibits a broad halo at $2\theta = 19°$, representing the content of the waxes that are amorphous (Le Roux, 1969; Dorset, 2000). An intense peak corresponding to a d-spacing length of 4.17 Å indicates hexagonal crystalline symmetry (Chichakli and Jessen, 1967), and a less intense peak at a spacing of 3.72 Å suggests traces of orthorhombic crystals (Ensikat et al., 2006). Non-cubic crystalline symmetry results in unit cells with a long length axis that contribute to the medium anisotropy. Waxes with hexagonal structure occur at higher temperatures near a phase transition, which is suggestive of a softer wax than that of petroleum-derived waxes (Dorset, 2000). Based on the definition of relative crystallinity given by ASTM D 5357, the percent crystallinity is determined from the ratio of the crystalline peak area to the sum of the area under the crystalline peaks and amorphous halo, and for reconstituted petunia petal cuticles, the waxes were found to be 51 ± 4% crystalline.

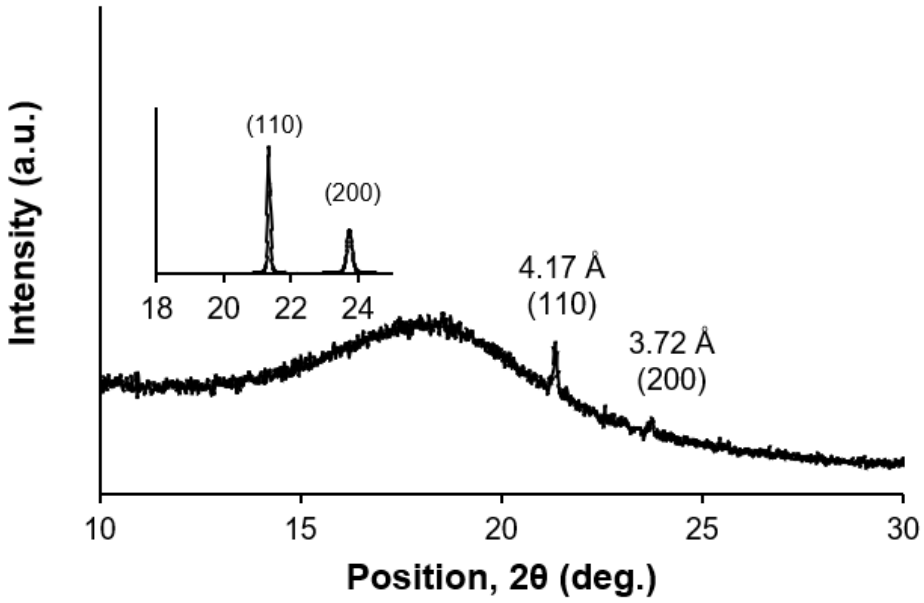

Fig. 3.5 – XRD-diagram of reconstituted petal waxes extracted from two-day post-anthesis *Petunia hybrida* flowers. Inset plot represents baseline-corrected XRD pattern.

3.5 Formulation of a model cuticle and measurement of wax permeability

The structure and ordering of the cuticle have been investigated and described in detail in sections 3.2 and 3.3. Combined chemical and physical analysis of petunia petal cuticles reveal a highly distributed wax composition comprised largely of linear aliphatic hydrocarbons, the majority of which is oxidized. Wax compounds primarily exhibit hexagonal symmetry, but a large fraction of these compounds has no crystalline order. By discriminating the chemical and physical features of petunia petals, we selected wax compounds that can be used as an *in vitro* model system representing the observed phase behavior and structural arrangements. The compounds selected were: (*i*) *n*-tetracosane ($C_{24}H_{50}$) representing the average aliphatic chain length of the petunia petal waxes; (*ii*) 1-docosanol ($C_{22}H_{45}OH$) representing the abundance of hydroxyl-containing groups; and (*iii*) 3-methylbutyl dodecanoate ($C_{17}H_{34}O_2$) to represent the amorphous waxes.

To measure the permeability of the reconstituted and model cuticles, we will employ *in vitro* diffusion cells and molecular dynamics simulations (Chapter 4). Diffusion cells are commonly used to measure the rate of mass transfer through synthetic polymeric membranes (Ng et al., 2010) or biological membranes (De et al., 2000; Davis et al., 2003). Diffusion cells fall into

three categories: static, side-by-side "Ussing" cells (Ussing, 1949); static, vertical "Franz" cells (Franz, 1975), or flow-through, vertical "Bronaugh cells" (Bronaugh and Steward, 1985). For the study of cuticular permeability, a Franz cell was used (custom-built by Permegear, Hellerstown PA, USA). The schematic of the Franz cell is show in Fig. 3.6. Static diffusion cells are comprised of a donor and receptor chamber, separated only by the permeable membrane. The mass transfer flux is obtained by time-course sampling of the concentration in the receptor chamber, as given by Fick's law:

$$J_i = -\frac{D_i}{RT} c_i \frac{\partial \mu_i}{\partial z} = D_i c_i \frac{\partial \ln a_i}{\partial z} \tag{3.1}$$

Where J_i is the diffusive flux, D_i is the diffusion coefficient, c_i is the concentration of the solute in the membrane, μ_i is the chemical potential, a_i is the thermodynamic activity, z is the axial position through the membrane, R is the universal gas constant, and T is the absolute temperature.

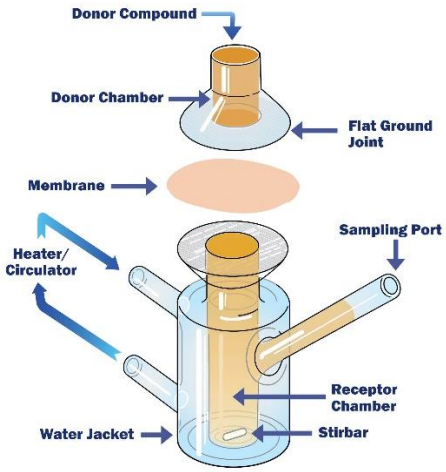

Figure 3.6 – Schematic of the Franz diffusion cell used for permeability assays. Membrane fit between donor and receptor chambers are wax films spun coat to PTFE membranes. Schematic includes adiabatic jacket which was not used for experiments conducted for this project.

The thermodynamic activity of the solute is defined as the ratio between the actual concentration and its solubility limit at temperature T. Thus, the thermodynamic activity is a description of the state of a substance at a given phase. However, the use of organic solvents as the carrier phase for lipophilic volatiles will result in solubilization of the wax membrane, thus the volatiles are dissolved in water for the *in vitro* diffusion methodology. As VOCs have low aqueous

solubility and partitioning, measurement of partition coefficients is necessary for the accurate estimation of diffusion coefficients. Sorption isotherms can be generated to obtain the VOC distribution between the organic membrane and the aqueous carrier solution. Applied to Fick's law, we can account for the partitioning between phases:

$$J_i = \frac{\mathrm{d}m_i^R}{\mathrm{d}t} = -\frac{AD_iK_{\mathrm{wax/water}}}{c_i^0} \cdot \frac{\Delta c}{\Delta z} = -\frac{AD_iK_{\mathrm{wax/water}}}{c_i^0 \Delta z} \cdot \left(\frac{m_i^R}{V^R} - \frac{m_i^D}{V^D}\right) \tag{3.2}$$

Where m_i^R and m_i^D are the mass of solute in the receptor and donor chambers, respectively, A is the interfacial area, $K_{\mathrm{wax/water}}$ is the wax/water partition coefficient, and c_i^0 is the saturation concentration of the solute. As mass of solute in the donor chamber is not measured over time, a total mass balance is used as another equation in the numerical analysis. Flux is measured over a zero order (steady-state) concentration profile in the receptor chamber.

3.5.1 Materials and methods

Chemicals

Model wax compounds *n*-tetracosane ($C_{24}H_{50}$, 99%), 1-docosanol (98%), and 3-methylbutyl dodecanoate (≥97%) were obtained from Sigma-Aldrich Co., St. Louis, MO, USA. Wax compound were dissolved in dissolved in chloroform at 5% w/v individually, with specific blends prepared by mixing measured volumes of the solubilized waxes together in glass scintillation vials. Chloroform was evaporated completely under a gentle stream of N_2, and dried wax mixtures were left to dry in a fume hood overnight. Prior to FTIR and XRD analyses, wax mixtures were heated to 80°C and allowed to cool to room temperature to ensure consistent measurement.

Wax film preparation

Both petunia petal cuticular waxes and model wax compounds were solubilized in chloroform (< 2 mg/ml). Reconstituted ultrathin wax films were produced by depositing 1 ml of wax solution onto a 25 mm PTFE membrane (25 mm diameter, 1.0 μm), held in place with vacuum under nitrogen conditions before beginning spin-coating procedure (Laurell Technologies, model WS-650MZ-23NPP). Spin-coating was performed at 1000 rpm for 1 minute. PTFE membranes

were weighed before and after spin-coating to obtain the total wax amount deposited. Thickness of wax film was estimated based on an approximate density of 800 kg/m^3.

Statistical analysis

FTIR spectral data analysis was performed in MATLAB version R2019 (MathWorks, Natick MA, USA) using the Principal Component Analysis (PCA) toolbox (Ballabio, 2015). First and second derivatives of absorbance data were performed using the forward difference method. PCA was performed on transformed datasets.

***In vitro* diffusion methodology**

An unjacketed Franz diffusion cell (inner diameter = 9 mm, receptor volume = 3 ml; donor volume = 1 ml; Permegear, Hellerstown PA, USA) was used for *in vitro* diffusion experiments. Water (3 ml) was loaded into the receptor chamber along with a magnetic stir bar, and prepared wax films was placed between the donor and receptor chambers (Fig. 3.6). Parafilm rings were cut and appended to both sides of the wax membrane to prevent leakage. Chambers were clamped shut, and 1 mL of the carrier formulation (VOCs in water below their aqueous solubility) was loaded into the donor chamber. At set time increments, about 100 µl was drawn from the receptor chamber through the sampling port. To ensure that the volume in the receptor chamber remained the same, sampled volume was replaced with fresh water by injection through the sampling port. VOCs were extracted from the aqueous samples using dichloromethane, and analyzed on an Agilent 7890A gas chromatograph couple to a 5975C inert MSD quadrupole mass spectrometer using a HP5-MS column (0.25 mm x 30 m x 0.25 µm, Agilent, Santa Clara, CA). The temperature program used was as follows: 40°C maintained for 2 min and raised from 40 to 150°C at 10°C/min, then from 150 to 250°C at 20°C/min with a final holding time of 2 min. Injector and detector temperatures were set at 250 and 230°C, respectively; and VOCs were identified based on known *m*/*z* values, and quantified from an external standard calibration curve.

Sorption isotherms

Sorption isotherms were obtained by immersing prepared wax films with varying concentrations of aqueous VOC solutions for 2 days. Wax films and aqueous solutions were independently extracted with dichloromethane, and VOC content was analyzes by GC-MS.

Isotherms were collected in standard laboratory conditions (~25 °C). Partition coefficients ($K_{wax/water}$) are directly obtained from solubility isotherms by measurement of the quantity of VOCs adsorbed onto the wax substrate. Due to the limit of detection on the GC-MS, the adsorption amount was measured by mass balance on the aqueous phase. Aqueous solutions were collected after 2 days of incubation and extracted for VOCs using dichloromethane, and extracts were analyzed for VOC content using GC-MS (see 3.4.1.4 for method). The partition coefficient is thus given by:

$$K_{\mathrm{wax/water}} = \frac{C_{\mathrm{wax}}}{C_{\mathrm{water}}} \tag{3.3}$$

Where C_{wax} and C_{water} are the equilibrium concentration of VOC in the wax and water phase, respectively. To account for amount lost to the headspace of the vial, blank vials with no reconstituted wax were incubated with the aqueous carrier formulation for 2 days. The adsorbed quantity was corrected for the ambient loss into the vial headspace at each concentration tested.
The amount adsorbed, q, was measured as follows:

$$q = \frac{(C_{\mathrm{water,eq}} - C_{\mathrm{water,0}})V_{\mathrm{solution}}}{m_{\mathrm{wax}}} \tag{3.4}$$

Where $C_{\mathrm{water,eq}}$ and $C_{\mathrm{water,0}}$ represent the equilibrium and starting concentration of the VOCs, respectively. The units for q are given as mass per unit mass (mg kg^{-1}).
As the sorption isotherm profiles were not linear, partition coefficients were obtained using the Freundlich isotherm:

$$q = K_{\mathrm{wax/water}} C_{\mathrm{water,eq}}^{1/n} \tag{3.5}$$

Where n is an arbitrary constant evaluated upon linearizing the equation. Calculated partition coefficients were then used to resolve the diffusion coefficient in equation 3.2.

3.5.2 Results and discussion

Validation of the model system

Infrared signal acquisitions were performed for the three wax compounds selected to formulate the model cuticle (Fig. 3.7). Individually, no wax compound could represent the molecular characteristics of the reconstituted petunia petal cuticle. However, the distinct vibrational frequencies identified in the IR spectra of reconstituted cuticles could be captured by some combination of all three compounds.

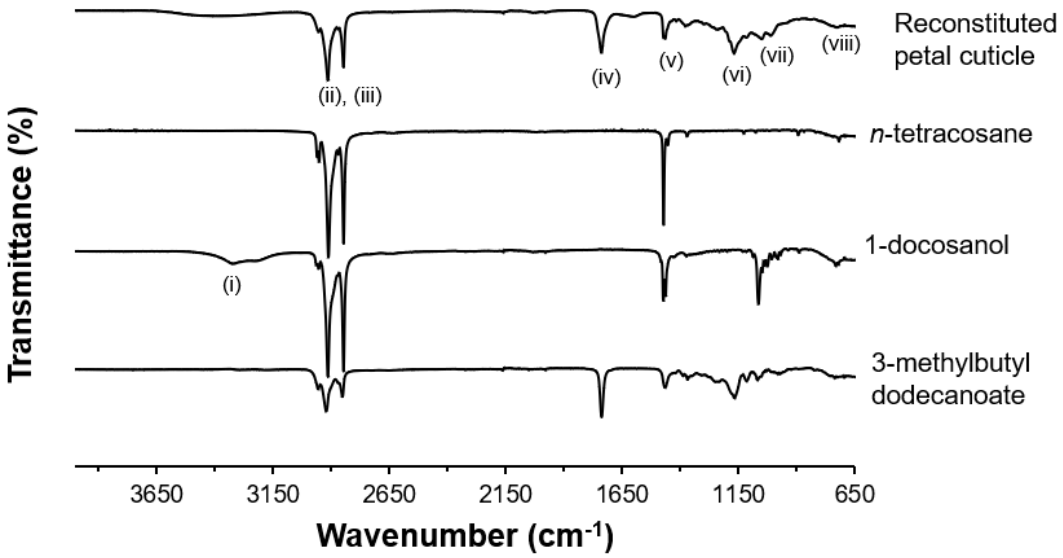

Fig. 3.7 – Transmission spectra of model wax compounds in contrast to reconstituted petunia petal cuticles. Annotated peaks correspond to vibration assignments (**Table 3.2**).

To determine if there was a wax blend that could achieve spectral alignment with the petal cuticle, a simple linear regression interaction model was employed. Prior to the multiple regression, ATR-FTIR absorbance spectra was preprocessed in MATLAB for baseline correction. Regression was performed on the first derivatives of the infrared spectra to ensure peaks were sufficiently discriminated from baseline noise. The following three-way interaction regression model was used:

$$\hat{y} = \beta_0 + \beta_1 x_1 + \beta_2 x_2 + \beta_3 x_3 + \beta_{12} x_1 x_2 + \beta_{13} x_1 x_3 + \beta_{23} x_2 x_3 + \beta_{123} x_1 x_2 x_3 \qquad (3.6)$$

Where $\hat{y}$ is the response variable (IR spectra of reconstituted petal waxes), β_{ijk} are the parameters representing the zero, first, second, and third order interactions, and x_i represents wax component *i*. Regression results are summarized in Table 3.3 and Fig. 3.8.

Table 3.3 – Parameter estimates for multiple regression model of first derivative infrared spectra.

Term	Definition	Estimate ($\times 10^3$)	S.E.	*t* ratio	$P > \|t\|$
β_0	Intercept	1.932	1.86e-3	1.04	0.3
β_1	$C_{24}H_{50}$	108.383	4.76e-3	22.86	< 0.0001
β_2	$C_{22}H_{45}OH$	177.573	5.91e-3	30.07	< 0.0001
β_3	$C_{17}H_{34}O_2$	564.756	1.13e-2	50.06	< 0.0001
β_{12}	$C_{24}H_{50}\times C_{22}H_{45}OH$	7.484	9.05e-4	8.27	< 0.0001
β_{13}	$C_{24}H_{50}\times C_{17}H_{34}O_2$	-67.171	9.56e-3	-7.03	< 0.0001
β_{23}	$C_{22}H_{45}OH\times C_{17}H_{34}O_2$	-52.794	1.11e-2	-4.74	< 0.0001
β_{123}	$C_{24}H_{50}\times C_{22}H_{45}OH\times C_{17}H_{34}O_2$	7.981	1.22e-3	6.56	< 0.0001

Regression analysis shows that for representation of the reconstituted petal cuticle, the regression coefficient for $C_{17}H_{34}O_2$ has the highest absolute value. From the FTIR transmission spectra (Fig. 3.7), methylene stretching at 2920 and 2850 cm^{-1} may bias the regression. Due to the aliphatic order of both $C_{24}H_{50}$ and $C_{22}H_{45}OH$, their respective regression coefficient estimates must be lower to diminish their high peak intensities at those wavelengths. Nonetheless, multiple regression of the spectral datasets supports the hypothesis that mixtures of these wax compounds can produce a model system representative of real cuticles.

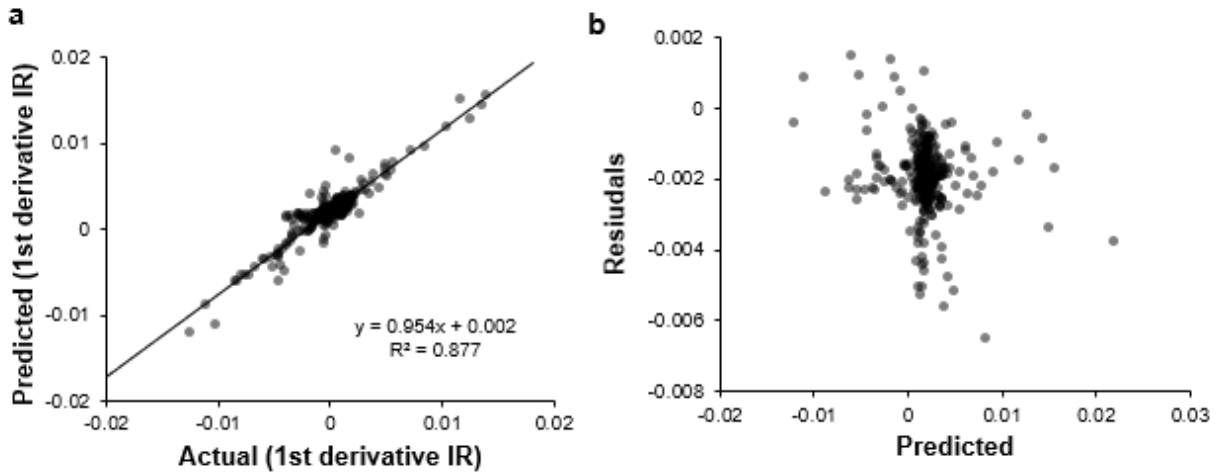

Fig. 3.8 – Multiple linear regression model for petunia absorbance spectra (first derivative). (a) Regression predicted values from linear fit (equation 3.6, Table 3.3). (b) Model residuals.

ATR-FTIR spectra was subsequently collected for sixteen wax formulations of the $C_{24}H_{50}/C_{22}H_{45}OH/C_{17}H_{34}O_2$ ternary system (Fig. B1). For validation of the model system, principal component analysis (PCA) was performed on the second derivatives of the IR spectra (Fig. 3.9a). Interestingly, analysis of individual principal components demonstrated that the IR spectra of mixtures containing $C_{22}H_{45}OH$, the most abundant wax metabolite detected from mass spectrometry analysis (9 ± 2 cuticle dry wt. %), clustered closest with that of the reconstituted cuticle. A ternary mixture of 26.8, 51.7, 21.4 wt. % of $C_{24}H_{50}$, $C_{22}H_{45}OH$, and $C_{17}H_{34}O_2$, respectively, demonstrated the greatest correlation with that of the reconstituted cuticle (Fig. 3.9b), and thus serves as the basis for the model cuticle chemical composition. The first principal component, accounting for 75% of the variance, exhibits major bands at wavelengths previously assigned to cuticle components (Fig. 3.9c), thus showing agreement with the molecular arrangements of the selected wax compounds and the reconstituted petunia petal cuticle. Variations in the proportions of the three wax compounds can hence be used to represent the effect of chemical composition on cuticle structure and molecular diffusion.

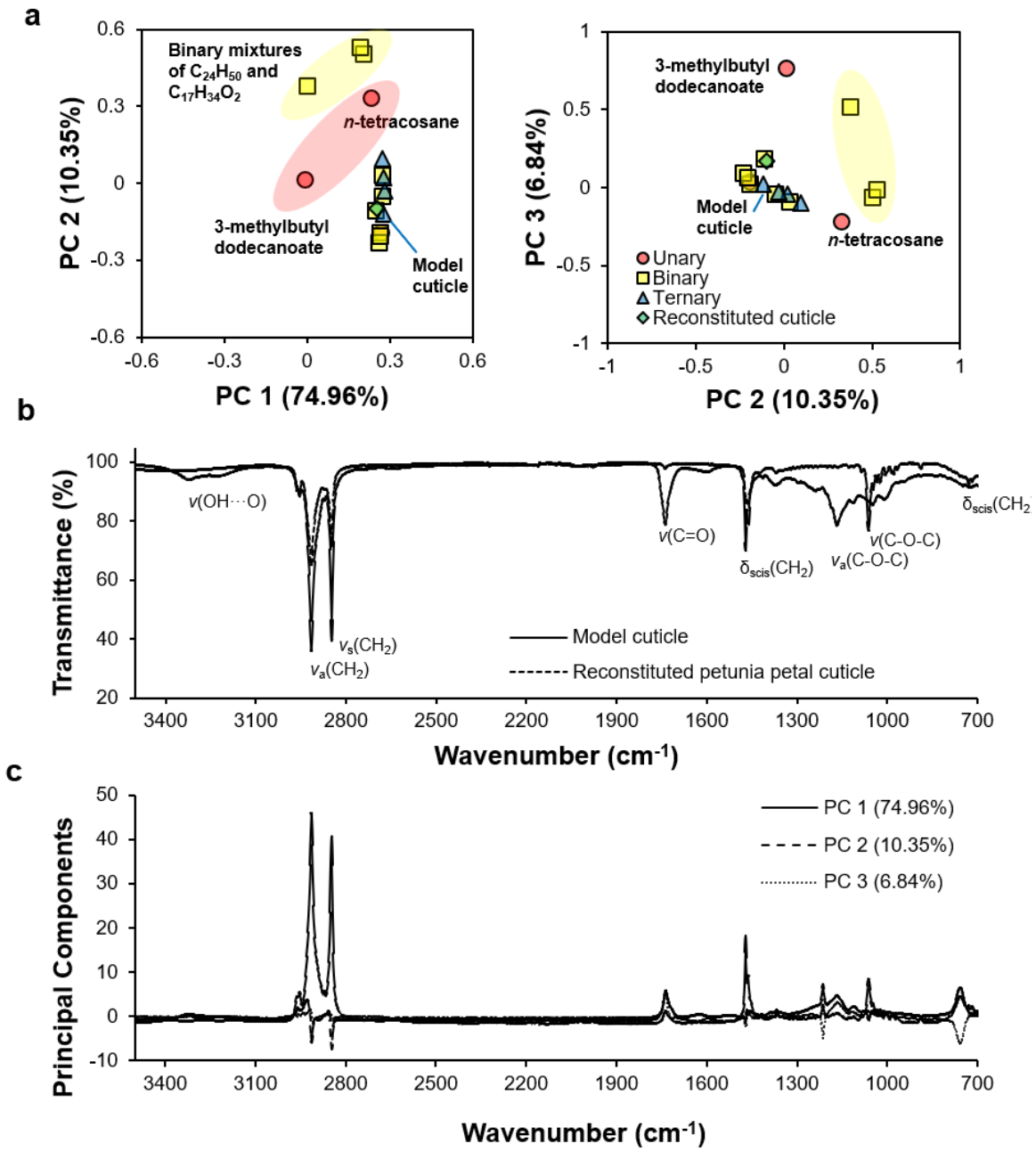

Fig. 3.9 – Principal component analysis for FTIR spectra of model and petunia petal cuticular waxes. (a) Principal components (PC) demonstrate separation of ATR-FTIR spectra (second derivative) of reconstituted petunia petal cuticles and (1-, 2-, 3-component) mixtures of model wax compounds. (b) Principal component loadings of transformed spectra demonstrating variations in wax vibration bands. (c) ATR-FTIR transmission spectra for model cuticle of composition 26.8/51.7/21.4 wt.% of $C_{24}H_{50}/C_{22}H_{45}OH/C_{17}H_{34}O_2$.

Effect of wax composition on aliphatic crystallinity

Paraffin and microcrystalline waxes are predominantly comprised of linear hydrocarbons with generally similar physical properties, i.e. solubility in organic solvents, melting points above 40°C, with orthorhombic crystal lattice symmetry below their hexagonal phase transition (Reynhardt, 1985). However, the natural waxes of plants contain a significant fraction of cyclic and branched hydrocarbons with varying functional groups (acids, alcohols, aldehydes, esters, ketones, etc.) that result in changes in crystalline symmetry and physical description (Jeffree, 1996; Ensikat et al., 2006). Thus, changes in the distribution of wax compounds with varying chain length, branching, and functional groups influence the dimensions, symmetry, and abundance of crystalline units. The details of wax crystallinity were analyzed using powder X-ray diffraction (Fig. 3.10 and Fig. B1). Diffraction patterns of the model cuticle components are used to analyze details about the dimensions and interatomic spacing between crystalline lattice planes. Below their rotator phase transition temperature, linear hydrocarbons are assembled parallel to each other and form layers, with the thickness of an individual layer equal to the length of the molecule. XRD patterns for n-tetracosane and 1-docosanol demonstrate two distinct region: a series of (00*l*)-peaks at low diffraction angles ($2\theta \leq 15°$, Fig. 3.10a) that show the thickness of molecular layers and (*hk*0)-peaks at high diffraction angles ($20 \leq 2\theta \leq 25°$, Fig. 3b) that represent the distances between unit cells. The index of peaks at low diffraction angles are used to directly calculate the length (*c*-axis) of the crystalline unit cell using Bragg's law (Table 3.4). For wax samples enriched with n-alkanes, these (00*l*)-peaks have high intensity indicating distinct ordering of the crystalline layers (inset of Fig. 3.10a). The relative intensity of these peaks does not indicate the thickness of a single molecular layer, but rather determines the extent of layering of repeating unit cells. Samples with increased peak intensities at low diffraction angles indicate increased crystalline layering. In contrast, the XRD pattern for 1-docosanol exhibits diminished intensities for (00*l*)-peaks, suggesting a lack of periodic order of wax chains. However, upon MD equilibration, 1-docosanol was observed to have periodic layering between crystalline units (inset of Fig. 3.10b) with a distinct "double-layer" arrangement where the terminal hydroxyl groups arranged in a head-to-head orientation. The intensity of peaks at low diffraction angles is attributed to the spacing between molecular layers, however, for 1-docosanol, this gap region is filled with oxygen atoms resulting in a difference in the atomic density thereby reducing overall peak intensity.

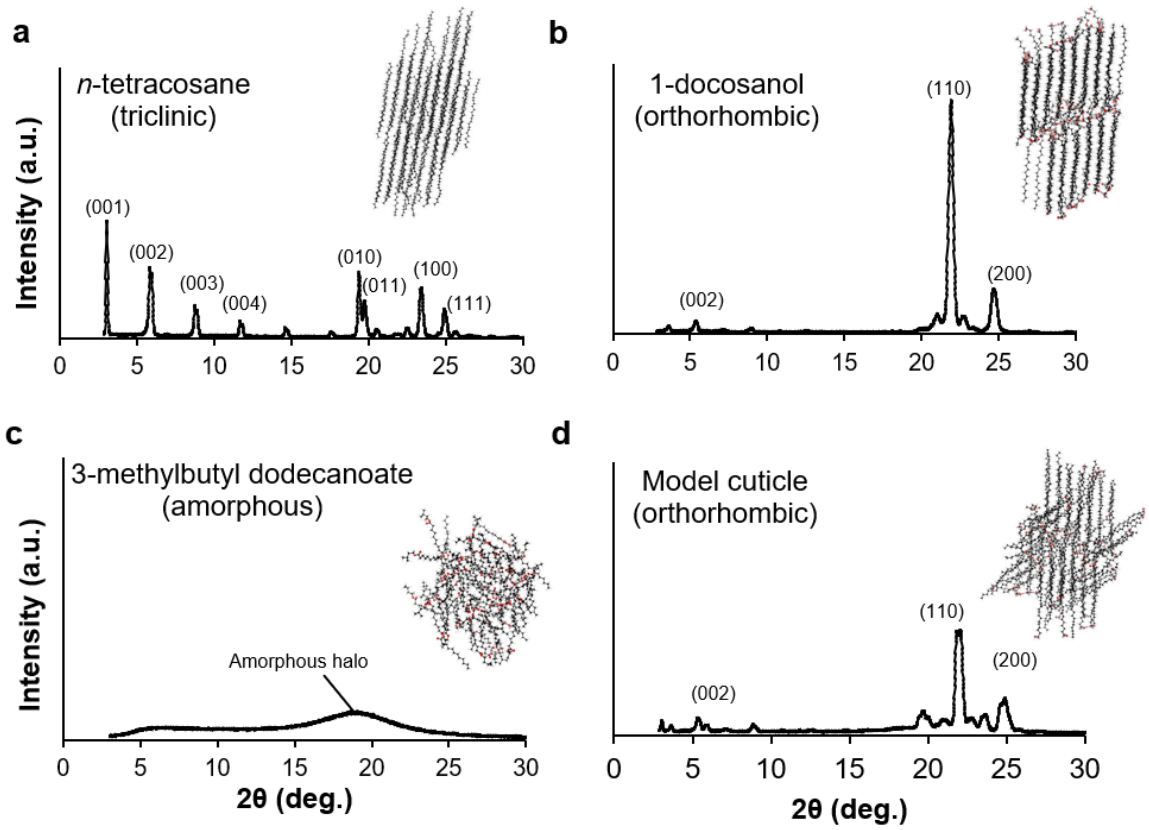

Fig. 3.10 – XRD-diagrams of reference wax compounds and representative characteristics. XRD-patterns for (a) *n*-tetracosane ($C_{24}H_{50}$), (b) 1-docosanol ($C_{22}H_{45}OH$), (c) 3-methylbutyl dodecanoate ($C_{17}H_{34}O_2$), and (d) the model cuticle of composition 26.8%/51.7%/21.4% $C_{24}H_{50}$/$C_{22}H_{45}OH$/$C_{17}H_{34}O_2$ by wt.%. Inset figures are the simulated structures of the wax system after simulated annealing from 400 K and equilibrated at 298 K and 1 bar for 10 ns (detailed description in Chapter 4).

Table 3.4 – Crystallinity of wax formulations.

Wax composition (wt. fraction)			Crystallinity			
$C_{24}H_{50}$	$C_{22}H_{45}OH$	$C_{17}H_{34}O_2$	Lattice parameters (a, b, c, α, β, γ)	Phase[†]	Maximum d-spacing (Å)	Aliphatic crystallinity (%)[‡]
1.000	0.000	0.000	(4.28, 4.82, 32.53, 86.40, 68.80, 72.67)	triclinic	4.58	93.08 (0.7)
0.757	0.243	0.000	(4.88, 7.59, 30.24, α = β = γ = 90)	ortho	4.56	93.09 (3.2)
0.509	0.491	0.000	(4.87, 7.55, 29.97, α = β = γ = 90)	ortho	4.09	95.21 (0.4)
0.257	0.743	0.000	(4.96, 7.41, 30.21, α = β = γ = 90)	ortho	4.12	96.78 (1.6)
0.000	1.000	0.000	(4.90, 7.21, 24.77, α = β = γ = 90)	ortho	4.06	97.88 (1.2)
0.000	0.784	0.216	(4.92, 7.22, 25.02, α = β = γ = 90)	ortho	4.07	93.28 (5.0)
0.000	0.547	0.453	(4.91, 7.23, 24.74, α = β = γ = 90)	ortho	4.06	67.37 (3.7)
0.000	0.287	0.713	(4.92, 7.65, 24.93, α = β = γ = 90)	ortho	4.53	30.29 (0.3)
0.000	0.000	1.000	-	I.L.		0.00
0.294	0.000	0.706	(a = b= 6.79, c = 28.18, α = β = 90, γ = 120)	hex	4.33	19.46 (0.0)
0.556	0.000	0.444	(a = b= 6.80, c = 30.10, α = β = 90, γ = 120)	hex	4.33	48.95 (0.0)
0.790	0.000	0.210	(a = b= 6.77, c = 30.08, α = β = 90, γ = 120)	hex	4.58	71.14 (3.4)
0.362	0.349	0.289	(a = b= 6.48, c = 31.32, α = β = 90, γ = 120)	hex	4.54	89.69 (0.2)
0.531	0.256	0.212	(4.80, 7.57, 31.32, α = β = γ = 90)	ortho	4.54	91.43 (0.8)
0.268	0.517	0.214	(4.87, 7.56, 29.83, α = β = γ = 90)	ortho	4.08	84.40 (5.8)
0.281	0.271	0.448	(4.85, 7.24, 30.18, α = β = γ = 90)	ortho	4.57	71.43 (0.7)

[†]Solid crystalline phase: ortho – orthogonal; hex – hexagonal, I.L. – isotropic liquid.

[‡]Uncertainty in measurement based on XRD peak integration.

Peaks at higher diffraction angles provide information on the lateral packing and spacing between wax chains. (110) and (200)-peaks corresponding to d-spacing values of approximately 4.2 and 3.8 Å were observed for most combinations of three wax compounds. Spacing at these distances originate from the perpendicular orientations of neighboring methylene chains consistent with orthogonal lattice symmetry (Ratnaswamy et al., 1973, Reynhardt, 1985). Some wax formulations exhibited reduced intensity of (200)-peaks suggesting hexagonal symmetry (Fig. B2). A shift from orthorhombic to hexagonal symmetry at a phase transition, where the wax methylene chains begin to rotate about their length axis. While most wax formulations exhibit both perpendicular and parallel arrangements of methylene chains, pure n-tetracosane exhibits a fully parallel arrangement suggesting monoclinic or triclinic symmetry. The XRD pattern for n-tetracosane has peaks with d-spacing values at 4.58 and 3.79 Å indicating triclinic symmetry, a known arrangement for even numbered n-alkanes (Dorset, 2000). Positions of these (*hk*0)-peaks can be used to measure the interatomic spacing and lattice dimensions based on the unit cell geometry. For most wax formulations, the a and b lattice parameters were found to be ~5.0 and ~7.5 Å, respectively, and this did not vary significantly. Despite large changes in chemical composition over the ternary system, interatomic spacing was found to only vary between 4.1 ± 0.5 Å, consistent with the short range of measured densities.

The XRD patterns for pure 3-methylbutyl dodecanoate (Fig. 3.10c) had no discernable crystalline peaks, and only have a broad peak (amorphous halo) centered at approximately $2\theta = 19°$. At 25°C, 3-methylbutyl dodecanoate is a viscous liquid with no solid crystalline order (inset of Fig. 3c), and only comprises a minor fraction of the wax constituents identified from isolated petunia petal waxes (< 0.002 dry wt. %). The disorder of plant cuticles arise due to the heterogeneous distribution of waxes with varying chain length, branching and functional groups; however, this chemical complexity is difficult to explore for an in vitro model of the cuticle. Despite its low abundance in the cuticle, introduction of 3-methylbutyl dodecanaote into wax mixtures allows for a wide range in aliphatic crystallinity. Wax mixtures containing 3-methylbutyl dodecanoate exhibit increased width and intensity of the amorphous halo (Fig. B2) thus creating a range from 0 to ~100% crystallinity to measure molecular diffusion. Even though the XRD pattern for the model cuticle exhibits the same crystalline symmetry as 1-docosanol (Fig. 3.10d), the (110)- and (200)-peaks are diminished due to an emerging halo. While pure 1-docosanol is measured to have a relative crystallinity of 97.9 ± 1.2%, the model cuticle crystallinity is significantly decreased

(84.4 ± 5.8%). Overall, mixtures containing major fractions of *n*-tetracosane and 1-docosanol demonstrate minimal changes in crystalline symmetry and spacing, but introduction of a third component, 3-methylbutyl dodecanoate, significantly influences the anisotropy of the *in vitro* cuticle.

Cuticle permeability measurements

Upon manipulation of the model cuticle chemical composition, significant changes in wax morphology was measured by ATR-FTIR and XRD. To determine if these physical changes in wax structure result in measurable changes in the transport properties of diffusing solutes, the permeability of petunia petal and model waxes was measured using a static diffusion cell.

Isolated petunia cuticles were reconstituted onto PTFE membranes using a spin coater, and the wax films were loaded into a Franz diffusion cell (Fig. 3.6). To prevent solubilization of the wax film, both donor and receptor fluids were water. Permeability of petunia volatiles benzaldehyde, methylbenzoate, 2-phenylethanol, isoeugenol, and benzylbenzoate were measured by time-course sampling of the receptor chamber (Fig. 3.11). Diffusion coefficients were obtained from equation 3.2, and are tabulated in Table 3.4. To calculate diffusion coefficients, solubility isotherms were obtained for all VOCs (Fig. 3.12) to calculate wax/water partition coefficients. VOC permeability assays of PTFE membranes revealed that diffusion coefficients were up to 3-4 orders of magnitude higher (Fig. B3), suggesting that the resistance imparted by the PTFE substrate is negligible. VOC diffusion was found to be size-dependent, with benzaldehyde (molar volume = 103 $Å^3$) experiencing 4.3-fold higher diffusion than benzylbenzoate (molar volume = 200 $Å^3$).

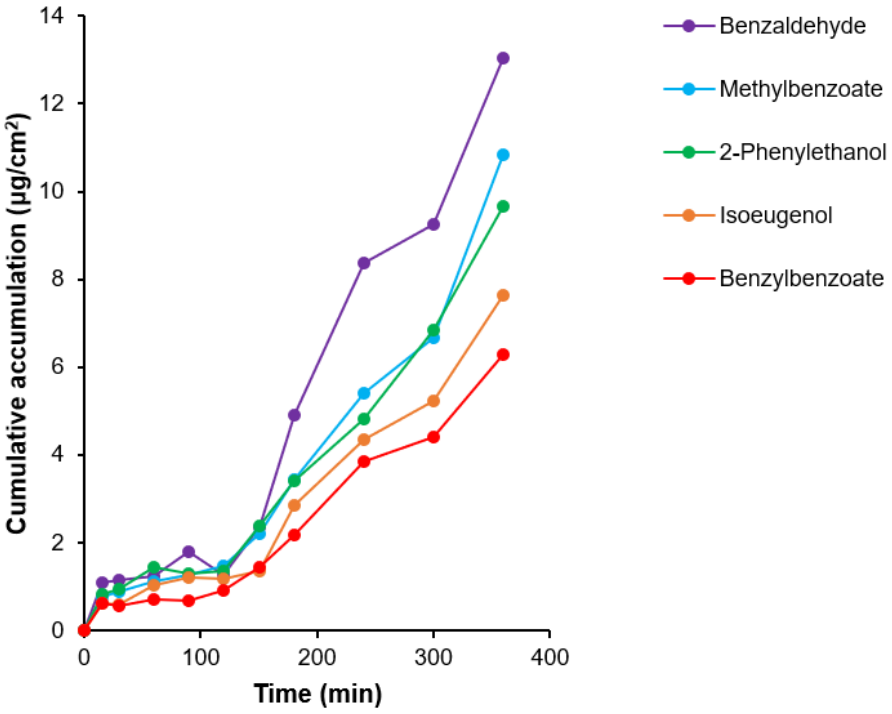

Fig. 3.11 – VOC permeability through reconstituted *Petunia hybrida* petal waxes in the static diffusion cell. Reconstituted wax films were prepared by spin coating solvent-extracted petal waxes of two-day post-anthesis petunia flowers (n = 40 flowers) onto a PTFE substrate.

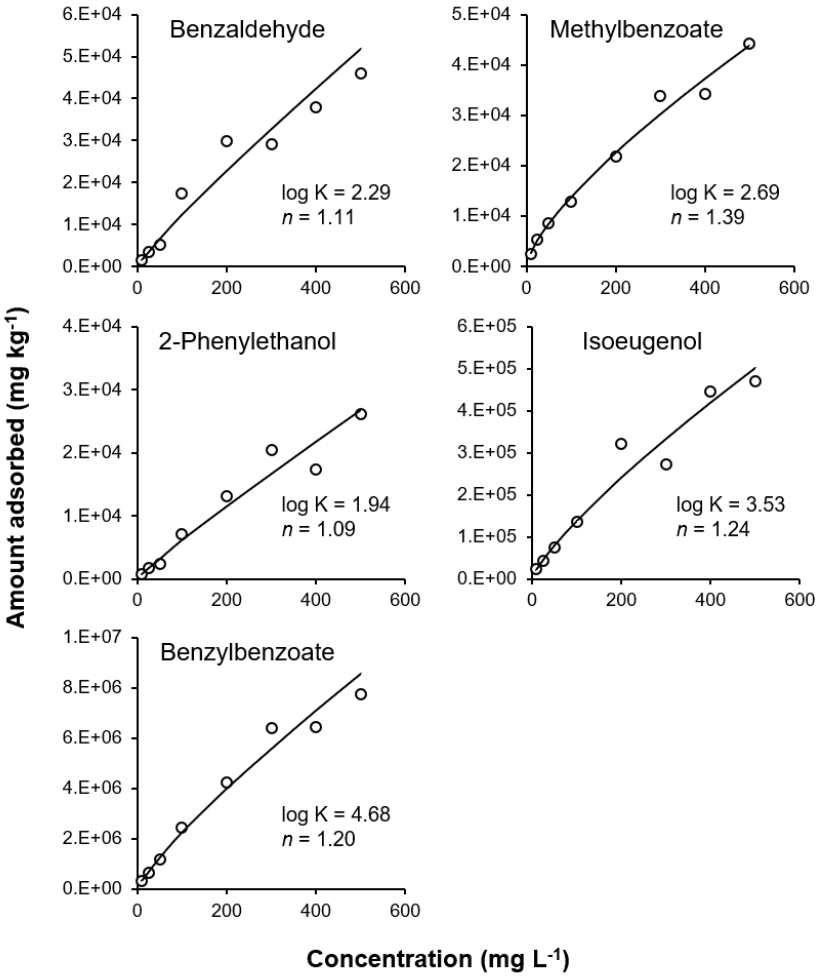

Fig. 3.12 – Sorption isotherms for petunia VOCs fit with nonlinear isotherm models.

To identify if changes in wax composition result in measureable changes in permeability of VOCs, model wax compounds were dissolved in chloroform in varying proportions and spun coat onto the PTFE substrate. Diffusion profiles (Fig. 3.13) and solubility isotherms (Fig. B2) for methylbenzoate were obtained to calculate diffusivity and partitioning over a broad range of wax compositions. Variations in wax composition resulted in negligible changes in partitioning of methlylbenzoate, suggesting that deviations in permeability arise from diverging diffusion coefficients. Indeed, permeability assays over the range of wax compositions resulted in measurable changes in diffusion coefficient (Table 3.5). From Section 3.5.1.7, the crystallinity of various wax compositions was obtained from XRD measurements. Methylbenzoate diffusivity varies up to 3.7-fold between a range of 30-100% absolute crystallinity (Fig. 3.14). The diffusion

coefficients for methylbenzoate varied between 2.3-7.9×10^{-16} m^2/s over the range of wax compositions tested, while in reconstituted petal cuticles, the diffusion coefficient was found to be 8.49 (±0.18) ×10^{-16} m^2/s, demonstrating similarity in model and petal wax permeability. As the diffusivity in the real cuticle is on the higher end of the measurement range, it suggests that petal cuticles are significantly more permeable to diffusing compounds compared to highly crystalline waxes.

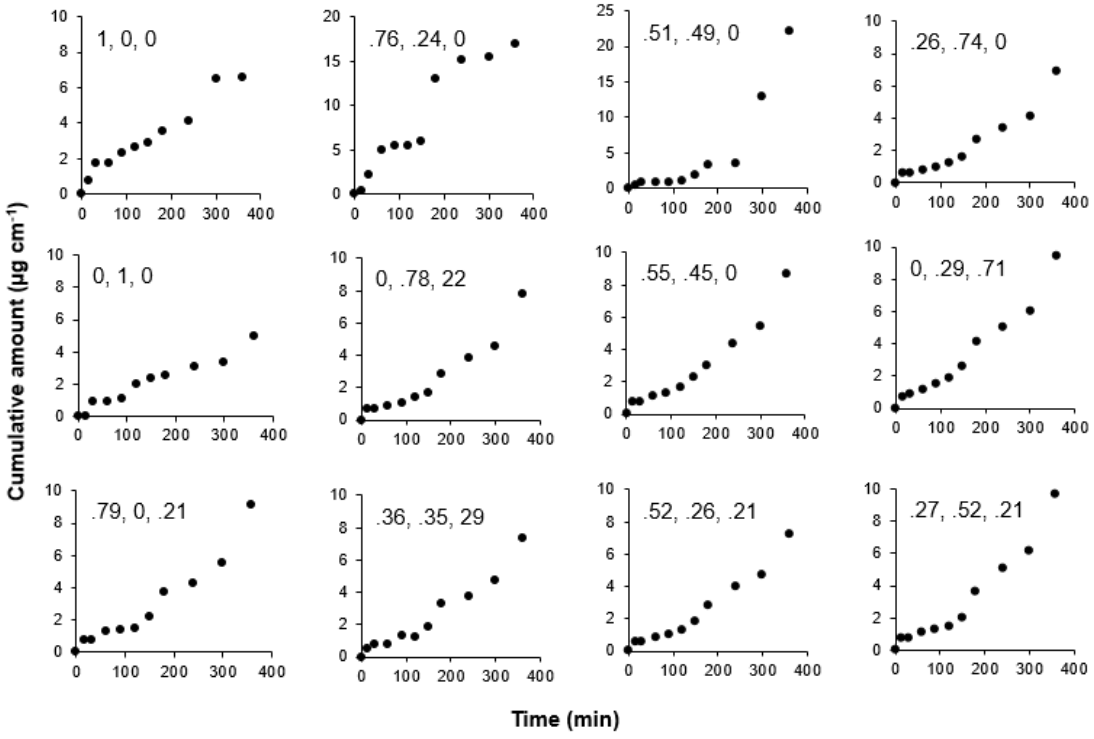

Fig. 3.13 – Methylbenzoate concentration profiles obtained from permeability assays through waxes of varying composition. Composition is given by weight fractions of $C_{24}H_{50}$, $C_{22}H_{45}OH$, $C_{17}H_{34}O_2$, respectively.

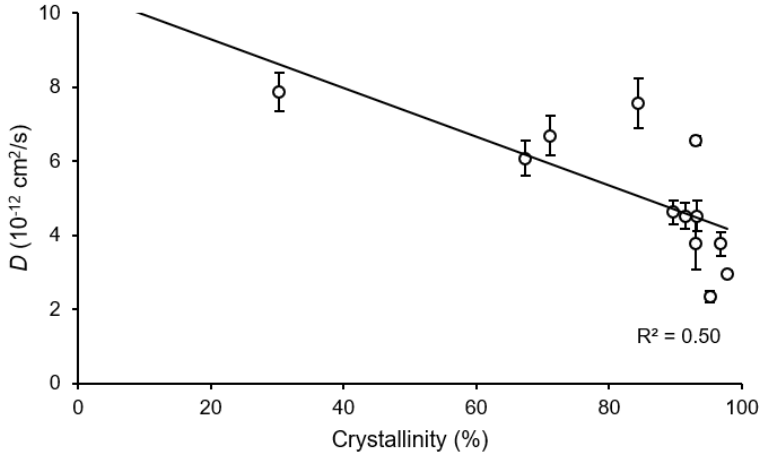

Fig. 3.14 – Effect of model cuticle crystallinity on methylbenzoate diffusion. Diffusion coefficients are obtained from methylbenzoate concentration profiles in static diffusion cells. Wax film crystallinity is obtained from XRD experiments (Table 3.4). Data are means ± S.E. (error is model (equation 3.2) regression error).

A limitation to the permeability assay is the difference in the physical setup of the experiment and the physiological conditions in the epidermal cell. For VOCs to permeate the cuticle, they must (*i*) diffuse through the static boundary layer formed at the interface between the cell wall and cuticle, (*ii*) diffuse through the cuticle, and (*iii*) volatilize off the surface of the petal into the surrounding atmosphere (Fig. 3.15). Models describing solute permeation across membranes with interfacial boundary layers utilize the resistance-in-series model of mass transfer, where the overall rate of mass transfer is dependent on local mass transfer resistances along the path length. Due to their relatively high volatility in ambient temperatures, the third resistance is negligible, and the overall mass transfer resistance across the cuticle is given by:

$$\frac{1}{K_{m,i}} = \frac{1}{k_{\mathrm{BL},i}} + \frac{1}{k_{\mathrm{cut},i}} \tag{3.7}$$

Where $K_{m,i}$ is the overall mass transfer coefficient, and $k_{\mathrm{BL},i}$ and $k_{\mathrm{cut},i}$ represent the individual mass transfer coefficients of the cell wall – cuticle boundary layer and cuticle respectively. The individual mass transfer coefficients are governed by diffusive path length, diffusivity, and inter-phase partition coefficients.

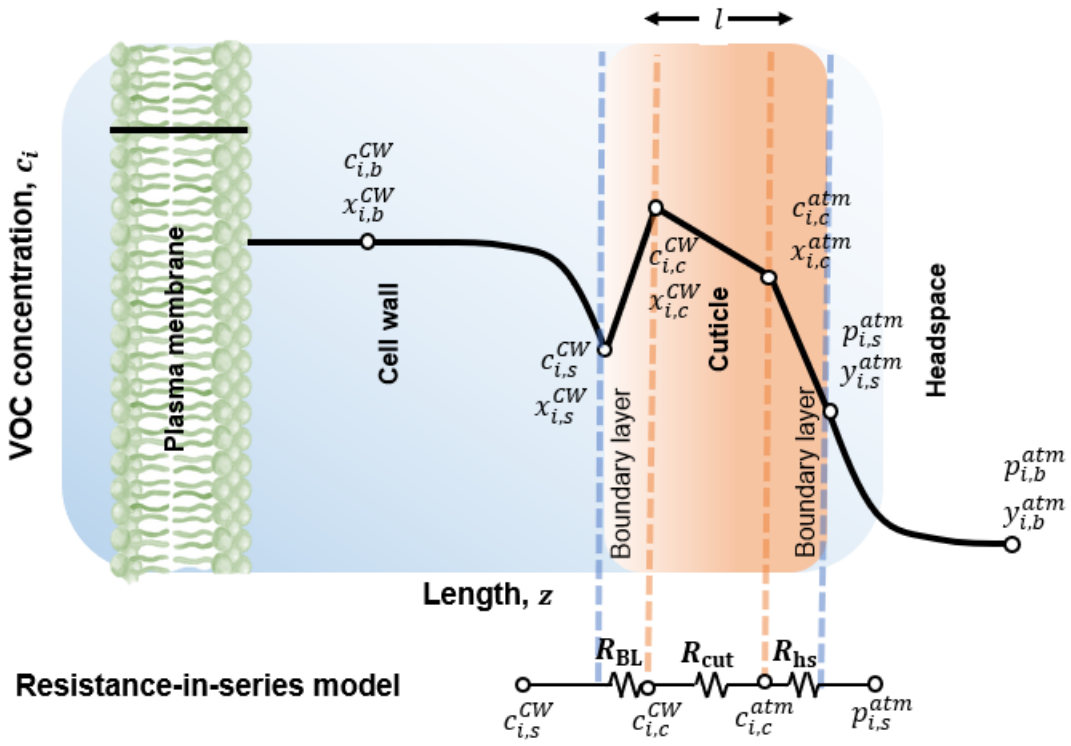

Fig. 3.15 – Mass transfer model of VOC export from plant epidermal cells. Solubility-diffusion model demonstrating the transport of VOCs across the cuticle of plant epidermal cells. Solid black lines are representative concentration profiles of a given VOC i as it is released from the lipid bilayer into the aqueous cell wall. Subscripts b, s, c represent bulk, surface, and cuticular concentrations of the VOC i, respectively. Superscripts CW and atm represent the cell wall and atmospheric phases, respectively. VOC concentration in the epidermis is given as c_i and its respective mole fraction x_i, while VOC concentration in the headspace is given by its partial pressure p_i or its respective vapor mole fraction y_i. Mass transfer resistances include the boundary layer (BL), the cuticle (cut) and the headspace (hs). The total diffusive path length across the cuticle is given by the thickness of the cuticle, l.

While the diffusion cell does capture the effects of the aqueous-wax interface, the receptor chamber is comprised of water, adding a third resistance term to the resistance-in-series model. Due to poor solubility and partitioning, VOCs are likely enriched in the wax layer over the duration of the permeability assay. This phenomenon is known as concentration polarization (Feng and Huang, 1994), and is known to result in inhibited diffusion across the membrane due to the build-up of solute in the membrane. This shift in diffusion behavior is not readily observed by measuring the concentration in the receptor chamber, but rather requires measurement of the membrane concentration (Wijmans *et al*, 1996), which is quite impractical based on the experimental configuration. A major consideration for this experiment would be to sample the donor chamber

in time-course to obtain the VOC content in the wax membrane via mass balance. Given the difference in experimental conditions and the physiological conditions inside the epidermal cell, it is possible that measured diffusion coefficients from the static diffusion cell will not apply to the real system. However, even with re-distributed mass transfer resistances among the various interfaces, comparing relative diffusivities is still informative with respect to the effect of crystallinity on diffusion. On a relative scale, it is clear that crystallinity has a significant effect on the diffusion of volatiles as observed from the *in vitro* diffusion cell experiments, where an ~70% decrease in crystallinity resulted in up to a 3.7-fold increase in diffusivity.

3.6 Conclusions

In summary, the distribution and characteristics of petunia petal waxes were obtained using GC-MS, ATR-FTIR, and XRD. Petal cuticles were found to be comprised largely of long chain linear hydrocarbons, primarily acids, alcohols, and alkanes, with a mean carbon chain-length of 24 atoms. The resulting physical character of the cuticle was that of a highly aliphatic wax, comprised of long methylene chain subcells that contribute to the anisotropy of the wax. Using statistical analysis, a model cuticle representing the physical characteristics of petunia waxes was formulated using a ternary system comprised of *n*-tetracosane, 1-docosanol, and 3-methylbutyl dodecanoate. Varying the proportions of the three wax compounds resulted in significant changes in aliphatic crystallinity as measured by XRD. Permeability assays for select wax formulations reveal that VOC permeability is dependent on the crystallinity of the wax, where a wax of 30% aliphatic crystallinity can experience up to 3-fold higher flux than that of a fully crystalline wax. Individual VOC diffusivity was found to be size-dependent, where low molecular weight compounds such as benzaldehyde and methylbenzoate had 3-4-fold high diffusion coefficients compared to large VOCs such as benzylbenzoate.

3.7 Acknowledgements

This work was supported by grant IOS-1655438 from the National Science Foundation awarded to Dr. Natalia Dudareva and Dr. John A. Morgan. I would like to thank the Research Instrumentation Center in the Department of Chemistry, Purdue University, for training and access to the Thermo Nicolet 6700 FT-IR Spectrophotometer. I would also like to Department of

Chemistry, Purdue University, for training and access to the Empyrean Powder X-ray Diffractometer. Finally, I thank the P.O.W.E.R. Lab (Davidson School of Chemical Engineering, Purdue University) group members and Dr. Bryan Boudouris for access to the spin-coater.

3.8 References

Aretz I., Meierhofer D. (2016) Advantages and pitfalls of mass spectrometry based metabolome profiling in systems biology. *International Journal of Molecular Science, 17* (632)

Athukorala Y., Mazza G. (2010) Supercritical carbon dioxide and hexane extraction of wax from triticale straw: Content, composition and thermal properties. *Industrial Crops and Products, 31*, 550–56

Baker EA. (1982). "Chemistry and morphology of plant epicuticular waxes," in The Plant Cuticle, Linnean Society Symposium Series Vol. 10 eds Cutler D. F., Alvin K. L., Price C. E., editors. (London: Academic Press) 139–165.

Ballabio, D. (2015). A MATLAB toolbox for Principal Component Analysis and unsupervised exploration of data structure. *Chemometrics and Intelligent Laboratory Systems, 149* B, 1-9

Barthlott W., Neinhuis C., Cutler D., Ditsch F., Meusel I., Theisen I., Wilhelmi H. (1998) Classification and terminology of plant epicuticular waxes. *Botanical Journal, 126* (3), 237-60

Bemis SM., Torii KU. (2007) Autonomy of cell proliferation and development programs during *Arabidopsis* aboveground organ morphogenesis. *Developmental Biology, 304*, 367-381.

Benítez JJ., Matas AJ., Heredia A. (2004). Molecular characterization of the plant biopolyester cutin by AFM and spectroscopic techniques. *Journal of Structural Biology. 147*, 179–84

Bergougnoux V., Caissard JC., Jullien F., Magnard JL., Scalliet G., Cock JM., Hugueney P., Baudino S. (2007). Both the adaxial and abaxial epidermal layers of the rose petal emit volatile scent compounds. *Planta, 226*, 853-866.

Bernard A, Joubès J (2013) Arabidopsis cuticular waxes: advances in synthesis, export and regulation. *Progress in Lipid Research, 52*, 110–29

Bessire M, Borel S, Fabre G, Carraça L, Efremova N, Yephremov A, Cao Y, Jetter R, Jacquat AC, Métraux JP, et al. (2011) A member of the PLEIOTROPIC DRUG RESISTANCE family of ATP binding cassette transporters is required for the formation of a functional cuticle in Arabidopsis. *Plant Cell, 23*, 1958–70

Bird D, Beisson F, Brigham A, Shin J, Greer S, Jetter R, Kunst L, Wu X, Yephremov A, Samuels L (2007) Characterization of Arabidopsis ABCG11/WBC11, an ATP binding cassette (ABC) transporter that is required for cuticular lipid secretion. *Plant Journal, 52*: 485–498

Borodich FM, Gorb EV, Gorb SN (2010) Fracture behaviour of plant epicuticular wax crystals and its role in preventing insect attachment: a theoretical approach. *Applied Physics A: Material Science and Processing, 100*, 63–71

Bronaugh R., Stewart R. (1985) Methods for *in vitro* percutaneous-absorption studies 4: The flow-through diffusion cell. *Journal of Pharmaceutical Sciences, 71*, 64-67

Chamel A., Maréchal Y. (1992). Characterization of isolated plant cuticles using Fourier Transform infrared (FTIR) spectroscopy. *Comptes rendus de l'Académie des Sciences Paris, 315*, 347–354

Chatterjee S., Matas AJ., Isaacson T., Kehlet C., Rose JKC., Stark R. (2015) Solid-State ^{13}C NMR Delineates the Architectural Design of Biopolymers in Native and Genetically Altered Tomato Fruit Cuticles. *Biomacromolecules, 17* (1), 215-24

Chen G, Komatsuda T, Ma JF, Nawrath C, Pourkheirandish M, Tagiri A, Hu YG, Sameri M, Li X, Zhao X, et al. (2011) An ATP-binding cassette subfamily G full transporter is essential for the retention of leaf water in both wild barley and rice. *Proceedings in the National Academy of Science USA, 108*, 12354–59

Chichakli M., Jessen FW. (1967) Crystal morphology in hydrocarbon systems. *Industrial & Engineering Chemistry Research*, *59*, 86-98

Davis CC., Kremer MJ. Schlievert PM., Squier CA. (2003) Penetration of toxic shock syndrome toxin-1 across porcine vaginal mucosa ex vivo: permeability characteristics, toxin distribution and tissue damage. *American Journal of Obstetrics and Gynecology*, *189*,1785-91

Debono A, Yeats TH, Rose JKC, Bird D, Jetter R, Kunst L, Samuels L (2009) Arabidopsis LTPG is a glycosylphosphatidylinositol-anchored lipid transfer protein required for export of lipids to the plant surface. *Plant Cell*, *21*, 1230–38

Deising HB, Werner S, Wernitz M (2000) The role of fungal appressoria in plant infection. *Microbes and Infection*, *2*, 1631–41

Domínguez E., Heredia-Guerrero JA., Heredia A. (2011). The biophysical design of plant cuticle: an overview. *New Phytologist, 189*, 938–949

Dorset DL. (2000). Crystallography of Real Waxes: Branched Chain Packing in Microcrystalline Petroleum Wax Studied by Electron Diffraction. *Energy Fuels, 14* (3), 685-91

Du X., Squier CA., Kremer MJ., Wertz PW. (2000) Penetration of N-nitrosonornicotine (NNN) across oral mucosa in the presence of ethanol and nicotine. *Journal of Oral Pathology & Medicine, 29*, 80-85

Dudareva N, Pichersky E. (2000) Biochemical and molecular genetic aspects of floral scents. *Plant Physiology*, *122* (3), 627–33

Ensikat H. J., Boese M., Mader W., Barthlott W., Koch K. (2006). Crystallinity of plant epicuticular waxes: electron and X-ray diffraction studies. *Chemistry and Physics of Lipids, 144*, 45–59.

Ensikat HJ, Neinhuis C, Barthlott W. (2000). Direct access to plant epicuticular wax crystals by a new mechanical isolation method. *International Journal of Plant Sciences, 161*, 143–48

España L, Heredia-Guerrero J., Segado JJ., Heredia A., Domínguez E. (2014) Biomechanical properties of the tomato (Solanum lycopersicum) fruit cuticle during development are modulated by changes in the relative amounts of its components. *New Phytologist, 202* (3): 790-802

Feng X., Huang RYM. (1994) Concentration polarization in pervaporation separation processes. *Journal of Membrane Science, 92,* 201-8

Franz T. (1975) Percutaneous absorption – relevance of in-vitro data. *Journal of Investigative Dermatology, 64*, 190-95

Glover BJ. (2000) Differentiation in plant epidermal cells. *Journal of Experimental Botany, 51,* 497-505.

Goodwin SM, Jenks M (2005) Plant cuticle function as a barrier to water loss. In M Jenks, PM Hasegawa, eds, Plant Abiotic Stress. Blackwell Publishing, Oxford, pp 14–36

Goodwin SM., Kolosova N., Kish CM., Wood KV., Dudareva N., Jenks MA. (2003) Cuticle characteristics and volatile emissions of petals in *Antirrhinum majus*. *Physiologia Plantarum, 117* (3), 435-443

Heredia A. (2003) Biophysical and biochemical characteristics of cutin, a plant barrier biopolymer. *Biochimica et Biophysica Acta, 1620,* 1-7

Heredia-Guerrero JA., Benítez JJ., Domínguez E., Bayer IS., Cingolani R., Athanassiou A., Heredia A. (2014) Infrared and Raman spectroscopic features of plant cuticles: a review. *Frontiers in Plant Science, 5* (305)

Javelle M., Vernoud V., Rogowsky PM., Ingram GC. (2010) Epidermis: the formation and functions of a fundamental plant tissue. *New Phytologist, 189* (1), 17-39

Jeffree CE. (1996) Structure and ontogeny of plant cuticles. In Kerstiens G ed; Plant cuticle: an integrated functional approach. BIOS Scientific publishers, Oxford. pp. 33–82

Jeffree CE. (2006) The fine structure of the plant cuticle. In M Riederer, C Müller, eds, Biology of the Plant Cuticle. Blackwell, Oxford, pp 11-125

Jenks MA., Ashworth EN. (1999) Plant epicuticular waxes: function, production and genetics. *Horticultural Reviews, 23,* 1-68

Jetter R., Kunst L., Samuels AL. (2006) Composition of plant cuticular waxes. In M Riederer, C Müller, eds, Biology of the Plant Cuticle. Blackwell, Oxford, pp 145-81

Kerstiens G. (1996a). Signalling across the divide: a wider perspective of cuticular structure–function relationships. *Trends in Plant Science, 1,* 125-29

Kerstiens G. 1996b. Cuticular water permeability and its physiological significance. *Journal of Experimental Botany, 47,* 1813-32

Knauth LP., Kennedy MJ. (2009) The late Precambrian greening of the Earth. *Nature, 460,* 728-32

Koch K., Dommisse A., Barthlott W. (2006). Chemistry and crystal growth of plant wax tubules of Lotus (Nelumbo nucifera) and Nasturtium (Tropaeolum majus) leaves on technical substrates. *Crystal Growth & Design, 11,* 2571-78

Kolattudky PE. (2011) Polyesters in higher plants. *Advances in Biochemical Engineering/Biotechnology, 71*, 1-49

Kolosova N., Sherman D., Karlson D., Dudareva N. (2002). Cellular and subcellular localization of S-adenosyl-L-methionine:benzoic acid carboxyl methyltransferase, the enzyme responsible for biosynthesis of the volatile ester methylbenzoate in snapdragon flowers. *Plant Physiology, 126* (3), 956-64

Koornneef M, Hanhart CJ, Thiel F (1989) A genetic and phenotypic description of eceriferum (cer) mutants in Arabidopsis thaliana. *Journal of Heredity*, *80*, 118-22

Krauss P, Markstädter C, Riederer M (1997) Attenuation of UV radiation by plant cuticles from woody species. *Plant, Cell & Environment*, *20*: 1079-85

Van der Krol AR., Chua N-H. (1993) Flower Development in Petunia. *The Plant Cell*, *5*, 1195-1203

Longhi S, Cambillau C (1999) Structure-activity of cutinase, a small lipolytic enzyme. *Biochimica et Biophysica Acta*, *1441*, 185-196

Lü S., Song T., Kosma DK., Parsons EP., Rowland O., Jenks MA. (2009) Arabidopsis CER8 encodes LONG-CHAIN ACYL-COA SYNTHETASE 1 (LACS1) that has overlapping functions with LACS2 in plant wax and cutin synthesis. *Plant Journal*, *59*, 553-64

Luque P., Heredia A. (1997). The glassy state in isolated cuticles: differential scanning calorimetry of tomato fruit cuticular membranes. *Plant Physiology and Biochemistry, 35*, 251-56

Lyons PC., Orem WH., Mastalerz M., Zodrow EL., Vieth-Redemann A., Bustin MR. (1995) ^{13}C NMR, micro-FTIR and fluorescence spectra, and pyrolysis-gas chromatograms of coalified foliage of late Carboniferous medullosan seed ferns, Nova Scotia, Canada: Implications for coalification and chemotaxonomy. *International Journal of Coal Geology, 27* (2-4), 227-48

Martin LB., Rose JK. (2014) There's more than one way to skin a fruit: formation and functions of fruit cuticles. *Journal of Experimental Botany, 65* (16), 4639-51

Matas AJ, Cobb ED, Bartsch JA, Paolillo DJ, Niklas KJ. (2004). Biomechanics and anatomy of *Lycopersion esculentum* fruit peels and enzyme treated samples. American Journal of Botany *91*, 352–60

Merk S., Blume A., Riederer M. (1998). Phase behaviour and crystallinity of plant cuticular waxes studied by Fourier transform infrared spectroscopy. *Planta, 204*, 44–53

Meusel I., Barthlott W., Kutzke H., Barbier B. (2000) Crystallographic studies of plant waxes. *Powder Diffraction, 15* (2), 123-29

Ng SF, Rouse J, Sanderson D, Eccleston G, A (2010) Comparative Study of Transmembrane Diffusion and Permeation of Ibuprofen across Synthetic Membranes Using Franz Diffusion Cells. *Pharmaceutics*, *2*, 209-23

Osorio S., Thi Do P., Fernie A.R. (2012) Profiling primary metabolites of tomato fruit with gas chromatography/mass spectrometry. In Hardy N.W., Hall R.D., editors. Plant Metabolomics: Methods and Protocols. Springer/Humana Press; New York, NY, USA, pp. 101–9

Petit J., Bres C., Mauxion J-P., Bakan B., Rothan C. (2017) Breeding for cuticle-associated traits in crop species: traits, targets, and strategies. *Journal of Experimental Botany*, *68* (19), 5369-87

Pfündel EE., Agati G., Cerovic ZG. (2006) Optical properties of plant surfaces. In M Riederer, C Müller, eds, Biology of the Plant Cuticle. Blackwell, Oxford, pp 216-49

Pighin JA, Zheng H, Balakshin LJ, Goodman IP, Western TL, Jetter R, Kunst L, Samuels AL (2004) Plant cuticular lipid export requires an ABC transporter. *Science, 306*, 702-4

Pollard M, Beisson F, Li Y, Ohlrogge JB (2008) Building lipid barriers: biosynthesis of cutin and suberin. *Trends in Plant Science, 13*, 236-46

Pulsifer IP, Kluge S, Rowland O (2012) Arabidopsis long-chain acyl-CoA synthetase 1 (LACS1), LACS2, and LACS3 facilitate fatty acid uptake in yeast. *Plant Physiology and Biochemistry, 51*, 31-9

Ramírez FJ., Luque P., Heredia A., Bukovac MJ. (1992). Fourier transform IR of enzymatically isolated tomato fruit cuticular membrane. *Biopolymers, 32*, 1425-29

Ratnaswamy P., Anand KS., Gupta DC. (1973) Structure and Properties of Microcrystalline Waxes. *Journal of Chemical Technology & Biotechnology, 23*,183-87

Reynhardt EC. (1985) NMR investigation of Fischer-Tropsch waxes. II. Hard wax. *Journal of Physics D: Applied Physics, 18*: 1185-97

Riederer M., Schneider, G. (1990). The effect of the environment on the permeability and composition of Citrus leaf cuticles: II. Composition of soluble cuticular lipids and correlation with transport properties. *Planta, 180* (2): 154-65

Riederer M., Schreiber L. (2001). Protecting against water loss: analysis of the barrier properties of plant cuticles. *Journal of Experimental Botany, 52* (363), 2023-32

Salminen TA., Eklund DM., Joly V., Blomqvist K., Matton DP., Edqvist J. Deciphering the Evolution and Development of the Cuticle by Studying Lipid Transfer Proteins in Mosses and Liverworts. *Plants-Basel, 7*(1), 6

Schönherr J, Riederer M. (1989). Foliar penetration and accumulation of organic chemicals in plant cuticles. *Reviews of Environmental Contamination and Toxicology, 108*, 1–70.

Schönherr J. (1976). Water permeability of isolated cuticular membranes: the effect of pH and cations on diffusion, hydrodynamic permeability and size of polar pores in the cutin matrix. *Planta, 128* (2), 113-26

Schreiber L, Schorn K, Heimburg T (1997) 2H NMR study of cuticular wax isolated from Hordeum vulgare L. leaves: identification of amorphous and crystalline wax phases. *European Biophysics Journal, 26*, 371-80

Shanmugarajah K., Linka N., Gräfe K., Smits SHJ., Weber APM., Zeier J., Schmitt L. (2019) ABCG1 contributes to suberin formation in Arabidopsis thaliana roots. *Scientific Reports, 9*, 11381

Sieber P, Schorderet M, Ryser U, Buchala A, Kolattukudy P, Métraux JP, Nawrath C (2000) Transgenic Arabidopsis plants expressing a fungal cutinase show alterations in the structure and properties of the cuticle and postgenital organ fusions. *Plant Cell, 12*, 721-38

Sørensen I., Pettolino FA., Bacic A., Ralph J., Lu F., O'Neil MA., Fei Z., Rose JFC., Domozych DS., Willats WG. (2011). The charophycean green algae provides insights into early origins of plant cell walls. *Plant J., 68,* 201-11

Still G.G., Davis D.G., Zander G.L. (1970) Plant epicuticular lipids: Alteration by herbicidal carbamates. *Plant Physiology, 46,* 307-14

Taiz, L. Zeiger, E., Moller, I.M. and Murphy, A. (2015) Plant Physiology and Development. 6th Edition, Sinauer Associates, Sunderland, CT.

Ussing H. (1949) The active ion transport through the isolated frog skin in the light of tracer studies. *Acta Physiologica Scandinavica, 17,* 1-37

Villena JF., Domínguez E., Heredia A. (2000). Monitoring biopolymers present in plant cuticles by FT-IR spectroscopy. *Journal of Plant Physiology, 156,* 419-22

Walton TJ., Kolattukudy PE. (1972). Determination of the structures of cutin monomers by a novel depolymerization procedure and combined gas chromatography and mass spectrometry. *Biochemistry, 11,* 1885-97

Waters ER. (2003) Molecular adaptation and the origin of land plants. *Molecular Phylogenetics and Evolution, 29,* 456-63

Wijmans JG., Athayde AL., Daniels JH., Kamaruddin HD., Pinnau I. (1996) The role of boundary layers in the removal of volatile organic compounds from water by pervaporation. *Journal of Membrane Sciences, 109,* 135-46

Yang W., Pollard M., Li-Beisson Y., Beisson F. Feig M., Ohlrogge J. (201) A distinct type of glycerol 3-phosphate acyltransferase with sn-2 preference and phosphatase activity producing 2-monoacylglycerol. *Proceedings in the National Academy of Science USA, 107,* 12040-45

Yeats TH., Rose JKC. (2013). The formation and function of plant cuticles. Plant Physiol. 163, 5-20

CHAPTER 4. MOLECULAR DYNAMICS OF VOLATILE ORGANIC COMPOUNDS IN THE EPICUTICLE OF PLANT EPIDERMAL CELLS

4.1 Abstract

Molecular-scale modeling was used to estimate diffusivities for petunia volatile organic compounds (VOCs) and water in models of petal cuticular waxes of varying chemical composition. Model cuticles were represented as a ternary system of *n*-tetracosane ($C_{24}H_{50}$), 1-docosanol ($C_{22}H_{45}OH$), and 3-methylbutyl dodecanoate ($C_{17}H_{34}O_2$), and were simulated by employing the OPLS-AA empirical force-field at 298 K using an NPT ensemble. The mean-square displacements for compounds diffusing through the model cuticles of varying chemical composition was measured to estimate diffusion coefficients. Cuticle anisotropy was found to be highly dependent on the elongation of methylene chains, restricting the dimensionality of the diffusion paths. Both decreases in lattice length and increases in gap width between crystalline units was found to result in increased diffusion for all compounds tested. Simulated X-ray diffraction patterns reflected the changes in crystalline unit gap widths and lengths as a result of varying chemical composition. VOC diffusivity was found to increased up to 30-fold in amorphous waxes, showing that wax composition controls cuticular permeability. These increases were found most significantly in water and high molecular weight VOCs, suggesting that mass transfer resistance exerted by the cuticle primarily effects larger and/or polar compounds *in planta*. In contrast, low molecular weight lipophilic compounds were found to be more insensitive towards perturbations of wax crystallinity. Comparing the estimated diffusion coefficients with the emission dynamics of petunia flowers reveal that low molecular weight VOCs experience negligible resistance from the cuticle, while larger compounds tend to accumulate in internal tissues to a greater extent. Taken altogether, compounds experience varying extent of mass transfer resistance in the cuticle, indicating that any regulation the cuticle plays in the exchange of matter is differential and highly dependent on the properties of the diffusing molecule. The cuticle itself adds another level of regulation in the export of VOCs, extending some control over the amount, mixture, and dynamics of emissions.

4.2 Introduction

4.2.1 Molecular dynamics (MD) simulations

Studying the mechanisms of diffusion in naturally occurring materials is important for understanding their biological, ecological, and even evolutionary roles. In biological systems, air, gas, water, nutrients, and macromolecules are constantly moving around via molecular diffusion. While *in vitro* studies of diffusion have allowed for the measurement of permeability of various organic membranes, these measurements are often limited by the ability to replicate physiological conditions. In contrast, computational measurements of diffusion have been shown to reliably estimate physical properties for complex systems under a variety of physiological conditions (Li et al., 1997). With added computational resources, diffusion coefficients obtained from simulations often require less time and effort than bench-top experiments over varying conditions.

Molecular dynamics (MD) is molecular modeling technique that integrates over Newton's equations of motion for successive configurations of a system. The result of an MD simulation is a trajectory that specifies the positions and velocities of all discrete particles in the system with respect to time. As diffusion is a time-dependent property, MD simulations have been used extensively to measure diffusivity of molecules in a variety of physical states. The ability to measure time-dependent properties is the primary advantage MD presents over other forms of molecular modeling such as the Monte Carlo method (Leach, 1996). MD has been employed extensively to study molecular diffusion over a broad range of polymorphic structures, such as polymers (Takeuchi, 1990; Charati and Stern, 1998), cell membranes (Ingólfsson et al., 2014), actin filaments (Pollard, 2007), and biopolyesters such as cutin (Matas and Heredia, 1999) and cellulose (Lindner et al., 2013). However, simulations of solute diffusion in natural plant waxes remains unstudied as yet using the MD method. Thus, we plan to use the model system presented in Chapter 3 and study the effect of aliphatic crystallinity on the diffusion of volatile scent compounds.

In general, MD simulations are performed by a series of steps (Fig. 4.1). The first step is to define the system based on the particle types, size of the system, arrangement of particles, etc. The interaction of these particles are pre-defined by an implemented force-field which dictates the total energy of the system. Definition of the initial coordinates, force-field parameters, and system boundary is broadly classified as *domain construction*.

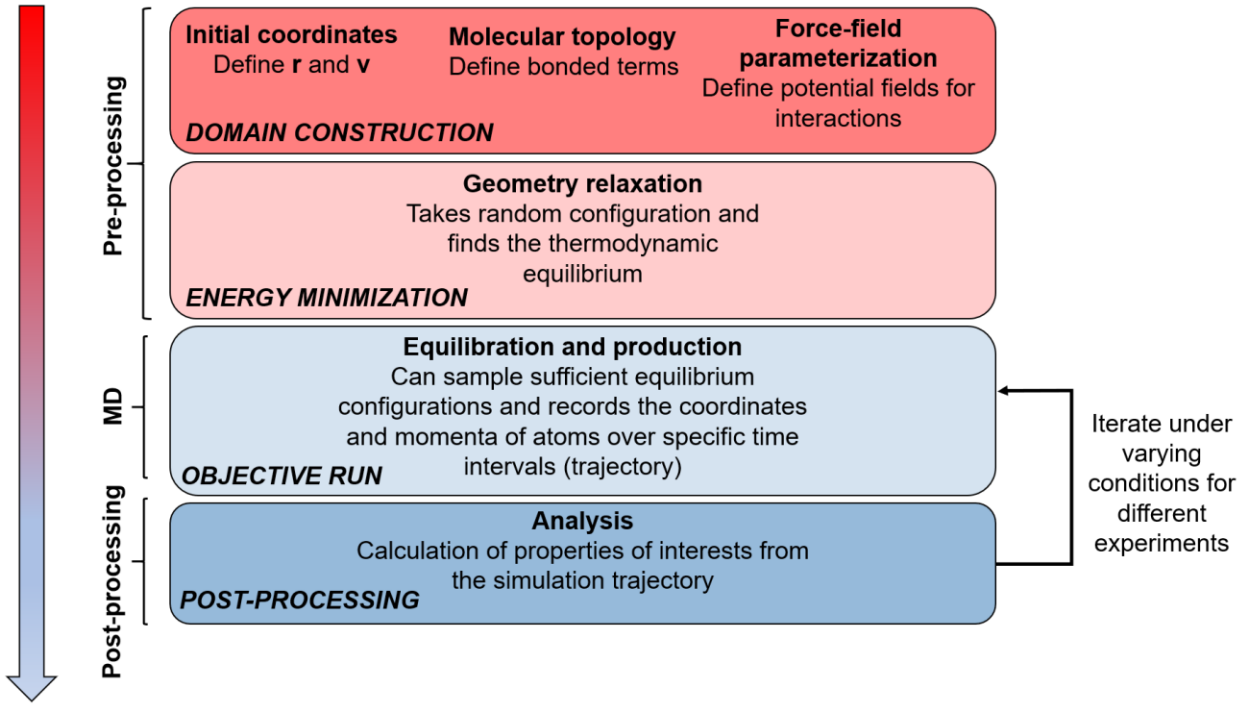

Fig. 4.1 – Steps of molecular dynamics simulations (steps included in detail in Chapter 7, Leach, 2006).

Following domain construction, the system must be relaxed to a global energy minimum which corresponds to the thermodynamic configuration of the system. To identify the configuration of the system that corresponds to the energy minimum, numerous *energy minimization* algorithms have been developed. Once the system is at a thermodynamic equilibrium, the *molecular dynamics simulation run* begins. During this step, the system is subjected to the desired experiment conditions, such as applied forces or thermal conditions. As the system progresses through the simulation, the position and velocities of particles are recorded at discrete time steps to generate the trajectory. The trajectory can then be analyzed by a myriad of *post-processing* numerical or visualization methods to obtain results.

4.2.2 Domain construction

In order to calculate state and dynamic properties of a system, the description of the forces and interactions between the particles comprising the system must be defined. This can be achieved by solving the quantum mechanics equations of all the atoms and electrons in the system, which is often computationally demanding for systems with a large number of particles. To compensate, force-field (or molecular mechanics) methods have been developed which ignore electronic contributions and calculate the system energy as a function of nuclear positions only. However, the downside to this is that force-field methods require a large number of atoms to average over in order to produce accurate results. In some cases, force-field methods produce results as accurate as high-level quantum computations in a fraction of the computational time. Thus, if one is to study properties unrelated to electronic forces and distributions, force-field methods present a viable strategy.

Force-field methods are dependent on a few assumptions, with the major assumption given by the Born-Oppenheimer (BO) approximation, which states that the motion of atomic nuclei and electrons can be treated separately. Without this approximation, the formulation of a force-field to parameterize a system of atoms with no electron orbits would be completely invalid. Thus molecular modeling in the absence of quantum contributions is based on a rather simple model of interactions within the system. Many molecular modeling force-fields employed today use a four-component visualization of the intra- and intermolecular forces within the system. The energetic penalties are associated with the deviation of these forces from a given reference, or "equilibrium", value. Classic force-fields used in molecular mechanics simulations are AMBER (Cornell et al., 1995), CHARMM (Brooks et al., 1983), GROMOS (van Gunsteren and Berendsen, 1987; Scott et al., 1999), OPLS (Jorgensen et al., 1988; Jorgensen et al., 1996), and UFF (Rappe et al., 1992), and share fairly similar functional forms, differing only in their parameterization and definition of particle types. The work presented in this thesis primarily utilized the optimized potentials for liquid simulations (OPLS) force-field which allows for definition of individual atom types, and has been used successfully to measure the properties of hydrocarbons (Siu et al., 2012). The total energy, E_{FF}, is expressed as:

$$E_{FF}(\mathbf{r}^N) = \sum_{\text{bonds}} k_r(r - r_0)^2 + \sum_{\text{angles}} k_\theta(\theta - \theta_0)^2 + \sum_{\text{dihedrals}} \sum_{i=1}^{4} \frac{1}{2} V_i(1 + (-1)^{i+1} \cos(i\phi)) + \sum_{i>j} \left\{ \frac{q_i q_j e^2}{4\pi\epsilon_0 r_{ij}} + 4\epsilon_{ij} \left[\left(\frac{\sigma_{ij}}{r_{ij}} \right)^{12} - \left(\frac{\sigma_{ij}}{r_{ij}} \right)^{6} \right] \right\} \quad (4.1)$$

where k_r and r_0 are the bond-specific harmonic force constant and equilibrium displacement, respectively; k_θ and θ_0 are the angle-specific harmonic force constant and equilibrium angle, respectively, V_i represents the dihedral-specific Fourier coefficients, r_{ij} are the interatomic separations, q_i are the partial atomic charges, e is the elementary charge, and ε_{ij} and σ_{ij} are the Lennard-Jones parameters for each pair-wise interaction. The total energy is calculated for the positions **(r)** of *N* particles. Particles can be counted as united atoms (UA) or all atoms (AA) with the use of the OPLS functional form. The first three terms are the bonded atom interactions, defined between two, three, and four atoms accounting for the stretching, bending, and rotation, respectively. The fourth term accounts for non-bonded interactions, the electrostatics and the van der Waals.

Bond stretching and angle bending are generally modeled with a Hooke's law (harmonic) functional form. The energy contribution of these terms are given by the deviation from the equilibrium configuration and a force constant. As less energy is needed to distort an angle away the equilibrium compared to the energy needed to stretch or compress a bond, angle bending force constants tend to be proportionately smaller (Urey and Bradley Jr., 1931).

Stretching and bending are considered the 'hard' degrees of freedom, where substantial energy is required to cause deformations from a reference value. Variations between simulations are more often accounted for by the interplay between torsional (dihedral) and non-bonded interactions. Most dihedral force-fields are parameterized by a Fourier expansion functional form (Allinger, 1977), with the coefficients V_i representing the energy barrier needed for rotation about the angle ϕ between two atoms separated by three bonds. For some molecules, "improper torsions" need to be parameterized. Improper torsions result from a four atom sequence not bonded in sequence, and an improper torsional potential is needed to maintain a specific geometry (e.g. planar molecules and stereochemistry at chiral centers). Improper torsional terms are often modeled with a harmonic potential instead of the Fourier expanded form (Claessens et al., 1983; Hunter and Saunders, 1990).

Interactions between atoms not connected by bonds are broadly referred to as the non-bonded interactions. These are the 'through-space' interactions and are usually modelled as a function of some inverse power of the distance. The non-bonded terms of the force-field are usually grouped as the electrostatics interactions and the van der Waals interactions. The most accurate form of calculating electrostatic interactions between atoms is to use the central multipole expansion, which is based on the electric moments, or multipoles: the charge, dipole, quadrupole, octopole, and so on. For the multipole expansion, the lowest non-zero electric moment is of importace, which for ionic species is their charge (Petersen et al., 1994). Many uncharged molecules have their dipole as the lowest non-zero moment, while for N_2 or CO_2, the lowest non-zero moment is their quadrupole. However, employing the multipole expansion can result in slow convergence of simulations, and so the simpler Coulomb's law is used to describe the potential between two point electric charges (first half of the fourth term in equation 4.1).

Van der Waals interactions can be decomposed into two components: the long-range dispersive interaction and the short-range repulsive interaction. The disperseive forces arise from induced dipole-dipole interactions due to fluctuations in electron positions and this varies at approximately $-\frac{1}{{r_{ij}}^6}$. The repulsive forces are attributed to the repulsion between electrons in the inter-nuclear region based on the Pauli principle (Urey and Bradley Jr., 1931). The Lennard-Jones 12-6 function (second half of the fourth term in equation 4.1) is the most widely used potential for describing van der Waals interactions (Berendsen et al., 1987). The determination of van der Waals parameters can be difficult and so it is common to assume that parameters for the cross interactions can be obtained from the parameters of pure atoms based on mixing rules. The commonly used mixing rules are the Lorentz-Berthelot (Lorentz, 1881), Waldman-Hagler (Waldman and Hagler, 1993), and Kong (Kong, 1973) mixing rules. While the Lorentz-Berthelot mixing rules are the most employed in MD simulations, Waldman-Hagler and Kong mixing rules tend to lead to smaller deviations from experimental values (Delhommell and Millié, 2001). For simulations of waxes, the Waldman-Hagler rules are used:

$$\sigma_{\mathrm{AB}} = \left[\frac{({\sigma_{\mathrm{AA}}}^6 + {\sigma_{\mathrm{BB}}}^6)}{2}\right]^{1/6} \tag{4.2}$$

$$\varepsilon_{\mathrm{AB}} = \frac{2{\sigma_{\mathrm{AA}}}^3{\sigma_{\mathrm{BB}}}^3}{{\sigma_{\mathrm{AA}}}^6 + {\sigma_{\mathrm{BB}}}^6}\sqrt{\varepsilon_{\mathrm{AA}}\varepsilon_{\mathrm{BB}}} \tag{4.3}$$

Where the collision diameter σ_{AB} and the well depth ε_{AB} for the A-B atomic interaction is given by the arithmetic and geometric means of pure component parameters, respectively.

4.2.3 Force-field parameterization

The OPLS force field (equation 4.1) was parameterized with respect to individual atom types given by the machine-readable protocol in Python (Savoie et al., 2017). The atom types were defined by Topologically Automated Force-Field Interactions (TAFFI) methodology. Following the TAFFI protocol, individual atom types are determined on the basis of topology distinctiveness out to two bonds. To build the topology of individual molecules, chemical bond connectivity graphs were formulated based on a Python-readable syntax. This syntax encodes atoms based on their atomic number (e.g. 1 – hydrogen, 6 – carbon, 8 – oxygen), and an adjacency list is populated based on their bonds. An example of the atom syntax and population of the adjacency matrix is shown for the scent compound methylbenzoate in Fig. 4.2.

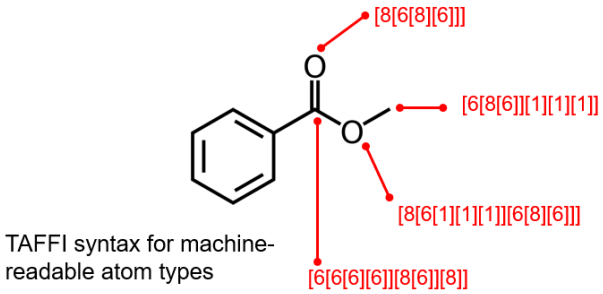

Adjacency matrix

O-[8[6[8][6]]]	0	0	0	0	0	0	1	0	0
C-[6[6[6][1]][6[6][1]][1]]	0	1	0	1	0	0	0	0	1
C-[6[8[6]][1][1][1]]	0	0	0	0	1	1	0	0	0
H-[1[6[6][6]]	0	1	0	0	0	0	0	0	1
H-[1[6[8][1][1]]]	0	0	1	0	0	0	0	0	0
O-[8[6[1][1][1]][6[8][6]]]	0	0	1	0	0	0	1	0	0
C-[6[6[6][6]][8[6]][8]]	1	0	0	0	0	1	0	1	0
C-[6[6[8][8]][6[6][1]][6[6][1]]]	0	0	0	0	0	0	1	0	1
C-[6[6[6][6]][6[6][1]][1]]	0	1	0	1	0	0	0	1	0

Fig. 4.2 – Example of syntax for atom type definitions for the petunia volatile methylbenzoate. Adjacency matrix denotes all bonds between unique atom types.

4.2.4 Geometry optimization

Even for the simplest systems, the potential energy function can be a multi-dimensional function of the molecular coordinates. The way the potential energy varies with coordinates is

referred to as the potential energy surface, of where there exists an energetic minimum. In a system with Cartesian coordinates, the potential energy surface for *N* atoms is a function of approximately 3*N* coordinates. In any molecular modeling experiment, we are interested in the minimum points on the potential energy surface representing the geometry of the system in real conditions. Due to the complexity of the energy landscape, obtaining the global minimum of the system is not generally a trivial matter. To identify the geometries of the system corresponding to the global minimum, we use minimization algorithms. There exists vast literature on minimization algorithms, many of which are applied to solve problems outside the scope of molecular modeling. These methods can be classified as derivative-based (first or second), or non-derivative methods (Ayala and Schlegel, 1997). First derivative methods such as the steepest descents method, line search method, and conjugate gradients method change the coordinates of atoms as the move closer to the minimum point. The starting point for each iterative step is the molecular configuration obtained from the previous step, and it follows the slope of the objective function (energy, force, etc.). Second derivative approaches such as the Newton-Raphson method and its variants use not only the first derivatives (gradients) but also the function curvature obtained by the second derivative. Second derivative methods are generally the most used minimization algorithm in molecular modeling due to its repeatability and robust profiling the potential energy surface (Leach, 1996). However, Newton-Raphson minimization is generally slower than the conjugate gradients or steepest descent algorithms, due to the need to invert the second derivative matrix, the Hessian, resulting in increased use of CPU and memory.

The alternatives to derivative-based methods are the derivative-free methods such as simplex minimization, simulated annealing, and optimization by genetic algorithms. For complex systems, simulated annealing has been found to be a particularly suitable method, especially when refining geometry in accordance to XRD and NMR data. In simulated annealing simulations for the MD method, a system begins at an initially high temperature, allowing it to overcome high energy barriers and is then cooled to the simulation temperature (Kannan and Zacharias, 2009). Simulated annealing is guaranteed to achieve the global optimum of a system as the time taken to cool the system approaches infinity. As MD simulations are not performed for an infinite time, the system becomes trapped in a local energy minimum, and the system will not shift from this minimum unless the system is further cooled. So while the method may not converge to the global

minimum, a local minimum is guaranteed. To ensure accuracy of measurements, simulated annealing is performed in replicates.

4.2.5 Newton's equations of motion

For a system of *N* particles, the potential energy $U(\mathbf{r}_1, \mathbf{r}_2, \ldots, \mathbf{r}_n)$ is a function of the position of all *N* particles. The trajectory is a list of the chronological configurations of the atoms in an MD simulation, obtained by solving Newton's second law:

$$F_{r_i} = -\frac{\partial U}{\partial \mathbf{r}_i} = m_i \frac{\mathrm{d}^2 \mathbf{r}_i}{\mathrm{d}t^2} \tag{4.4}$$

Where the force of a given particle, F_{r_i}, is proportional to the acceleration of a particle with mass m_i. Equilibrium properties are measured from the corresponding motions of atoms. In order to obtain a MD trajectory, numerical integration of Newton's law is carried out by finite difference methods. The velocity Verlet algorithm (Verlet, 1968) is the most widely used numerical integration algorithm for MD simulations (Leach, 1996). The Verlet algorithm uses the positions and accelerations at time *t*, and the positions from the previous step, $\mathbf{r}(t - \delta t)$, to calculate the new positions at times $t + \delta t$, $\mathbf{r}(t + \delta t)$. The general form of the algorithm is given by:

$$\mathbf{r}(t + \delta t) = \boldsymbol{r}(t) + \delta t \mathbf{v}(t) + \frac{1}{2}\delta t^2 \mathbf{a}(t) + \cdots \tag{4.5}$$

$$\mathbf{r}(t - \delta t) = \mathbf{r}(t) - \delta t \mathbf{v}(t) + \frac{1}{2}\delta t^2 \mathbf{a}(t) - \cdots \tag{4.6}$$

Adding equations 4.5 and 4.6 gives the basic form of the Verlet algorithm:

$$\mathbf{r}(t + \delta t) = 2\mathbf{r}(t) - \mathbf{r}(t - \delta t) + \delta t^2 \mathbf{a}(t) + \cdots \tag{4.7}$$

The algorithm is simple to implement, accurate, and provides stable solutions. In order for meaningful data to be extracted from the integration of a molecular trajectory, the time step increments and duration must be suitably selected. There are no strict rules with respect to selection of the time step; too small and the trajectory will only cover a limited portion of the phase space,

and too large will result in possible instability in the integration algorithm (violation of energy and momentum conservation). The selection of the discrete time steps and simulation duration often must be iteratively tested to ensure calculations are both repeatable and accurate.

4.2.6 Periodic boundary conditions, cut-offs, and neighbor lists

The goal of any molecular scale model is to obtain physical properties of a macroscopic system. However, the size of molecular models is often limited by the available computational resources. The correct treatment of boundaries and boundary effects is critical for simulation methods as it permits the sampling of a 'macroscopic' system using a small number of atoms. As an example, an individual petunia flower yields approximately 1 mg of wax, accounting for approximately 1.5×10^{18} wax molecules (well over 10^{20} atoms). In order to produce a three-dimensional trajectory, $6N$ (N atoms) differential equations would need to be solved, which is nearly impossible with current computational resources (LeSar, 2013). The number of particles in a Monte Carlo or molecular dynamics simulation frequently are between 1000-2000 atoms. However, simulations of < 2000 atoms are not indicative of bulk properties, requiring an alternative strategy to account for the missing atomistic continuum. The most common method is to implement periodic boundary conditions (Fig. 4.3).

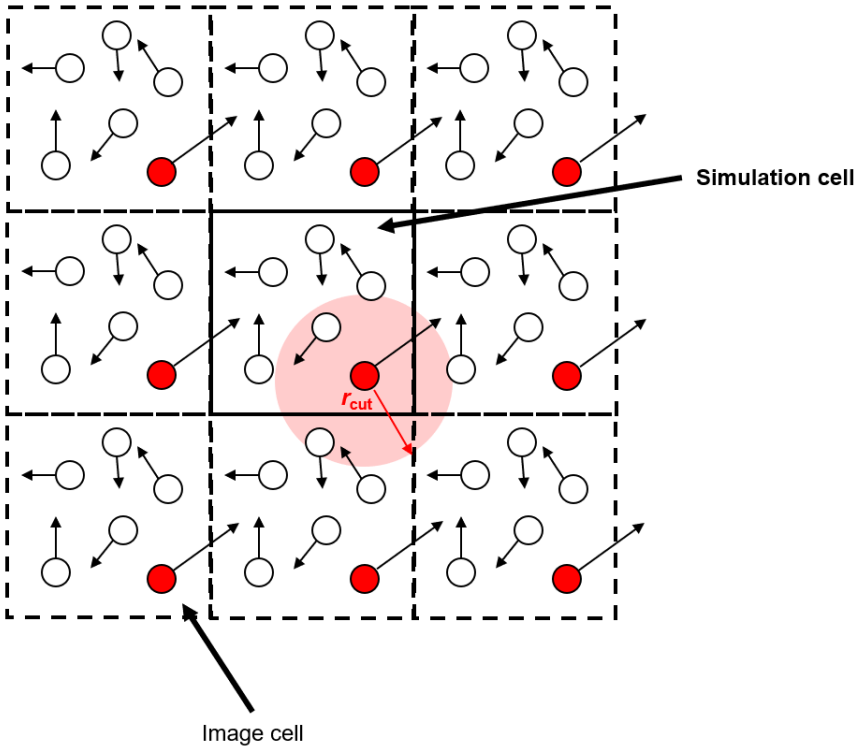

Fig. 4.3 – Periodic boundary conditions for a simple cubic system. The central cell is the simulation cell and is replicated for all six faces of the cube. When a particle in the simulation cell moves, the same particle in the image cells move in the exact same way. The pre-determined cut-off radius, r_{cut}, is used to determine all neighbor particles to calculate non-bonded interactions. Particles outside of the cut-off radius are not part of the non-bonded neighbor list.

Using this method, the domain is viewed as an infinite array of equivalent finite systems, where individual atoms are replicated through space beyond the system boundaries. When an atom exists in the simulation cell, it re-enters the cell from the opposite face, rendering the number of atoms in the box fixed in number. Use of periodic boundary conditions also allow atoms to interact with other atoms in adjacent image cells. The cubic simulation cell is the simplest and most commonly implemented in MD simulations. For simulations that involve materials of complex geometries (e.g. nanotubes) or have side-specific boundary conditions (e.g. surface adsorption), more effort is needed to program the system (Adams, 1983). However, diffusion in explicit solvents is readily studied by simple cubic simulation cells with periodic boundary conditions.

The most time-consuming component in molecular simulations is the calculation of non-bonded energies and forces. The total bond-stretching, angle-bending and dihedral terms in the force-field model are proportional to the number of atoms N, but the number of non-bonded terms that are to be evaluated increases by an order of N^2 to account for all pair-wise interatomic terms.

Without any enforcement, a simulation would calculate every atom pair interaction term at each time step. For most molecular scale models, this level of calculation is unnecessary. The Lennard-Jones potential drastically decreases over long distances, where at a separation r = 2.5σ the Lennard-Jones potential is only 1% of the maximum value. With a cut-off distance r_{cut} specified, the interaction potential between two atoms separated by $r > r_{\text{cut}}$ is set to zero and prevents the simulation from computing this value. The value for r_{cut} is system-dependent and may require some iterative simulations to determine an optimum value, however, the general rule-of-thumb for setting a cut-off is for r_{cut} to not exceed half the length of the shortest side of the simulation cell. In simulations with where the Lennard-Jones potential is dominant, the cut-off radius is selected to be r_{cut} = 2.5σ, and gives minimal error (Ding et al., 1992).

By itself, a specified cut-off radius may not be sufficient to reduce computational time. As systems simulated are generally dynamic, atoms vibrate in and out of the range of the specified cut-off. To determine which atoms are within the cut-off range, the simulation must calculate $N(N-1)$ distances, which in itself can become a laborious step for the computer. To account for this, non-bonded neighbor lists are calculated at specified intervals during the simulation (Thompson, 1983). The neighbor list for a specific atom contains the list of all atoms within the cut-off radius distance and will only calculate non-bonded interactions for those atoms only. This list is not generally updated at individual time steps as atoms may remain within proximity of one another for significant periods of time. Thus, to limit the computational power needed, neighbor lists are updated less frequently than the actual simulation time increment. It is important to update the neighbor list at an appropriate frequency; if the updating frequency is too high, the simulation is inefficient, and if the updating frequency is too low, then there will be errors in the calculation of energies and forces due to poor sampling (Greengard and Rokhlin, 1987).

4.2.7 Time-dependent properties

Molecular dynamics produces configurations of the system that are connected in time, allowing us to determine time-dependent or time-averaged properties. This is the inherent advantage of using MD simulations over the Monte Carlo method. Time-dependent properties can be referred to as time correlation coefficients, which are obtained from correlation functions (Adler and Wainwright, 1970). Correlation functions provide numerical values encapsulating the

statistical correlation between two random variables, contingent on the spatial or temporal spacing between those variables. For two data sets *x* and *y*, we can define the correlation function C_{xy}:

$$C_{xy} = \frac{1}{M}\sum_{i=1}^{M} x_i y_i \equiv \langle x_i \cdot y_i \rangle \tag{4.8}$$

Where *M* is the number of values in the x_i and y_i datasets. For MD simulations, if one of the two datasets is a function of time, the correlation function is referred to as a time-correlation function. If x_i and y_i are two independent variables, C_{xy} is referred to as a cross-correlation function, and if x_i and y_i are the same variable, then C_{xy} is an autocorrelation function. In MD simulations, we are often interested in obtaining the transport properties such as diffusivity or viscosity. Transport properties are generally obtained from velocity autocorrelation functions (VAF):

$$C_v(t) = \langle v(0) \cdot v(t) \rangle \tag{4.9}$$

The VAF is calculated over Δt time steps, and properties such as diffusion coefficients are obtained by numerical integration of the VAF. The VAF decays to zero at long times, and if equation 4.9 is integrated numerically from $0 \leq t \leq \infty$, the Green-Kubo (Kubo, 1957) relationship is obtained:

$$D_i = \frac{1}{3}\int_0^{\infty} \langle v(0) \cdot v(t) \rangle \mathrm{d}t \tag{4.10}$$

Alternatively, the Einstein relationship arises from differentiating the velocity autocorrelation function with respect to time to obtain the mean-square displacement. For simulations of hydrocarbons using the OPLS-AA or UA (united atoms) force-field, both Green-Kubo and Einstein relations provide similar results for diffusivity measurements. (Lee and Chang, 2003; Kondratyuk et al., 2016).

4.2.8 Time and ensemble averages

In order to represent the various interactions, such as heat and mass transfer, of the surrounding environment with the system, coupling procedures corresponding to specific statistical ensembles are used. Thermodynamic properties are dependent on the position $\mathbf{r}^N(t)$ and momenta $\mathbf{p}^N(t)$ of the *N* atoms that comprise the system. Over time, the instantaneous value of property *A* fluctuates as a result of the interactions between atoms. When the property is measured over time *t*, it is the "time-average." As *t* approaches infinity, the measurement of *A* approaches the true thermodynamic value:

$$A_{\text{ave}} = \lim_{\tau\to\infty} \frac{1}{\tau} \int_{t=0}^{\tau} A(\mathbf{p}^N(t), \mathbf{r}^N(t))\mathrm{d}t \tag{4.12}$$

Thus, calculation of time averaged properties requires dynamic simulations, with values calculated from trajectories of atoms. However, for some properties, time averaging over small time scales results in inaccurate values. Boltzmann and Gibbs developed statistical mechanics where a single system evolving in time is replaced by a large number of replications of the system that are considered simultaneously. Averaging over these large number of replications is referred to as the "ensemble-average:"

$$\langle A \rangle = \int\int d\mathbf{p}^N d\mathbf{r}^N A(\mathbf{p}^N, \mathbf{r}^N)\rho(\mathbf{p}^N, \mathbf{r}^N) \tag{4.13}$$

Where $\langle A \rangle$ is the ensemble-average, or expectation value, of the property *A*. The probability density $\rho(\mathbf{p}^N, \mathbf{r}^N)$ is the probability of finding the system configuration with momenta $\mathbf{p}^N$ and position $\mathbf{r}^N$. The ensemble-average of property *A* is determined by integrating over all possible configurations of the system and can be done so for either a specific time of the simulation, or even averaged over the duration of the simulation. In accordance to the ergodic hypothesis, an axiom of statistical mechanics, the ensemble-average is equal to the time-average (Leach, 1996). Under mass conservation conditions, constant volume and temperature, the probability density is given by the familiar Boltzmann distribution:

$$\rho(\mathbf{p}^N, \mathbf{r}^N) = \frac{1}{Q} \exp\left(-\frac{E(\mathbf{p}^N, \mathbf{r}^N)}{k_{\text{B}}T}\right) \tag{4.14}$$

Where $E(\mathbf{p}^N, \mathbf{r}^N)$ is the energy, Q is the partition function, k_B is Boltzmann's constant, and T is the temperature. The partition function is more generally written in terms of the Hamiltonian, $\widehat{H}$, where for a system of *N* atoms the partition function for the canonical ensemble is given by:

$$Q_{NVT} = \frac{1}{N!}\frac{1}{h^{3N}}\int\int d\mathbf{p}^N d\mathbf{r}^N \exp\left[-\frac{\widehat{H}(\mathbf{p}^N, \mathbf{r}^N)}{k_\mathrm{B}T}\right] \tag{4.15}$$

The canonical ensemble (NVT) is the statistical ensemble corresponding to constant temperature, number of particles, and volume. MD simulations often use the NVT or the isothermal-isobaric ensemble (NPT) for the calculation of thermodynamic properties. Measurement of these properties is reliant primarily on constant temperature, a condition that can be difficult to achieve due to the kinetic energy of the system of atoms vibrating. A straightforward approach to control the temperature would be to scale the atomic velocities during the simulation to reset temperature to desired value. However, doing so would disrupt the dynamics of the system and result in trajectory artifacts (Anderson, 1980). A superior approach is the implementation of temperature coupling algorithm (or thermostat), such as the Berendsen thermostat (Berendsen et al., 1984) or the Nosé-Hoover thermostat (Hoover and Holian, 1996).

The Berendsen thermostat is enforced by coupling the system to an external heat bath with reference temperature T_0. The change in temperature is proportional to the system temperature and the heat bath temperature, with a coupling strength determined by a coupling parameter τ:

$$\frac{\mathrm{d}T}{\mathrm{d}t} = \frac{T_0 - T}{\tau} \tag{4.16}$$

The heat flow in and out of the system is achieved by scaling the velocity every step with a scaling factor λ:

$$\lambda = \sqrt{1 + \frac{\Delta t}{\tau}\left(\frac{T_0}{T} - 1\right)} \tag{4.17}$$

The Berendsen thermostat is simple to implement and can efficiently relax the system to the target temperature from temperatures far from equilibrium conditions. However, it does not often produce an accurate NVT or NPT ensemble due to exclusion of the stochastic contribution of thermal fluctuations at a microscopic level. The Berendsen thermostat is more commonly used only for energy minimization schemes, and not for the production run.

For accurate measurement of the microscopic level thermal fluctuations, the Nosé-Hoover thermostat is more commonly applied. In this algorithm, an additional degree of freedom is introduced with a friction parameter ξ accounting for momentum added to Newton's second law:

$$\frac{\mathrm{d}^2 r_i}{\mathrm{d}t^2} = \frac{F_i}{m_i} - \xi \frac{dr_i}{dt} \tag{4.18}$$

Implementation of the correct thermostats allows for the efficient but accurate simulation of molecular systems.

4.2.9 Motivations and objectives

To measure the diffusivity in the cuticle we build atomistic systems of epicuticular waxes and measure the time-dependent displacement of compounds. In Chapter 3, the major structural properties of waxes were explored as a function of their chemical composition. Under ambient conditions, waxes were found to have a range of crystalline content varying from amorphous liquid phase waxes to hardened crystalline waxes. The cuticles of higher plants can exist in a wide range of crystalline phases (Barthlott et al., 1998), however, the effect of this crystallinity on the permeability of solutes has not been investigated. Here, we use molecular dynamics simulations of volatile scent and water molecules to characterize the effect of crystallinity on the transport properties of natural waxes.

4.3 Materials and methods

4.3.1 Simulation details

Molecular dynamics (MD) simulations were performed using a non-polarizable force-field that was parameterized using the Topologically Automated Force-Field Interactions (TAFFI)

methodology for systematic atomic indexing (Savoie et al., 2017). The TAFFI protocol dictates unique atom types determined on the basis of molecular topology, where a unique atom type is governed by atoms up to two bonds in distance. Each unique atom type is thus distinguished by its local bond connections. The resulting syntax describing the molecular architecture is given by an adjacency matrix describing the connectivity of all the unique atom types, which is readily machine-coded to atomic numbers (1 – hydrogen, 6 – carbon, 8 – oxygen). The force-field describing the bonds, angles, dihedrals, and non-bonded interactions are written in this syntax and parameterized using the "all atoms" optimized potentials for liquid simulations (OPLS-AA) distributed by TINKER (Jorgensen et al., 1996; Ponder, 2003; Siu et al., 2012). The total force field energy, *E*, is given by the sum of the individual energy potentials (equation 4.1):

All MD simulations were performed within the LAMMPS (http://lammps.sandia.gov) distribution suite (Plimpton, 1995). MD simulations employed periodic boundary conditions, particle-particle-particle-mesh (pppm) evaluations of long-range interactions beyond a 14 Å cut-off, a Nosé-Hoover barostat and thermostat with 1000 fs and 100 fs relaxation, respectively, under NPT conditions. Neighbor lists were constructed every time step with a maximum of 10,000 neighbors stored during each iterative construction. Newton's equations of motions were integrated using the velocity-Verlet algorithm over 1 fs increments for all simulations. Each simulation representing the model cuticle was comprised of the three wax components (*n*-tetracosane, 1-docosanol, and 3-methylbutyl dodecanoate) over varying compositions for a total of 36 wax monomers to ensure a minimum of 2000 atoms in the simulation cell. With each composition of the model cuticle, five VOCs (benzaldehyde, methylbenzoate, 2-phenylethanol, benzylbenzoate, and phenylethylbenzoate) or five water (TIP-3P water model) molecules were inserted with the wax compounds initially, such that they would also be subjected to the same geometry optimization routine prior to MD equilibration runs.

Geometry optimization and relaxation were conducted using 10,000,000 energy minimization steps with simulated annealing from 400 K to the simulation temperature of 289-304 K and a pressure of 1 bar, with atomic displacements limited to 0.01 Å per step. Following geometry relaxation, NPT dynamics at the simulation temperature and pressure of 1 bar were run for an additional 1 ns (using 2 fs time steps) prior to MD equilibration run. Equilibration was for 10 ns (10 fs timesteps) under NPT conditions at the simulation temperature and 1 bar, employing a Nosé-Hoover thermostat (100 fs relaxation timescale) and barostat (1000 fs relaxation timescale).

Each simulation was performed using a varying composition of the ternary wax system containing either all five parameterized volatile compounds or five water molecules for a total of 32 simulation variations. Standard error for measured quantities was obtained over five repeated trajectories for each simulation variation, leading to a total of 160 simulations performed. An example simulation initialization script (.init) can be found in Appendix C.

4.3.2 Trajectory analysis

Simulation trajectories were obtained in the form of LAMMPS trajectory files (.lammpstrj). Ensemble- and time-averaged properties such as MSD, radius of gyration, pair correlation distribution functions were all calculated from data autocorrelation or cross-correlation functions written in Python.

VOC and water displacement in a specified wax system was measured over five independent trajectories. Diffusion coefficients were obtained over the 10 ns NPT equilibration steps using the Einstein equation (4.19):

$$D_i = \lim_{t\to\infty} \frac{\mathrm{d}\langle|\mathbf{r}_i(t) - \mathbf{r}_i(0)|^2\rangle}{6\mathrm{d}t} \tag{4.19}$$

where D_i is the diffusion coefficient of the diffusing compound i, and $|\mathbf{r}_i(t) - \mathbf{r}_i(0)|^2$ is the mean-square displacement (MSD) of the diffusing compound evaluated over the timescale t. Measurement of the time-derivative of the MSD was performed using a finite difference method over 10 ps increments, and diffusivity values were obtained directly from the derivatives. Due to sub-diffusive behavior in some simulations, the range at which the derivative was obtained was modified to ensure that diffusion coefficients were obtained during free diffusive behavior. Wax chain structural arrangements were analyzed using atom pair radial-distribution functions, $g_{AB}(r)$, by parsing the equilibration simulation timescale to average the positions of carbon-carbon, carbon-oxygen, and oxygen-oxygen pair distributions. End-to-end radius of gyration was obtained directly from an ensemble-averaged autocorrelation function over the 10 ns equilibration trajectories, using 10 ps increments.

To determine the chain conformations of the wax, the radius of gyration was calculated. As chain conformations change over simulation duration, the radius of gyration is averaged for all wax units and over the entire simulation duration to obtain the ensemble average:

$$\langle R_g^2 \rangle = \frac{1}{N} \langle \sum_{i=1}^{N} (\mathbf{r}_i - \mathbf{r}_{\text{mean}})^2 \rangle \tag{4.20}$$

Simulated XRD patterns were calculated using the method described in (Coleman et al., 2013), with C++ scripts available with the VESTA package (Momma and Izumi, 2011). During X-ray diffraction, each reciprocal lattice point is associated with a reciprocal lattice vector *K* describing the deviation between diffracted and incidence waves, given by vectors k_D and k_I, respectively:

$$K = k_D - k_I = \alpha B_1 + \beta B_2 + \gamma B_3 \tag{4.21}$$

Where α, β, and γ is any real number, and B_n is the reciprocal lattice axis corresponding to the n = 1, 2, or 3 edge of the simulation cell. Assuming a monochromatic incident radiation of wavelength λ, the diffraction angle θ is computed utilizing the geometric relationship between the reciprocal lattice vector and the wavelength through Bragg's law:

$$\frac{\sin\theta}{\lambda} = \frac{|K|}{2} \tag{4.22}$$

To calculate the diffraction intensity, the structure factor F (K) must be evaluated. The structure factor is calculated from the atomic positions r_j:

$$F(K) = \sum_{j=1}^{N \text{ atoms}} f_j(\theta) \exp(2\pi i K \cdot r_j) \tag{4.23}$$

Where f_j are the atomic scattering factors which account for the reduction in diffraction intensity from an individual atom due to Compton scattering and vary by atom type, angle of diffraction θ, and the wavelength λ. At each diffraction angle, the atomic scattering factors are computed using numerical approximations parameterized by specific atom types. For X-ray

diffraction, the analytical approximation of the atomic scattering factor is found from the summation of four Gaussian functions:

$$f_j \frac{\sin\theta}{\lambda} = \sum_i^4 a_i \exp\left(-b_i \frac{\sin^2\theta}{\lambda^2}\right) + c \tag{4.24}$$

Where the coefficients a_i, b_i, and c are empirical constants for specific atom types. These coefficients have been tabulated for most atom types and were obtained from Fox et al., 1989. In addition to the structure factor, the Lorentz-polarization factor must also be calculated:

$$Lp(\theta) = \frac{1 + \cos^2(2\theta)}{\cos\theta \sin^2\theta} \tag{4.25}$$

With both the structure factor and Lorentz-polarization factor calculated at discrete diffraction angles, the intensity can be calculated:

$$I(K) = Lp(\theta) \frac{F(K)\bar{F}(K)}{N} \tag{4.26}$$

The diffraction intensity is given by the product of the structure factor and its complex conjugate normalized to *N* atoms in the simulation. Generally, XRD line profiles are created by virtually rotating the Ewald sphere (a sphere of radius equal to the reciprocal of the wavelength λ) around the origin of the reciprocal space to all possible orientations, like that of a powder X-ray diffraction experiment. As all diffraction orientations are equally probable, all the reciprocal lattice points will intersect the surface of the Ewald sphere. Line profiles simulating powder XRD are constructed by collecting all reciprocal lattice points into bins corresponding to their scattering angle 2θ calculated from equation 4.22 and summing all the intensity data.

For all trajectories, pair correlation functions were calculated for carbon-carbon, carbon-oxygen, and oxygen-oxygen atom pairs. The pair correlation function is calculated using the statistical mechanics definition of the radial distribution function (RDF) between two atom types *A* and *B*:

$$g_{AB}(r) = \frac{1}{N_A N_B} \sum_{i=1}^{N_A} \sum_{j=1}^{N_B} \langle \delta |\mathbf{r}_{ij}| - r \rangle \tag{4.27}$$

Where δ is the Dirac delta function and $\mathbf{r}_{ij}$ is the interatomic separation between the atom types.

4.3.3 Visualization

All visualization was performed using the Visual Molecular Dynamics (University of Illinois at Urbana-Champaign, USA) software package, version 1.9.4. Figures were produced by Tachyon ray-tracing on a local GPU. Crystal figures were refined on VESTA (Momma and Izumi, 2011).

4.4 Results and discussion

4.4.1 Simulation initialization and production

A total of sixteen variations in wax composition were simulated using the LAMMPS molecular dynamics (MD) package with the OPLS force field (equation 4.1). Each simulation box contained 36 wax chains and five VOCs or five water molecules. All compounds were parameterized with the "all atoms" definitions provided by TINKER (Jorgensen et al., 1993; Ponder, 2003; Siu et al., 2012), and randomly inserted into the simulation box prior to geometry optimization. The initial simulation box size was thus dependent on the size of the molecules used.

Geometry optimization was performed using 1 ns of simulated annealing from 400 K to the simulation temperature (Fig. 4.4). For this chapter, the simulations are all performed at 298 K. The total system potential energy was monitored over the 1 ns of annealing to ensure an energy minimum was reached prior to the MD production run (Fig. 4.5a).

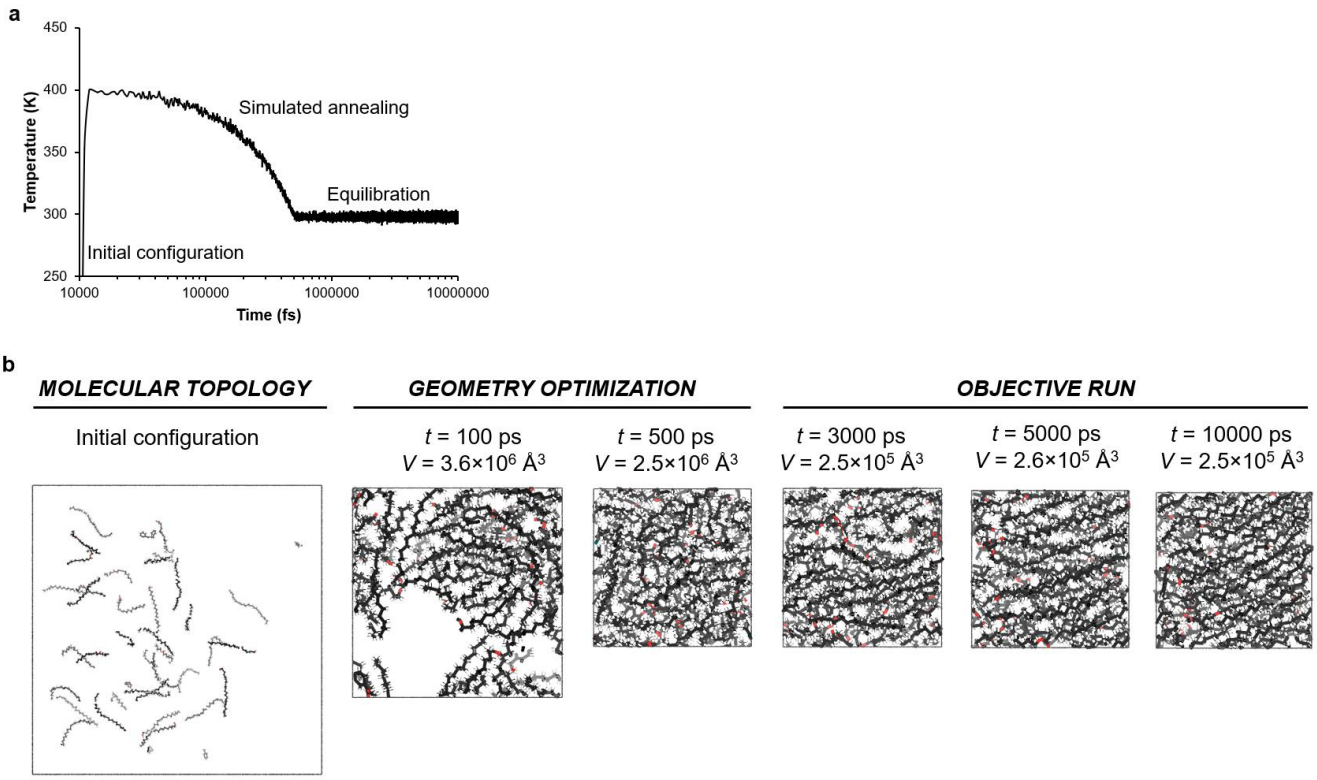

Fig. 4.4 – Simulated annealing procedure for a model wax system over 1 ns. (a) Thermal ramp from high temperature of 400 K to MD simulation (equilibration) temperature of 298 K. (b) Snapshots of the model cuticle system over the simulation duration.

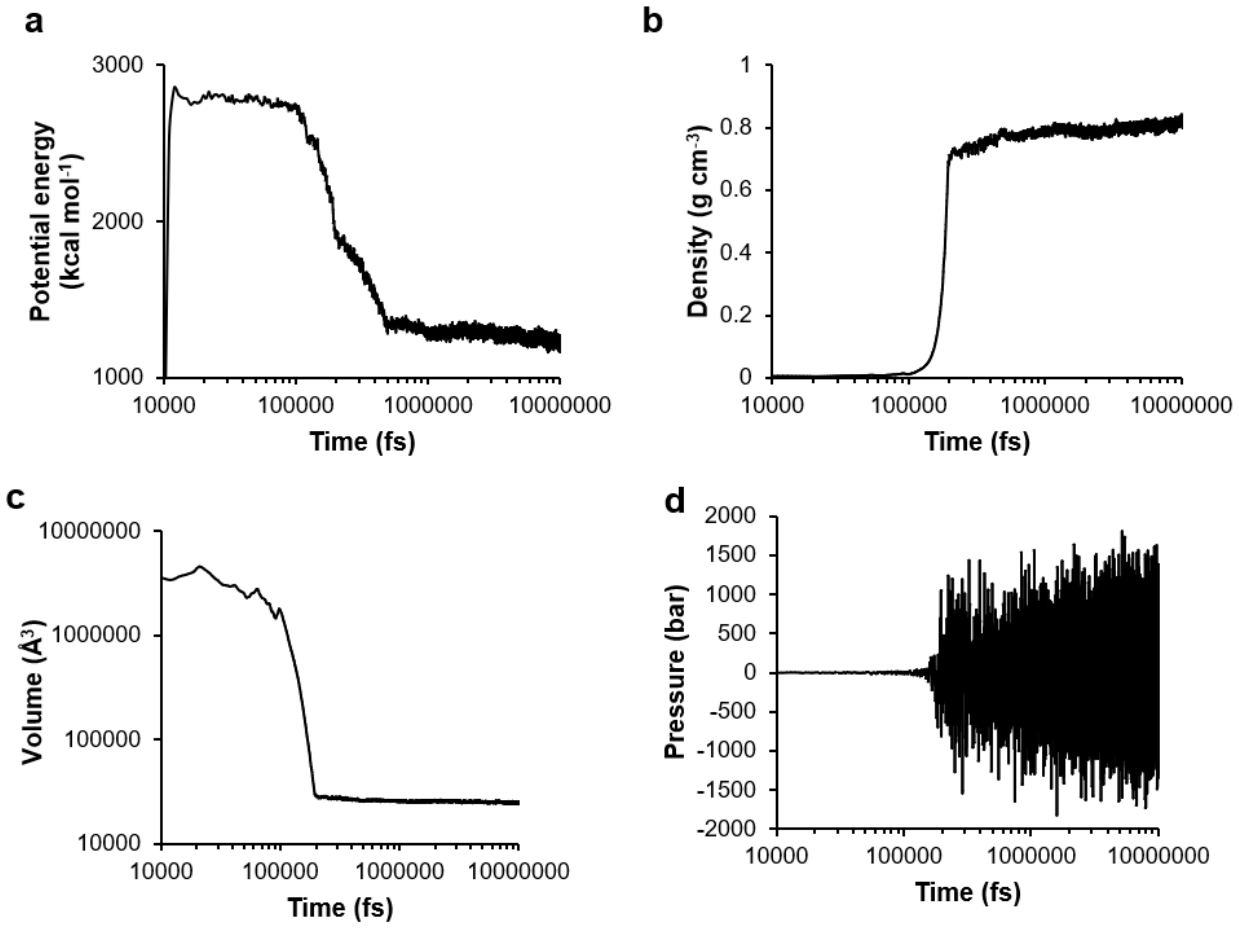

Fig. 4.5 – Simulation parameters during simulated annealing and equilibration. Parameters computed are (a) potential energy, (b) density (c) volume (d) pressure.

System properties such as density (Fig. 4.5b) and volume (Fig. 4.5c) influence the dynamic properties of the system, so it is important to know whether calculated diffusivity values during the production phase are the result of a realistic system and not the result of simulation artifacts. To ensure consistent and accurate measurements, each simulation was performed with five independent replicates. Geometry optimization via simulated annealing may be dependent on the initial configuration of a heterogeneous system, so each independent replicate was produced by completely random insertion of compounds to avoid any bias. All calculated system properties for the sixteen wax formulations can be found in Table 4.1.

Table 4.1 – System properties for wax mixtures obtained from NPT equilibration at 298 K and 1 bar. Percentage standard error is given in parenthesis.

Wax composition (g·g wax^{-1})			**Simulation property**					
			System volume	Total potential energy	Dihedrals	Van der Waals (Lennard-Jones)	Electrostatics (Coulombic)	Enthalpy
$C_{24}H_{50}$	$C_{22}H_{45}OH$	$C_{17}H_{34}O_2$	V, Å^3	E_{FF}, kcal mol^{-1}	$E_{dihedrals}$, kcal mol^{-1}	E_{LJ}, kcal mol^{-1}	E_{elec}, kcal mol^{-1}	ΔH, kcal mol^{-1}
1.000	0.000	0.000	1364.35 (0.87)	-144.59 (1.39)	-1099.69 (3.32)	396.72 (1.15)	3822.62 (0.38)	1364.35 (5.30)
0.757	0.243	0.000	1300.81 (0.82)	-150.47 (1.44)	-1072.91 (3.19)	349.03 (1.15)	3721.49 (1.99)	1300.81 (5.33)
0.509	0.491	0.000	1204.91 (0.73)	-156.00 (1.55)	-1062.47 (3.08)	286.81 (1.11)	3585.00 (2.82)	1204.91 (5.40)
0.257	0.743	0.000	1056.48 (0.69)	-160.31 (1.74)	-1066.44 (2.92)	186.02 (1.05)	3398.96 (4.78)	1056.48 (5.72)
0.000	1.000	0.000	1015.87 (0.91)	-157.02 (2.20)	-892.97 (3.16)	109.57 (1.43)	3193.88 (13.06)	1015.87 (5.80)
0.000	0.784	0.216	1095.78 (0.83)	-104.59 (1.92)	-964.26 (4.80)	224.47 (1.24)	3262.50 (5.12)	1095.78 (5.67)
0.000	0.547	0.453	1219.17 (1.04)	-34.45 (1.68)	-904.08 (17.17)	-904.08 (1.79)	3265.15 (1.79)	1219.17 (5.43)
0.000	0.287	0.713	1275.36 (1.81)	26.38 (2.53)	-894.93 (24.82)	449.14 (2.99)	3196.45 (1.63)	1275.36 (5.51)
0.000	0.000	1.000	1477.64 (1.21)	111.23 (1.35)	-765.18 (6.66)	550.40 (1.79)	3268.87 (0.93)	1477.64 (5.00)
0.294	0.000	0.706	1366.76 (0.93)	31.01 (1.36)	-914.02 (19.67)	516.96 (1.30)	3323.71 (0.71)	1366.76 (5.24)
0.556	0.000	0.444	1391.49 (1.05)	-25.57 (1.53)	-952.43 (23.75)	475.49 (1.58)	3517.96 (0.68)	1391.49 (5.17)
0.790	0.000	0.210	1201.89 (1.00)	-76.26 (1.58)	-939.70 (6.37)	386.91 (1.44)	3250.48 (0.53)	1201.89 (5.53)
0.362	0.349	0.289	1231.75 (0.93)	-77.19 (1.61)	-993.71 (6.78)	354.71 (1.20)	3416.35 (3.07)	1231.75 (5.46)
0.531	0.256	0.212	1293.99 (0.78)	-91.50 (1.37)	-1011.94 (5.83)	381.56 (1.15)	3545.52 (1.70)	1293.99 (5.31)
0.268	0.517	0.214	1238.04 (1.21)	-94.83 (2.01)	-958.70 (5.87)	312.24 (1.88)	3454.52 (3.07)	1238.04 (5.39)
0.281	0.271	0.448	1287.35 (0.93)	-31.41 (1.61)	-956.73 (19.00)	421.28 (1.43)	3372.63 (1.71)	1287.35 (5.37)

Upon reaching the simulation temperature, a Nosé-Hoover thermostat was employed to fix the temperature and pressure to maintain NPT conditions. In MD simulations, pressure is calculated from the system kinetic energy and the virial, and LAMMPS utilizes a pressure coupling barostat to ensure NPT conditions are held. Whether or not pressure coupling is used within a simulation, pressure can oscillate significantly (Fig. 4.5d). Instantaneous pressure oscillation is meaningless, where for short timescales (<5 picoseconds) the measure of pressure has no meaning. The average pressure should converge to the barostat pressure, and if this is not the case, then longer simulation times are needed to obtain time-averaged properties. The fluctuation in pressure can vary in the order of hundreds of bar (Huang et al., 2010).

4.4.2 Effect of chemical composition on wax chain conformations

For the simulated wax systems, equilibrium properties were obtained (Table 4.2). Calculated densities, ensemble-averaged square radii of gyration $\langle R_g \rangle^2$, and self-diffusion coefficients were in good agreement with previous MD simulations using similar compounds and force-field parameterization (Goo et al., 2002; Makrodimitri et al., 2011).

Table 4.2 – Static and dynamic properties for wax mixtures obtained from NPT equilibration at 298 K and 1 bar. Standard error is given in parenthesis.

Wax composition (g·g wax^{-1})			**Properties**			Intradiffusion coefficients (10^{-7} cm^2/s)		
$C_{24}H_{50}$	$C_{22}H_{45}OH$	$C_{17}H_{34}O_2$	ρ (g·cm^{-3})†	$\langle R_g^2 \rangle$ (Å^2)	*trans* dihedrals (%)	$C_{24}H_{50}$	$C_{22}H_{45}OH$	$C_{17}H_{34}O_2$
1.000	0.000	0.000	0.800 (7)	53.21 (1.1)	67.28 (0.5)	2.81 (0.8)	-	-
0.757	0.243	0.000	0.807 (7)	51.37 (1.1)	65.92 (0.3)	4.41 (1.6)	3.59 (1.4)	-
0.509	0.491	0.000	0.822 (6)	49.67 (1.1)	65.70 (0.2)	1.38 (0.4)	1.39 (0.6)	-
0.257	0.743	0.000	0.843 (6)	47.68 (1.5)	64.97 (0.3)	1.46 (0.6)	1.06 (0.6)	-
0.000	1.000	0.000	0.809 (7)	44.72 (2.0)	65.67 (0.4)	-	2.90 (1.8)	-
0.000	0.784	0.216	0.836 (7)	41.22 (1.8)	65.65 (0.4)	-	1.31 (0.3)	2.67 (0.3)
0.000	0.547	0.453	0.829 (9)	36.00 (2.3)	63.68 (0.4)	-	2.24 (0.7)	4.37 (1.3)
0.000	0.287	0.713	0.846 (15)	31.77 (2.6)	62.75 (0.2)	-	3.54 (1.6)	11.26 (2.9)
0.000	0.000	1.000	0.801 (10)	25.41 (3.2)	60.25 (0.2)	-	-	25.21 (4.0)
0.294	0.000	0.706	0.835 (8)	33.70 (2.5)	63.25 (0.3)	8.48 (1.9)	-	8.81 (1.5
0.556	0.000	0.444	0.813 (9)	39.81 (2.4)	63.86 (0.4)	4.73 (1.4)	-	6.33 (2.0)
0.790	0.000	0.210	0.819 (8)	46.67 (1.8)	64.73 (0.5)	0.56 (0.2)	-	2.62 (1.7)
0.362	0.349	0.289	0.825 (8)	42.54 (1.4)	65.56 (0.2)	1.91 (0.6)	1.30 (0.3)	3.04 (0.8)
0.531	0.256	0.212	0.820 (6)	44.72 (1.7)	65.00 (0.2)	1.96 (0.8)	0.80 (0.2)	3.58 (1.5)
0.268	0.517	0.214	0.814 (10)	39.20 (2.4)	64.59 (0.2)	2.29 (1.2)	1.67 (0.4)	5.17 (1.4)
0.281	0.271	0.448	0.833 (8)	41.99 (2.0)	64.26 (0.3)	4.08 (1.6)	1.55 (0.5)	6.76 (1.2)

†Uncertainty in parenthesis is for last digit(s)

Over the range of chemical compositions tested, wax density only varied between 0.8-0.85 g cm^{-3}, suggesting that the packing of individual wax chains is comparable between compositions. However, radius of gyration (Fig. 4.6a) and wax self-diffusion (Fig. 4.7) were found to be highly dependent on chemical composition, specifically the average-chain length of the wax. Therefore, major variations in wax structure arise from the distribution of lengths of individual hydrocarbon chains. The contribution of the aliphatic chain length can be observed in the radial distribution functions (RDFs) calculated for carbon-carbon atom pairs (Fig. 4.6b). Carbon pair correlations provide information on the preferred arrangements of the chains averaged over the MD simulation. Sharp peaks at approximately 1.5 and 2.5 Å correspond to carbon atoms separated by one and two bonds from a reference carbon atom, respectively. Lower intensity peaks at 3.2 and 3.9 Å correspond to pairs of carbon atoms separated by three bonds in their gauche and trans conformations, respectively. A distinct peak at ~5.0 Å emerges from the occurrence of successive pairs of trans conformation along a five-carbon atom sequence, while a separation of 4.5 Å corresponds to a successive trans-gauche conformation. Peaks beyond 5.0 Å correspond to carbon atom pairs separated by at least five bonds and provide no further insight into the configurations of the wax chains.

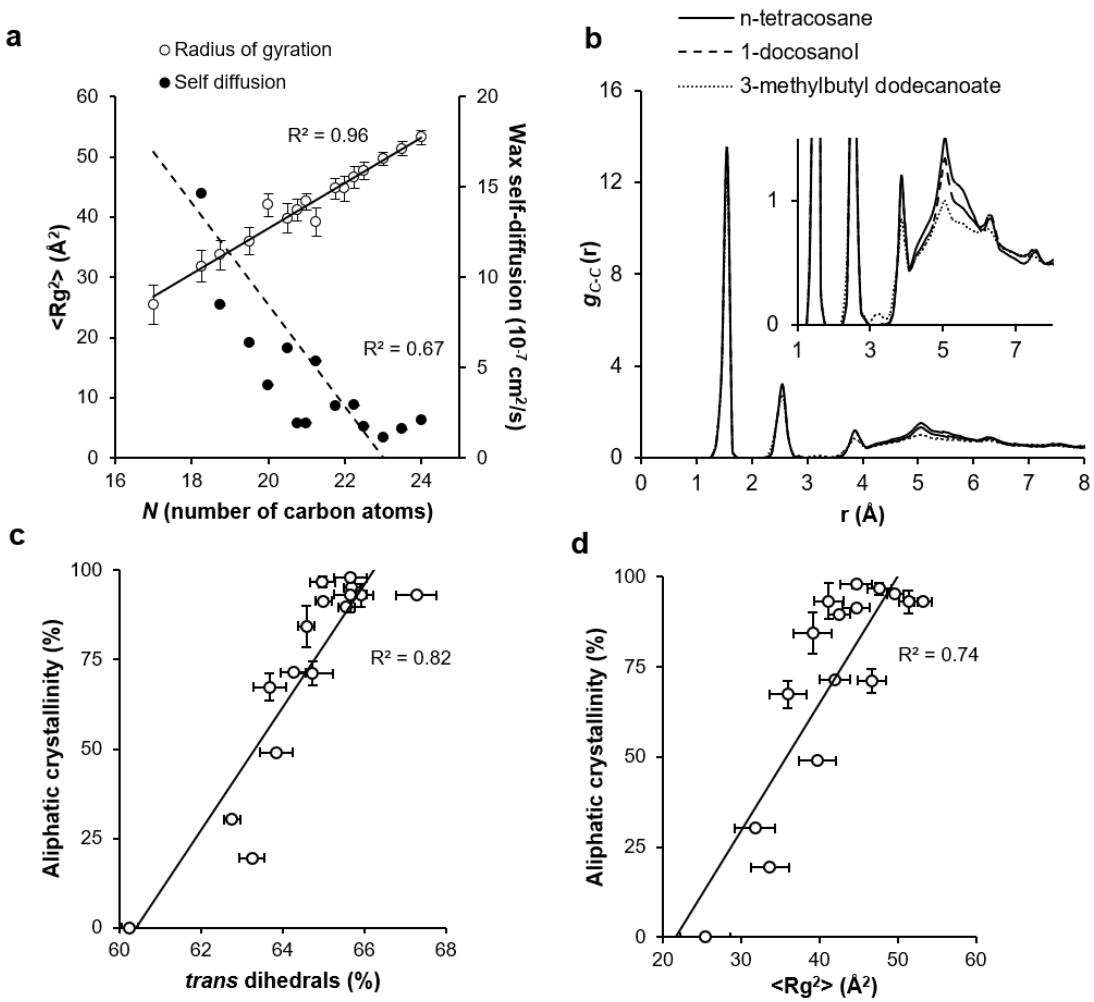

Fig. 4.6 – Properties of mixtures of model cuticle constituents from MD simulations at 298 K and 1 bar. (a) Effect of wax chain distribution on square radii of gyration and average self-diffusion. (b) Radial distribution function (RDF) of carbon-carbon pair correlations for pure wax components. Measured aliphatic crystallinity (from powder XRD) with respect to (c) percent of dihedrals in the trans conformation and (d) radius of gyration.

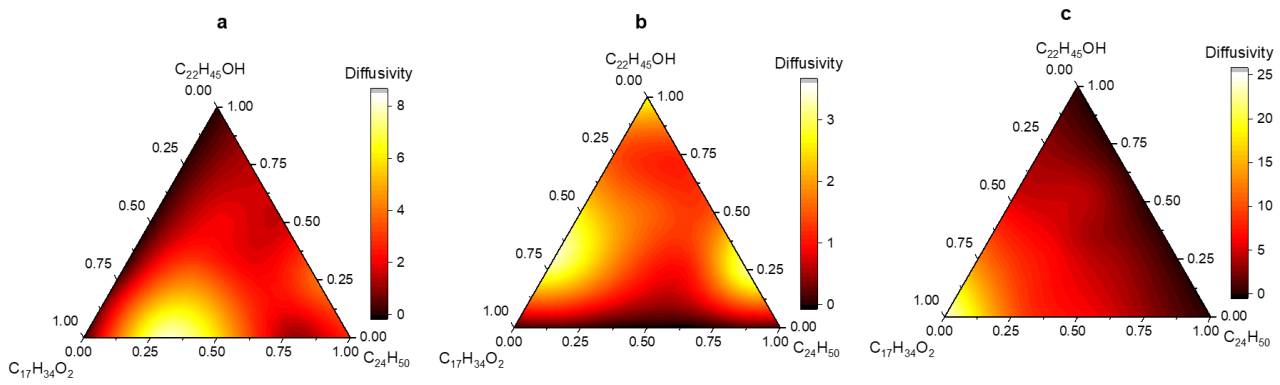

Fig. 4.7 – Intradiffusion (self) coefficients (10^{-7} cm^2/s) for (a) *n*-tetracosane, (b) 1-docosanol, and (c) 3-methylbutyl dodecanoate in the ternary model system.

The major difference in the RDFs between the three wax constituents is observed at the separation of 5.0 Å, where the intensity of the peak indicates the proportion of wax chains that are fully elongated. Anisotropy of waxes is attributed to an elongated rotator phase (long axis) of crystalline unit cells, suggesting that the relative aliphatic crystallinity is dependent on the stretching of dihedrals along the methylene chain (Fig. 4.6c). This elongation is determined from the carbon chain radius of gyration, serving as a measure of the length of the crystalline cell. Radius of gyration was found to significantly correlate with aliphatic crystallinity (Fig. 4.6d), suggesting that the abundance of crystalline units is determined by the rotator axis of the crystalline unit cell.

In Chapter 3, the effect of wax composition on aliphatic crystallinity was explored in detail. The major features of the XRD-patterns that were described were the (00*l*)-peaks describing the nematic ordering of unit cells, the (*hk*0)-peaks describing the packing of the cells, and the broad amorphous halo describing the portion of the phase with no crystalline order. Powder-XRD patterns of the blended waxes demonstrated that wax composition can result in significant differences in lattice symmetry and crystalline abundance. To determine if these patterns are obtained from atomistic scale simulations of the waxes, simulated X-ray diffraction patterns were calculated after 10 ns of MD equilibration (Fig. 4.8).

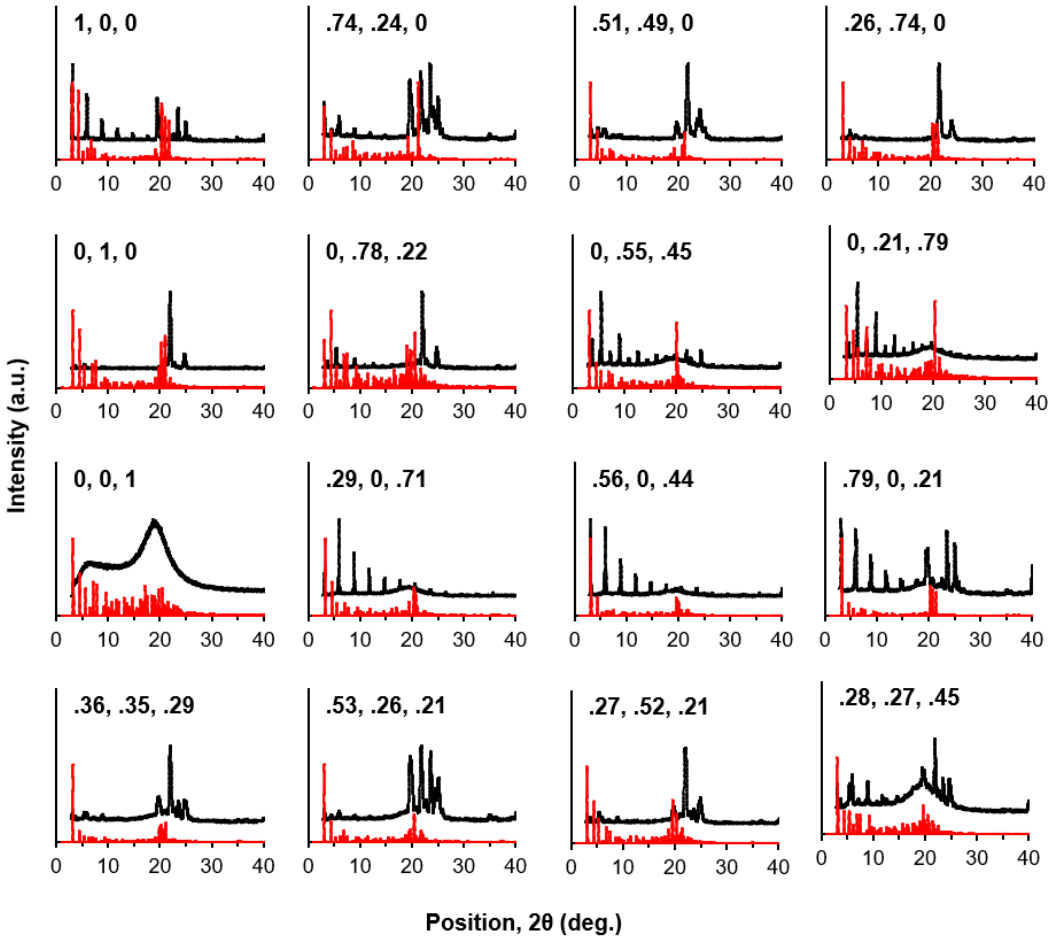

Fig. 4.8 – XRD patterns for wax mixtures ($C_{24}H_{50}$, $C_{22}H_{45}OH$, $C_{17}H_{34}O_2$ by weight fraction). Experimental (black) and simulated (red) XRD patterns for all wax mixtures tested.

Simulated XRD patterns are unable to replicate the halo that arises from disorder, and instead provides systematic noise. For most of the simulated structures, the simulated XRD patterns indicates that the crystalline unit cells have a long-length axis with major peaks emerging at $2\theta \leq 15°$. These peaks do not emerge in samples with an abundance of 1-docosanol, the reason for which was discussed in section 3.4.17. The diminished peaks are due to the increased atomic density between crystalline chains that are occupied by oxygen containing groups. However, the oxygen containing groups do cluster closely in waxes containing a high fraction of the primary alcohol during the MD simulations (Fig. 4.9), indicating that the density in the gap region is greater than that of waxes with less polar groups. The higher scattering caused by the clustered oxygen atoms cause destructive interference of the X-rays for these low angle peaks, resulting in diminished intensity. MD simulations support the hypothesis of the head to head arrangement of

wax groups; however, it cannot be captured by simulated XRD patterns. In general, the simulated XRD patterns do show peaks within the same range as those captured experimentally.

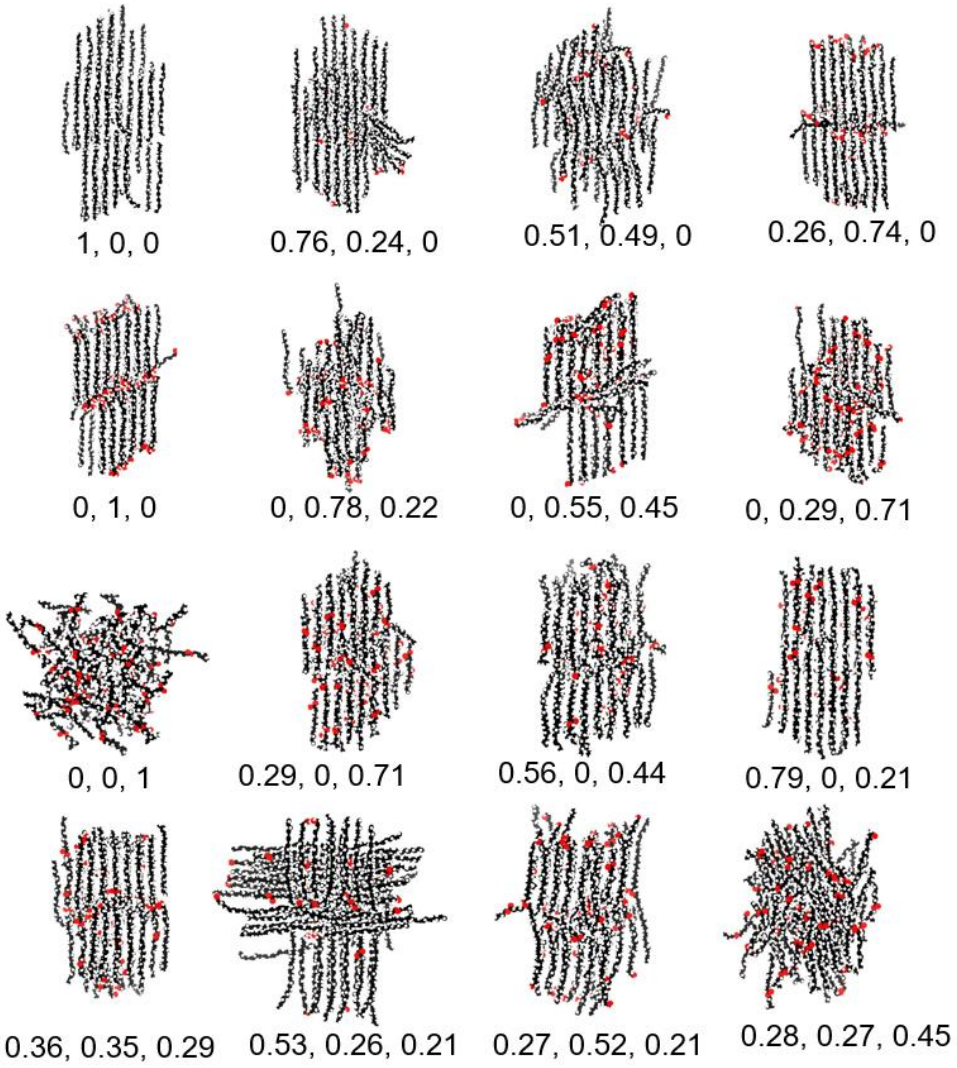

Fig. 4.9 – Snapshots of the representative structure of wax mixtures ($C_{24}H_{50}$, $C_{22}H_{45}OH$, $C_{17}H_{34}O_2$ by weight fraction). Structures were refined in VESTA (Momma and Izumi, 2011) after 10 ns of MD equilibration at 298 K and 1 bar.

4.4.3 Effect of wax composition on molecular diffusion

Petunia volatiles selected for MD simulations were compounds found either in the headspace (Fig. 4.10a) and/or internal pools (Fig. 4.10b) of day 2 post-anthesis petunia flowers during peak scent emission. Diffusion coefficients for scent (Fig. 4.11a) and water molecules (Fig. 4.11b) were calculated from 10 ns MD simulations through the model cuticle and other ternary

wax mixtures. Diffusion coefficients were obtained from the mean-square displacements (MSD) of the particles with respect to a reference position (Fig. 4.11c). For most wax compositions, VOC displacement was size-dependent; smaller VOCs such as benzaldehyde and methylbenzoate experienced upwards of 5-6-fold greater displacement than benzylbenzoate and phenylethylbenzoate.

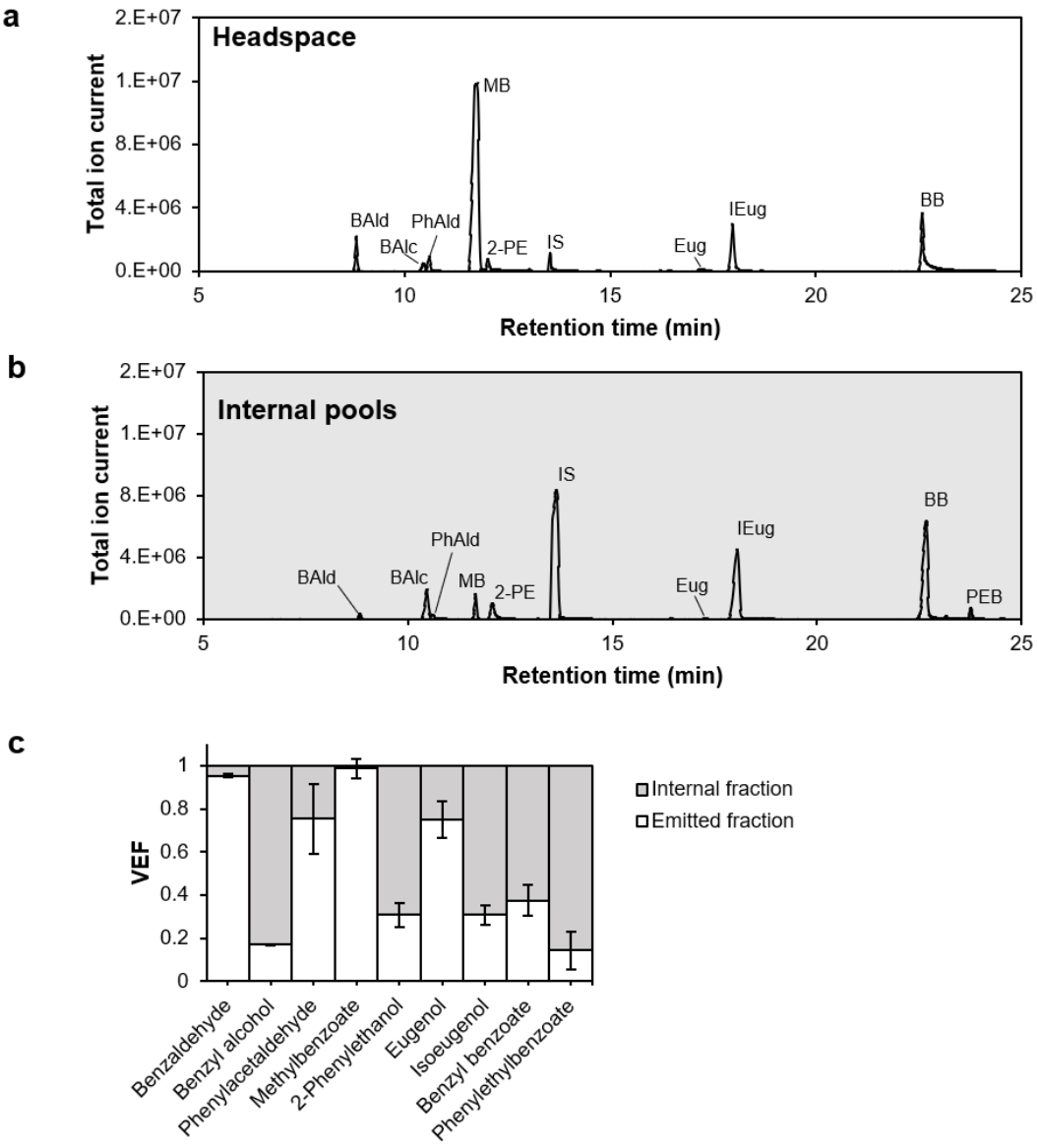

Fig. 4.10 – Petunia VOC emissions and internal pools at 22:00 h. Representative mass spectrum of the (a) headspace and (b) internal pools of two-day-old petunia flowers at 22:00 h. (c) Volatile emission factor (VEF) of petunia volatiles calculated from dynamic collection of VOCs between 18:00-22:00 h. Data are mean ± S.E. (n = 4 biological replicates).

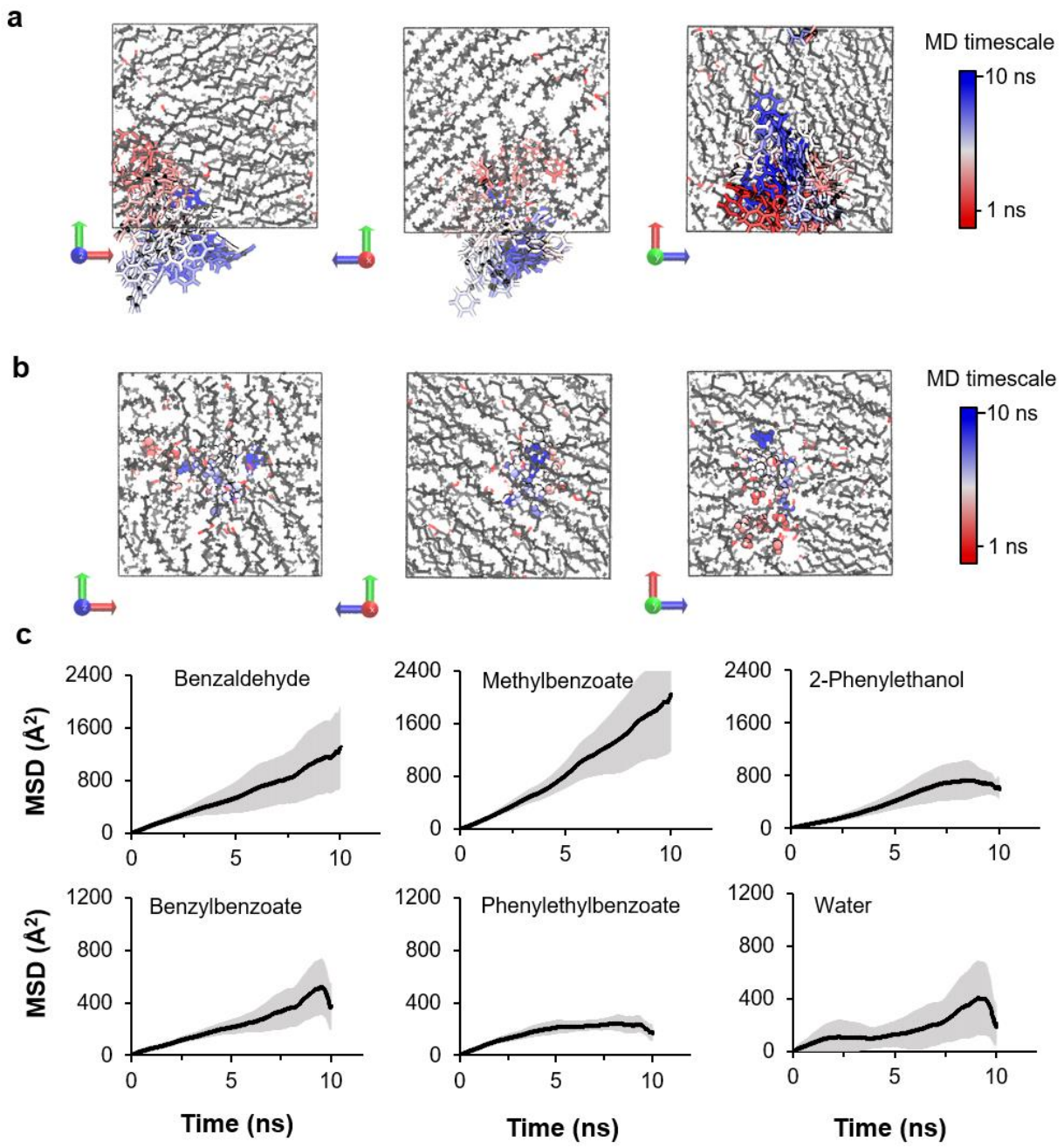

Fig. 4.11 – Average trajectory of displacement of individual benzenoid/phenylpropanoid volatiles in the model cuticle at 298 K and 1 bar. Orthographic views (from left to right: xy-plane, yz-plane, xz-plane) of (a) benzylbenzoate diffusion and (b) water diffusion in the model cuticle with a chemical composition of 26.8%/51.7%/21.4% $C_{24}H_{50}$/$C_{22}H_{45}OH$/$C_{17}H_{34}O_2$ by wt.%. Diffusing compounds are colored based on timescale between 1 and 10 ns in 100 ps increments during MD simulation at 298 K and 1 bar. (c) Mean-square displacement (MSD) of all VOCs and water molecules over the simulation time. Shaded region represents the standard error of the measurement.

Varying the proportions of the individual wax constituents of the model cuticle revealed significant differences in calculated diffusion coefficients (Fig. 4.12a). For VOCs, diffusivity was highest when the wax was solely composed of 3-methylbutyl dodecanoate and lowest in wax formulations enriched (>75 wt. %) with 1-docosanol. Over the range of wax compositions tested, VOC diffusion coefficients varied between 2×10^{-11}-6×10^{-10} m^2/s (~30-fold variation), while water diffusivity varied between 8×10^{-12}-3×10^{-10} m^2/s (~38-fold variation) (Fig. 4.12b). Interestingly, the size-dependent effect of VOC diffusion did not extend to water molecules, which experienced similar or even lower displacement to that of compounds with higher molecular weight. Previous assessments of cuticular permeability have found that the size-exclusion effects differ significantly between hydrophilic and lipophilic molecules, suggesting the possibility of separate polar and nonpolar diffusion paths for compounds of varying physicochemical properties (Schreiber, 2005). Measurement of water, benzoic acid, and salicylic acid permeability in the cuticles of *Hedera helix* L. leaves exhibited similar mass transfer rates through the isolated cuticle despite the substantial differences in molecule size, partitioning, and solubility (Popp et al., 2005). The major function of cuticles is to protect the plant against enhanced water loss, where low aqueous solubility and partitioning in hydrophobic waxes limit transport through the cuticle. As the focus of this study is primarily on the cuticle structural effects on diffusion, analysis of compound solubility, molecular interactions, and alternative polar diffusion paths are left for future analysis.

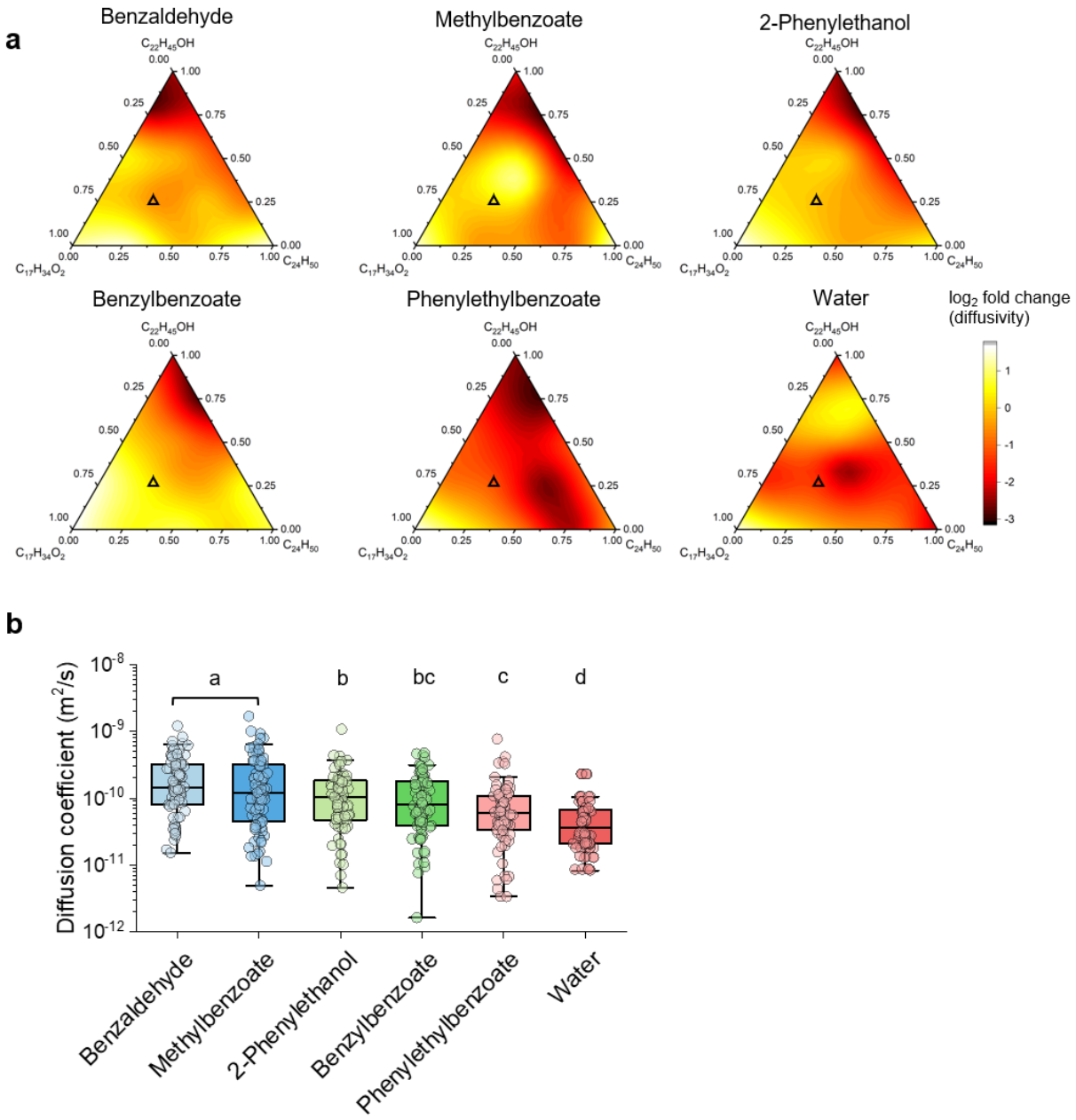

Fig. 4.12 – Effect of chemical composition on the diffusivity of benzenoid/phenylpropanoid VOCs through the model cuticle. (a) Ternary contour plots displaying the effect of model cuticle chemical composition on the diffusivity of individual VOCs and water. Diffusion coefficients are scaled to 1 (where 1 is the maximum diffusion coefficient for a given diffusing solute). Vertices of ternary diagrams represent a pure component, and axes of the diagrams represent mole fraction of the wax component. (b) The distribution of diffusion coefficients measured over the range of model cuticle compositions tested. Box whiskers represent the range of values, line represents the median value, and distribution is the smoothed kernel density distribution (n = 80 simulations). Letters indicates a significant difference in means, $P < 0.05$ by Student's *t*-test.

Diffusive walks for compounds in amorphous and crystalline waxes in the *xy*- and *yz*-planes of an orthogonal cubic unit cell at 298 K and 1 bar are shown in Fig. 4.13a and Fig. 4.13b, respectively. In an isotropic medium, diffusion is unhindered and compounds diffuse indiscriminately in the *x*-, *y*-, and *z*-dimensions of the Cartesian simulation cell over the 10 ns simulations. For crystalline waxes, diffusion is restricted from the confined motion of the wax chains, resulting in fewer vacancies for diffusing compounds to explore. As previously determined for the model cuticle and other crystalline wax blends, anisotropy in waxes occur due to the stretching of aliphatic chains. In fully crystalline waxes, compounds must diffuse parallel to that of the direction of the long length axis of the crystalline unit cell. For compounds to traverse through the wax chains, they must diffuse between the rigid methylene chains, which have a measured interatomic spacing between < 4.6 Å (Table 3.4). As benzene rings have an approximate diameter of 2.78 Å, VOCs with a single aromatic group are not restricted from diffusion between parallel methylene chains. However, the equilibrium orientation for both benzylbenzoate and phenylethylbenzoate results in their two aromatic groups lying out of plane with each other (Fig. 4.13c), resulting in effective diameters of 9 Å and greater. Diffusion of these compounds consequently experience significantly hindered displacement over the simulation time, contributing to the observed size-dependent diffusion. For the model cuticle, there was a strong negative dependence between the diffusivity and size of the VOCs (Fig. 4.13d).

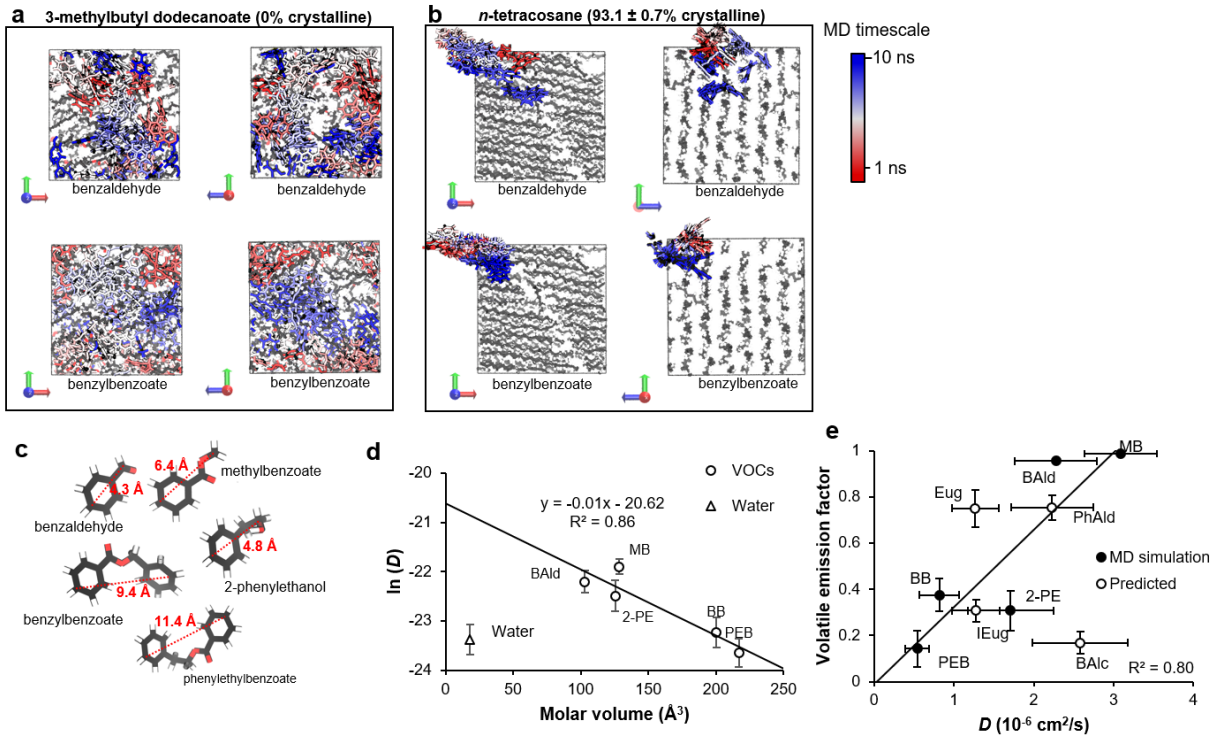

Fig. 4.13 – Effect of cuticular size exclusion on lipophilic molecule diffusion. Benzaldehyde and benzylbenzoate trajectory walks in (a) amorphous wax (pure 3-methylbutyl dodecanoate) and (b) and crystalline wax (pure n-tetracosane). (c) Petunia VOCs with maximum measured distances during MD simulations. (d) Correlation of diffusion coefficient of molecules in the model cuticle with respect to molar volume. (e) Correlation of simulated diffusion coefficients with the volatile emission factors (VEF) calculated for petunia VOCs by sampling the internal pools and headspace of two day old petunia flowers between 18:00-22:00 hr. Data are mean ± S.E. (vertical error bars obtained from dynamic headspace and internal pool sampling, n = 4 biological replicates, horizontal error bars obtained from MD simulations, n = 5 trajectories).

The effect of size-dependent diffusion through the cuticle may contribute to the enrichment of low molecular weight scent compounds found in the headspace of petunia flowers. VOC analysis in petunia flowers during peak emission revealed that smaller phenylalanine-derived VOCs such as benzaldehyde, phenylacetaldehyde, and methylbenzoate were abundant in the headspace (Fig. 4.10a), while larger VOCs such as isoeugenol, benzylbenzoate, and phenylethylbenzoate were more abundant in the internal pools (Fig. 4.10b). To determine if the cuticular size-exclusion affects the dynamics of scent emission, we define a volatile emission factor (VEF), the ratio of the emission to biosynthesis flux of an individual VOC. Biosynthesis and emission fluxes were measured between 18:00-22:00 h by dynamic sampling of the headspace

and internal pools of petunia flowers (Fig. 4.10c). Biosynthesis ($\nu_{\mathrm{syn},i}$) is defined as the sum of the accumulation of VOC internal pools (C_i) and the emission flux ($\nu_{\mathrm{emi},i}$):

$$\frac{\mathrm{d}C_i}{\mathrm{d}t} = \nu_{\mathrm{syn},i} - \nu_{\mathrm{emi},i} \tag{4.28}$$

The efficiency by which VOCs are released into the atmosphere upon synthesis is thus given by the VEF. Compounds with high VEF values (VEF → 1.0) are considered biosynthesis-limited, while compounds with low VEF values (VEF < 0.50) are considered to be mass-transfer limited. Calculated VOC diffusion coefficients in the model cuticle were found to be positively correlated (R^2 = 0.80) with the measured VEF values (Fig. 4.13e). For VOCs with a small molar volume, emissions experience less resistance through the cuticle. Only for VOCs large enough to be hindered by the interatomic spacing between methylene chains does there appear to be significant diffusive mass-transfer resistance. Therefore, the role of the cuticle in the VOC emission network is attributed to the differential control on mass transfer of individual VOCs, effecting the composition, amount, and dynamics of scent emission.

Variations in wax chemical composition resulted in substantial differences in percent crystallinity. Overall, increased amorphous wax content resulted in enhanced diffusion for VOCs and water, and diffusion in fully amorphous wax (pure 3-methylbutyl dodecanoate) was up to 30-fold higher than in crystalline waxes (Fig. 4.14a). For 2-phenylethanol, benzylbenzoate, phenylethylbenzoate, and water, measured diffusion coefficients varied almost linearly over the range of aliphatic crystallinity, suggesting that perturbations in cuticle structure significantly affect the mobility of these compounds through the cuticle. In contrast, benzaldehyde and methylbenzoate diffusion coefficients were insensitive to small changes in wax crystallintiy. Based on their VEF values, benzaldehyde and methylbenzoate experience negligible mass transfer resistance through petal cuticles, and also experience unhindered diffusion between methylene chains during simulations. As the spacing between crystalline cells did not change significantly over the range of chemical compositions, the net result is a limited dependence between net displacement and crystallinity.

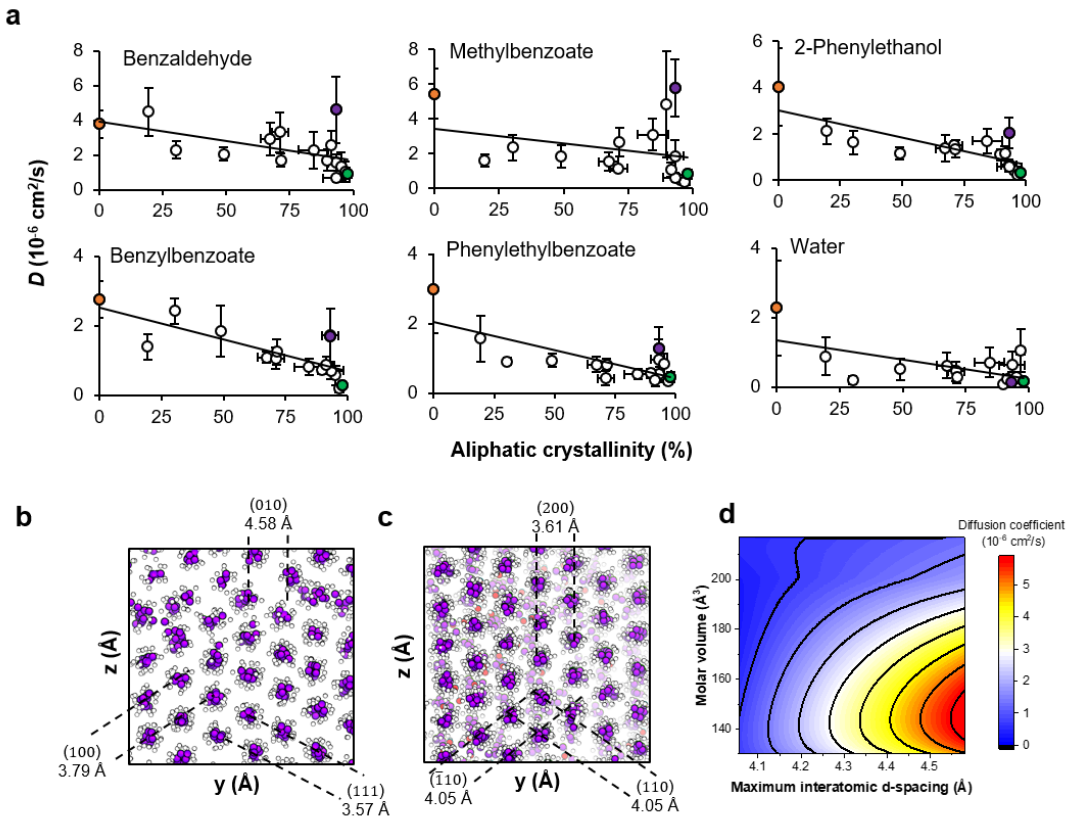

4.14 – Simulation of molecular diffusion in anisotropic waxes at 298 K and 1 bar. (a) Effect of aliphatic crystallinity on the diffusion coefficients. Data are mean ± S.E. (x-axis error bars are obtained from peak integration error propagation, y-axis error bars represent the standard error of the mean of five independent trajectories). Pure component waxes are colored by identity ($C_{24}H_{50}$ – purple; $C_{22}H_{45}OH$ – green; $C_{17}H_{34}O_2$ – orange). Representative snapshots of single layers of simulated (b) *n*-tetracosane and (c) 1-docosanol. (d) Effect of the maximum interatomic spacing on the diffusivity of VOCs. Effect on diffusion coefficients (10^{-6} cm2/s) are shown by the contours.

The linear dependence of diffusion coefficients with percent crystallinity was weaker at relatively high crystalline amounts (> 84% crystallinity). This is most apparent when comparing displacement of VOCs in pure *n*-tetracosane and pure 1-docosanol, both of which are highly crystalline during simulations, yet the displacement of VOCs in 1-docosanol is 3-6 fold lower than in pure *n*-tetracosane. The two possibilities for this discrepancy can be due to differences between interatomic spacing between chains or the elongation of methylene chains, or a combination of both effects.

XRD analysis of the peaks at large diffraction angles for *n*-tetracosane and 1-docosanol demonstrated differences in d-spacing values (Fig. 3.10), and varying proportions of these waxes result in measurable changes in methylene chain spacing. The gaps between individual alkane

chains are given by the (010)-, (100)- and (111)-peaks corresponding to d-spacing values of 4.58, 3.79, and 3.57 Å, respectively (Fig. 4.14b). In contrast, the spacing between 1-docosanol crystalline units is given by the (110)- and (200)-peaks corresponding to 4.05 and 3.61 Å, respectively (Fig. 4.14c). Thus, the maximal spacing between methylene chains is significantly greater for *n*-tetracosane, increasing the gaps through which VOCs can diffuse. This maximal spacing between methylene chains measurably increases with increasing abundance of triclinic alkane units (Table 3.4) and had a significant effect on the diffusivity of VOCs (Fig. 4.14d). This effect was distinctly greater for the VOCs with a molar volume below 180 $Å^3$, further evidence of size-limiting characteristics of the cuticle on diffusing molecules.

Elongation of crystalline unit cells was observed for wax composed pure of 1-docosanol, where wax chains are oriented in a polar head-to-head orientation that results in a double layer structure supported by hydrogen bonding. Radial distribution functions for oxygen-oxygen correlations exhibit a sharp peak at ~2.8 Å separation, the distance between a pair of hydroxyl oxygen atoms supported by hydrogen bonding, for wax mixtures with significant amounts of 1-docosanol (Fig. 4.15). The double layer structure can be observed readily in wax systems enriched with the primary alcohol (Fig. 4.9). Due to this layering of methylene chains, crystalline 1-docosanol is characterized as having an increased nematic order compared to *n*-alkanes of similar chain length, with a gap region between stacks of methylene chains filled with oxygen atoms (Kreger, 1948). Consequently, diffusion of compounds in waxes with a double layer structure is significantly lower due to increased molecular obstructions and longer apparent diffusion path.

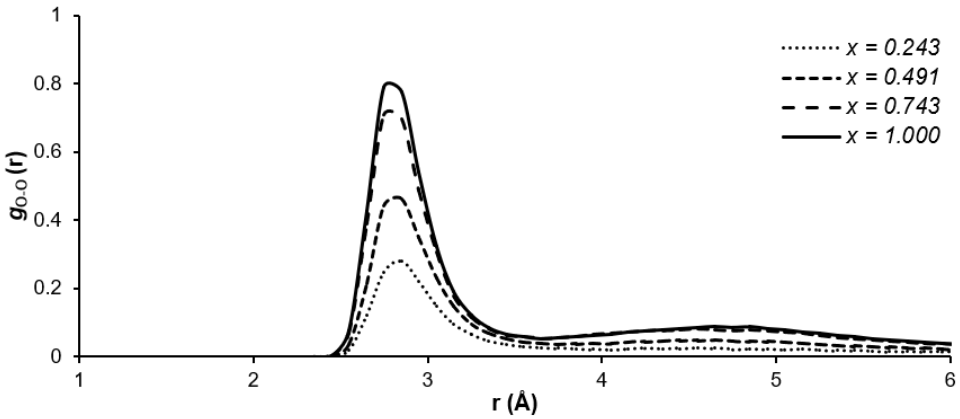

Fig. 4.15 – RDF for oxygen-oxygen pair correlation. RDF for wax mixtures with varying wax blends containing x (mass fraction) of $C_{22}H_{45}OH$.

4.5 Conclusions

In summary, we formulated a model cuticle which represents the molecular arrangements of wax constituents and the aliphatic crystallinity of the floral waxes of *Petunia hybrida*. Using MD simulations, we tested the effects of varying the chemical composition on wax structure and its subsequent effect on molecular diffusion. Despite large perturbations in the chemical compositions, the crystalline symmetry remained largely orthorhombic, but the relative abundance of crystalline waxes was significantly modified with increasing amounts of an amorphous constituent. In crystalline wax systems, diffusion paths were determined by the anisotropy of the cuticle, where the displacement of compounds was parallel to methylene chains. Displacement of VOCs was also highly size-dependent, where larger VOCs were hindered by their ability to diffuse between crystalline units. Calculated VOC diffusion coefficients through the model cuticle was found to correlate with the efficiency by which individual volatiles are released into the flower headspace. Larger VOCs experienced significantly lower displacement over 10 ns simulations, indicative of relatively high mass transfer resistance. Enrichment of low molecular weight VOCs in the petunia headspace suggests that differences in individual compound mass transfer resistance plays a significant role in the distribution of scent compounds emitted. While molar volume dictated diffusivity for the lipophilic volatiles, this relationship did not extend to water molecules, which experienced comparable diffusion to much larger compounds. Empirical relationships for cuticular diffusion are limited to compounds of similar physicochemical properties and effects arising from varying solubility or hydrophobic interactions need to be considered in subsequent

analysis. Changes in wax composition contribute to changes in diffusivity for all compounds, and in many conditions, this change was greater than 2-fold. Thus, cuticle composition can be considered a significant determinant for relative permeability. The caveat to this is that plant cuticles have a high degree of chemical and physical complexity, and thus genetic manipulation of cuticle biosynthetic and export genes may result in only minimal changes in composition. Studying the crystalline behavior of multi-component waxes with significant chemical heterogeneity would be the next step to better characterize how small perturbations in composition can result in structural changes.

4.6 Acknowledgments

This work was supported by grant IOS-1655438 from the National Science Foundation awarded to Dr. Natalia Dudareva and Dr. John A. Morgan. I would like to thank Dr. Brett Savoie for his assistance with the molecular dynamics framework and access to computational resources to carry out simulations.

4.7 References

Adams DJ. (1983) Alternatives to the Periodic Cube in Computer Simulations. *CCP5 Quarterly, 10*, 30-6

Adler BJ., Wainwright TE. (1970) Decay of the Velocity Autocorrelation Function. *Physical Review, A1*, 18-21

Allinger NL. (1977) Conformational analysis. 130. MM2. A hydrocarbon force field utilizing V1 and V2 torsional terms. *Journal of the American Chemical Society, 99* (25), 8127-34

Anderson HC. (1980) Molecular dynamics simulations at constant pressure and/or temperature. *The Journal of Chemical Physics, 72* (4), 2384-93

Ayala PY., Schlegel HB. (1997) A combined method for determining reaction paths, minima, and transition state geometries. *Journal of Physical Chemistry, 107*, 375-84

Ballabio, D. (2015). A MATLAB toolbox for Principal Component Analysis and unsupervised exploration of data structure. *Chemometrics and Intelligent Laboratory Systems 149 B*, 1-9

Barthlott W., Neinhuis C., Cutler D., Ditsch F., Meusel I., Theisen I., Wilhemi H. (1998) Classification and terminology of plant epicuticular waxes. *Botanical Journal, 126* (3), 267-60

Berendsen HJC., Grigera JR., Straatsma TP. (1987) The missing term in effective pair potentials. *Journal of Physical Chemistry, 91* (24), 6269-71

Berendsen HJC., Postma JPM.; van Gunsteren WF., DiNola A., Haak JR. (1984) Molecular-Dynamics with Coupling to an External Bath. *The Journal of Chemical Physics, 81* (8), 3684-90

Brooks BR., Bruccoleri RE., Olafson BD., States DJ., Swaminathan S., Karplus M. (1983) CHARMM: A program for macromolecular energy, minimization, and dynamics calculations. *Journal of Computational Chemistry, 4* (2), 187–217

Charati SG., Stern SA. (1998) Diffusion of gases in silicone polymers: molecular dynamics simulations. *Macromoloecules, 31* (16), 5529-35

Claessens M., Ferrario M. Ryckaert JP. (1983) The structure of liquid benzene. *Molecular Physics, 50* (1), 217-227

Coleman SP., Spearot DE., Capolungo L. (2013) Virtual diffraction analysis of Ni [0 1 0] symmetric tilt grain boundaries. *Modelling and Simulation in Materials Science and Engineering, 21* (5)

Cornell WD., Cieplak P., Bayly CI., Gould IR., Merz KM Jr., Ferguson DM., Spellmeyer DC., Fox T., Caldwell JW., Kollman PA. (1995). A Second Generation Force Field for the Simulation of Proteins, Nucleic Acids, and Organic Molecules. *Journal of the American Chemical Society, 117* (19), 5179–97

Ding H-Q., Karasawa N., Goddard III WA. (1992) The Reduced Cell Multipole Method for Coulomb Interactions in Periodic Systems with Million-Atom Unit Cells. *Chemical Physics Letters, 196*, 6-10

Fox AG., O'Keefe MA., Tabbernor MA. (1989) Relativistic Hartree–Fock x-ray and electron atomic scattering factors at high angles. *Acta Crystallographica A, 45*, 786–93

Greengard L., Rokhlin V. (1987) A Fast Algorithm for Particle Simulations. *Journal of Computational Physics, 135* (2), 280-92

Goo G-H., Sung G., Lee S-H., Chang T. (2002) Diffusion Behavior of n-Alkanes by Molecular Dynamics Simulations. *Bulletin- Korean Chemical Society, 23* (11), 1595-1603

Hoover WG., Holian BL. (1996) Kinetic moments method for the canonical ensemble distribution. *Physics Letters A, 211* (5), 253–57

Hunter CA., Saunders JKM. (1990) The nature of π- π interactions. *Journal of the American Chemical Society, 112* (14), 5525-34

Huang C., Li C.,, Choi PYK., Nandakumar K., Kostiuk LW. (2010) A novel method for molecular dynamics simulation in the isothermal–isobaric ensemble. *Molecular Physics, 109* (2), 191-202

Ingólfsson HI., Melo MN., van Eerden FJ., Arnarez C., Lopez CA., Wassenaar TA., Periole X., de Vries AH., Tieleman DP., Marrink SJ. (2014) Lipid organization of the plasma membrane. *Journal of the American Society, 136* (41), 14554-59

Jorgensen WL., Maxwell, DS., Tirado-Rives J. (1996). Development and Testing of the OPLS All-Atom Force Field on Conformational Energetics and Properties of Organic Liquids. *Journal of the American Society 118* (45), 11225-11236

Kannan S., Zacharias M. (2009) Simulated annealing coupled replica exchange molecular dynamics – An efficient conformational sampling method. *Journal of Structural Biology*, *166* (3) 288-94

Kondratyuk ND., Norman GE., Stegailov VV. (2016) Self-consistent molecular dynamics calculations of diffusion in higher *n*-alkanes. *The Journal of Chemical Physics*, *145*

Kong CL. (1973) Combining rules for intermolecular potential parameters. II. Rules for the Lennard-Jones (12–6) potential and the Morse potential. *The Journal of Chemical Physics*, *59* (5), 2464

Kubo R. (1957) Statistical-Mechanical Theory of Irreversible Processes. I. General Theory and Simple Applications to Magnetic and Conduction Problems. *Journal of the Physical Society of Japan, 12*, 570-86

Leach, A. (1996) Molecular Modelling: Principles and Applications (Second Edition). *Prentice Hall* ISBN-10: 0582382106

Lee S-H., Chang T. (2003) Viscosity and Diffusion Constants Calculation of *n*-Alkanes by Molecular Dynamics Simulations. *Bulletin of the Korean Chemical Society*, *24* (11), 1590-98

LeSar R. (2013) Introduction to Computational Materials Science: Fundamentals to Applications. *Cambridge University Press* ISBN-10: 9781139033398

Li T., Kildsig DO., Park K. (1997) Computer simulation of molecular diffusion in amorphous polymers. *Journal of Controlled Release*, *48*, 57-66

Lindner B., Petridis L., Schulz R., Smith JC. (2013). Solvent-Driven Preferential Association of Lignin with Regions of Crystalline Cellulose in Molecular Dynamics Simulation. *Biomacromolecules*, *14* (10), 3390-98

Lorentz H.A. (1881) *Ueber die Anwendung des Satzes vom Virial in der kinetischen Theorie der Gase*. *Annalen der Physik, 248* (1), 127–36

Makrodimitri ZA., Unruh DJM., Economou IG. (2012) Molecular simulation and macroscopic modeling of the diffusion of hydrogen, carbon monoxide and water in heavy n-alkane mixtures. *Physical Chemistry Chemical Lipids*, *14*, 4133-41

Matas A, Heredia A. 1999. Molecular dynamics modellization and simulation of water diffusion through plant cutin. *Zeitschrift für Naturforschung*, *54*c, 896–902

Momma K., Izumi F. (2011). VESTA 3 for three-dimensional visualization of crystal, volumetric and morphology data. *Journal of Applied Crystallography 44*, 1272-1276

Petersen HG., Soelvaso D., Perram JW., Smith ER. (1994) The Very Fast Multipole Method. *Journal of Chemical Physics*, *101*, 8870-76

Plimpton S. (1995). Fast Parallel Algorithms for Short-Range Molecular Dynamics. *Journal of Computational Physics 117*, 1-19

Pollard TD. (2007) Regulation of actin filament assembly by Arp2/3 complex and formins. *Annual review of biophysics and bimolecular structure*, *36*, 451-77

Ponder JW. Washington University Medical School. Available at http://dasher.wustl.edu/tinker

Popp C., Burghardt M., Friedmann A., Riederer M. (2005) Characterization of hydrophilic and lipophilic pathways of *Hedera helix L.* cuticular membranes: permeation of water and uncharged organic compounds. *Journal of Experimental Botany, 56* (421), 2797-806

Rappe AK., Casewit CJ., Colwell KS., Goddard III WA., Skiff WM. (1992) UFF, a full periodic table force field for molecular mechanics and molecular dynamics simulations. *Journal of the American Chemical Society, 114* (25), 10024-35

Savoie BM., Webb MA., Miller III TF. (2017). Enhancing Cation Diffusion and Suppressing Anion Diffusion via Lewis-Acidic Polymer Electrolytes. *The Journal of Physical Chemistry Letters 8*, 641-646.

Schreiber L. (2005) Polar Paths of Diffusion across Plant Cuticles: New Evidence for an Old Hypothesis. *Annals of Botany, 95* (7), 1069-73

Scott WRP., Huenenberger PH., Tironi IG., Mark AE., Billeter SR., Fennen J., Torda AE., Huber T., Krueger P., van Gunsteren WF. (1999) The GROMOS Biomolecular Simulation Program Package. *The Journal of Physical Chemistry A, 103*, 3596–607

Siu SWI., Pluhackova K., Böckmann RA. (2012). Optimization of the OPLS-AA Force Field for Long Hydrocabons. *Journal of Chemical Theory and Computation 8*, 1459-1470.

Takeuchi H. (1990). Molecular dynamics simulations of diffusion of small molecules in polymers: Effect of chain length. *The Journal of Chemical Physics, 93* (6), 4490

Thompson SM. (1983) Use of Neighbor Lists in Molecular Dynamics. *CCP5 Quarterly, 8*, 20-28

Urey HC., Bradley Jr. CA. (1931) The Vibrations of Pentatonic Tetrahedral Molecules. *Physical Review, 38*, 1969-78

van Gunsteren WF., Berendsen HJC. (1987) Groningen Molecular Simulation (GROMOS) Library Manual, BIOMOS b.v., Groningen.

Verlet L. (1968) Computer "Experiments" on Classical Fluids. II. Equilibrium Correlation Functions. *Physical Review, 165*, 201-14

Waldman M., Hagler AT. (1993) New combining rules for rare gas van der waals parameters. *Journal of Computational Chemistry, 14* (9), 1077–84

CHAPTER 5. THERMOTROPIC POLYMORPHISM OF PLANT CUTICLES

5.1 Abstract

As a model for the epicuticular waxes of plant cuticular membranes, we studied the phase behavior of varying mixtures of *n*-tetracosane ($C_{24}H_{50}$), 1-docosanol ($C_{22}H_{45}OH$), and 3-methylbutyl dodecanoate ($C_{17}H_{34}O_2$) using differential scanning calorimetry (DSC). X-ray diffraction (XRD) experiments of wax mixtures reveal that the model cuticle primarily exhibits orthorhombically-packed solid phase at temperatures far below their melting point. Upon heating, wax mixtures exhibit a solid-solid phase transition from the orthorhombic symmetry to a hexagonally-packed solid phase. This metastable state was found to exist only for a narrow temperature range, where upon further heating, wax mixtures reached their melting transition. Using DSC and XRD data, binary and ternary phase diagrams were constructed for the wax system. Thermal characterization of wax mixtures showed that the transition region of a wax mixture is dependent purely on the chemical composition and is reflective of the relative abundance and arrangements of crystalline wax. Molecular dynamics (MD) simulations of the model cuticle was performed between 5-45°C to obtain temperature-dependent effects of volatile organic compound (VOC) and water diffusion. At temperatures approaching and above the hexagonal phase transition, wax fluidity increases resulting in increased time-dependent displacement of molecules. Temperature was found to have significant contribution towards the molecular diffusion in the cuticle. Using a combination of experimental and computational methods, we discuss the relevance of studying phase behavior of simple binary and ternary systems in context of far more complex phase behavior for plant epicuticular waxes

5.2 Introduction

5.2.1 Adaptive role of cuticles to abiotic stress

The cuticles of higher plants are adapted primarily to efficiently control water deficit, the foremost prerequisite for plant survival and environmental competitiveness (Kerstiens, 1996). The water permeability through the cuticle determines the minimum and unavoidable water loss. Low

cuticular water permeability is therefore one of the principal factors supporting the survivability and viability of plants under water scarce conditions. Riederer and Schreiber (2001) measured water permeance in isolated leaf and fruit cuticles of several plant species and found that the permeability values clustered based on species and climate of origin. Lowest water permeability was observed in leaves from plants growing in a tropical climate, such as epiphytes or climbing plants. The next clustered group with higher water permeance belonged to leaves with from xeromorphic plants growing in the warm, dry Mediterranean climate. The group with the greatest water permeability was mesomorphic leaves growing in temperate climates with higher precipitation. The permeance for water in cuticles from mesomorphic leaves was found to be comparable or even lower than that of synthetic polymer films such as high-density polyethylene (HDPE), polypropylene (PP), and polyethylene terephthalate (PET). While these commonly used plastics are used ubiquitously for food packaging and protective covers, plant cuticles can limit water permeance to greater extents at comparable thicknesses. However, when the water permeance of the cuticles was compared to the total wax coverage, there was no correlation between thickness and permeability (Kerstiens, 1996; Riederer and Schreiber, 2001; Jeffree, 2006), suggesting that wax composition controls the rate of mass transfer across the cuticle (Goodwin and Jenks, 2005, Martin and Rose, 2014). From Chapter 4, the diffusion of water across the cuticle was found to be dependent on the anisotropy of the waxes (Fig. 4.14a). As crystallinity of waxes is a function of the distribution of individual wax compounds, it is likely that the plant cuticle composition is adapted to the environment. While plants have evolved to exist in varying terrestrial conditions, abiotic stresses such as temperature (Baker, 1974), humidity (Koch et al., 2006), UV irradiation (Barnes et al., 1996), soil salinity (Kosma et al., 2009) and drought (Huihui et al., 2017) have been linked to changes in cuticle morphology, deposition, and permeability. Thus, wax biosynthetic pathways are regulated by environmental conditions, which can result in differences in wax composition and morphology (Shepard and Griffiths, 2006).

In addition to the variability in environmental conditions that arise naturally, there is potential for anthropogenic climate change to greatly impact cuticle biosynthesis. While there are no studies linking climate change to changes in cuticle development, elevated atmospheric carbon levels have been linked to increases in leaf thickness and area (Kovenock and Swann, 2018). Changes in leaf architecture likely induce changes in cuticle coverage and composition due to decreased productivity, which can have significant impacts on the plant water balance and

transpiration rate. While limiting water loss is the primary function of the cuticle, our discussion in previous chapters have linked the importance of cuticle composition and the efficacy of volatile emissions. Like water, the relative mixture of volatile scent compounds emitted is affected by the crystallinity of the cuticle. Enhanced plant VOC emissions have also been linked to climate change (Zhao et al., 2016), where the increased emissions can form secondary organic aerosols (SOA) that can influence cloud formation and local climate. These effects are rapid and can impact the development of cuticles. Thus, an understanding of the cuticle permeability as it relates to composition (and its regulation), is of vital importance for the viability of natural ecosystems as well as for the breeding of crops for improved environmental tolerance and performance under stress.

5.2.2 Thermotropic phase behavior of cuticles

From the previous chapter, the effect of crystalline size and quantity on the diffusivity of volatile scent compounds was analyzed in detail. The physical state of an mixture is a function of both the composition and physical variables such as temperature and pressure, and analysis of the state is best understood by the construction of phase diagrams. While phase diagrams for complex mixtures such as the real cuticles of plants are impossible to obtain due to the excess degrees of freedom that are to be resolved, the model cuticle studied in the previous chapters is well suited for physical state analysis. In this present work, we examine phase diagrams constructed for the model cuticle system defined in Chapter 3.

Based on X-ray diffraction (XRD) patterns of various wax mixtures in the ternary system, the polymorphism of linear long-chain hydrocarbons favors orthorhombic crystalline symmetry. However, at wax mixtures with high quantities of the amorphous 3-methylbutyl dodecanoate ($C_{17}H_{34}O_2$) exhibited hexagonal packing symmetry. For long chain primary alcohols, the hexagonal phase has been reported to be a temporary transition state (Watanabe, 1961), with increased rotational freedom about the long axis (McClure, 1968). The transition into the rotator phase results in a softer, more fluidic wax film, and likely enhances the permeability of solutes across the cuticle. Individual crystalline phases are readily measured by XRD or IR spectroscopy, however identification of the phase transition requires temperature-dependent measurements of crystallinity. Calorimetry is a viable method for measuring the wax orthorhombic to hexagonal phase transition temperature (Carreto et al., 2002; Reynhardt and Riederer, 1991). Polymorphism

of solids can be readily studied using differential scanning calorimetry (DSC). Calorimetric techniques can be used to obtain melting and glass transition temperatures of samples of both biological (lipids, polysaccharides, etc.) and synthetic (polymers, waxes, etc.) samples. DSC is used to measure heat flow to and from a sample compared to a reference pan, upon a heating or cooling cycle. Endothermic and exothermic effects are recorded to quantify temperature and enthalpies of transition, in addition to the specific heat capacity. Determination of parameters in a series of mixtures facilitates the construction of binary (T-x) or ternary phase diagrams.

Assessment of the model cuticle aliphatic crystallinity by XRD revealed that large compositional perturbations were needed to impact the anisotropy of the system. However, missing from that analysis was the transition states and how they may change at varying chemical composition. Differing mixtures can result in drastic shifts in melting and glass transition temperatures in wax blends (Fagerström et al., 2014), and thus we use DSC to assess the orthorhombic-hexagonal phase transition. Using the same atomistic simulation methodology from Chapter 4, we evaluate the effect of thermal transitions on molecular diffusion.

5.2.3 Motivations and objectives

While we have established a relationship between the crystallinity of waxes and the diffusion of volatile scent and water molecules, the effect of wax phase transitions was not characterized. In particular, the phase transition between mixtures of *n*-tetracosane ($C_{24}H_{50}$) and 1-docosanol ($C_{22}H_{45}OH$) is of interest due to the significant differences in simulated diffusion coefficients. While both compounds exhibit ~100% crystallinity at purity, VOC diffusion coefficients in pure 1-docosanol were 3-6 fold lower at 298 K compared to that of pure *n*-tetracosane. Thus, the abundance of crystalline unit cells does not solely contribute to diffusivity across the cuticle. Analysis of the wax phase transitions will provide further insight into the physical state of a given wax mixture.

In this chapter, binary and ternary phase diagrams are constructed for the model cuticle system analyzed previously. As temperature is a significant factor affecting the permeability of the cuticle with relation to water loss (Schönherr et al., 1979), we use molecular dynamics simulations to assess the effect of temperature on the diffusion coefficients of VOCs and water. Understanding how environmental factors such as temperature can affect the permeability and phase state of the cuticle is crucial for assessing the plants viability.

5.3 Materials and methods

5.3.1 Plant materials and growth conditions

Detailed in Section 3.2.1.1 – Plant materials and growth conditions.

5.3.2 Chemicals

Wax compounds used were the same as used in Section 3.4.1.1 - Chemicals. Wax mixtures were prepared in the same composition as those listed in Table 3.4.

5.3.3 Sample preparation

Model wax compounds were solubilized in chloroform (< 2 mg/ml). To prepare the wax mixtures, solubilized waxes were added to glass scintillation vials in measured quantities. Solvent was evaporated under a gentle stream of N_2 and dried wax mixtures were left to dry overnight in the fume hood.

5.3.4 DSC measurements

DSC measurements were carried out on a TA Instruments TA Q-20 Differential Scanning Calorimeter (New Castle DE, USA) in the POWER Laboratory (Davidson School of Chemical Engineering, Purdue University, West Lafayette IN, USA). The instrument was calibrated for heat flow and temperature using 10 mg of indium (melting point, T_m = 156.6°C, ΔH = 28.45 J g^{-1}). Samples were weighed (2-10 mg) into Tzero hermetic aluminum pans, with an empty sealed pan used as the reference. Dry N_2 gas (50 ml min^{-1}) was used to purge the furnace chamber. Each sample was first heated to 165°C at a ramp of 5°C/min and held at 165°C for 10 mins. Samples were then cooled to -40°C at a ramp of 5°C/min and held for another 10 mins, concluding the first cycle. A total of five heating and cooling cycles were used to negate variance that arises from hysteresis.

5.3.5 Simulation details

The molecular dynamics (MD) method is described in detail in Chapter 4, with simulation details provided in Section 4.2.1.1 – Simulation details. A sample LAMMPS script is included in Appendix C. Simulations were performed under NPT conditions at 1 bar and between 278-318 K.

5.4 Results and discussion

5.4.1 DSC measurements of reconstituted petunia cuticles

The petal adaxial cuticular waxes from day 2 post-anthesis *Petunia hybrida* flowers were isolated using solvent-extraction and evaluated using DSC (Fig. 5.1a). Extracted petunia waxes show a broad pronounced transition peak with phase transition occurring at 28.2°C. The total transition covers a range between 27.9 to 47.5°C. Over the temperature range analyzed, no other endothermic peaks were observed despite the significant distribution of wax compounds identified by GC-MS. At 25°C, petunia waxes were found to predominantly exhibit hexagonal rotator phase (Fig. 3.5), which is generally considered a metastable phase for waxes (Watanabe, 1961; Ensikat et al., 2006). As no phase transitions are observed below 25°C for the petal waxes, it is likely that the hexagonal symmetry is the primary stable phase. At temperatures above 48°C, petal waxes exist as an isotropic liquid. This relatively low melting point is consistent for a wax that has a significantly high amorphous content.

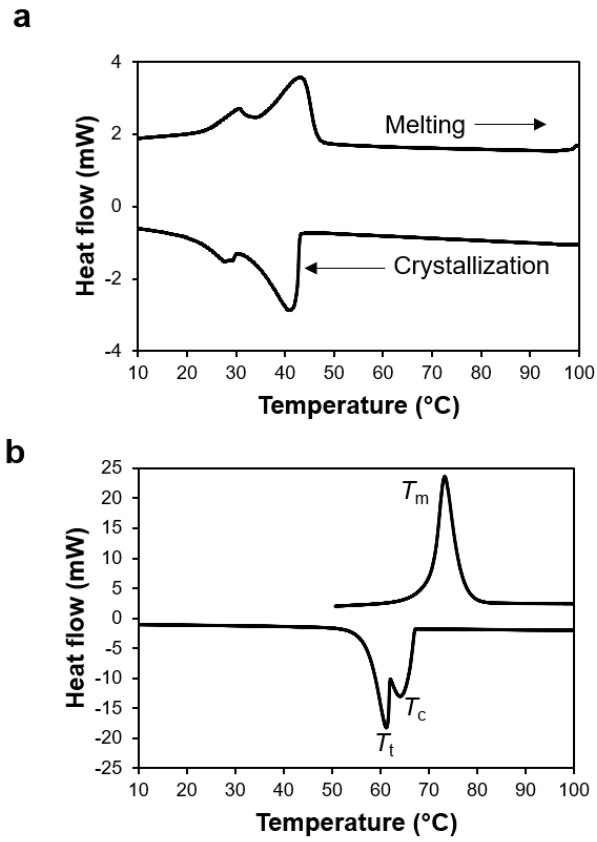

Fig. 5.1 – Thermograms for (a) two-day post-anthesis *Petunia hybrida* flower petal waxes and (b) 1-docosanol obtained at a scan rate of 5°C min^{-1}. DSC thermograms depict heating and cooling cycles to obtain melting and crystallization behavior, respectively. T_m, T_c, and T_t correspond to melting, crystallization, and transition temperatures, respectively (identified at peak apex).

In contrast, the thermogram for 1-docosanol ($C_{22}H_{45}OH$) exhibits a narrow peak centered at 73.6°C with a melting completion temperature at 79°C (Fig. 5.1b). The exothermic curve demonstrates two distinct peaks for the crystallization temperature of 63.4°C and transition temperature of 60.1°C. Therefore, there exists a metastable hexagonal rotator phase between 63-74°C for 1-docosanol. At temperatures below the transition temperature, 1-docosanol exhibits orthorhombic symmetry. In general, long-chain hydrocarbons are known to freeze from an isotropic liquid phase to a solid phase at a characteristic crystallization temperature T_c. This resulting solid phase is typically hexagonal packing symmetry (McClure, 1968). In the case of many wax compounds, such as primary alcohols and acids, the hexagonal phase is only metastable, and will undergo a solid to solid transition into orthorhombic crystals, which lack rotational freedom about their long *c*-axis (Reynhardt and Riederer, 1994). This solid to solid phase transition is well characterized in primary alcohols (Watanabe, 1964; Pradhan et al., 1970; Kuchhal et al.,

1979). Comparing the petunia cuticular waxes to 1-docosanol, the most abundant wax constituent in petunia petal waxes, reveals that the distribution of wax compounds not only reduces the overall crystallinity of the wax, but also depreciates the phase transition substantially. Given that the phase transition range of epicuticular waxes begins at 28°C, natural thermal variations arising from weather patterns can lead to changes in the cuticle permeability.

5.4.2 Binary ($C_{24}H_{50}$ + $C_{22}H_{45}OH$) phase diagram

Both *n*-tetracosane ($C_{24}H_{50}$) and 1-docosanol ($C_{22}H_{45}OH$) exhibit high crystallinity (>90%) at 25°C as measured by XRD (Fig. 3.10a and b), however, diffusion of volatile and water molecules was 3-6 fold lower in pure 1-docosanol compared to pure *n*-tetracosane (Fig. 4.12a). The differences were primarily attributed to changes in crystal morphology between the two compounds, where 1-docosanol chains were found to pack closer together and possess increased nematic layering because of hydrogen bonding between polar head groups. However, the differences in unit cell gap spacing were slight (< 0.5 Å), and may not fully resolve the differences in measured diffusion coefficients by MD simulation. Instead, we can characterize the thermal phase behavior to identify changes in phase transition that occur as a result of compositional changes.

The thermal phase behavior of $C_{24}H_{50}$ and $C_{22}H_{45}OH$ was investigated by DSC analysis of binary mixtures (Fig. 5.2). As is the case for the pure wax components, the completion of melting was observed to be greater than that of the crystallization temperature, suggesting that binary mixtures undergo the metastable solid-solid phase transition. Mixtures with compositions close to purity exhibit a single endothermic peak similar to that of the pure compound. However, for most compositions, phase transition was completed with two endothermic transitions occurring at varying temperatures. The lack of overlap between the two peaks suggests a heterogenous solid phase, where the alcohol and *n*-alkane form independent crystals.

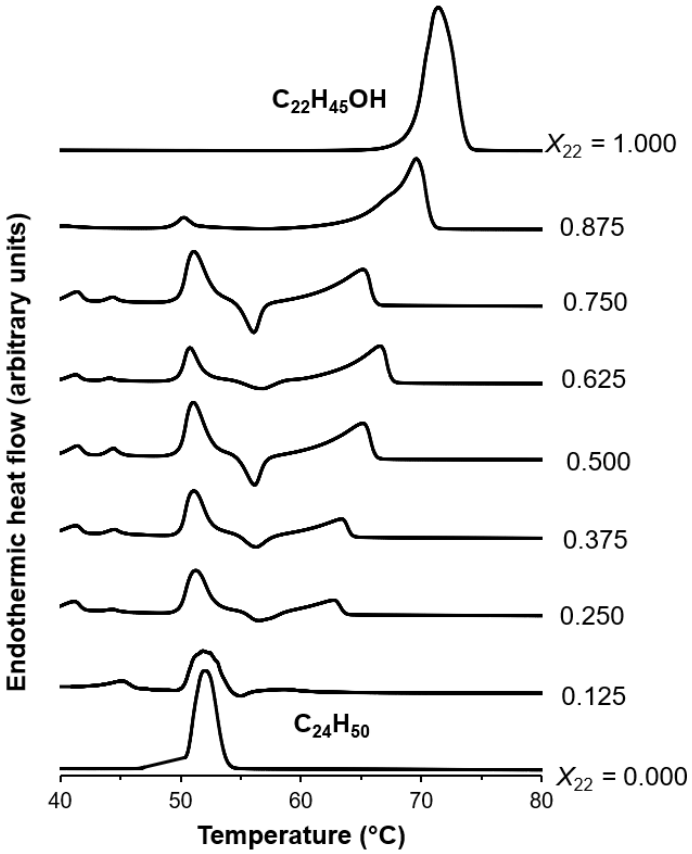

Fig. 5.2 – DSC heating scans for binary mixtures of $C_{24}H_{50}$ and $C_{22}H_{45}OH$ obtained at a scanning rate of 5°C min^{-1}. Numbers correspond to the weight fraction of $C_{22}H_{45}OH$ in the sample.

The onset of melting and melting completion temperatures from the heating thermogram was used to construct the binary phase diagram (Fig. 5.3). The upper curve corresponds to the liquidus line, above which the wax mixture is completely an isotropic liquid. A potential eutectic point exists between 67.5-82.5 weight % of $C_{22}H_{45}OH$. Between weight fractions of 0-75 wt. % $C_{22}H_{45}OH$, the mixture remains solid below ~50°C. Below this solidus line, the two components are present as separate crystalline phases, with *n*-tetracosane exhibiting triclinic rotator phase and 1-docosanol exhibiting orthorhombic symmetry. Between the solidus and liquidus lines exists a regime where the two components exhibit phase transitions. At high temperatures, *n*-alkanes (particularly even numbered alkanes) are known to transition from their low temperature triclinic phase into the high-temperature hexagonal rotator phase (Chazhengina et al., 2003). In the transition phase of binary mixtures of long chain alcohols and alkanes, there may exist eutectic points where all phases occur equally. Fagerström et al. (2013) observed a eutectic point for a

binary phase diagram of dotriacontane ($C_{32}H_{66}$) and 1-docosanol ($C_{22}H_{45}OH$) at 40% 1-docosanol by weight. Conversely, in a phase diagram of 1-tetradecanol ($C_{24}H_{29}OH$) and 1-octadecanol ($C_{18}H_{39}OH$) there was no observed eutectic transition between the solidus and liquidus phase transitions (Carreto et al., 2002). In this intermediate regime of the phase diagram, no eutectic transition is observed, which may be due to insufficient sampling along the composition axis. Thus, the two components exist as independent solid crystals with some mixing in the liquid phase. Only at weight fractions greater than 75% does the onset of melting significantly shift towards the melting temperature of 1-docosanol. Thus, it is readily evident how changes in wax composition can result in notable shifts in phase behavior.

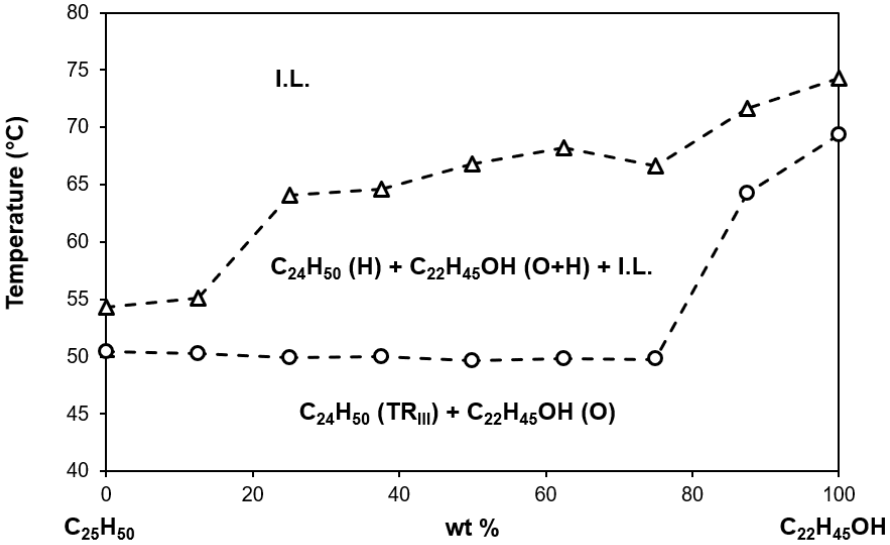

Fig. 5.3 – Phase diagram obtained for the $C_{24}H_{50}$ + $C_{22}H_{45}OH$ binary wax mixture. Points are experimentally obtained from the onset of melting (circles) and melting completion temperatures (triangles) observed from endothermic heating thermograms. Dashed lines indicate the solidus (bottom) and liquidus (top) transitions. I.L. – isotropic liquid; O – orthorhombic crystalline phase; H – hexagonal crystalline rotator phase; T_{RIII} – triclinic crystalline rotator phase.

While the anisotropy of the waxes was found to significantly impede diffusion through the cuticle, the extent to which individual crystalline phases was not thoroughly examined. As observed from the thermograms of petunia petal waxes, naturally occurring thermal shifts may result in changes in solid phase behavior. While binary mixtures of *n*-tetracosane and 1-docosanol exhibit a high degree of crystallinity (> 90% relative crystallinity), the phase behavior can shift with changes in their relative proportions. Between pure *n*-tetracosane and 1-docosanol, the

melting temperature can shift from 54 to 74°C. While outdoor temperatures do not reach this range, melting and crystallization temperatures are indicative of the physical state of a mixture at any given temperature. In Chapter 4, diffusion coefficients were calculated at 25°C for multiple wax mixtures, including binary compositions of *n*-tetracosane and 1-docosanol. When observing the diffusivity of VOCs in binary wax mixtures with respect to melting temperature T_m, it is evident that the physical state can affect diffusion well below the actual phase transition point (Fig. 5.4). Lower molecular weight VOCs (benzaldehyde, 2-phenylethanol, methylbenzoate) can experience up to 4-fold greater diffusion in waxes with lower melting temperatures. Even though binary mixtures of $C_{24}H_{50}$ and $C_{22}H_{45}OH$ exhibit a high degree of aliphatic crystallinity at 25°C, the state of the wax crystals can differ based on their intermolecular vibrations. This trend was not observed for water molecules, which were insensitive to changes in wax melting temperature. Water diffusion is thus more likely dependent on the absolute crystallinity and hydrophobicity of the cuticle, rather than the vibrational motions of the wax.

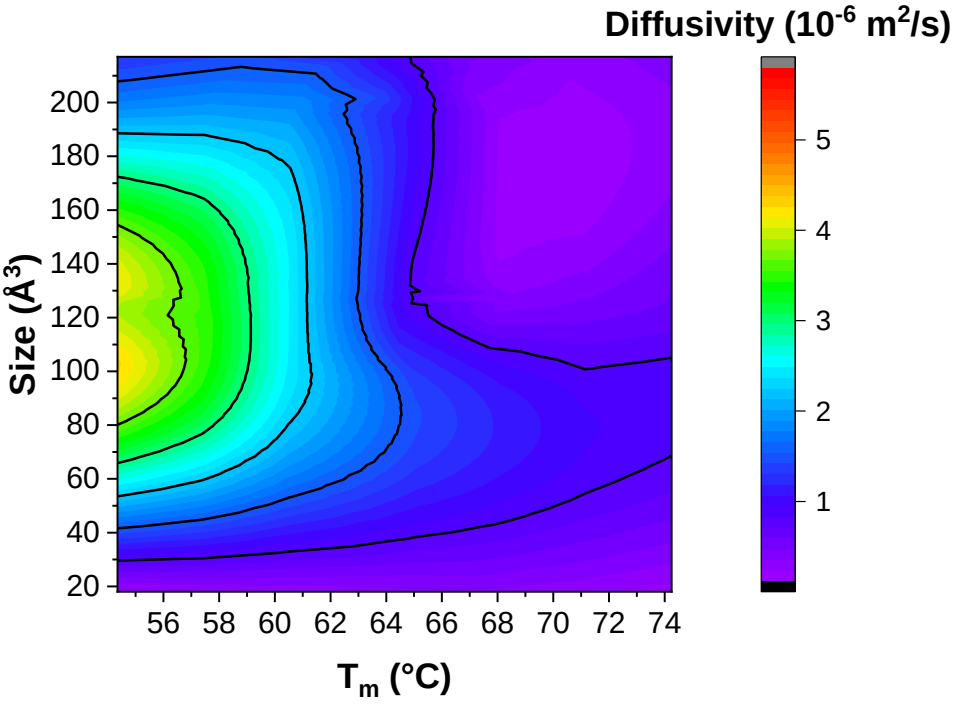

Fig. 5.4 – Diffusivity of compounds with respect to melting temperature T_m. Diffusion coefficients are obtained from molecular dynamics NPT simulations of VOCs and water in binary mixtures of $C_{24}H_{50}$ and $C_{22}H_{45}OH$ at 298 K and 1 bar.

5.4.3 Ternary ($C_{24}H_{50}$ + $C_{22}H_{45}OH$ + $C_{17}H_{34}O_2$) phase diagrams

While shifts in phase behavior were readily observed in binary wax mixtures, discerning the phase transitions in more complex systems is more conducive towards understanding the physical state of plant cuticles. Heating thermograms of pure components typically exhibit a single endothermic peak corresponding to the solid-liquid phase transition. However, heating binary mixtures can exhibit two endothermic peaks, corresponding to the melting of the individual components, and the position of these peaks can shift based on the thermodynamics of mixing. In Chapter 3, statistical analysis of infrared spectral data was used to predict a ternary wax mixture representing the physical characteristics of petunia petal cuticles. Shifts in phase behavior are apparent from the heating thermogram of the model cuticle (Fig. 5.5). The amorphous wax component 3-methylbutyl dodecanoate ($C_{17}H_{34}O_2$) is a liquid well below room temperature, and the first endothermic peak is observed at -15.1°C. The peak associated with the phase transition of $C_{24}H_{50}$ shifts from 53.4 to 47°C, indicative of how the solid phase can be readily affected by compositional changes.

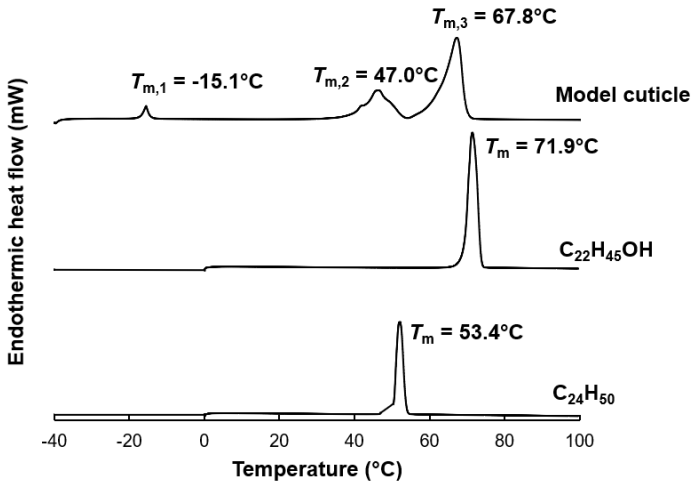

Fig. 5.5 – Heating thermogram of the model cuticle of composition 26.8, 51.7, 21.4% $C_{24}H_{50}$, $C_{22}H_{45}OH$, $C_{17}H_{34}O_2$ obtained at a scanning rate of 5°C min^{-1}. Thermograms for $C_{24}H_{50}$ and $C_{22}H_{45}OH$ are provided as reference.

DSC measurements were conducted for multiple ternary mixtures of the model system to obtain transition shifts, crystallization, and melting temperatures. The thermal behavior of the ternary system (T-*xyz*) demonstrates how the physical phase behavior shifts with composition (Fig. 5.6). Waxes enriched with $C_{17}H_{34}O_2$ have a significant portion of waxes that are liquid below room

temperature (Fig. 5.6a), which in turn lowers the solid-solid transition state (Fig. 5.6b). While most of the waxes found in this mixture still exhibit crystallinity, the transition between orthorhombic/triclinic (RI rotator phase) to the hexagonal (RII rotator phase) results in crystals of greater flexibility and rotational degree of freedom. The high melting point of $C_{22}H_{45}OH$ can measurably increase the liquid transition state for wax mixtures, even at relatively low abundance (Fig. 5.6c). Based on the thermal transitions, schematic ternary phase diagrams were produced based on the measurements of transition, crystallization, and melting temperatures (Fig. 5.7).

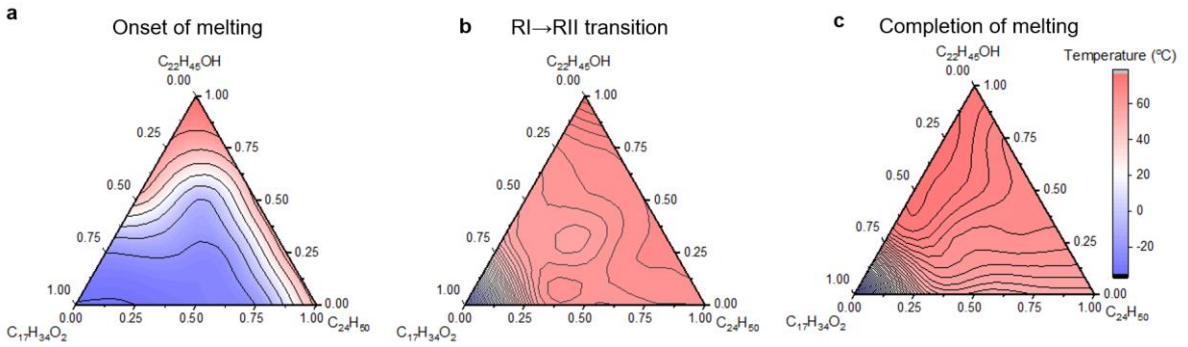

Fig. 5.6 – Ternary thermal phase contour plots for the $C_{24}H_{50}$ + $C_{22}H_{45}OH$ + $C_{17}H_{34}O_2$ wax system. (a) Onset of melting temperature obtained from heating thermograms of ternary wax mixtures. (b) The transition temperature obtained from cooling thermograms of ternary wax mixtures. RI - primary low temperature solid crystalline phase, RII – metastable high temperature hexagonal rotator phase. (c) Completion of melting temperature obtained from heating thermograms of ternary wax mixtures.

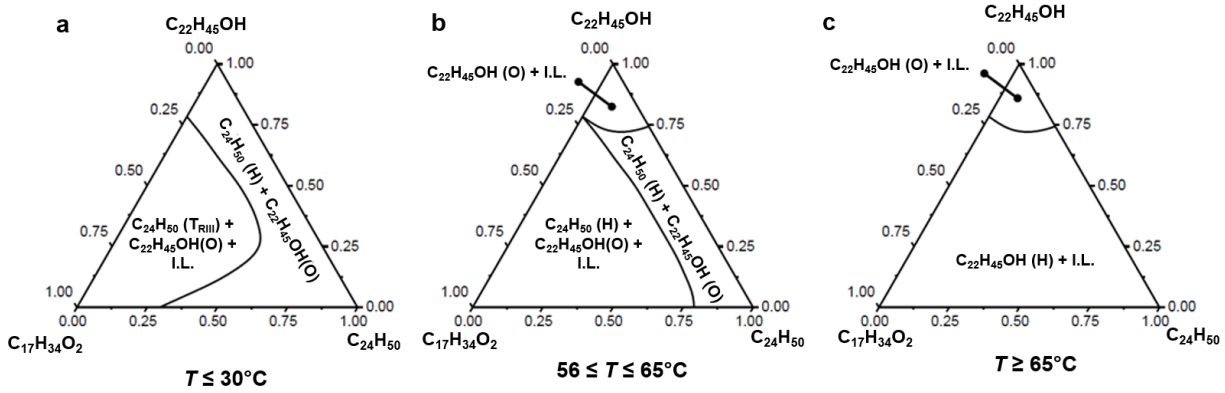

Fig. 5.7 – Schematic ternary phase diagrams for the $C_{24}H_{50}$ + $C_{22}H_{45}OH$ + $C_{17}H_{34}O_2$ wax system at (a) <30°C, the lower-bound solidus line, (b) at ~56°C, the approximate phase transition temperature between RI→RII crystalline rotator phase, and (c) > 65°C, the temperature where $C_{24}H_{50}$ has completed melting in mixtures.

As observed from the melting behavior of ternary phase waxes, the change in phase (RI→RII) transition is dependent on composition (Fig. 5.6b). While waxes may be highly crystalline under ambient conditions, some compositions of waxes may be more sensitive to fluctuations in temperatures more than others. Indeed, waxes enriched with $C_{17}H_{34}O_2$ are found to experience melting with lesser changes in temperature (Fig. 5.6c). It becomes crucial to study the mixing properties of wax compounds in cuticles to determine how thermal fluctuations can effect the fluidity of the cuticle.

5.4.4 Thermal effects on cuticle structure and diffusion

To test the effect of temperature on the diffusion coefficients of compounds in the model cuticle, NPT molecular dynamics simulations were performed between 5-45°C, a range of temperature that is reflective of global climate patterns. The model cuticle does not experience complete melting below 47°C (Fig. 5.5), thus, the physical state of the wax is mostly solid in this range of temperatures. As expected from the measurement of thermal transitions using DSC, the simulated XRD spectra of the model system exhibits orthorhombic symmetry between 5-45°C (Fig. 5.8a). However, at the highest temperature there is some observed decrease in the (00*l*)-peaks at low diffraction angles, suggesting some decrease in the crystalline layer order. Additionally, there is a shift in the (110)-peaks between samples, indicating increases in the gap width between crystalline unit cells. Indeed, with respect to temperature, the maximal d-spacing was found to increase linearly (Fig. 5.8b). The distinct layer order is readily observed for waxes at low temperature (Fig. 5.9a). As temperature increases, wax compounds deviate from linear ordering, which can result in decreased anisotropy. Bends in the methylene chains also result in shifts in the gap spacing, as was observed in the simulated XRD patterns (Fig. 5.9b).

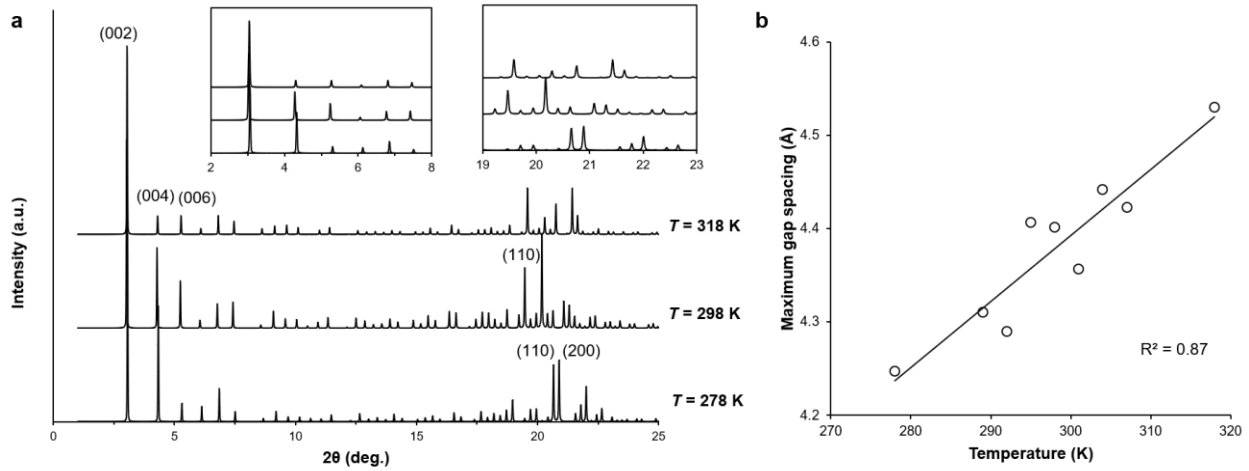

Fig. 5.8 – Crystallinity of the model cuticle with respect to temperature. (a) Simulated XRD spectra for the model cuticle obtained after 10 ns of equilibration at NPT conditions at 278, 298 and 318 K. Inset plots show the series of (00*l*)-peaks and (*hk*0)-peaks at low and high diffraction angles, respectively. (b) Maximum d-spacing between crystalline unit cells as a function of temperature. Spacing is obtained directly from (110)-peaks from simulated XRD spectra for simulated wax structures at respective temperatures.

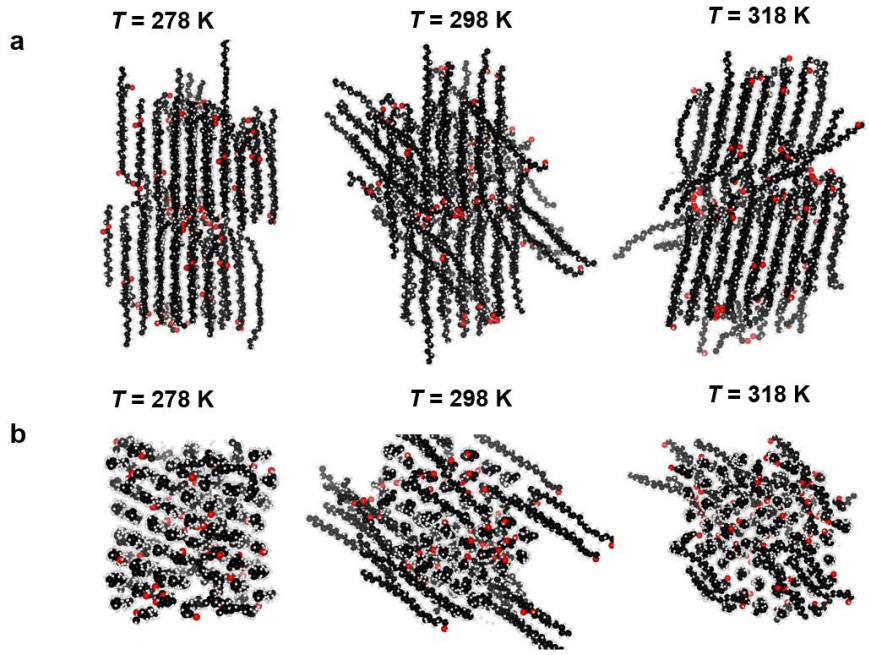

Fig. 5.9 – Structures of the model cuticle after 10 ns NPT equilibration at 278, 298, and 318 K. (a) Orthographic side view of the cuticle. (b) Orthographic top view of the cuticle.

Despite the observed change in unit cell layer order and spacing, measurement of the time-averaged carbon-carbon pair distribution function did not display any major changes in the wax chain elongation (Fig. 5.10). The broad peak centered at a separation of 5.0 Å corresponding to

successive trans-trans dihedrals did not decrease significantly between 278-318 K, indicative of an elongated structure. Despite any shifts in lattice symmetry, the structure of the wax remains orthorhombic with a long length axis.

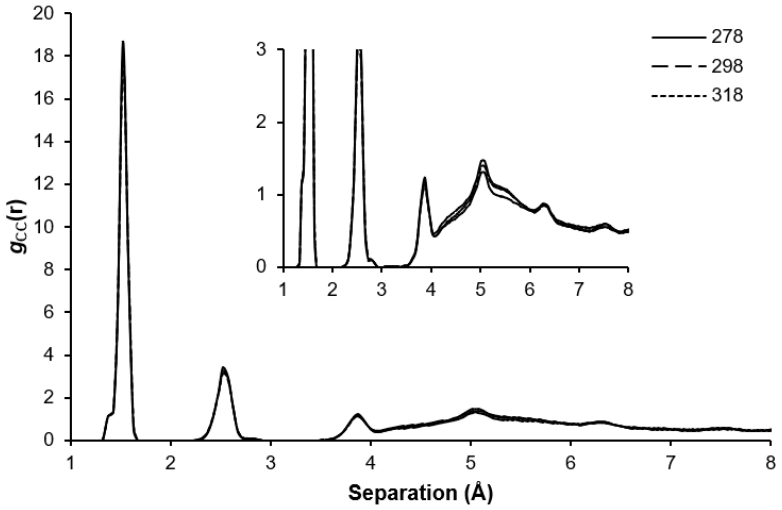

Fig. 5.10 – Radial distribution functions for carbon-carbon pairs ($g_{C\text{-}C}$) obtained for the model cuticle after NPT equilibration at 278, 298, and 318 K.

Over the MD simulations for the model cuticle, the displacement of volatile scent and water molecules was observed at various temperatures (Fig. 5.11). The distance walked by compounds was greater at higher temperatures. At 298 K and lower, the displacement of compounds was subdued, primarily due to the anisotropy of the waxes. However, at 318 K, the displacement drastically increased despite the significant crystallinity still observed during the simulation. Increase in diffusion may be attributed to the enhanced motion of the individual compounds due to the increase in system kinetic energy, however, the methylene chains themselves are likely vibrating with greater frequency to increase the voids for which compounds can explore.

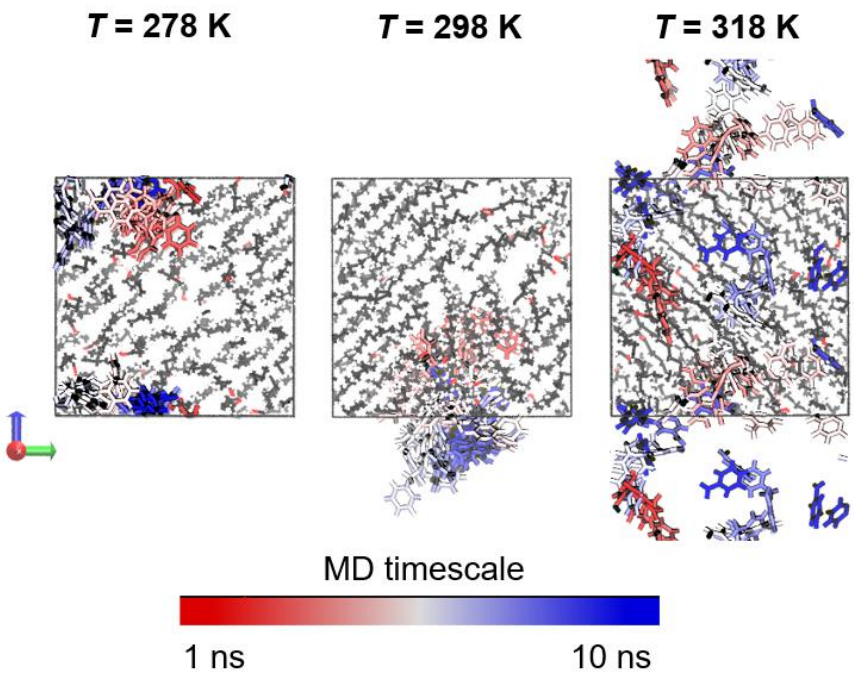

Fig. 5.11 – Diffusive walks for benzaldehyde in the model cuticle at 278, 298, and 318 K. Displacement is shown in color from 1:0.2:10 ns.

The diffusion coefficients for all compounds are temperature-dependent based on the Arrhenius equation:

$$D = D_0 \exp\left(\frac{-E_a}{RT}\right) \tag{5.1}$$

Where E_a is the activation energy, R is the universal gas constant, T is the temperature, and D_0 is the temperature-dependent pre-exponential term with the units of diffusivity. Between 278 to 318 K, diffusion coefficients increased between 4 to 33-fold, indicating that VOC emissions are temperature-dependent. Linearizing equation 5.1 allows for the determination of the activation energy (Fig. 5.12). From the Arrhenius plots for all compounds, activation energy was found to vary between 21-73 kJ mol^{-1}. While activation energy values are unmeasured for the petunia VOCs, water temperature-dependent permeance has been measured in isolated cuticles. Riederer (2006) measured water permeance in isolated leaf cuticles from 14 plant species between 10-35°C and obtained values for E_a ranging between 15.2-52.5 kJ mol^{-1}. Between 35-55°C, the range in values for E_a increased to 52.2-117.3 kJ mol^{-1}. Similarly, Schönherr (1979) measured water permeance in *Citrus auratium* L. leaf cuticles between 5-35°C and obtained E_a values ranging from 36-65 kJ

mol^{-1}. Measured activation energy from MD simulations thus falls within a reasonable range for temperature dependent diffusivity obtained experimentally. Overall, activation energy values were similar for VOCs and water, indicating that changes in temperature will produce similar changes in molecular diffusion. Fluctuations in environmental conditions will result in changes in cuticle phase behavior, crystallinity, and permeability. Characterizing the effect of composition and state on the wax physical properties is of great significance for understanding the adaptive role of the cuticle.

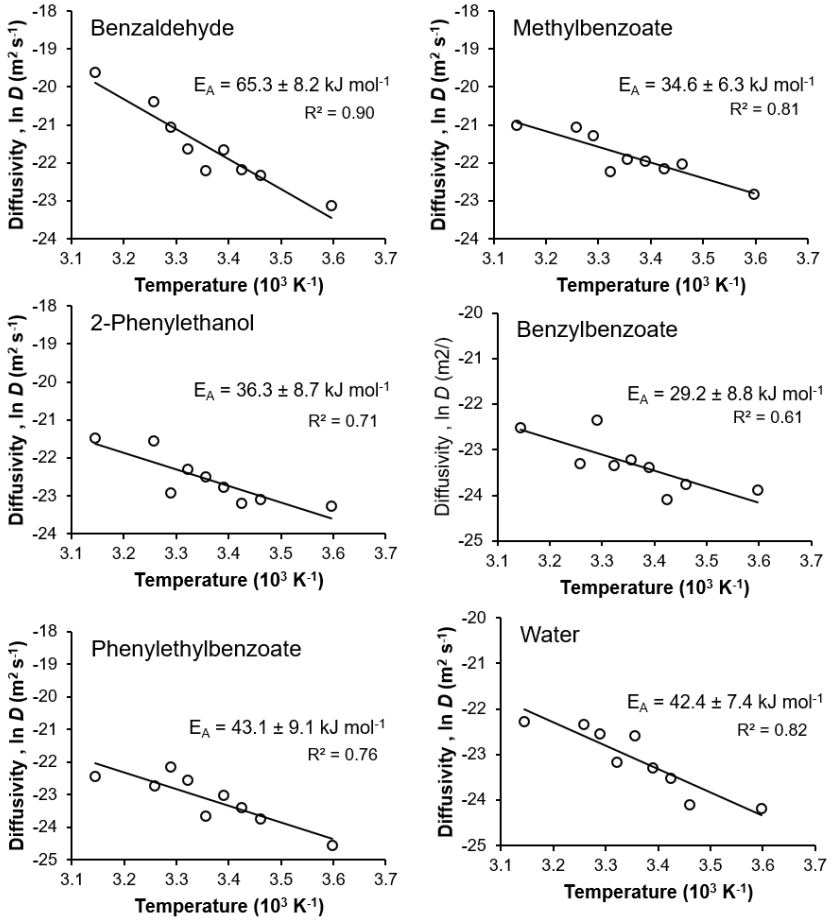

Fig. 5.12 – Arrhenius plots for overall diffusion coefficient in the model cuticle obtained between 5-45°C. Diffusion coefficients were obtained from the mean-square displacements from 10 ns NPT simulations.

5.5 Conclusions

Petunia petal cuticles were found to exhibit a relatively low melting point, which can experience changes in fluidity and variation in its mosaic structure with changes in ambient

conditions. While petal cuticles are highly distributed in chemical composition, the wax components comprising the model system demonstrates significant phase immiscibility. This contributes to temperature ranges where solid-solid phase transitions can occur. While the individual wax components form their own crystalline units, mixing wax components can lead to shifts in phase transitions. Phase diagrams present a reliable way to observe these thermal transitions, but are impossible to construct for real cuticles. Using model wax constituents to replicate the physical state of plant cuticles provides an alternative towards establishing a relationship between composition and phase.

Over the last three chapters, we have exhaustively examined the composition, crystallinity, and phase behavior of petunia petal cuticles and a representative model system. Based on the results for a relatively simple ternary system, it appears that aliphatic wax compounds possess complex mixing characteristics. For extremely complex wax mixtures present in the epicuticles of plants, phase immiscibility likely dominates the physical state. While individual components can have high melting points well above that of temperatures a plant cuticle will be exposed to, increasing amounts of fluidic waxes at ambient temperatures can result in shifts in phase transitions. Cuticles from *Citrus auratium* L. leaves (Reynhardt and Riederer, 1991) and *Hordeum vulgare* L. leaves (Schreiber et al., 2007) were found to have waxes with coexisting crystalline and fluid phases at ambient temperatures. Daily and seasonal weather variations thus likely affect the phase properties of the cuticle, which in turn can influence the permeance across the waxes.Varying temperature demonstrate a significant increase in the diffusivity of VOCs and water through the model wax, attributed in part to changes in cuticle crystalline lattice symmetry and increased methylene chain vibrations. To what extent plants have adapted their cuticle phase properties to their environment is unknown, and whether plants can adapt to rapidly shifting ecosystems and atmospheric conditions are yet to be determined.

5.6 Acknowledgements

This work was supported by grant IOS-1655438 from the National Science Foundation awarded to Dr. Natalia Dudareva and Dr. John A. Morgan. I would like to thank Dr. Brett Savoie for his assistance with the molecular dynamics framework and access to computational resources to carry out simulations. I would also like to thank the P.O.W.E.R. Lab (Davidson School of

Chemical Engineering, Purdue University) group members and Dr. Bryan Boudouris for training and access to the TA Q-20 Differential Scanning Calorimeter.

5.7 References

Baker EA. (1974) The influence of environment on leaf wax development in *Beassica oleracea* var. *gemmifera*. *New Phytologist, 73,* 955-66

Barnes JD., Percy KE., Paul ND., Jones P., McLaughin CK., Mullineaux PM., Creissen G, Wellburn AR. (1996) The influence of UV-B radiation on the physiochemical nature of tobacco (*Nicotiana tabacum L.*) leaf surfaces. *Journal of Experimental Botany, 47,* 99-109

Carreto L., Almeida AR., Fernandes AC., Vaz WLC. (2002) Thermotropic Mesomorphism of a Model System for the Plant Epicuticular Wax Layer. *Biophysical Journal*, *82* (1), 530-40

Carreto L., Almeida AR., Fernandes AC., Vaz WLC. (2002) Thermotropic Mesomorphism of a Model System for the Plant Epicuticular Wax Layer. *Biophysical Journal*, *82* (1), 530-40

Chazhengina SY., Kotelnikova EN., Filippova IV., Filatov SK. (2003) Phase transitions of n-alkanes as rotator crystals. *Journal of Molecular Structure*, *647* (1-3), 243-57

Ensikat H. J., Boese M., Mader W., Barthlott W., Koch K. (2006). Crystallinity of plant epicuticular waxes: electron and X-ray diffraction studies. *Chemistry and Physics of Lipids*, *144*, 45–59

Fagerström A., Kocherbitov V., Ruzgas T., Westbye P., Bergström K., Mamontova V., Engblom J. (2013). Characterization of a plant leaf cuticle model wax, phase behavior of model wax-water systems. *Thermochimica Acta, 571,* 42-52

Fagerström A., Kocherbitov V., Westbye P., Bergström K., Arnebrant T., Engblom J. Surfactant softening of plant leaf cuticle model wax – A Differential Scanning Calorimetry (DSC) and Quartz Crystal Microbalance with Dissipation (QCM-D) study. *Journal of Colloid and Interface Science, 426,* 22-30

Goodwin SM, Jenks M (2005) Plant cuticle function as a barrier to water loss. In M Jenks, PM Hasegawa, eds, Plant Abiotic Stress. Blackwell Publishing, Oxford, pp 14-36

Huihui B., Kovalchuk N., Langridge P., Tricker PJ., Lopato S., Borisjuk N. (2017) The impact of drought on wheat leaf cuticle properties. *BMC Plant Biology, 17* (85)

Jeffree CE. (1996) Structure and ontogeny of plant cuticles. In Kerstiens G ed; Plant cuticle: an integrated functional approach. BIOS Scientific publishers, Oxford. pp. 33–82

Jeffree CE. (2006) The fine structure of the plant cuticle. In M Riederer, C Müller, eds, Biology of the Plant Cuticle. Blackwell, Oxford, pp 11-125

Kerstiens G. (1996) Cuticular water permeability and its physiological significance. *Journal of Experimental Botany, 47,* 1813-32

Koch K., Hartmann KD., Schreiber L., Barthlott W., Neinhuis C. (2006) Influences of air humidity during the cultivation of plants on wax chemical composition, morphology and leaf surface wettability. *Environmental and Experimental* Botany, *56,* 1-9

Kosma DK., Bourdenx B., Bernard A., Parsons EP., Lü S., Jérôme J., Jenks MA. (2009) The Impact of Water Deficiency on Leaf Cuticle Lipids of Arabidopsis. *Plant Physiology, 151*, 1918-29

Kovenock M., Swann ALS. (2018) Leaf Trait Acclimation Amplifies Simulated Climate Warming in Response to Elevated Carbon Dioxide. *Global Biogeochemical Cycles, 32* (10), 1437-48

Kuchhal YK, Shukla RN., Biswas AB. (1979) Differential thermal analysis of n-long chain alcohols and corresponding alkoxy ethanols. *Thermochimica Acta*, *31*, 61-70

Martin LB., Rose JK. (2014) There's more than one way to skin a fruit: formation and functions of fruit cuticles. *Journal of Experimental Botany, 65* (16), 4639-51

McClure DW. Nature of the rotational phase transition in paraffin crystals. *The Journal of Chemical Physics, 49,* 1830-39

Pradhan SD., Katti SS., Kulkarni B. (1970) Dielectric properties of n-long chain alcohols, alkoxyethanols and alkoxypropanols. *Indian Journal of Chemistry, 8,* 632-37

Reynhardt EC, Riederer M (1991) Structure and molecular dynamics of the cuticular wax from leaves of *Citrus aurantium L*. *Journal of Physics D: Applied Physics, 24*, 478-86

Reynhardt EC, Riederer M (1994) Structure and molecular dynamics of plant waxes: II. Cuticular waxes from leaves of *Favus sylvatica* L. and *Hordeum vulgare* L. *European Biophysics Journal, 23*, 59-70

Riederer M. (2006) Thermodynamics of the water permeability of plantcuticles: characterization of the polar pathway. *Journal of Experimental Botany*, *57* (12), 2937-42

Riederer M., Schreiber L. (2001). Protecting against water loss: analysis of the barrier properties of plant cuticles. *Journal of Experimental Botany*, *52* (363), 2023-32

Schönherr J., Eckl K., Gruler H. (1979) Water permeability of Plant Cuticles: The Effect of Temperature on Diffusion of Water. *Planta, 147*, 21-6

Schreiber L., Schorn K., Heimburg T. (1997) ^{2}H-NMR studies of cuticular wax isolated from *Hordeum vulgare L.* leaves: identification of amorphous and crystalline wax phases. *European Biophysics Journal, 26,* 371-80

Shephard T., Griffiths DW. (2006) The effects of stress on plant cuticular waxes. *New Phytologist, 171*, 469-99

Watanabe A. (1961) Synthesis and physical properties of normal higher primary alcohols. IV. Thermal and X-ray studies on the polymorphism of the alcohols of even carbon numbers from dodecanol to tetratriacontanol. *Bulletin of the Chemical Society of Japan, 34,* 1728-34

CHAPTER 6. CUTICLE THICKNESS AFFECTS DYNAMICS OF VOLATILE EMISSION FROM PETUNIA FLOWERS INTO THE ATMOSPHERE

6.1 Abstract

The plant cuticle is the final barrier for volatile organic compounds (VOCs) to cross for release to the atmosphere, yet its role in the emission process is poorly understood. Here, using a combination of reverse-genetic and chemical approaches, we demonstrate that the cuticle not only imposes significant resistance to VOC mass transfer, but also serves as a sink for VOCs that protects cells from toxic effects of these hydrophobic compounds. Reduction in cuticle thickness has differential effects on individual VOCs depending on their volatility, and leads to their intracellular redistribution, a shift in mass transfer resistance sources and altered VOC synthesis. These results reveal that the cuticle is not simply a passive diffusion barrier for VOCs to cross but plays a more complex role in the emission process than previously anticipated as an integral member of the overall VOC biosynthetic network.

6.2 Introduction

6.2.1 Genetics of cuticle permeability

In Chapters 3-5, we investigated the effect of wax composition on cuticle crystallinity, phase behavior and diffusion using a model ternary system and found that variation in composition can significantly affect the cuticles physical and transport properties. Based on the Gibbs phase rule, a ternary system with two physical states (liquid and solid) has three degrees of freedom, two being the number of components and one being a state property such as temperature. Over the previous chapters, the composition and temperature were varied to thoroughly investigate volatile organic compound (VOC) diffusion through the cuticle as it pertains the chemical composition. However, cuticles covering the plant epidermis are multicomponent mixtures, with wax components of varying chain-length, functional groups, and branching. Manipulation of only one component in a highly distributed mixture will likely not produce a change that is easily measured by characterization tools such as microscopy, spectroscopy, or X-ray diffraction. Additionally, much of the genetic regulation for the biosynthesis of cuticle components still remains unknown

(Yeats and Rose, 2013), making rational metabolic engineering to induce specific cuticle phenotypes a challenge. However, use of chromosome/primer walking and T-DNA tagging have been used to elucidate gene sequences from plant cuticle mutants and identify many of the biochemical mechanisms governing cuticle development (Goodwin and Jenks, 2005). Using *Arabidopsis thaliana* as a model system for the study of wax and cutin biosynthesis, major progress has been made in deciphering the genetics of plant cuticle mutants (Kunst and Samuels, 2009). Genes relating to different mechanisms such as wax export by *ABCG11*/*12* (Pighin et al., 2004), fatty acid oxidation by *ATT1* (Xiao et al, 2004), cuticle development by *BDG* (Kurdyukov et al., 2006), alkane synthesis by *CER1* (Bourdenx et al., 2011), VLCFA synthesis by *CUT1* (Millar et al, 1999), transcriptional control by *SHN3* (Aharoni et al., 2004) and wax synthesis by *WAX2* (Chen et al., 2003) have been characterized in Arabidopsis.

However, little is known about the proteins that are encoded for by their respective genes or how genetic perturbations affect the cuticle biosynthetic network. As a result, genetic manipulations of plant cuticles often result in phenotypes that are not readily explained by the employed metabolic engineering strategy (Goodwin and Jenks, 2005).

Several studies were conducted to identify how permeability is influenced by changes in the cuticle physicochemical properties. Most studies have investigated permeability of solutes in the isolated cuticles of different plant species and found that factors such as the solute, system temperature, and species of origin significantly impact diffusion (Schönherr, 1976; Schönherr et al., 1984; Riederer and Schreiber, 2001). An advantage to this approach is the sampling of diverse cuticle compositions allowing for measurable changes in permeability. However, with large differences in the distribution of cuticle components across plant species, determining which wax constituents specifically affect the permeability become difficult to discriminate. Genetic manipulations of cuticles presents an alternative strategy; perturbations of a single gene can be induced to observe the effect on cuticle structure and permeability. Sadler et al. (2016) performed radiolabeled water transport assays in the isolated cuticles of six Arabidopsis mutants and found that permeability either stayed the same or increased in the mutants relative to the wild-type control. While the study analyzed the chemical composition of the cuticle mutants, no phase or physical characterization was performed, preventing one from conclusively stating which compositional features contribute to the changes in cuticle structural and transport properties.

The majority of studies on cuticle permeability focused on water loss and transpiration, or the delivery of active ingredients. The effect of the cuticle on VOC emissions is significantly less studied in the literature. Plants lacking stomata or trichomes must release VOCs through the cuticle (Effmert et al., 2006). While we have investigated the effect of VOC diffusion in reconstituted cuticles (Chapter 3) and *in silico* (Chapter 4), these measurements cannot be used to explain any regulatory effect the cuticle plays in the VOC emission network. As mentioned earlier, the role of plant cuticles on VOC emissions has not been experimentally determined in the literature. Numerical models fit to measured emission rates have predicted that diffusion through the cuticle is transport rate-limiting (Niinemets and Reichstein, 2002; Niinemets et al., 2014, Widhalm et al., 2015). On the other hand, analysis of methylbenzoate emissions, internal pools, and cuticle development in snapdragon flowers indicated that the emission rates of methylbenzoate are independent of the cuticle thickness, with the cuticle imparting negligible resistance towards emission (Goodwin et al., 2003). Thus, the question into the role of the cuticle in the VOC emission network remains unresolved. To address this, we will genetically modify *Petunia hybrida* flowers by targeting previously characterized cuticle genes and measure the effect on cuticle composition and VOC emissions in the resultant transformed lines.

6.2.2 Motivations and objectives

VOCs must be emitted from epidermal cells to fulfill functions important to plant reproduction, defense, and fitness. However, the presence of the transport-limiting cuticle is seemingly at odds with the function of VOCs, giving rise into the function of the cuticle with respect to the VOC emission network. Floral cuticles may provide an auxiliary level of regulation over VOC emissions, however, this has yet to be observed in the existing literature. We therefore will use genetic engineering strategies to modify the cuticles of *Petunia hybrida* flowers to observe the effect on the dynamics, amount, and distribution of volatile emissions.

6.3 Materials and methods

6.3.1 Plant materials and growth conditions

Wild-type and transgenic *Petunia hybrida* cv. Mitchell diploid (W115; Ball Seed Co., West Chicago, IL) were grown under standard greenhouse conditions with a light period from 6:00 h to

21:00 h. Both *PhABCG11*-RNAi and *PhABCG12*-RNAi constructs were synthesized by Genscript (Piscataway, NJ). The *PhABCG11*-RNAi construct contained two spliced *PhABCG11* cDNA fragments corresponding to nucleotides 1234-1733 (in sense orientation) and 1234-1533 (in antisense orientation to form a hairpin structure), while *PhABCG12*-RNAi construct included two spliced *PhABCG12* cDNA fragments corresponding to nucleotides 225-724 (in sense orientation) and 225-524 (in antisense orientation), and both constructs were synthesized with flanking AttL1 and *AttL2* sequences. Both the *PhABCG11* and *PhABCG12* constructs were verified to target only the desired genes using the Sol Genomics Network VIGS Tool (http://vigs.solgenomics.net/). Each of the synthetic RNAi fragments was placed under the control of the petal development-specific MYB1 promoter from Japanese morning glory (*Ipomoea nil*) (pDONRG-P4PIR-InMYB1pro vector, a kind gift courtesy of Dr. Y. Oshima) (Azuma et al., 2016) in the binary destination vector R4pGWB5_stop_HSP[41] using the MultiSite Gateway Three-Fragment Vector Construction Kit (Invitrogen, Carlsbad, CA). Transgenic *P. hybrida* plants were obtained via *Argobacterium tumefaciens* (strain GV3101 18 carrying the final *PhABCG11*-RNAi or *PhABCG12*-RNAi constructs) leaf disc transformation using a standard transformation protocol (Horsch et al., 1985).

6.3.2 Cuticular wax extraction and analysis

Protocol is included in Section 3.2.1.2 – Wax extraction and GC-MS analysis.

6.3.3 RNA extraction and qRT-PCR analysis

Sample collection, RNA extraction, and qRT-PCR was carried out as described previously (Klempien et al., 2012) with minor modifications. Briefly, RNA was isolated from petals collected at the indicated developmental stages and times of the day using the Spectrum Plant Total RNA Kit (Sigma-Aldrich, St. Louis, MO, USA). Total RNA (2 µg) was treated by DNase I (Promega, Madison, WI, USA) before reverse transcription to cDNA using a 5x All-In-One RT MasterMix (Applied Biological Materials, Richmond, BC, Canada). Changes in *PhABCG11* and *PhABCG12* expression during flower development were analyzed by qRT-PCR using elongation factor 1-α (EF1-α) as a reference gene36,44. Relative quantification of *PhABCG1*, *PhABCG11*, *PhABCG12*, *PhDAHPS*, *PhEPSPS*, *PhCM1*, *PhCM2*, and *PhODO1* transcripts were performed by qRT-PCR relative to the reference gene *PhUBQ10* (Adebesin et al., 2017; Qian et al., 2019). qRT-PCR data

were analyzed according to the $2^{-\Delta\Delta Ct}$ method (Schmittgen and Livak, 2008). Primers used for qRT-PCR are listed in Table 6.1.

Table 6.1 – Primers used in this work

Primer name	Sequence	Prupose
ABCG11-RNAi-F	5'-TGTGCATCTTTCGTCTTTGGA-3'	Cloning
ABCG11-RNAi-R	5'-TGGGATGTCATTGGGGAGTC-3'	Cloning
ABCG12-RNAi-F	5'-TGGGAAGAAGAGGAGGTTGG-3'	Cloning
ABCG12-RNAi-R	5'-AGACGAGATAACCGTTCTTCCA-3'	Cloning
PhABCG1 qRT F	5'-TGGCGGATTTTTTCGATTAC-3'	qRT-PCR
PhABCG1 qRT R	5'-ACTCGTTCTTGAACATCCCTTCA-3'	qRT-PCR
PhABCG11 qRT F	5'-GACTCCCCAATGACATCCCA-3'	qRT-PCR
PhABCG11 qRT R	5'-TGATATTGCCCCTGGAGTGC-3'	qRT-PCR
PhABCG12 qRT F	5'-TTTCCGTTTGCTGCCAGATC-3'	qRT-PCR
PhABCG12 qRT R	5'-TGTAAACCCCATGCCCCATA-3'	qRT-PCR
PhCM1 qRT F	5'-CCTGCTGTTGAAGAGGCTATCA-3'	qRT-PCR
PhCM1 qRT R	5'-CAGGGTCACCTCCATTTTCTG-3'	qRT-PCR
PhCM2 qRT F	5'-TGCAACTACTGCTGCCTGTGAT-3'	qRT-PCR
PhCM2 qRT R	5'-TCGTCAGAGCAATCCCTGAAT-3'	qRT-PCR
DAHPS qRT F	5'-CAAAGCTCCGTGTGGTCTTAAA-3'	qRT-PCR
DAHPS qRT R	5'-TCCTGGGTGGCTTCCTTCTT-3'	qRT-PCR
EPSPS qRT F	5'-CACCCCACCGGAGAAACTAA-3'	qRT-PCR
EPSPS qRT R	5'-TGACGGGAACATCTGCACAA-3'	qRT-PCR
ODO1-4 qRT F	5'-CCACTCAAGAAAGAAGCAAATCTAAGT -3'	qRT-PCR
ODO1-4 qRT R	5'-TGCCGCTGTGACATTTGTACTC-3'	qRT-PCR
PhUBQ qRT F	5'-GTTAGATTGTCTGCTGTCGATGGT-3'	qRT-PCR
PhUBQ qRT R	5'-AGGAGCCAATTAAAGCACTTATCAA-3'	qRT-PCR
PhEF1-α F	5'-CCTGGTCAAATTGGAAACGG-3'	qRT-PCR
PhEF1-α R	5'-CAGATCGCCTGTCAATCTTGG-3'	qRT-PCR
PhABCG11_frag_F	5'-CTGCCTTTGTCGTGAGCAAC-3'	Absolute qRT-PCR
PhABCG11_frag_R	5'-TCGCCAGGGATCTTTGGAAG-3'	Absolute qRT-PCR
PhABCG12_frag_F	5'-AGAAAGGCTTAACGGGCACT-3'	Absolute qRT-PCR
PhABCG12_frag_R	5'-ACAAAACAGATCACATGCAGCTT-3'	Absolute qRT-PCR

6.3.4 Transmission electron microscopy

Small pieces (1 mm in diameter) of wild type and transgenic petals on day 2 postanthesis were fixed in 2% paraformaldehyde and 2% glutaraldehyde in 0.1 M sodium cacodylate buffer. After primary fixation, samples were rinsed and post-fixed in buffered 1% osmium tetroxide containing 0.8% potassium ferricyanide. Subsequently, samples were dehydrated with a graded series of ethanol, transferred into acetonitrile and embedded in EMbed-812 resin. Thin sections (80 nm) were prepared on a Leica UC6 ultramicrotome and stained with 4% uranyl acetate and lead citrate. Sections were imaged on a FEI Tecnai T12 electron microscope equipped with a tungsten source and operating at 80 kV. Images were acquired in DM4 format on a Gatan Orius SC200 camera and converted to obtain TIFF files. To analyze cuticle thickness in conical epidermal cells from 20 transgenic and WT petals, cuticle thickness shown in TEM images was measured by ImageJ software version 1.52a (Abràmoff et al., 2004).

6.3.5 Cryo-scanning electron microscopy (cryo-SEM)

Wild-type and transgenic petals on day 2 postanthesis were mounted with OCT cryo-sectioning media on a flat specimen holder and cryo fixed by immersion in a nitrogen slush using a Gatan Alto 2500 Cryo-Preparation System (Gatan Inc. Pleasanton, CA). Samples were immersed until liquid nitrogen boiling ceased, and then cryo transferred into the Gatan preparation chamber set at -170°C. Samples were then immediately inserted into the SEM cryo stage set at -90°C to sublimate surface frost and for initial viewing. Once frost free, samples were returned to the cryo-preparation chamber, allowed to cool and halt sublimation before sputter coating with a platinum target with 18 mA for 120 sec at -170°C. Final imaging was done at -140°C with an accelerating voltage of 5 kV and spot size 3 on the Nova Nano 200 SEM (Hillsboro, OR).

6.3.6 Collection and analysis of plant volatiles

Floral volatiles were collected using headspace collections on columns containing 50 mg Poropak Q (80–100 mesh) (Sigma-Aldrich) and analyzed by GC-MS as described previously (Orlova et al., 2006; Adebesin et al., 2017). Briefly, emitted floral volatiles were collected from

detached transgenic and control flowers on day 2 postanthesis from 6 PM to 10 PM. Subsequently, ~280 µL dichloromethane containing 52 nmol of internal standard (naphthalene) was used to elute volatiles from collection columns for GC-MS analysis. Internal pools of volatiles from transgenic and control tissues collected at 22:00 h on day 2 postanthesis were extracted according to 10 and quantified by GC-MS as described previously (Orlova et al., 2006). Briefly, 0.5 g of petal tissue was collected, ground to a fine powder in liquid nitrogen, and internal pools were extracted in 5 mL of dichloromethane containing 52 nmol of internal standard (naphthalene) for 12 h at 4°C with shaking. Samples were concentrated to ~ 200 µL under a stream of nitrogen gas before analysis by GC-MS.

6.3.7 Toluidine blue staining

Toluidine blue staining was performed following published protocol as follows (Tanaka et al., 2004; Li-Beisson et al., 2009). Excised petals of petunia flowers on day 2 postanthesis collected at 3 PM were submerged in 0.05% toluidine blue aqueous solution. Flowers were incubated for 2 or 4 h, as indicated, before imaging.

6.3.8 Water loss measurement

Water loss measurements were carried out according to (Zhang et al., 2005; Wang et al., 2011) with some modifications. 2-day old petunia flowers (3 flowers per replicate) were detached and left in ambient laboratory conditions. The fresh weight of the flowers was recorded at the indicated times over 24 h to obtain total water loss rate.

6.3.9 Propidium iodide staining and confocal laser scanning microscopy

Petals of wild-type and *PhABCG12*-RNAi flowers collected at 3 PM on day 2 postanthesis were stained in propidium iodide solution (10 µg/mL, Invitrogen, Carlsbad, CA) for 1 h with shaking at room temperature. Confocal fluorescence microscopy was performed as described previously (Yanagisawa et al., 2015; Adebesin et al., 2017) with minor modifications. Briefly, propidium iodide-stained samples were excited with a 561-nm laser and images were recorded by a 617/73 emission filter using a Zeiss LSM 880 Upright Confocal system and operated using Zeiss

Efficient Navigation (ZEN)-Black Edition software (Zen 2.3 SP1, Carl Zeiss Inc., Oberkocken, Germany).

6.3.10 Dewaxing of petunia petals

To determine the quantity of volatiles in petunia epicuticular waxes, petals on day 2 postanthesis were rapidly dipped in hexane (< 5 seconds) and then were lightly dried under the fume hood to remove excess hexane. Care was taken to prevent full submersion of petals so that only the adaxial surface of the flower touched the solvent. Hexane pools were independently profiled for volatiles and wax quantity using GC-MS as described above, while dewaxed petals were sampled for VOC internal pools and emissions as described above. Total cuticular volatile fractions were determined according to the formula:

$$\text{Cuticular VOC fraction} = \frac{C_i^{\text{hex}}}{C_i^{\text{total}}}\frac{1}{R} \tag{6.1}$$

where C_i^{hex} is the volatile pool in the hexane fraction, C_i^{total} is the total volatile pool, and R is the fraction of the total wax recovered during the dewaxing.

To test whether dewaxed flowers retained biosynthetic capability, dewaxed wild-type petals were fed with 15 and 150 mM Phe and VOC internal pools and emission were subsequently analyzed between 6 PM and 10 PM. In addition, PAL activity was measured in dewaxed and nondewaxed wild-type petals on day 2 postanthesis as described previously (Kolosova et al., 2001l Maeda et al., 2010), except that assays were adapted to high-performance liquid chromatography (HPLC) detection of cinnamic acid formation from L-Phe. In brief, 100 µl reaction mixture containing protein samples from dewaxed and non-dewaxed petals (5-30 µg), 2 mM L-Phe, and 0.1 M sodium borate (pH 8.8) was incubated at room temperature for 1 h and then terminated by adding 5 µl of 6 N HCl. After centrifugation, 10 µl of the supernatant was analyzed by HPLC equipped with the Agilent Poroshell 120 EC-C18 column (3.0 × 150 mm × 2.7 µm) held at 35°C using an 8-min linear gradient of 5-70% acetonitrile in 0.1% formic acid at a flow rate of 0.4 mL min^{-1}. Cinnamic acid was detected by UV absorbance (equation 6.1) at 270 nm and quantified based on authentic standard. Control assays including (*i*) with all reaction components with boiled

protein extracts; (*ii*) with all reaction components except protein extracts, and (*iii*) with all components except for L-Phe, did not produce cinnamic acid.

6.3.11 Metabolic flux analysis with $^{13}C_6$-phenylanine labeling

Wild-type and *PhABCG12*-RNAi-9 petunia corollas excised from flowers 2 days postanthesis were placed in a cut 1.7-ml eppendorf tube contain 300 µl solution of 150 mM ring-labeled $^{13}C_6$-Phe (Cambridge Isotope Laboratories, Andover, MA). Emitted and internal pools of volatiles were collected between 6 PM -10 PM as described above at 30-, 60-, 120-, and 240-min time points after beginning of feeding and analyzed by GC-MS. Labeled volatiles were identified by M+6 and M+12 (for VOCs with two aromatic rings) shifts in *m/z* and labeling percentage was determined based on the peak areas of labeled and unlabeled volatiles. Metabolic fluxes were calculated by applying mass balances and *in vivo* metabolite labeling profiles as described previously (Boatright et al., 2004). Emission fluxes and time-dependent accumulation of internal pools were estimated using linear regression, with the variances of the estimated slopes calculated using the standard linear regression procedure described previously (Press, 2007). As fluxes are a function of the linear regression and other experimental measurements, flux variances are derived by considering the propagation of errors based on the following equation:

$$\sigma_y^2 = \sum_{i=1}^{n} \sigma_{x_i}^2 \left(\frac{\partial y}{\partial x_i}\right)^2 \qquad (6.2)$$

where $y = f(x_1, \ldots, x_n)$.

6.3.12 Benzaldehyde feeding

Wild-type petunia corollas on day 2 postanthesis were collected at 9 AM and fed with 0 and 15 mM of benzaldehyde for 6 h, as described previously (Adebesin et al., 2017). Mock and benzaldehyde-fed petunia corollas were collected at 3 PM, ground to a fine powder in liquid nitrogen, and used for subsequent RNA extraction, cDNA synthesis, and qRT-PCR analysis as described above.

6.3.13 Calculation of volatile emission factor

Biosynthetic and emission fluxes were estimated from dynamic sampling of volatile internal pools and emissions from detached transgenic and control petunia flowers on day 2 postanthesis from 6 PM to 10 PM. Time-dependent accumulation of volatile internal pools and the rate of emission were estimated using linear regression, with propagation of regression and experimental errors calculated using equation 2. Biosynthetic flux was determined from the mass balance for an individual volatile:

$$\frac{\mathrm{d}C_i}{\mathrm{d}t} = \nu_{\mathrm{syn},i} - \nu_{\mathrm{emi},i} \tag{6.3}$$

where $\nu_{\mathrm{syn},i}$ and $\nu_{\mathrm{emi},i}$ are the biosynthetic and emission fluxes of a volatile compound *i*, respectively. The volatile emission factor (VEF) is the ration between the emission and biosynthesis of a volatile compound:

$$\mathrm{VEF}_i = \frac{\nu_{\mathrm{emi},i}}{\nu_{\mathrm{syn},i}} \tag{6.4}$$

6.3.14 Measurement of flower fresh weight, corolla diameter and corolla fresh weight

Flower fresh weight and corolla diameter of wild type, empty vector control and 3 independent *PhABCG12*-RNAi lines (7, 8 and 9) were measured on 2-day-old detached flowers collected at 6 PM. Corolla fresh weight of all the above lines was recorded at 10 PM for 2-day-old detached flowers after scent collection.

6.3.15 High humidity experiment

To test whether the phenotypic changes in *PhABCG12*-RNAi lines were caused by water stress, 2-month-old wild-type and 3 independent *PhABCG12*-RNAi lines (7, 8 and 9) were moved from standard greenhouse conditions with a normal humidity (< 50%) to a growth chamber with a high relative humidity (75%) and allowed to acclimate for 1 week. Then, 2-day-old flowers were

collected at 6 PM and flower fresh weight was recorded and compared to that of control 2-day-old flowers growing in the standard greenhouse conditions with normal humidity.

6.4 Results and Discussion

6.4.1 Generation of petunia flowers with altered cuticles

Our mathematical modeling of VOC emission predicted that the cuticle is the barrier with the highest resistance that VOCs have to cross to be emitted to the atmosphere (Widhalm et al., 2015). However, the specific role of the cuticle in emission has not been directly experimentally evaluated. To determine whether cuticle of petunia flowers retains VOCs, cuticular waxes were extracted from flowers on day 2 postanthesis, the developmental stage with the highest VOC emission (Colquhoun et al., 2010), by briefly submerging the petals in hexane, and analyzing recovered VOCs by GC-MS. This analysis revealed that cuticle holds 53 ± 4% of total VOC internal pools in wild-type petunia flowers (Fig. 6.1a).

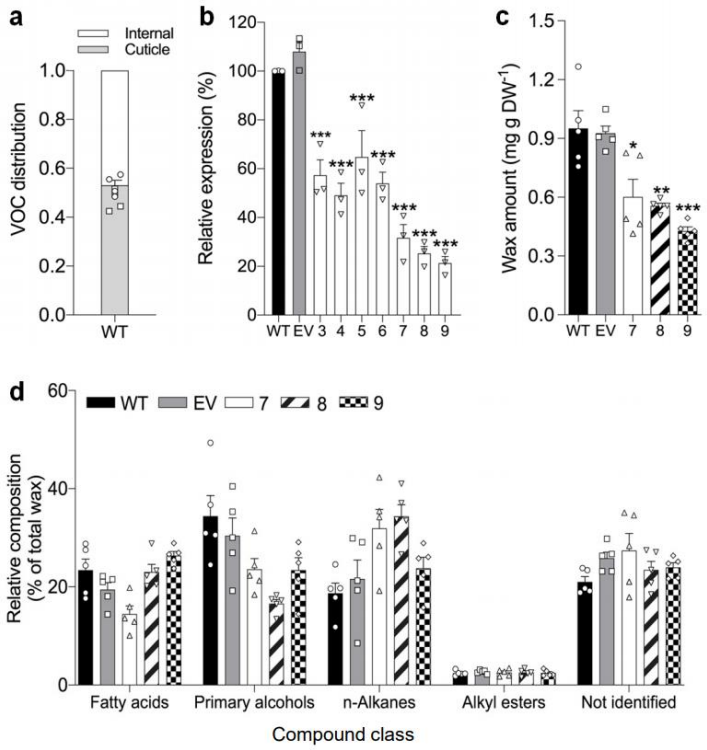

Fig. 6.1 – VOC distribution within cell and effect of *PhABCG12* down-regulation on total wax amount and cuticle composition in petunia flowers. a, Cellular VOC distribution in 2-day-old wild-type petunia flowers. Data are means ± S.E. (n = 4 biological replicates). b, *PhABCG12* mRNA levels determined by qRT-PCR in buds (3-4 cm) of wild type (WT), empty vector (EV) control and seven independent *PhABCG12*-RNAi lines. Data are shown as a percentage of *PhABCG12* expression in WT set as 100% and are presented as means ± S.E. (n = 3 biological replicates). *** $P < 0.001$ by Student's *t*-test. c, Total wax levels in 2-day-old flowers of WT, EV control and the three transgenic lines with greatest reduction in PhABCG12 expression (lines 7, 8 and 9). d, Wax composition by major constituent classes: acids, primary alcohols, n-alkanes, and alkyl esters in in 2-day-old flowers of WT, EV control and transgenic lines 7, 8, and 9. In c and d, data are means ± S.E. (n = 5). *, $P < 0.05$; **, $P < 0.01$; ***, $P < 0.001$ by Student's t-test.

Previous studies have shown that cuticle formation can be altered via perturbing transport of wax precursors, as they have to move from the site of their biosynthesis at the endoplasmic reticulum across the plasma membrane and through cell wall to be deposited at the cell surface (Javelle et al., 2010). Although some steps of this export process remain poorly understood, it is well established that transport of cuticular wax monomers across the plasma membrane requires ABC transporters (reviewed in Yeats and Rose (2013)). In Arabidopsis, loss-of-function mutants of any of three closely related transporters, AtABCG11, AtABCG12, or AtABCG13, result in cuticle-deficient phenotypes (Pighin et al., 2004; Bird et al., 2007; Luo et al., 2007; McFarlane et

al., 2010; Panikashvili et al., 2010; Panikashvili et al., 2011). While investigating transport of VOCs across the plasma membrane, we identified 17 ABCG transporters expressed in petunia flowers, two of which formed a clade with the three aforementioned Arabidopsis wax transporters (Adebesin et al., 2017). These two putative petunia wax transporters, Ph9795 and Ph13519 are designated as PhABCG11 and PhABCG12, respectively, as they exhibit 78%/86% and 66%/80% identity/similarity to the corresponding AtABCG11 and AtABCG12. Expression of *PhABCG12* was 53% higher than *PhABCG11*, and mRNA levels of both genes were developmentally regulated, with highest expression occurring early in flower development, consistent with the timing of cuticle formation in flowers (Fig. 6.2). Expression of both *PhABCG11* and *PhABCG12* did not follow the developmental profile of scent biosynthetic genes, which have the highest levels on day 2 postanthesis (Colquhoun et al., 2010; Adebesin et al., 2017), and were 12- and 20-fold lower, respectively, than *PhABCG1* VOC transporter at that developmental stage (Adebesin et al., 2017). Taken together, these results suggested that these two genes are promising targets for experimental perturbation of cuticle properties for subsequent analysis of the role of cuticle in VOC emission.

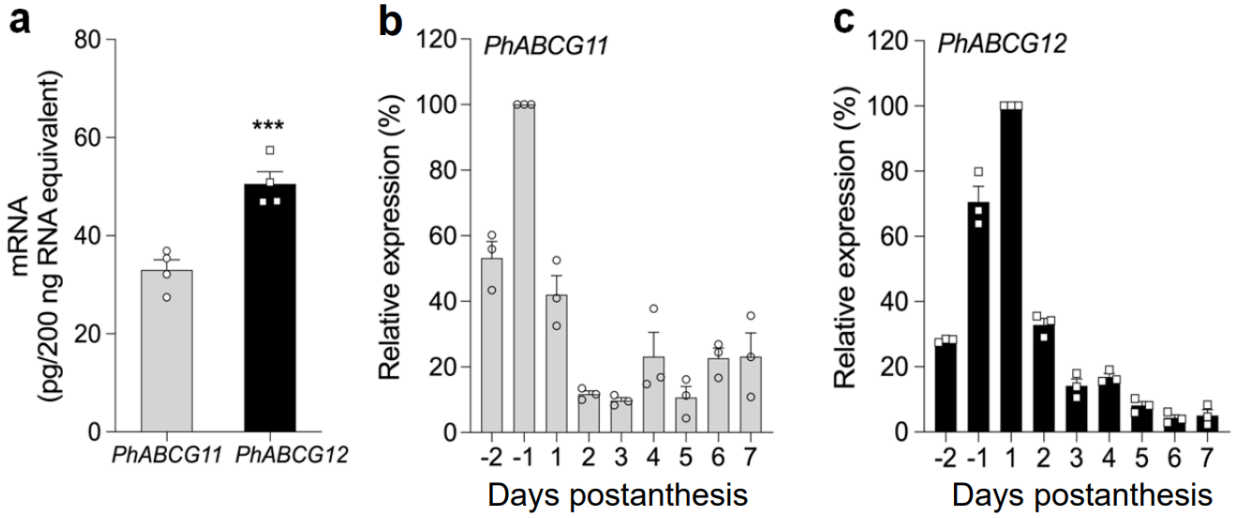

Fig. 6.2 – Expression profiles of *PhABCG11* and *PhABCG12* in wild-type petunia flowers. a, Absolute mRNA levels of PhABCG11 and PhABCG12 were analysed by qRT-PCR in corollas of buds (3-4 cm) at 3:00 PM and are shown as pg/200 ng total RNA. Data are means ± S.E. (n = 4 biological replicates). ***, $P < 0.005$ by Student's t-test. b, Developmental *PhABCG11* expression profile in corollas from day -2 (buds, 2 cm) through day 7 post-anthesis determined at 3 PM. c, Developmental *PhABCG12* expression profile in corollas from day -2 (buds, 2 cm) through day 7 post-anthesis determined at 3 PM. Transcripts levels in b and c were determined by qRT-PCR and presented relative to the day of highest expression, set as 100%. Data are means ± S.E. (n = 3 biological replicates).

Therefore, we attempted to downregulate expression of each gene using RNAi approach under the control of the petal-specific *MYB1* promoter from Japanese morning glory (Azuma et al., 2016). No transgenic lines with *PhABCG11* downregulation were recovered, consistent with previous reports on the Arabidopsis *atabcg11* mutants, which exhibited very severe phenotypes including dwarfism, gametophyte sterility, and organ fusion (reviewed in Do et al. (2018)). However, seven transgenic lines with varying levels of *PhABCG12* suppression were obtained, and three lines, *PhABCG12- 7*, *-8* and *-9*, with the greatest reduction in transcript levels (68-79%) were selected for further analysis (Fig. 6.1b). Quantification of cuticular wax accumulation in these lines revealed that total wax loads were reduced by 35-55% relative to wild-type and empty vector control (Fig. 6.1c), while the chemical composition and the ratios between wax constituents were not significantly altered (Fig. 6.1d and Fig. 6.3). The flowers of transgenic plants displayed visible changes relative to wild-type and empty vector control (Fig. 6.4a upper panel). They were smaller, had less smooth flower surface, reduced flower fresh weight and more translucent petals (Fig. 6.4a and Fig. 6.5). Several independent approaches were used to assess changes in the cuticle, including transmission electron microscopy (TEM), cryo-scanning electron microscopy (cryo SEM), and toluidine blue (TB) staining. Analysis of conical epidermal cells by TEM revealed a 22% reduction in cuticle thickness in petals of *PhABCG12-9*, the line with greatest reduction in *PhABCG12* expression, relative to wild type (Figs. 6.4b, c, and Fig. 6.6). As cuticular defects can be detected by increased permeability to TB (Tanaka et al., 2004), staining was performed. Indeed, petals from transgenic lines, but not wild-type or empty vector control, exhibited Class II staining (Tanaka et al., 2004) with TB after 4 h of incubation (Fig. 6.4a lower panel). Examination of flower petals by cryo-SEM revealed that some epidermal cells lost their conical shape and became flattened (Fig. 6.7). This morphological change was not uniform across the petal surface but affected approximately 23% of the petal area (Fig. 6.8) and may be a result of petal-to-petal fusion prior to flower opening, in agreement with the established role of cuticle in preventing organ fusion during development (Luo et al., 2007; Panikashvili et al., 2011). In general, the plant cuticle protects organs/tissues from excessive water loss (Bernard and Joubès, 2013). Consistent with reduction in cuticle thickness, transgenic *PhABCG12* RNAi flowers lost water faster than control plants (Fig. 6.9). However, observed phenotypic changes (Fig. 6.4a and Fig. 6.5) were not entirely attributable to enhanced water loss, as growth of transgenic plants in growth chamber with higher relative humidity did not recover to the wild type phenotype (Fig. 6.10). Overall, these results demonstrate

that *PhABGC12* RNAi petunia lines have altered cuticle thickness, allowing analysis of the effect of cuticle on VOC emission.

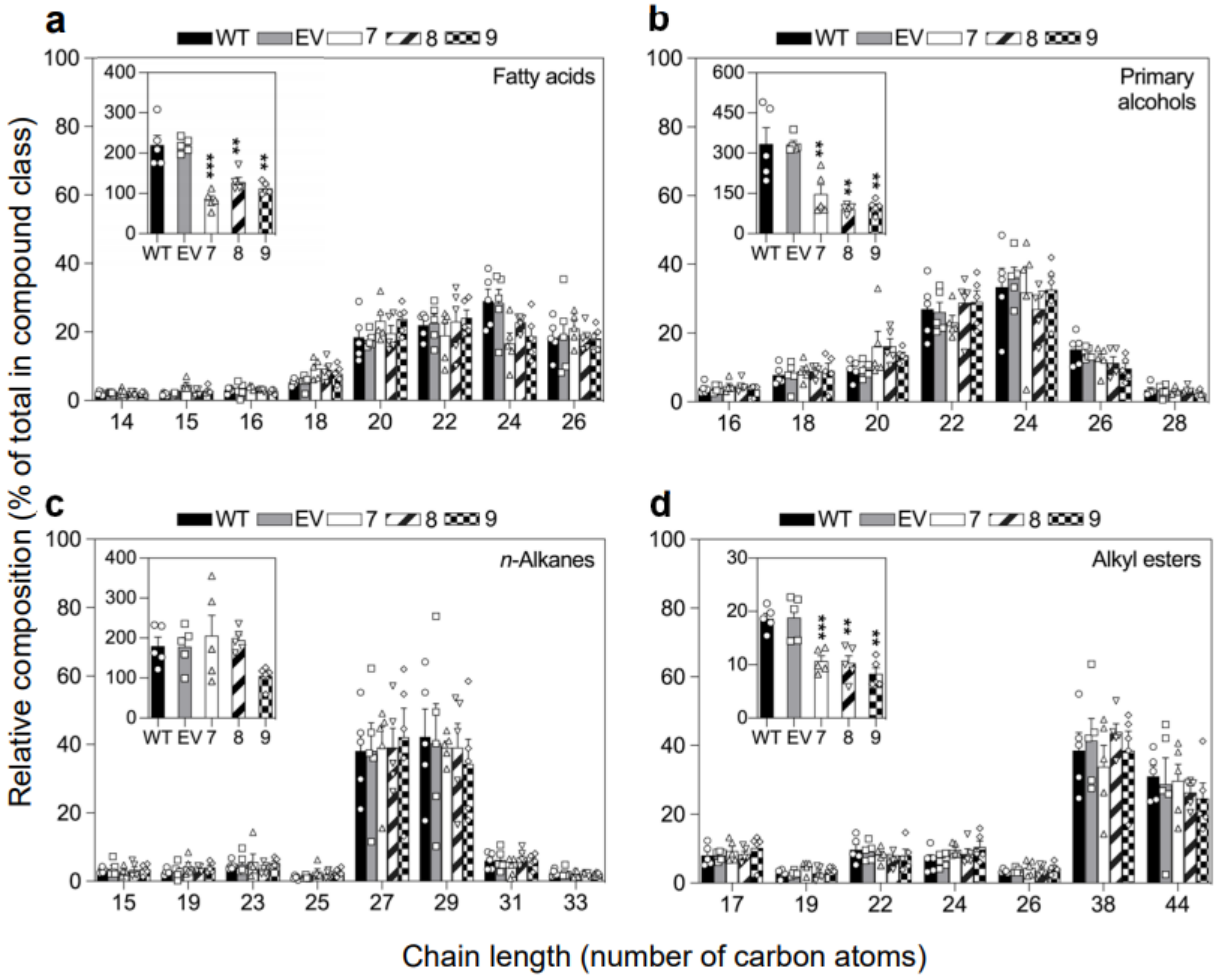

Fig. 6.3 – Effect of *PhABCG12* downregulation on individual wax constituents in cuticles of 2-day-old petunia petals. Relative amounts of each wax constituent are presented as a percentage of the total in their respective compound class. The major constituents identified are classified as (a) saturated fatty acids, (b) primary alcohols, (c) n-alkanes, and (d) alkyl esters. Horizontal axis represents the chain length (number of carbon atoms) for each constituent. Inset graphs show total amount of each class (µg·g DW^{-1}). Data are means ± S.E. (n = 5 biological replicates), **, $P < 0.01$; ***, $P < 0.001$ by Student's *t*-test.

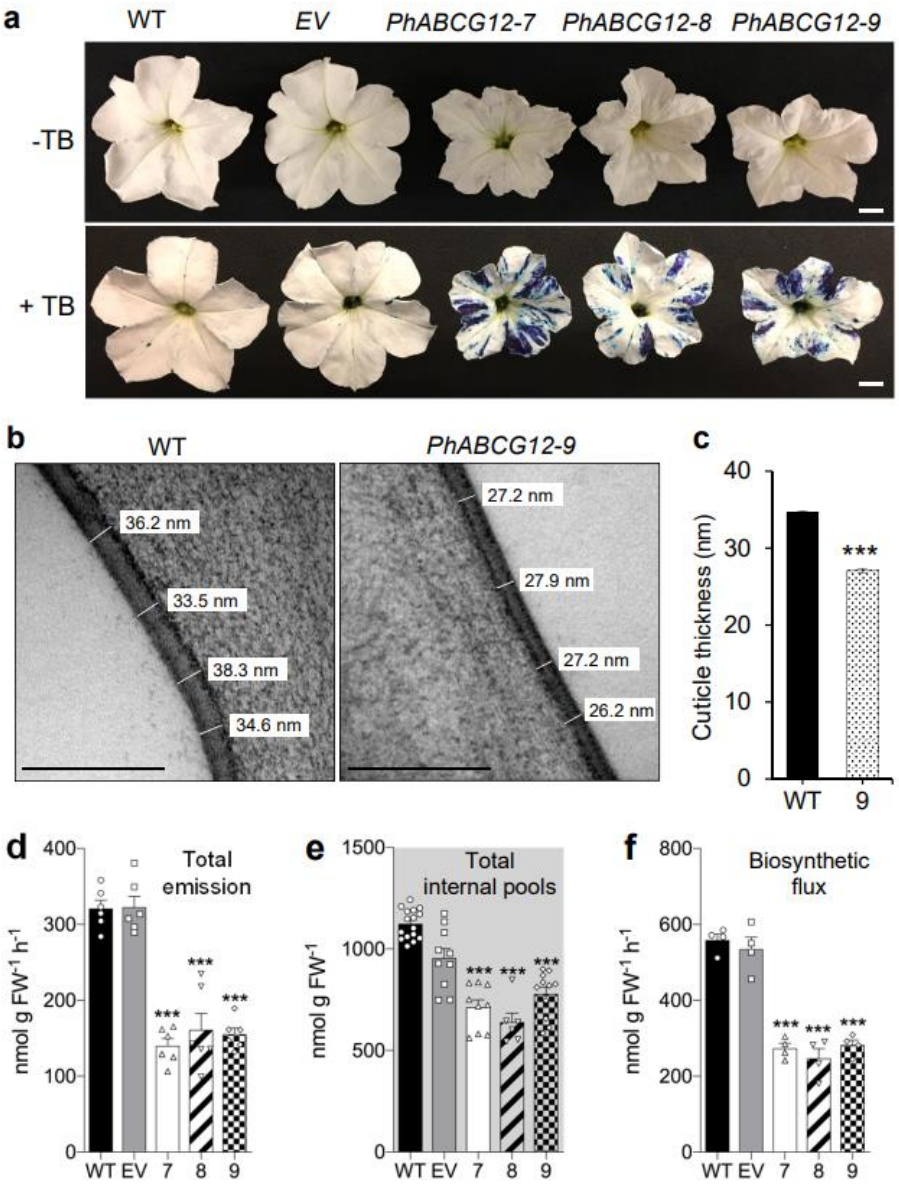

Fig. 6.4 – Effect of *PhABCG12* down-regulation on flower phenotype, cuticle properties and scent network in petunia flowers. a, Representative 2-day-old petunia flowers from WT, EV control and three independent *PhABCG12*-RNAi lines (7, 8 and 9) before (upper panel) and 4 h after staining with toluidine blue (lower panel). Scale bar, 1 cm. b, Representative transmission electron microscopy (TEM) pictures of cross-sections of epidermal cells from adaxial petal surface of 2-day-old WT and *PhABCG12*-9 flowers. Scale bar, 200 nm. c, Cuticle thickness measured in conical epidermal cells of 2-day-old WT and *PhABCG12*-9 flowers as shown in b. Data are means ± S.E. (n = 675 measurements for each). ***, $P < 0.001$ by Student's *t*-test. Total emissions (d), total internal pools (e) and biosynthetic fluxes (f) in 2-day-old flowers from WT, EV control and three *PhABCG12*-RNAi lines 7, 8 and 9. Data are means ± S.E. (n = 6 biological replicates in d; n = 6 - 16 biological replicates in e; and n = 4 biological replicates in f). ***, $P < 0.001$ by Student's *t*-test.

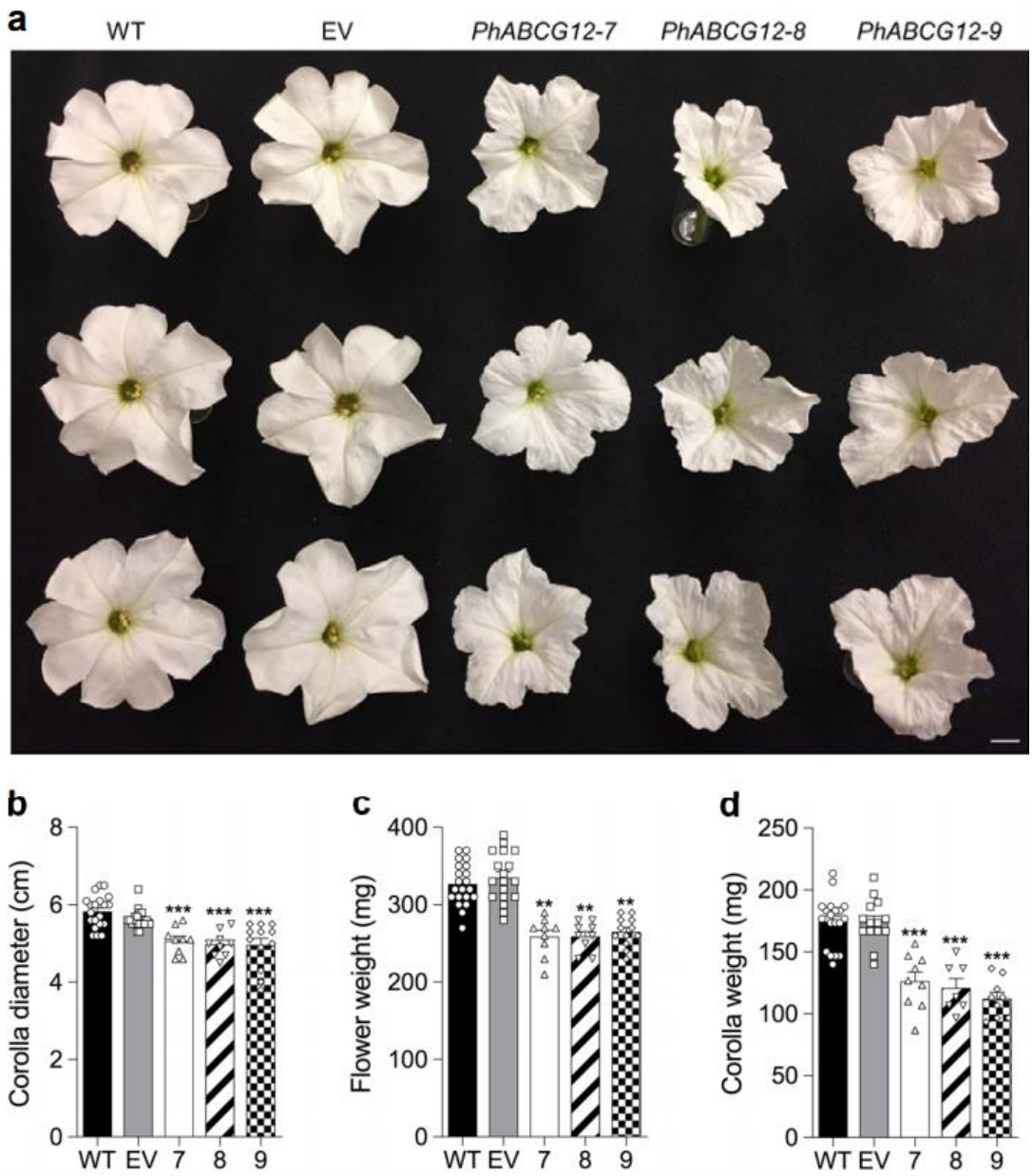

Fig. 6.5 – Effect of *PhABCG12* down-regulation on petunia flower phenotype. a, Representative 2-day-old flowers from wild type (WT), empty vector control (EV) and 3 independent *PhABCG12*-RNAi lines (7, 8 and 9). b, Corolla diameter, c, flower weight and d, corolla weight from WT, empty vector (EV)-transformed flowers and 3 independent *PhABCG12*-RNAi lines (7, 8 and 9). Data are means ± S.E. (n = 7 – 21 biological replicates). **, $P < 0.01$; ***, $P < 0.005$ by Student's *t*-test. Scale bar in a, 1 cm.

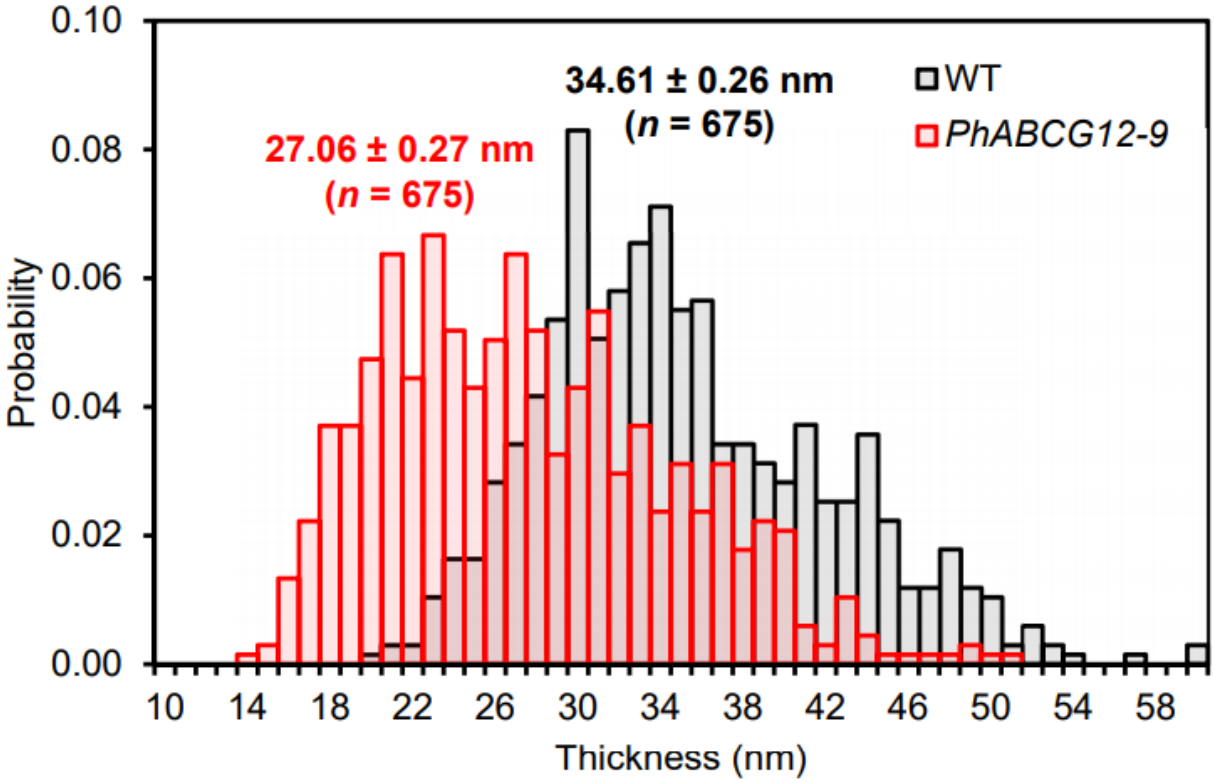

Fig. 6.6 – Histogram showing wax thickness distribution in wild-type and *PhABCG12* petunia flowers. Cuticle thickness probability distribution in epidermal cells of 2-day-old wild type (WT) and *PhABCG12*-RNAi line 9 flowers. To be consistent cuticle thickness was measured only in conical cells. The distribution is presented as the probability of different cuticle thickness values over 675 measurements. Data are means ± S.E. (n = 675 measurements). Measurements were taken from discreet locations in a minimum of 11 cells per genotype.

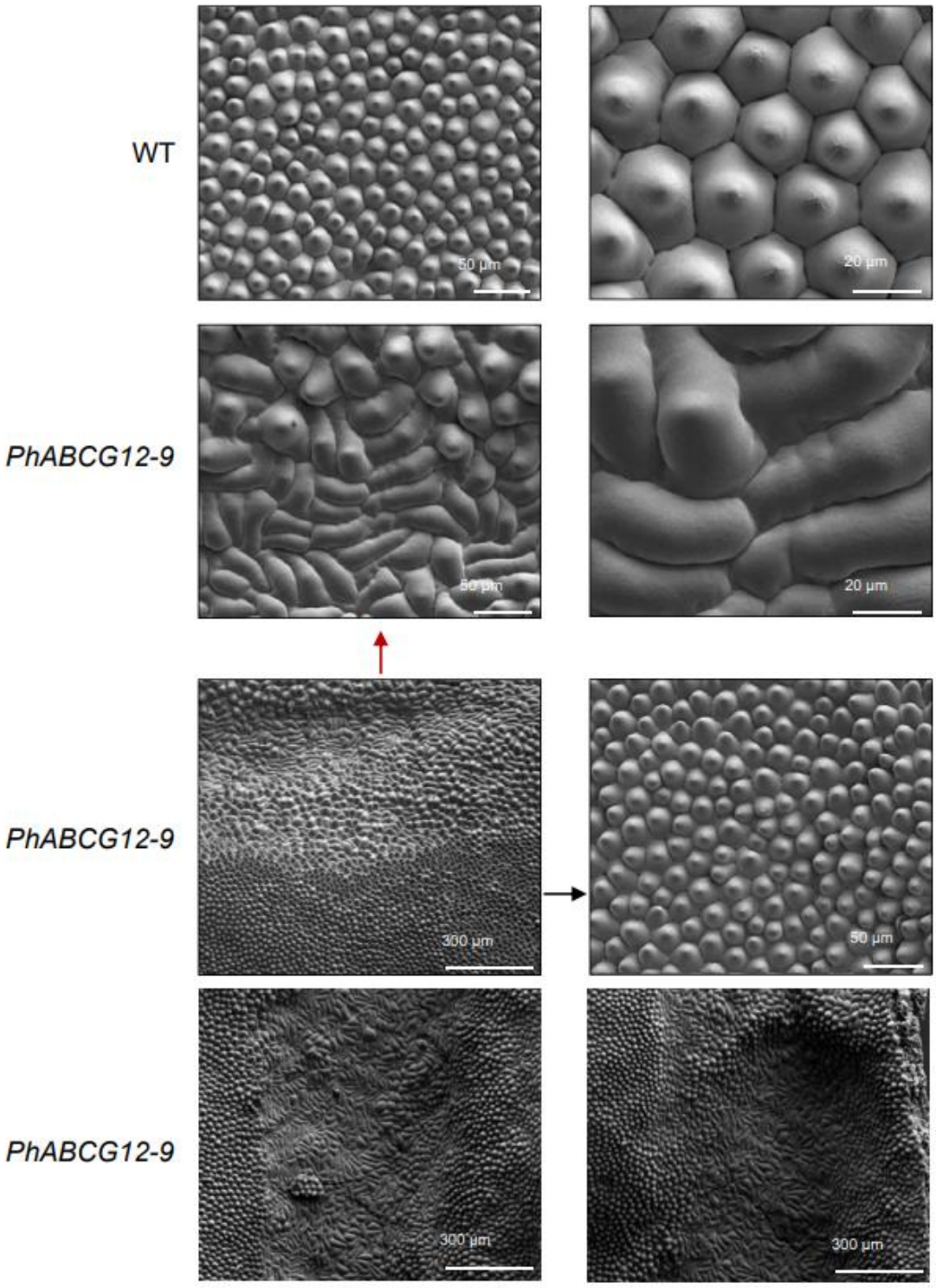

Fig. 6.7 – Effect of *PhABCG12* down-regulation on flower epidermal cell morphology. Representative cryo-scanning electron micrographs (cryo-SEM) of inner epidermal cells of 2-day-old wild type (WT) and *PhABCG12*-9 petals. Black arrow points to normal conical cells, red arrow points to abnormal epidermal cells.

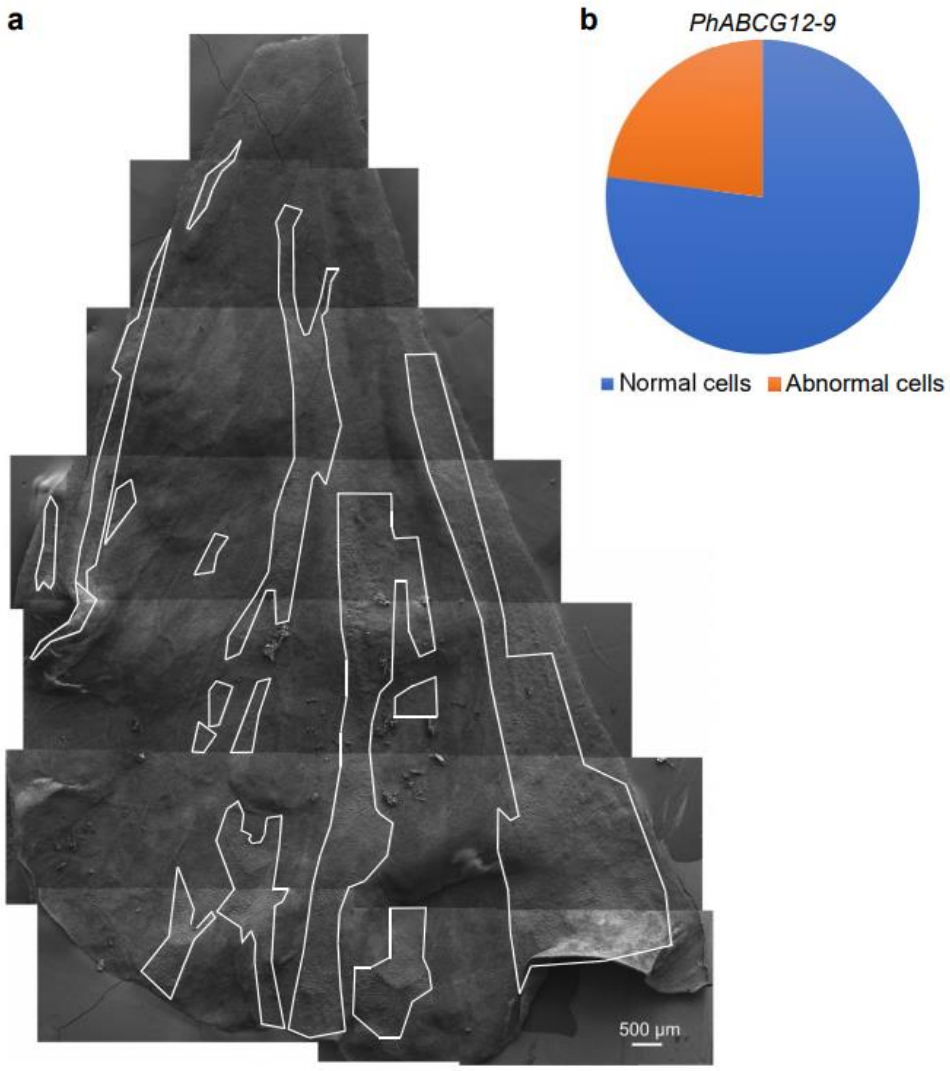

Fig. 6.8 – Representative cryo-SEM photographs showing the distribution of flattened cells in 2-day-old *PhABCG12*-RNAi line 9 petals. a, Representative composite of 24 cryo-SEM pictures of a petal from *PhABCG12*-9 flower. Patches of flatten cells are outlined in white. Scale bar, 500 µm. b, Pie chart showing percentage of normal and abnormal (flattened) cells determined from 81 cryo-SEM pictures from three distinct petal sections.

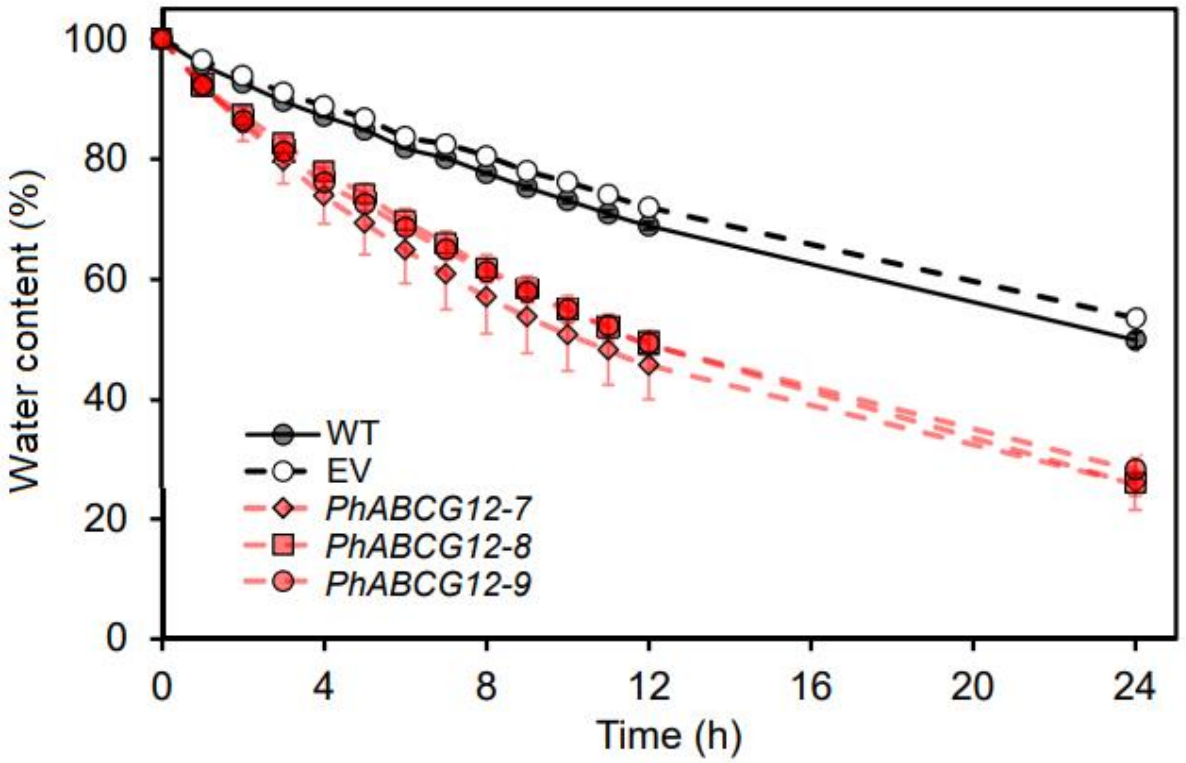

Fig. 6.9 – Effect of *PhABCG12* down-regulation on water permeability of petunia corollas. Weights of detached 2-day-old flowers from wild-type, empty vector control (EV) and 3 independent *PhABCG12*-RNAi lines (7, 8 and 9) were recorded over 24 h and expressed relatively to starting weight. Data are means ± S.E. (n = 4 biological replicates of three flowers each).

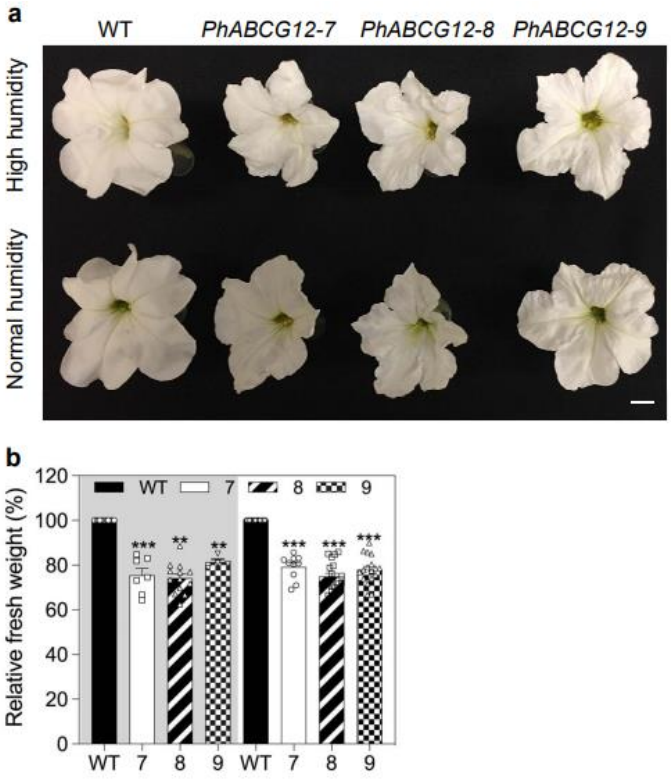

Fig. 6.10 – Effect of high humidity on flower phenotype of 2- day-old *PhABCG12*-RNAi flowers. a, Representative petunia flowers from wild type (WT), and three independent *PhABCG12*-RNAi lines (7, 8 and 9) grown under high (75%) or normal (< 50%) humidity. Scale bar, 1 cm. b, Fresh weight of flowers from wild-type (WT) and three independent *PhABCG12*-RNAi lines (7, 8 and 9) relative to corresponding WT measurements set as 100%, under high (grey background) and normal (white background) humidity. Data are means ± S.E. (n = 4 - 22 biological replicates). **, $P < 0.01$; ***, $P < 0.005$ by Student's *t*-test.

6.4.2 Cuticle serves as an essential member of the volatile metabolic network

The translocation of VOCs across the cuticle involves three physical processes: (*i*) partitioning of VOCs from the aqueous cell wall into the nonpolar waxes, (*ii*) diffusion across the cuticle, and (*iii*) vaporization of the VOCs from the cuticle surface into the atmosphere. Out of these steps, it has been hypothesized that cuticular diffusion is the major barrier to VOC emission (Widhalm et al., 2015), and therefore a thinner cuticle would be expected to permit increased VOC release. However, metabolic profiling of emitted VOCs and their internal pools in transgenic *PhABCG12*-RNAi flowers revealed that their total emission was unexpectedly reduced by 50-56% (Fig. 6.4d) along with a decrease in internal pools by 31-43% relative to controls (Fig. 6.4e). Out of nine individual Phe-derived 8 compounds emitted by petunia flowers, only two low-abundant

compounds comprising < 1% of total released VOCs, phenylethylbenzoate and eugenol, remained unaffected by changes in cuticle thickness (Fig. 6.11). The effect of *PhABCG12* RNAi downregulation on total VOC internal pools was opposite to that previously observed for RNAi downregulation of *PhABCG1* transporter, which transports VOCs across plasma membrane (Adebesin et al., 2017), confirming differential effects of these two transporters on VOC emission.

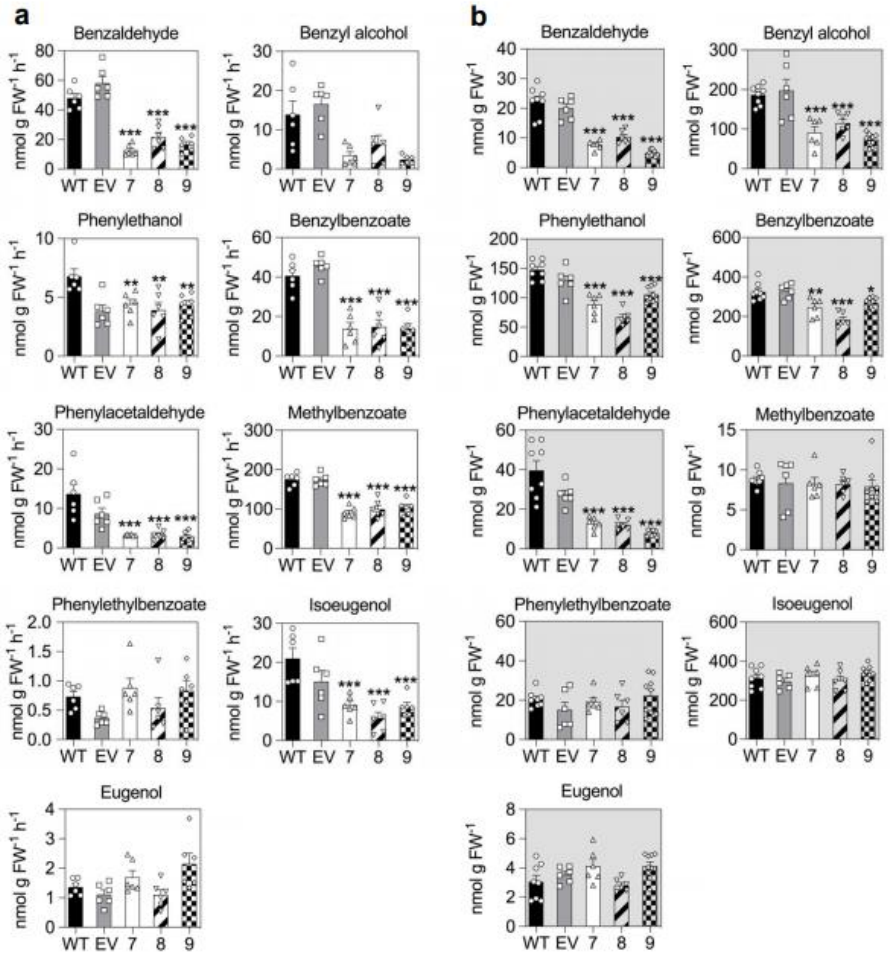

Fig. 6.11 – Effect of *PhABCG12* down-regulation on emissions and internal pools of individual benzenoid/phenylpropanoid volatiles in 2-dayold petunia flowers. Emission rates (a) and internal pools (b) of individual VOCs in wild type (WT), empty vector (EV) control and three independent *PhABCG12*-RNAi lines (7, 8 and 9). Data are means ± S.E. (n ≥ 6 biological replicates). *, $P < 0.05$; **, $P < 0.01$; ***, $P < 0.005$ by Student's t-test.

Reduction in both emission and internal pools of VOCs in transgenic lines indicates that VOC formation is reduced. Indeed, evaluation of the total biosynthetic flux, determined as the sum of total emission and the changes in corresponding internal pools over time, in control and

transgenics flowers showed that biosynthesis was reduced by 52 ± 7.8 % in *PhABCG12* RNAi transgenic flowers (Fig. 6.4f). Such reduction in VOC formation could occur at the level of precursor availability or directly at the biosynthesis of volatile compounds. To determine where in the scent biosynthetic network inhibition takes place, either upstream of volatile phenylpropanoid/benzenoid compound synthesis (Phe biosynthesis) or downstream of Phe (VOC biosynthesis), emission and internal pools were measured over a 4-h period in wild-type and *PhABCG12-9* flowers fed with 150 mM $^{13}C_6$-Phe and subjected to metabolic flux analysis (Fig. 6.12). Similar total biosynthetic fluxes in wild-type and transgenic flowers after Phe feeding indicate that VOC biosynthetic capacity was not affected in *PhABCG12*-RNAi flowers (Fig. 6.12c), suggesting that inhibition of VOC production occurred in the Phe biosynthetic network. To determine whether reduced Phe production is the result of transcriptional regulation, we performed qRT-PCR analysis of transcript levels for genes encoding proteins involved in Phe biosynthesis, including (*i*) 3-deoxy-D-arabino-heptulosonate 7-phosphate synthase (DAHPS, which catalyzes the first committed step in the shikimate pathway (Bentley and Haslam et al., 1990; Hermann and Weaver et al., 1999, Fig. A2); (*ii*) key 9 enzymes of the shikimate pathway (e.g. 5-enolpyruvylshikimate 3-phosphate synthase, EPSPS) and Phe biosynthesis (chorismate synthases CM1 and CM2) (Colquhoun et al., 2010; Qian et al., 2019), as well as (*iii*) petunia shikimate pathway transcriptional regulator ODORANT1 (ODO1) (Verdonk et al., 2005). Expression of all these genes were down-regulated in *PhABCG12*-RNAi lines relative to control from 33 to 62 % on day 2 postanthesis, a time of flowers development with the highest VOC emission (Fig. 6.13).

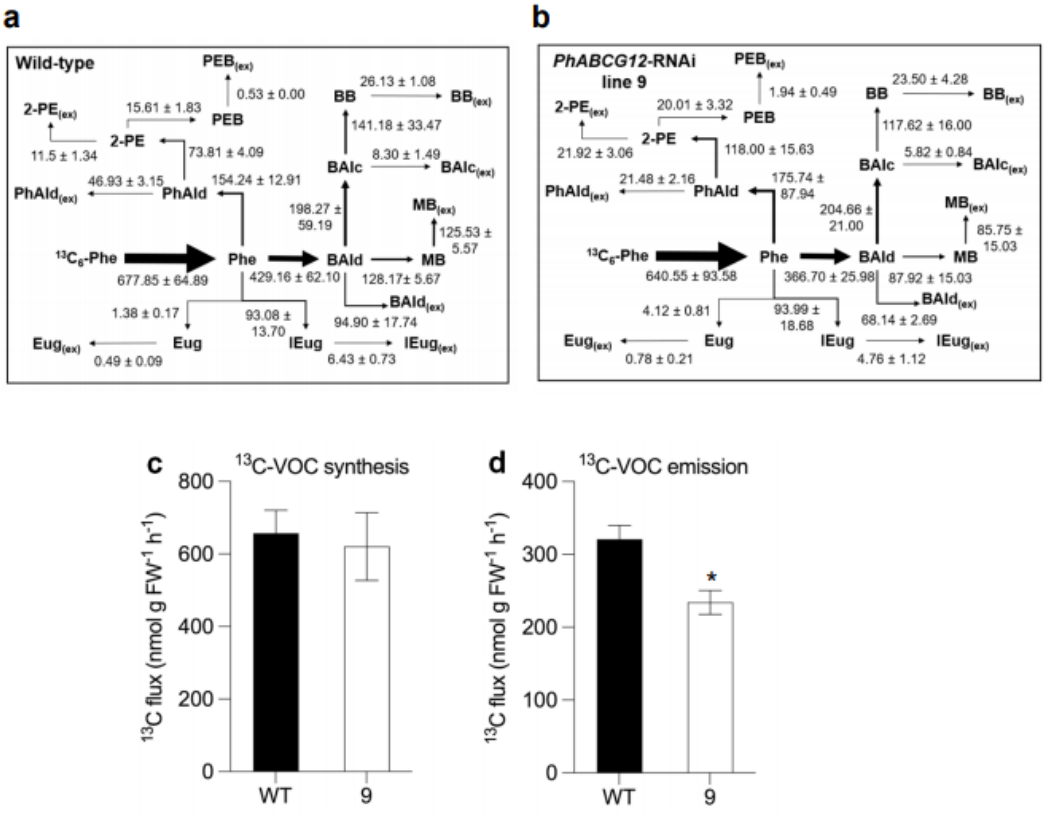

Fig. 6.12 – Metabolic flux analysis of benzenoid and phenylpropanoid VOCs from petunia flowers supplied with 150 mM $^{13}C_6$- phenylalanine. Metabolic flux maps of 2-day-old wild-type (a) and *PhABCG12*-9 (b) petunia petals fed with 150 mM $^{13}C_6$-Phe. Fluxes were obtained from time-course measurements of label incorporation in the endogenous pools and headspace collections of Phe-derived VOCs. Thickness of arrows reflect the relative value of fluxes normalized to the incoming flux (turnover of $^{13}C_6$-Phe). BAlc, benzyl alcohol; BAld, benzaldehyde; BB, benzylbenzoate; Eug, eugenol; IEug, isoeugenol; MB, methylbenzoate; 2-PE, 2-phenylethanol; PEB, phenylethylbenzoate; and PhAld, phenylacetaldehyde. The total labeled biosynthetic (c) and emission (d) fluxes shown in (a) and (b). Flux values are given in nmol·g $FW^{-1}\cdot h^{-1}$, and deviations were calculated by propagation of measurement standard error (n = 3 biological replicates) and regression error. *, $P < 0.05$ by Student's *t*-test.

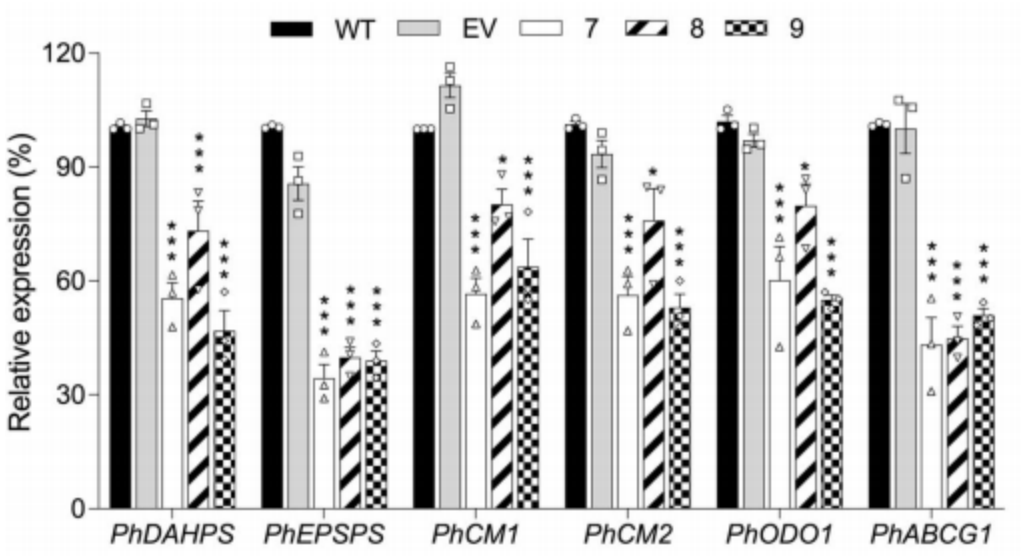

Fig. 6.13 – Effect of *PhABCG12* downregulation on expression of *PhDAHPS*, *PhEPSPS*, *PhCM1*, *PhCM2*, *PhODO1* and *PhABCG1* in 2-day-old petunia flowers. Transcript levels in flowers from wild type (WT), empty vector control (EV) and 3 independent *PhABCG12*-RNAi lines (7, 8 and 9) were determined by qRT-PCR at 3 PM and calculated relative to corresponding levels in wild type, set as 100%. Data are means ± S.E. (n = 3 biological replicates). *, $P < 0.05$; **, $P < 0.01$; *** $P < 0.005$ as determined by Student's *t*-test.

While $^{13}C_6$-Phe feeding compensated for the reduced internal pools in transgenics and led to a similar isotopic labeling of internal pools in control and transgenic petals (Figs. 6.14a and c), it was not able to restore emission in *PhABCG12* silenced flowers over 4 h despite similar to control isotopic labeling (Figs. 6.12d, 6.14b and d). If the cuticle is the primary resistance to net movement of volatiles out of the cell (mass transfer), it is expected that Phe feeding would result in higher VOC efflux from transgenic versus wild-type flowers. However, the lag in emission (Fig. 6.14b), which resulted in the inability of transgenic flowers to catch up to wild-type levels of total emission despite a rapid buildup in internal pools (Fig. 6.14a), suggests the existence of intracellular transport limitation(s) upstream of cuticle. Indeed, expression of *PhABCG1*, which encodes the plasma membrane-localized transporter of phenylpropanoid/benzenoid compounds, was reduced by 54% in transgenic flowers versus control (Fig 6.13), but membrane transport capacity remains sufficient to sustain high emission under feeding conditions (Fig. 6.14b).

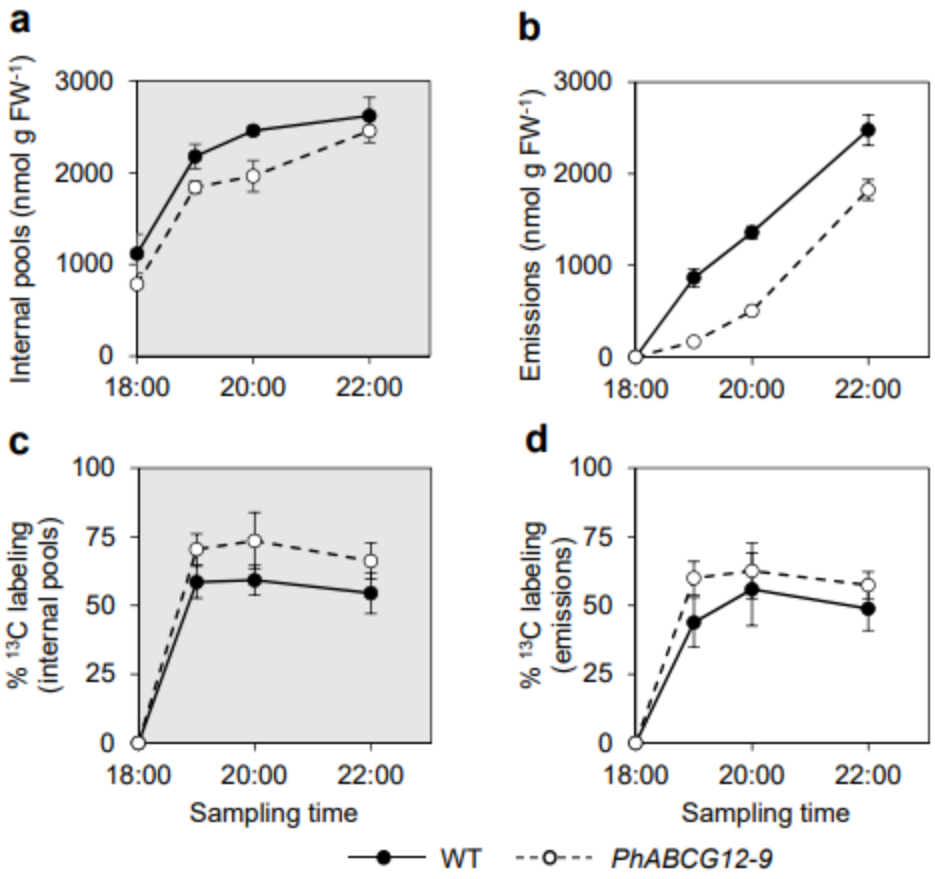

Fig. 6.14 – Pool sizes and isotopic abundances of total endogenous (internal pools) and exogenous (emitted) VOCs in control and *PhABCG12*-9 petunia petals fed with 150 mM $^{13}C_6$-Phe. Total internal pools (a) and emissions (b) of VOCs from wild-type (solid circles) and *PhABCG12*-9 (open circles) petunia corolla supplied with 150 mM $^{13}C_6$-Phe for 4 h. Isotopic labeling of internal pools (c) and emitted volatiles (d) over 4 h, from 6 PM till 10 PM. Data are means ± S.E. (n = 3 biological replicates).

Reduction in cuticle thickness has differential effect on dynamics of individual VOCs.

As biosynthesis of VOCs was reduced in *PhABCG12*-RNAi flowers, to account for this reduction in comparative analysis of wild type and transgenics, we defined a VOC emission factor (VEF) as 10 the ratio of emission flux to corresponding total biosynthetic flux (equation 6.4). A VEF value approaching 1 indicates that VOC emission is controlled mainly by biosynthesis, while VEF values lower than 1 reflect the existence of mass transfer limitations. VEF greater than 1 means that emission continues at a higher rate compared to decreasing biosynthesis. A reduction in cuticle thickness in *PhABCG12*-RNAi flowers did not increase VEF but instead led to its decrease (Fig. 6.15a), which was contrary to our hypothesis that a thinner cuticle would be more permissive to VOC release. A comparison of VEF of individual volatiles produced in wild-type

petunia petals revealed that two compounds, methylbenzoate and benzaldehyde, have the highest values close to 1 (Fig. 6.15b). Out of all compounds emitted by petunia flowers, they have the highest volatility based on vapor pressure (Table 6.2) and were more abundant in the mixture of emitted volatiles with relatively small internal pools within the cell (Fig. 6.11). Indeed, emission and biosynthetic fluxes overlaid for each of these two compounds when compared in wild-type petunia flowers over a 15-h period (Fig. 6.15d), suggesting that methylbenzoate and benzaldehyde emissions are driven solely by their biosynthesis. In contrast, volatiles with lower ambient vapor pressures such as benzylbenzoate, isoeugenol, 2-phenylethanol, and benzyl alcohol (Table 6.2), had lower VEF (Fig. 6.15b) and thus substantially larger internal pools relative to their corresponding emissions (Fig. 6.11), when compared with methylbenzoate and benzaldehyde. Moreover, these compounds displayed a clear delay between the peak of biosynthesis and emission, and reduction in cuticle thickness did not change these patterns (Fig. 6.15e, Fig. 6.16a and b), suggesting the existence of a mass transfer limitation for less volatile compounds. Thinner cuticles in transgenics had negligible effect on VEF of methylbenzoate and benzaldehyde, but decreased those of benzylbenzoate, isoeugenol, 2-phenylethanol and benzylalcohol (Fig. 6.15c). Thus, the trend towards internal build up rather than 11 emission for only less volatile compounds in transgenic petals (Fig. 6.15b) suggests that effect of cuticle thickness on VOC dynamics depends on physicochemical properties of compounds.

Table 6.2 – Vapor pressure for benzenoid/phenylpropanoid volatile organic compounds produced by *Petunia hybrida* flowers.

Compound	Vapor pressure[a] (mmHg) at 25°C
Benzaldehyde	1.27×10^{0}
Benzyl alcohol	9.40×10^{-2}
Benzylbenzoate	2.50×10^{-4}
Eugenol	1.00×10^{-2}
Isoeugenol	1.00×10^{-2}
Methylbenzoate	3.80×10^{-1}
Phenylacetaldehyde	3.68×10^{-1}
2-Phenylethanol	8.68×10^{-2}
Phenylethylbenzoate	3.40×10^{-5}

[a]Vapor pressure data deposited in or computed by PubChem.

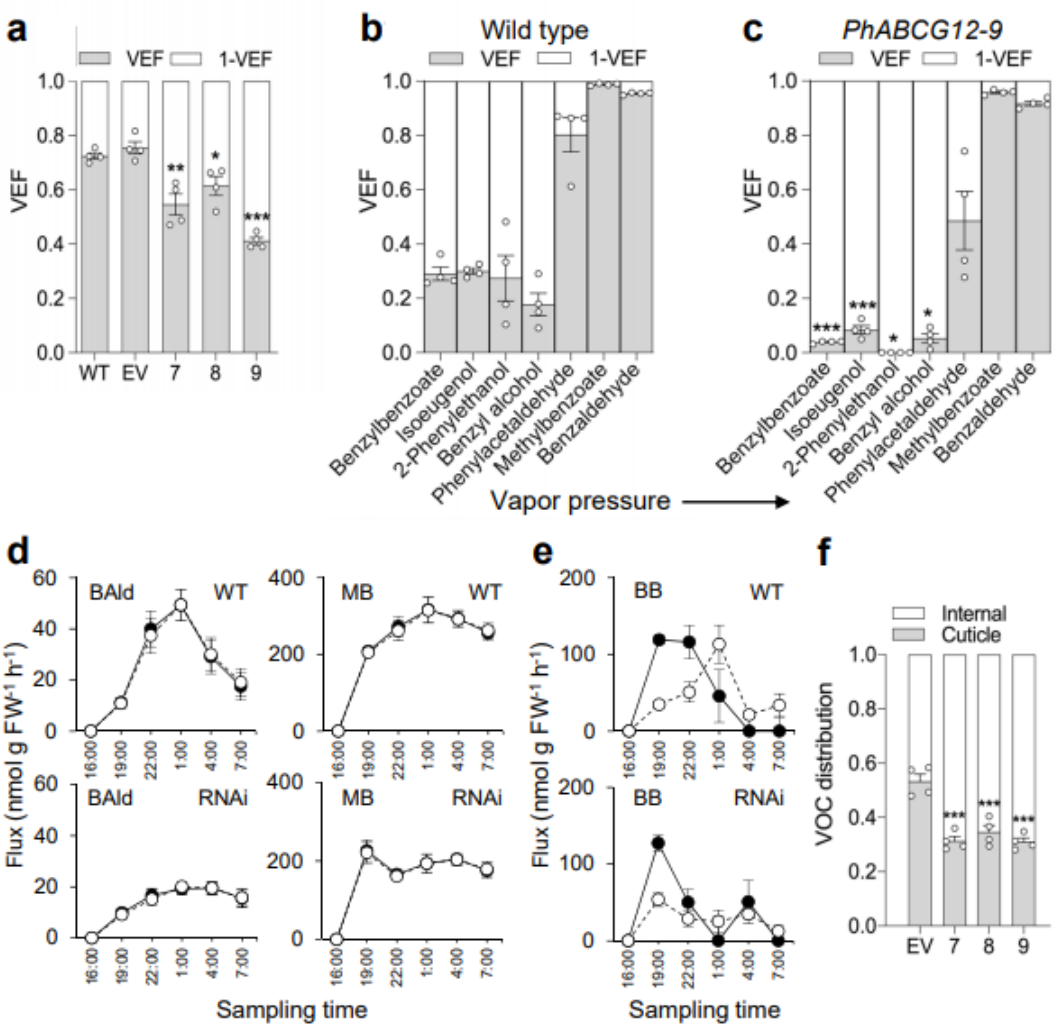

Fig. 6.15 – Effect of *PhABCG12* down-regulation on VEFs, emission and biosynthetic fluxes of representative VOCs and cellular distribution of VOCs in 2-day-old petunia flowers. a, Overall VEF for WT, EV control and three independent *PhABCG12*-RNAi lines 7, 8 and 9. Data are means ± S.E. (n = 4 biological replicates). *, $P < 0.05$; **, $P < 0.01$; ***, $P < 0.001$ by Student's t-test. b, VEF of individual volatiles emitted by WT and *PhABCG12*-9 flowers (c), shown in order of increasing compound volatility. Data are means ± S.E. (n = 4 biological replicates). *, $P < 0.05$; **, $P < 0.01$ by Student's *t*-test. d, Emission (open circles) and biosynthetic (solid circles) fluxes for benzaldehyde (BAld), methylbenzoate (MB) and (e) benzylbenzoate (BB) in WT (upper panels) and *PhABCG12*-9 line (lower panels). Data are means ± S.E. (n = 3 biological replicates). f, Cellular VOC distributions in petunia flowers of EV control and three independent *PhABCG12*-RNAi lines 7, 8 and 9. Data are means ± S.E. (n = 4 biological replicates). ***, $P < 0.001$ by Student's *t*-test.

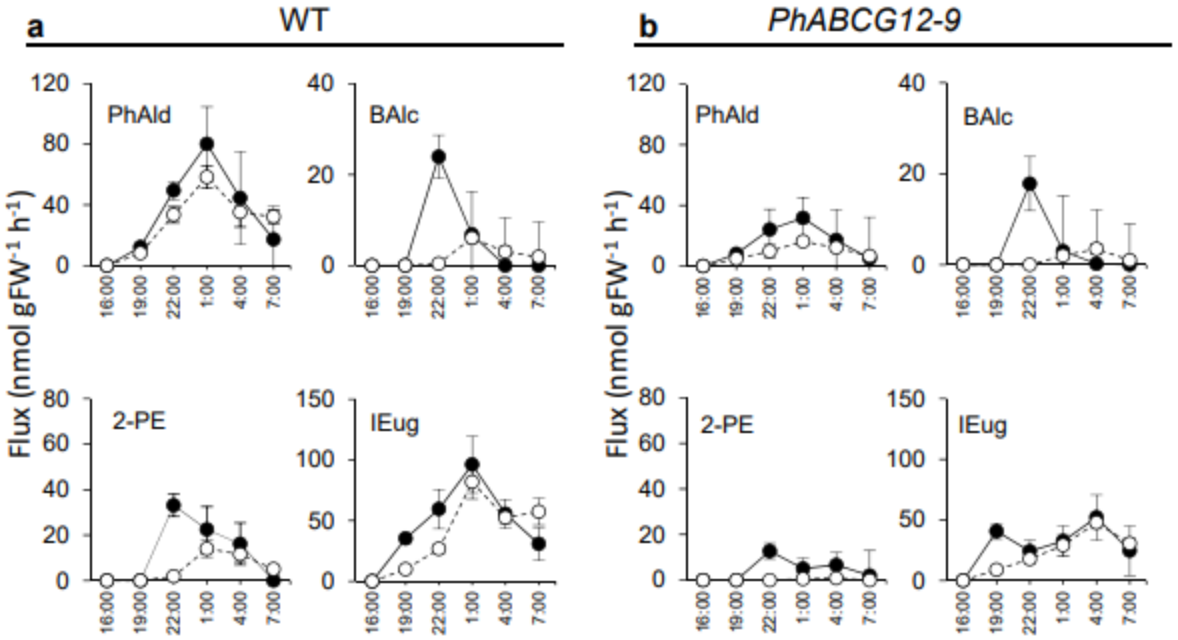

Fig. 6.16 – Effect of *PhABCG12* down-regulation on emission and biosynthetic fluxes of individual benzenoid/ phenylpropanoid VOCs. Emission (open circles) and biosynthetic fluxes (solid circles) for individual benzenoid/phenylpropanoid VOCs in 2-day-old wild-type (a) and *PhABCG12*-9 (b) petunia flowers. BAlc, benzyl alcohol; IEug, isoeugenol; 2-PE, 2-phenylethanol; PhAld, phenylacetaldehyde. Data are means ± S.E. (n = 3 biological replicates).

Analysis of VOC internal pools' distribution within the cell revealed that thinner cuticle holds a smaller proportion of VOCs, 32 ± 2% on average in transgenic plants (Fig. 6.15f) versus 53 ± 4% of total internal pools in wild-type flowers (Fig. 6.1a). Reduction in cuticle thickness decreased the relative cuticular abundance of all VOCs in transgenic petunia flowers relative to control (Fig. 6.17a), leading to their accumulation within the cell. Previously, it has been proposed and experimentally confirmed (Widhalm et al., 2015; Adebesin et al., 2017) that intracellular buildup of VOCs has a detrimental effect on membrane integrity leading to cellular toxicity. To test whether changes in VOC internal pools' distribution would lead to similar damaging effects despite an overall decrease in pool sizes in transgenic flowers, we performed staining with propidium iodide, which diffuses into cells and stains nucleic acids only if plasma membrane is disrupted (Rolny et al., 2011). Indeed, nuclei staining was observed in some cells of 2-day-old *PhABCG12*-9 petunia petals but not in those of wild-type (Fig. 6.18), consistent with the observed subcellular VOC redistribution.

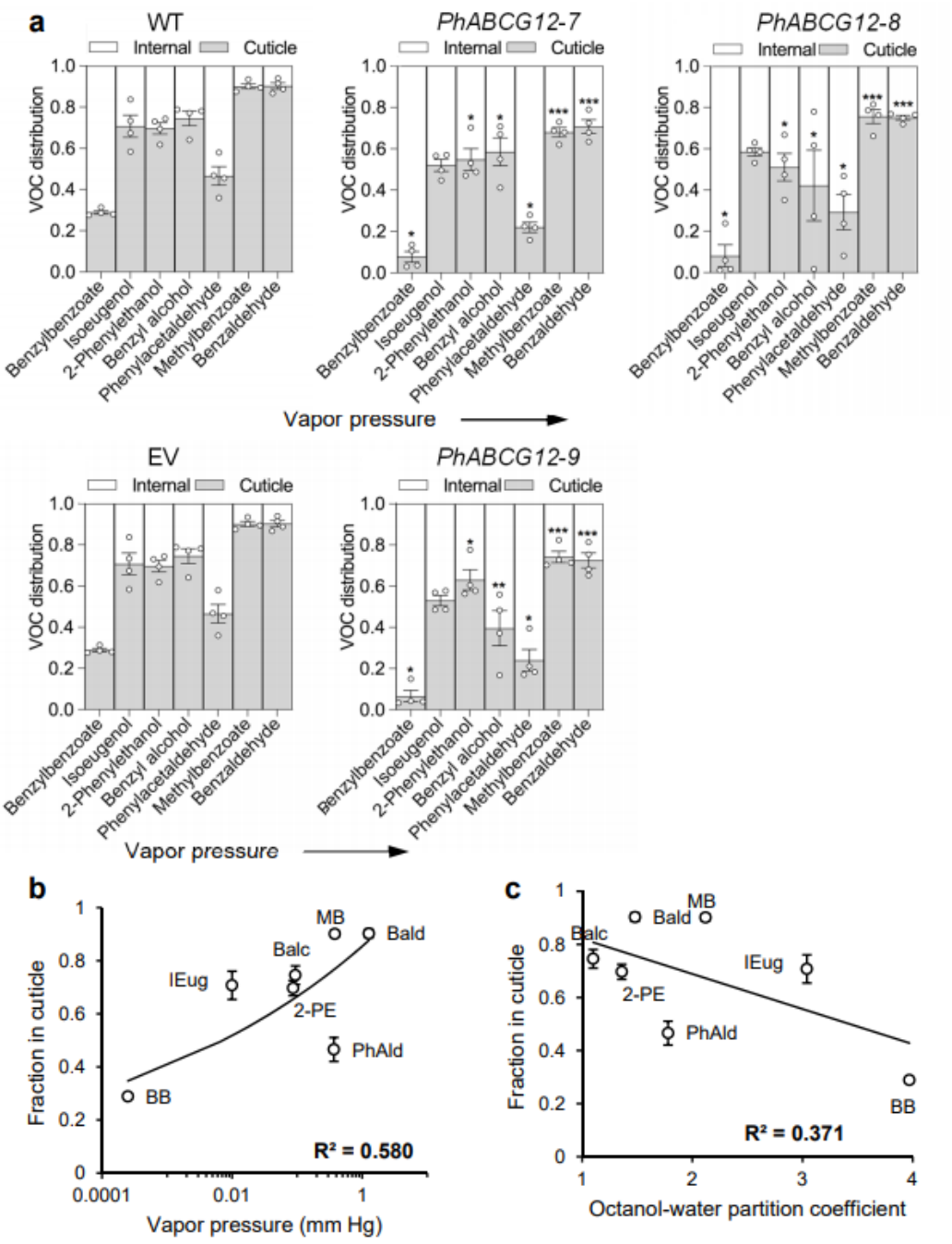

Fig. 6.17 – Effect of *PhABCG12* down-regulation on cellular distribution of individual benzenoid/phenylpropanoid VOCs in 2-day-old petunia flowers. a, Distribution of individual VOCs in wild-type (WT), empty vector control (EV) and *PhABCG12*-RNAi lines 7, 8 and 9. VOCs are shown in order of increasing volatility (left to right). Data are means ± S.E. (n = 4 biological replicates). *, $P < 0.05$; **, $P < 0.01$; ***, $P < 0.005$ by Student's t-test. Relationships between distribution of individual VOCs in the cuticle and their corresponding (b) vapor pressure and (c) octanol-water partitioning. Data are means ± S.E. (n = 4 biological replicates). BAlc, benzyl alcohol; BAld, benzaldehyde; BB, benzylbenzoate; IEug, isoeugenol; MB, methylbenzoate; 2- PE, 2-phenylethanol; PhAld, phenylacetaldehyde.

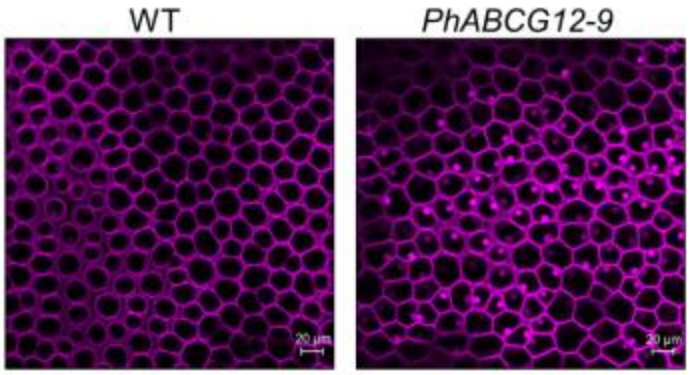

Fig. 6.18 – Effects of *PhABCG12* down-regulation on cell membrane integrity in petunia flowers. Representative confocal microscopy images of 2-day-old wild type (WT) and *PhABCG12*-9 flowers stained with propidium iodide. Scale bars, 20 µm.

Internal pools of VOCs with relatively higher ambient vapor pressures such as benzaldehyde and methylbenzoate were more abundant in the wild-type cuticle relative to the rest of the cell (> 90% of total internal pools, despite their small internal pool sizes) when compared to that of less volatile compounds, and this trend was conserved in transgenic lines (Fig. 6.17a). Cuticular VOC concentration is determined by the equilibria at both the cuticle-atmosphere and cell wall-cuticle interfaces, which depend on compound relative volatility and octanol-water partition coefficient (as a proxy for wax-water partitioning), respectively. Comparisons of individual VOC distributions within the cell with corresponding compound volatility and octanol-water partition coefficient (Fig. 6.17b and c) reveal that VOC volatility better correlates with their partitioning in the cuticle. This suggests that the cuticle-atmosphere interface plays a greater role in intracellular VOC distribution, consistent with the "pulling" effect of the atmosphere on compounds with relatively high volatility. The poor correlation between VOC enrichment in the cuticle and octanol-water partitioning coefficient may reflect existence of additional mechanisms, such as previously proposed for VOC trafficking through the cell wall (Widhalm et al., 2015).

Taken together, our results show that (*i*) > 50% of VOC internal pools are stored in the cuticle; (*ii*) representation of compounds within the cuticle is correlated with their volatility and VOCs with higher volatility are more abundant in the cuticle relative to the rest of the cell; (*iii*) reduction in cuticle thickness leads to redistribution of internal pools of VOCs between different intracellular regions; (*iv*) cuticle provides little resistance for compounds with relatively high volatility, but does limit diffusion of VOCs with lower volatility; and (*v*) cuticle is more than a simple diffusion barrier, but a member of scent metabolic network. Cells are able to sense changes

in VOC distribution within the cell as a result of decrease in cuticle thickness and feedback inhibit VOC biosynthesis by transcriptional downregulation of Phe supply as well as VOC transport out of the cell.

6.4.3 Reduction in cuticle thickness affects rhythmicity of VOC emission

Previously it has been shown that VOC emission from petunia flowers occurs in rhythmic manner with highest flux at night (Verdonk et al., 2003; Kolosova et al., 2001) and is under control of the circadian clock (Fenske et al., 2015). To dissect the effect of reduced cuticle thickness on VOC dynamics around the peak of emission, floral volatiles and their internal pools were collected from 2-day-old wild-type and *PhABCG12*-9 flowers over 15 h period. In wild-type flowers, a rapid accumulation of internal pools was observed between 4 PM and 10 PM and 13 remained constant until 4 AM (Fig. 6.19a). This increase in endogenous VOC internal pools correlated with a notable peak in emissions (Fig. 6.19b) between 10 PM and 1 AM, and such profile was conserved for all individual VOCs (Fig. 6.20). In contrast to wild-type flowers, rhythmicity in VOC emission was practically absent in *PhABCG12-9* flowers (Fig. 6.19b), while internal pools exhibited similar to wild type profile, but only approached ~73% of the maximum value found in wild-type petals (Fig. 6.19a). Although transgenic petals still exhibited a clear temporal peak in accumulation of VOC internal pools, the lack of a corresponding peak in emission suggests VOC redistribution upstream of the cuticle, thus restricting their release from the cell.

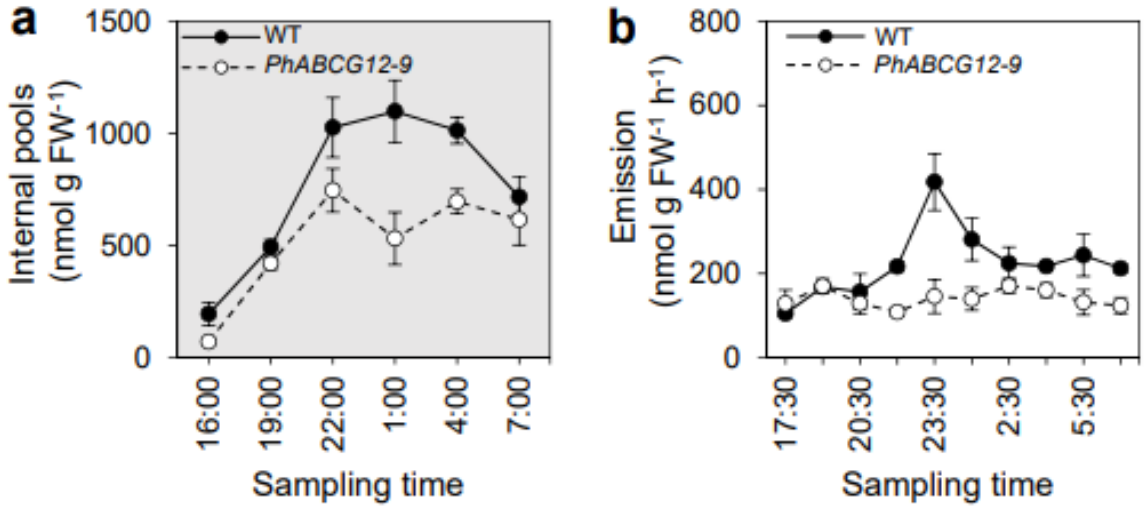

Fig. 6.19 – Total internal pools and emissions of benzenoid/ phenylpropanoid VOCs from 2-day-old petunia flowers around peak of emission. Total internal pools (a) and emissions (b) of VOCs collected from WT (solid circles) and *PhABCG12*-9 (open circles) flowers over 15 h period. Data are means ± S.E. (n = 3 biological replicates).

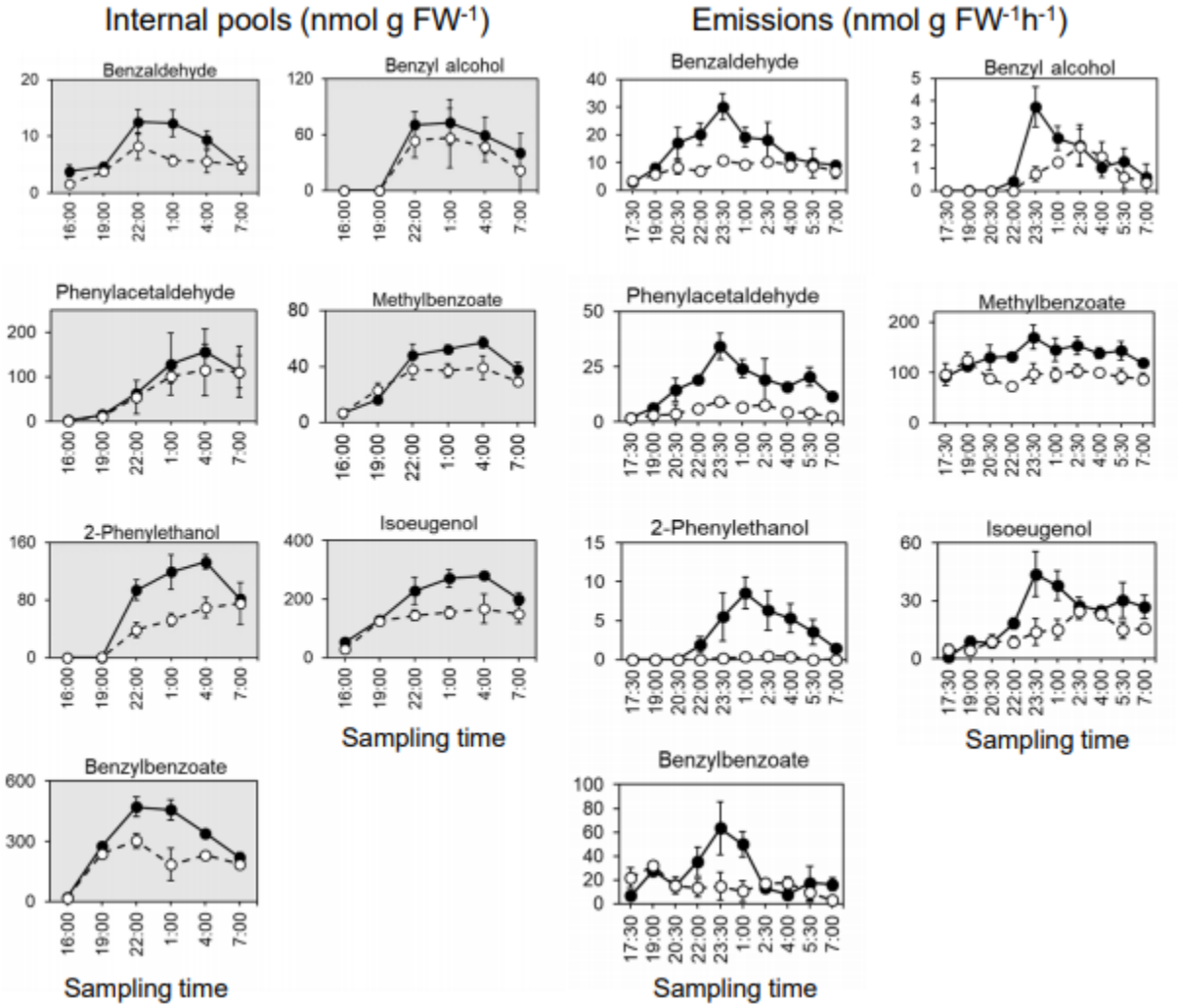

Fig. 6.20 – Internal pools and emissions of individual benzenoid/phenylpropanoid VOCs from 2-day-old petunia flowers around peak of emission. Internal pools (a) and emissions (b) of individual VOCs collected from wild-type (solid circles) and *PhABCG12*-9 flowers (open circles) over 15 h period. Data are means ± S.E. (n = 3 biological replicates).

6.4.4 Impact of cuticle partial removal on rate of VOC emission and accumulation: an independent strategy

In addition to the genetic approach, solvent-based dewaxing of petunia petals was used to examine the impact of reduced wax coverage on VOC emission without the potential influence of morphological changes observed in transgenic flower petals. Cuticle waxes were stripped from 2-

day-old wild-type petunia flowers by briefly submerging the petals in hexane. The total wax content, emission of VOCs and their internal pools were then analyzed over 4 h-period from 6 PM till 10 PM, the time interval with highest emission (Kolosova et al., 2001). Dewaxing removed 70 ± 6% of wax and petals became susceptible to toluidine blue staining (Fig. 6.21a and b). Analysis of VOCs in dewaxed flowers revealed that relative to the non-dewaxed control, total VOC emission and internal pools were both reduced by over 80% at the end of the 4-h collection period (Fig. 6.21c). To ensure that the decrease in VOC production is not due to a loss of petal metabolic potential during dewaxing process, the activity of phenylalanine ammonia lyase (PAL), which catalyzes the first committed step in the phenylpropanoid pathway was measured before and 4 h after dewaxing and was found to be unchanged (Fig. 6.22a). Moreover, exogenous feeding of 14 dewaxed flowers with 150 mM Phe was able to recover 92 ± 7% of the VOC emission observed in fed non-dewaxed flowers (Fig. 6.22b) and resulted in similar total biosynthetic fluxes (Fig. 6.22c). The fact that feeding of dewaxed flowers with 150 mM Phe was able to recover only 62 ± 10% of VOC internal pools, despite a similar to non-dewaxed flowers absolute increase in internal pools upon feeding (1742 ± 52 nmol·g FW^{-1} versus 1510 ± 277 nmol·g FW^{-1} in non-dewaxed and dewaxed petals, respectively; Fig. 6.22d), reflects the loss of the cuticular reservoir of VOCs. Taken together these results demonstrate that (*i*) flowers remain metabolically active 4 h after dewaxing and (*ii*) similar to *PhABCG12* RNAi transgenic flowers removal of cuticle leads to a decrease in VOC production via feedback inhibition of Phe formation by internally accumulated volatile compounds, thereby alleviating toxicity. Indeed, inducing internal VOC accumulation to toxic levels by feeding with 15 mM benzaldehyde (Adebesin et al., 2017) was sufficient to decrease expression of Phe biosynthetic genes, as well as *ODO1* transcription factor and *PhABCG1* transporter (Fig. 6.23).

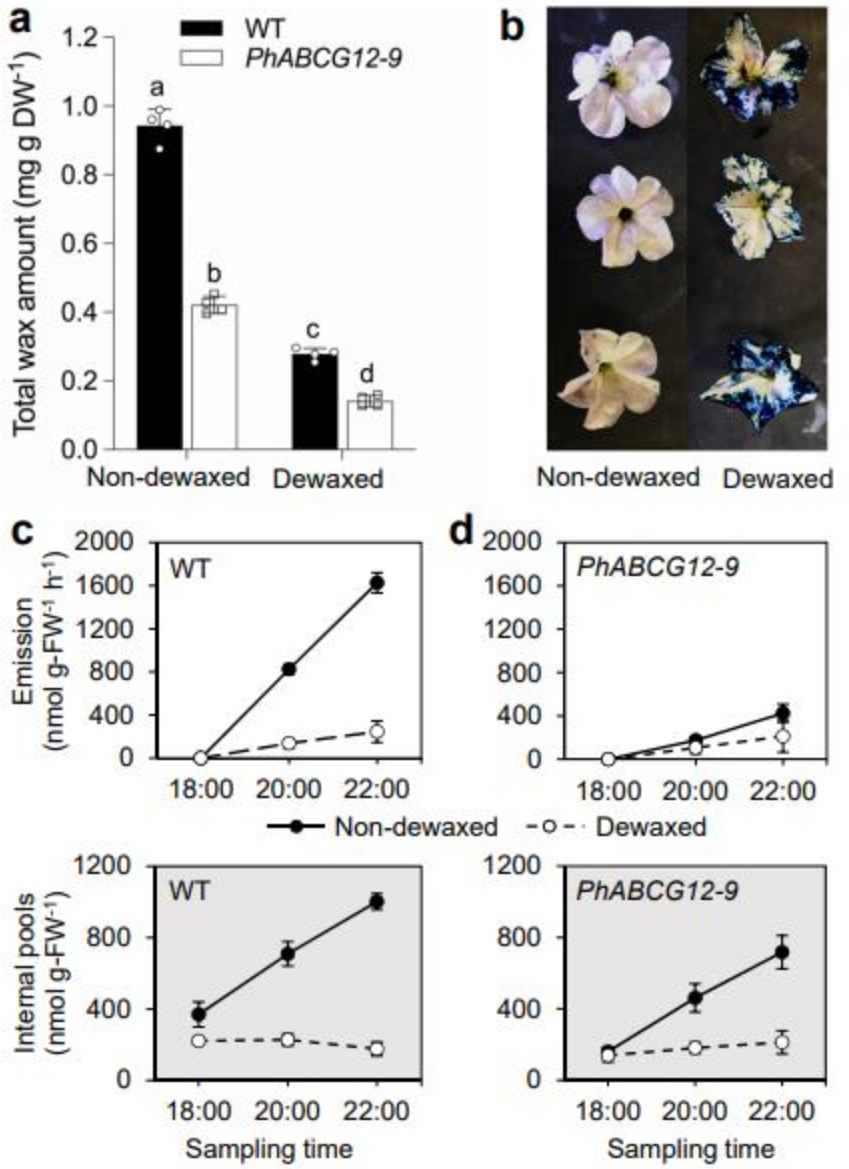

Fig. 6.21 – Effect of dewaxing on corolla wax levels, cuticle permeability, VOC internal pools and emissions in 2-day-old petunia flowers. a, Total wax levels before and after dewaxing of wild-type and *PhABCG12*-RNAi line 9 flowers. Letters indicate statistically significant differences ($P < 0.05$). Data are means ± S.E (n =4 biological replicates). b, Representative non-dewaxed and dewaxed wild-type flowers 2 h after staining with toluidine blue. c, Emission fluxes and VOC internal pools over a 4-h period in non-dewaxed (solid circles) and dewaxed (open circles) wild-type and *PhABCG12*-RNAi line 9 (d) flowers. Data are means ± S.E (n =4 biological replicates).

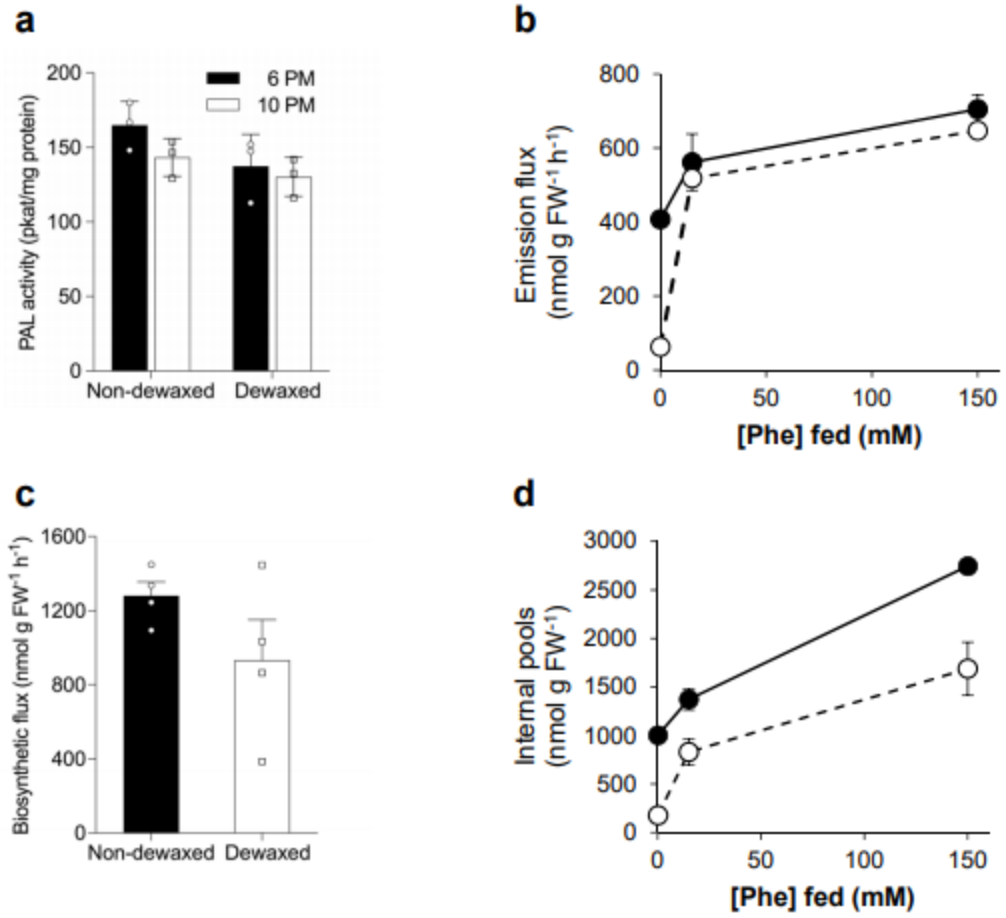

Fig. 6.22 – Analysis of metabolic potential of petunia flowers after dewaxing. a, PAL activity detected in non-dewaxed and dewaxed 2-day-old wild-type flowers in the beginning (6 PM) and the end (10 PM) of scent collection period. Data are means ± S.E. (n = 3 biological replicates). PAL activity was not statistically different between non-dewaxed and dewaxed petals ($P > 0.05$ by Student's t-test). b, Volatile emission from non-dewaxed and dewaxed wild-type flowers upon feeding different (0 - 150 mM) Phe concentrations. c, VOC biosynthetic fluxes in non-dewaxed (solid circles) and dewaxed (open circles) wild-type flowers fed with 150 mM Phe. d, Internal VOC pools in non-dewaxed (solid circles) and dewaxed (open circles) wild-type flowers upon feeding different (0 -150 mM) Phe concentrations. Data in b - d are means ± S.E. (n = 4 biological replicates).

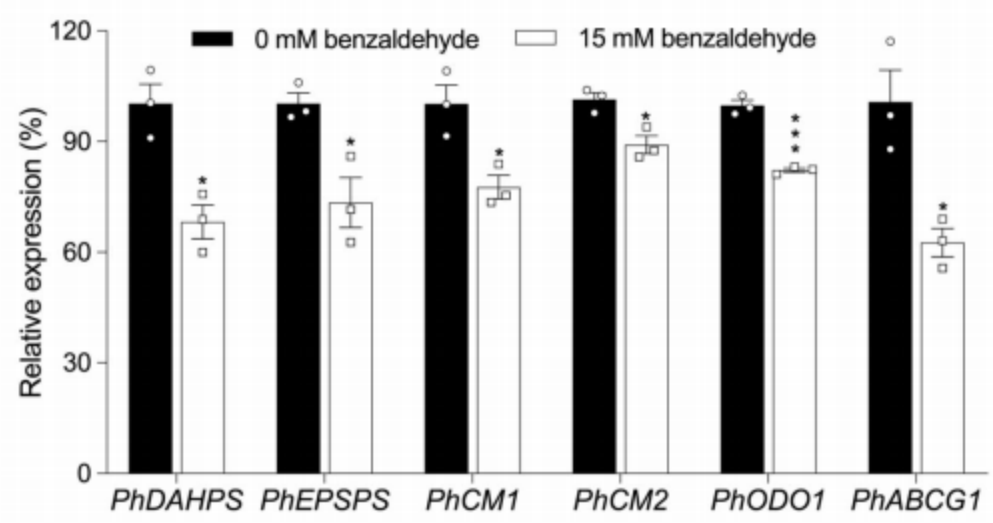

Fig. 6.23 – Effect of benzaldehyde feeding on expression of *PhDAHPS*, *PhEPSPS*, *PhCM1*, *PhCM2*, *PhODO1* and *PhABCG1* in 2- day-old petunia flowers. Transcript levels in wild-type flowers treated with 15 mM benzaldehyde for 6 h were determined by qRT-PCR at 3 PM and calculated relative to corresponding levels in mock treated wild type flowers, set as 100%. Data are means ± S.E. (n = 3 biological replicates). *, $P < 0.05$; ***, $P < 0.005$ as determined by Student's *t*-test.

6.4.5 Reduction in cuticle thickness shifts mass transfer resistance towards other cellular barriers

Dewaxing of wild-type petunia petals led to an increase in VEF value (Fig. 6.24a), as these flowers continue to emit VOCs, albeit at a low level, without changes in internal pools over the sampling time (Fig. 6.21c) further supporting the hypothesis that reduction of cuticle decreases overall resistance. As petal dewaxing reduces VOC formation, to determine whether the high VEF value would be sustained under elevated VOC biosynthetic flux, dewaxed wild-type petunia petals were fed with 150 mM Phe. Unexpectedly, an increase in VOC biosynthesis decreased VEF (Fig. 6.24a), which could occur only if VOCs accumulate inside the cell in the absence of cuticle sink, thus demonstrating redistribution in the source of mass transfer resistance. VEF was also reduced in non-dewaxed wild-type petunia petals fed with 150 mM Phe relative to the non-fed control and was very similar to the VEF of dewaxed wild-type petals fed with 150 mM Phe (Fig. 6.24a). Comparisons of individual VOC distributions within the cuticle with and without 150 mM Phe feeding revealed that compounds with low relative volatility accumulate internally under high

biosynthetic flux (Fig. 6.24b), suggesting a shift in mass transfer resistance source upon increased VOC biosynthesis (Fig. 6.25).

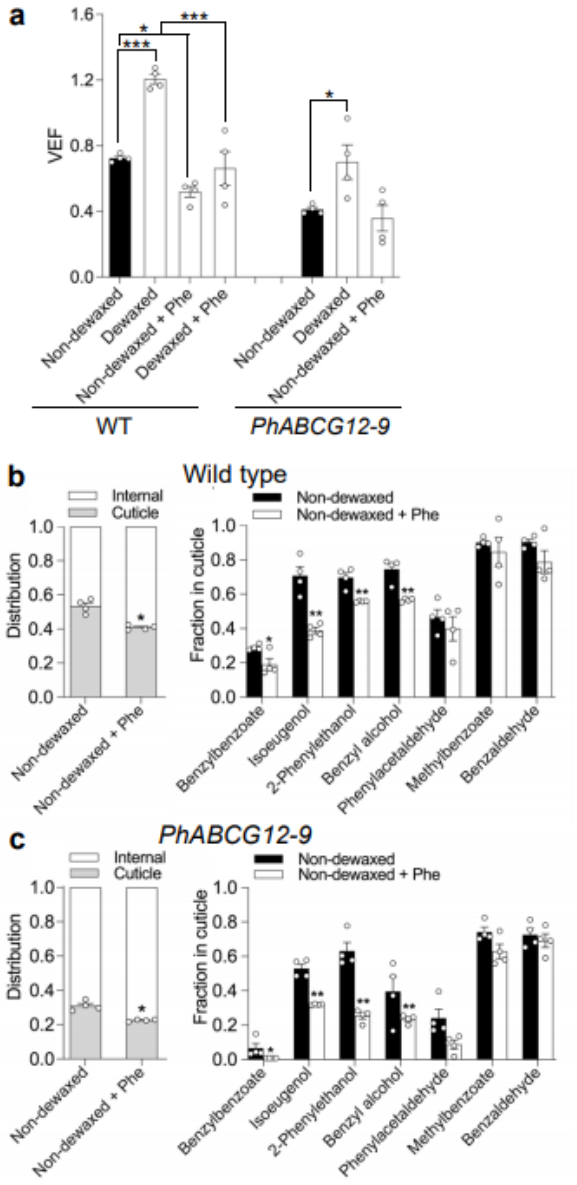

Fig. 6.24 Effect of dewaxing and Phe feeding on VEFs and cellular VOC distributions in 2-day-old petunia flowers. a, Overall VEFs for non-dewaxed and dewaxed wild-type and *PhABCG12*-RNAi line 9 flowers with and without feeding with 150 mM Phe over 4 h period from 6 PM till 10 PM. Data are means ± S.E. (n = 4 biological replicates). *, P < 0.05; ***, P < 0.001 by Student's t-test. b, Cellular distributions of total (left panel) and individual VOCs (right panel) in non-dewaxed wild type and *PhABCG12*-9 line (c) flowers with and without Phe feeding. Data are means ± S.E. (n = 4 biological replicates). *, *P* < 0.05; **, *P* < 0.01; ***, *P* < 0.001 by Student's *t*-test.

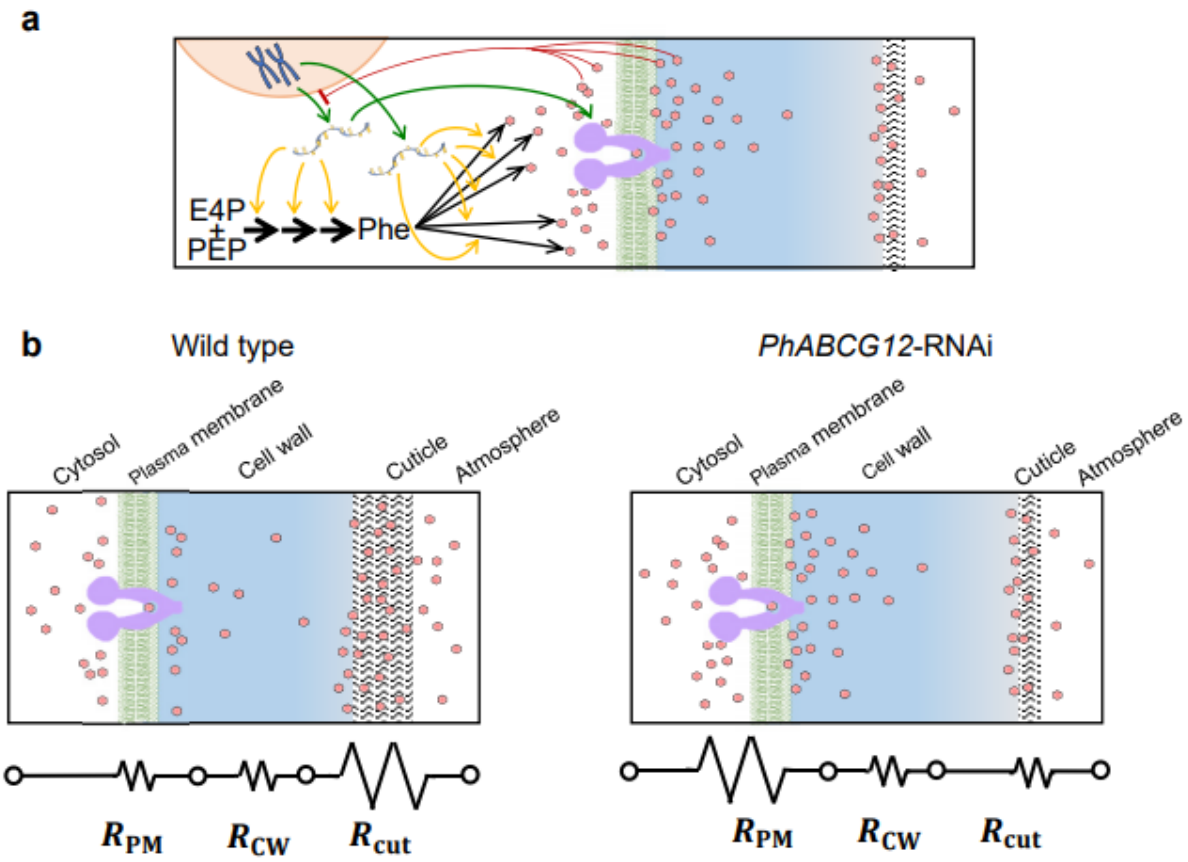

Fig. 6.25 – Schematic presentation of shift in the mass transfer resistance sources upon reduction in cuticle thickness. a, Schematic representation of VOC (red icons) feedback effect on transcription of Phe biosynthetic genes. Black arrows represent enzymes, orange arrows represent RNA translation, and green arrows represent gene transcription. Red lines show feedback inhibition of Phe biosynthetic gene transcription by accumulating VOCs via unknown mechanisms. b, Overall resistance shown by a resistance-in-series model. The barrier with the highest contribution to overall resistance to VOC (red icons) mass transfer out of the cells is shown by the largest resistor symbol. Purple icon in plasma membrane represents previously characterized *PhABCG1* transporter (Adebesin et al 2017).

To test if this effect was conserved in transgenic petals, *PhABCG12-9* RNAi flowers were subjected to dewaxing (Fig. 6.21a). Similar to wild-type flowers, dewaxing of *PhABCG12-9* petals resulted in reduced emission flux and internal pool accumulation relative to the non-dewaxed *PhABCG12-9* petals (Fig. 6.21d). Like in wild-type flowers, dewaxing of transgenic petals led to an increase in VEF (Fig. 6.24a), but the value remained below 1 and was still lower than that in control dewaxed petals. Thus, despite an 85% reduction in wax amount in *PhABCG12-9* petals upon dewaxing relative to non-dewaxed wild-type petals (Fig. 6.21a), VOCs still continue to accumulate internally (Fig. 6.21d). The inability to discharge the VOC internal pools upon

combined RNAi reduction of cuticle thickness and dewaxing suggests that the resistance to mass transfer in transgenic flowers has shifted from the cuticle to other sources of mass transfer resistance, such as the plasma membrane and cell wall. Consistent with the shift in mass transfer resistance source, feeding of *PhABCG12-9* flowers with 150 mM Phe did not affect VEF (Fig. 6.24a), and similar to wild-type petunia flowers, led to the redistribution of VOC internal pools of only compounds with low relative volatility (Fig. 6.24c).

Taken together, these results show that (*i*) cuticle serves as a significant resistance barrier for VOC emission; (*ii*) without enough cuticle present to act as a sink, VOCs accumulate internally, leading to inhibition of precursor formation to prevent toxicity; (*iii*) compounds with lower relative 16 volatility experience greater resistance at the cuticle; and (*iv*) other barriers, as a result of a shift in the mass transfer resistance, control emission under high VOC biosynthetic flux

6.5 Conclusions

The cuticle is the final barrier VOCs cross before being released into the atmosphere. Our results show that cuticle of petunia flowers holds > 50% of internal VOCs (Fig. 6.1a), thus acting as the main site of intracellular VOC storage, and serving as the major source of mass transfer resistance. However, it mainly provides resistance to VOCs with low relative volatility with negligible effect on highly volatile compounds, physiological emissions of which largely depend on their biosynthesis (Figs. 6.15, 6.17, 6.24). The latter compounds have small internal pools relative to their emission flux, and these pools are predominantly allocated to the cuticle (Fig. 6.17a). To sustain efficient emission, VOCs have to accumulate in the cuticle and decreasing the ability of cuticle to act as a concentrator/sink not only reduces overall emission (Figs. 6.4d and 6.21c), but also eliminates rhythmicity in VOC release (Figs. 6.17b and 6.19b). The inability for VOCs, particularly those with low relative volatility, to build up in the cuticle due to a reduction in its thickness via RNAi downregulation of *PhABCG12* transporter (Fig. 6.4a and c) leads to a redistribution of internal VOC pools (Figs. 6.15f and 6.17a), thus resulting in cellular damage (Fig. 6.18). To mitigate this detrimental effect, cells reduce production of VOCs by decreasing biosynthesis of the precursor Phe (Fig. 6.13 and Fig. 6.25a), a feedback effect that was also observed in flowers after chemical dewaxing (Fig. 6.21) but could be bypassed by Phe feeding (Fig. 6.22b and d). Finally, the decrease in cuticle thickness leads to a shift in mass transfer resistance to other internal barriers (i.e. plasma membrane and cell wall), and this shift is more

pronounced under high biosynthetic flux (Fig. 6.25b), likely reflecting the limited capacity of the plasma-membrane localized VOC transporter, PhABCG1 (Adebesin et al., 2017). Taken together, these results reveal that the cuticle, despite being biologically passive, is nonetheless an integral member of the overall scent biosynthetic network.

6.6 Acknowledgements

This work was supported by grant IOS-1655438 from the National Science Foundation awarded to Dr. Natalia Dudareva and Dr. John A. Morgan. I would like to thank Dr. Benoît Boachon transformation of *Petunia hybrida* lines. I would like to thank Dr. Pan Liao for performing experiments pertaining to the measurement of transcript levels (Figs. 6.1b, 6.2, 6.15), phenotyping (Figs. 6.5, 6.10, 6.12, 6.16), TEM and SEM (Figs. 6.4, 6.6, 6.7, 6.7), and assaying for PAL activity (Fig. 6.22a).

6.7 References

Abràmoff MD., Magelhães PJ., Ram SJ. (2004) Image Processing with ImageJ. *Biophotonics International*, *11* (7), 36-42

Adebesin F., Widhalm JH., Boachon B., Lefèvre F., Pierman B., Lynch JH., Alam I., Junqueira B., Benke R., Ray S., Porter JA., Yanagisawa M., Wetzstein HY., Morgan JA., Boutry M., Schuurink RC., Dudareva N. (2017) Emission of volatile organic compounds from petunia flowers is facilitated by an ABC transporter. *Science*, *356* (6345), 1386-88

Aharoni A., Dixit S., Jetter R., Thoenes E., van Arkel G., Pereira A. (2004) The SHINE clade of AP2 domain transcription factors activates wax biosynthesis, alters cuticle properties, and confers drought tolerance when overexpressed in Arabidopsis. *Plant Cell*, *6*, 2463-80

Azuma M., Morimoto R., Hirose M., Morita Y., Hoshino A., Iida S., Oshima Y., Mitsuda N., Ohme-Takagi M., Shiratake K. (2016) A petal-specific InMYB1 promoter from Japanese morning glory: a useful tool for molecular breeding of floricultural crops. *Plant Biotechnology Journal*, *14* (1), 354-63

Bentley R., Haslam E. (1990) The Shikimate Pathway – A Metabolic Tree with Many Branches. *Critical Reviews in Biochemistry and Molecular Biology*, *25* (5), 307-84

Bernard A., Joubès J. (2013) Arabidopsis cuticular waxes: advances in synthesis, export and regulation. *Progress in Lipid Research*, *52*, 110-29

Bird DA., Beisson F., Brigham A., Shin J., Greer S., Jetter R., Kunst L., Wu X., Yephremov A., Samuels L. (2007) Characterization of Arabidopsis ABCG11/WBC11, an ATP binding

cassette (ABC) transporter that is required for cuticular lipid secretion. *Plant Journal*, *52* (3), 485-98

Boatright J., Negre F., Chen XL., Kish CM., Wood B., Peel G., Orlova I., Gang D., Rhodes D., Dudareva N. (2004) Understanding in vivo benzenoid metabolism in petunia petal tissue. *Plant Physiology*, *135*, 1993–2011

Bourdenx B., Bernard A., Domergue F., Pascal S., Léger A., Roby D., Pervent M., Vile D., Haslam RP., Napier JA., Lessire R., Joubès J. (2011) Overexpression of Arabidopsis ECERIFERUM1 promotes wax very-long-chain alkane biosynthesis and influences plant response to biotic and abiotic stresses. *Plant Physiology*, *156* (1), 29-45

Chen X., Goodwin S., Boroff V., Liu X., Jenks M. (2003) Cloning and characterization of the WAX2 gene of Arabidopsis involved in cuticle membrane and wax production. *Plant Cell*, *15*, 1170-85

Colquhoun TA., Verdonk JC., Schimmel BC., Tieman DM., Underwood BA., Clark DG. (2010) Petunia floral volatile benzenoid/phenylpropanoid genes are regulated in a similar manner. *Phytochemistry*, *71*, 158-67

Do THT., Martinoia E., Lee Y. (2018) Functions of ABC transporters in plant growth and development. *Current Opinion in Plant Biology*, *41*, 32-8

Effmert U., Buss D., Rohrbeck D., Piechula B. (2006) Localization of the Synthesis and Emission of Scent Compounds within the Flower. In: N Dudareva, E Pichersky, eds, Biology of Floral Scent. London: Taylor & Francis Group, 105–24

Goodwin SM, Jenks M (2005) Plant cuticle function as a barrier to water loss. In M Jenks, PM Hasegawa, eds, Plant Abiotic Stress. Blackwell Publishing, Oxford, pp 14–36

Hermann KM., Weaver LM. (1999) The Shikimate Pathway. *Annual Review of Plant Physiology and Plant Molecular Biology*, *50*, 473-503

Horsch RB., Fry J., Hoffmann N., Neidermeyer J., Rogers SG., Fraley RT. (1985) Leaf disc transformation. In: Gelvin S.B., Schilperoort R.A., Verma D.P.S. (eds) Plant Molecular Biology Manual. Springer, Dordrecht

Klempien A., Kaminaga Y., Qualley A., Nagegowda DA., Widhalm JR., Orlova I., Shasany AJ., Taguchi G., Kish CM., Cooper BR., D'Auria JC., Rhodes D., Picherky E., Dudareva N. (2012) Contribution of CoA ligases to benzenoid biosynthesis in petunia flowers. *The Plant Cell*, *24* (5), 2015–30

Kolosova N., Gorenstein N., Kish CM., Dudareva, N. (2001). Regulation of circadian methyl benzoate emission in diurnally and nocturnally emitting plants. *Plant Cell*, *13*, 2333-47

Kunst L., Samuels L. (2009) Plant cuticles shine: advances in wax biosynthesis and export. *Current Opinion in Plant Biology*, *12* (6), 721-27

Kurdyukov S., Faust A., Nawrath C., Bar S., Voisin D., Efremova N., Franke R., Schreiber L., Saedler H., Metraux JP., Yephremov A. (2006) The epidermis-specific extracellular BODYGUARD controls cuticle development and morphogenesis in Arabidopsis. *Plant Cell*, *18*, 321-39

Li-Beisson T., Pollard,M., Sauveplane V., Pinot F., Ohlrogge J., Beisson F. (2009) Nanoridges that characterize the surface morphology of flowers require the synthesis of cutin polyester. *Proceedings in the National Academy of Science, 106* (51), 22008-13

Luo B., Xue X-Y., Hu W-L., Wang L-J., Chen X-Y. (2007) An ABC transporter gene of Arabidopsis thaliana, AtWBC11, is involved in cuticle development and prevention of organ fusion. *Plant Cell & Physiology, 48* (12), 1790-1802

Maeda H., Shasany AK., Schnepp J., Orlova I., Taguchi G., Cooper BR., Rhodes D., Pichersky E., Dudareva N. (2010) RNAi suppression of arogenate dehydratase1 reveals that phenylalanine is synthesized predominantly via the arogenate pathway in petunia petals. *Plant Cell, 22*, 838-49

McFarlane HE., Shin JJH., Bird DA., Samuels AL. (2010) Arabidopsis ABCG transporters, which are required for export of diverse cuticular lipids, dimerize in different combinations. *Plant Cell, 22* (9), 3066-75

Millar A., Clemens S., Zachgo S., Giblin E., Taylor D., Kunst L. (1999) CUT1, an Arabidopsis gene required for cuticular wax biosynthesis and pollen fertility, encodes a very-long-chain fatty acid condensing enzyme. *Plant Cell, 11*, 825-38

Niinemets Ü., Fares S., Harley P., Jardine KJ. (2014) Bidirectional exchange of biogenic volatiles with vegetation: emission sources, reactions, breakdown and deposition. *Plant, Cell & Environment, 37* (8), 1790-1809

Niinemets Ü., Reichstein M. (2002) A model analysis of the effects of nonspecific monoterpenoid storage in leaf tissues on emission kinetics and composition in Mediterranean sclerophyllous Quercus species. *Global Biogeochemical Cycles, 16* (4), 1-26

Orlova I., Marshall-Colon A., Schnepp J., Wood B., Varbanova M., Fridman E., Blakeslee JJ., Peer WA., Murphy AS., Rhodes D., Pichersky E., Dudareva N. (2006) Reduction of benzenoid synthesis in petunia flowers reveals multiple pathways to benzoic acid and enhancement in auxin transport. *Plant Cell, 18*, 3458–75

Panikashvili D., Shi J-X., Bocobza S., Franke RB., Schreiber L., Aharoni A. (2010) The Arabidopsis DSO/ABCG11 transporter affects cutin metabolism in reproductive organs and suberin in roots. *Molecular Plant, 3*, 563-75

Panikashvili D., Shi J-X., Schreiber L., Aharoni A (2011) The Arabidopsis ABCG13 transporter is required for flower cuticle secretion and patterning of the petal epidermis. *New Phytologist, 190*, 113-24

Pighin JA, Zheng H, Balakshin LJ, Goodman IP, Western TL, Jetter R, Kunst L, Samuels AL (2004) Plant cuticular lipid export requires an ABC transporter. *Science, 306*, 702-4

Press WH. (2007) Numerical Recipes: The Art of Scientific Computing. *Cambridge University Press*

Qian Y., Lynch JH., Guo L., Rhodes D., Morgan JA., Dudareva N. (2019) Completion of the cytosolic post-chorismate phenylalanine biosynthetic pathway in plants. *Nature Communications, 10*, 15

Riederer M., Schreiber L. (2001). Protecting against water loss: analysis of the barrier properties of plant cuticles. *Journal of Experimental Botany, 52* (363), 2023-32

Ronly N., Costa L., Carrión C., Guaimet JJ. (2011) Is the electrolyte leakage assay an unequivocal test of membrane deterioration during leaf senescence? *Plant Physiology and Biochemistry*, *49*, 1220-27

Sadler C., Schroll B., Zeisler V., Waßmann F., Franke R., Schreiber L. (2016) Wax and cutin mutants of Arabidopsis: Quantitative characterization of the cuticular transport barrier in relation to chemical composition. *Biochimica et Biophysica Acta (BBA) - Molecular and Cell Biology of Lipids*, *1861* (9B), 1336-44

Schmittgen TD., Livak KJ. (2008) Analyzing real-time PCR data by the comparative C(T) method. *Nature Protocols, 3* (6), 1101-8

Schönherr J. (1976) Water permeability of isolated cuticular membranes: The effect of cuticular waxes on diffusion of water. *Planta, 131*, 59-194

Schönherr J., Eckl K., Gruler H. (1979) Water permeability of Plant Cuticles: The Effect of Temperature on Diffusion of Water. *Planta, 147*, 21-6

Tanaka T., Tanaka H., Machida C., Watanabe M, Machida Y. (2004) A new method for rapid visualization of defects in leaf cuticle reveals five intrinsic patterns of surface defects in Arabidopsis. *Plant Journal, 37* (1), 139-46

Verdonk JC., Ric de Vos CH., Verhoeven HA., Haring MA., van Tunen AJ., Schuurink RC. (2003) Regulation of floral scent production in petunia revealed by targeted metabolomics. *Phytochemistry, 67* (6), 997-1008

Verdonk JC., Haring MA., van Tunen AJ., Schuurink RC. (2005) ODORANT1 regulates fragrance biosynthesis in petunia flowers. *Plant Cell, 17* (5), 1612-24

Wang Z-Y., Xiong L., Li W., Zhu JK., Zhu J. (2011) The plant cuticle is required for osmotic stress regulation of abscisic acid biosynthesis and osmotic stress tolerance in Arabidopsis. *Plant Cell, 23* (5), 1971-84

Widhalm JR., Jaini R., Morgan JA., Dudareva N. (2015) Rethinking how volatiles are released from plant cells. *Trends in Plant Science, 20* (9), 545-50

Xiao F., Goodwin S., Xiao Y., Sun Z., Baker D., Tang X., Jenks M., Zhou J. (2004) Arabidopsis CYP86A2 represses Pseudomonas syringae type III genes and is required for cuticle development. *EMBO Journal, 23*, 2903-13

Yanagisawa M., Desyatova AS., Belteton SA., Mallery EL., Turner JA., Szymanski DB. (2015) Patterning mechanisms of cytoskeletal and cell wall systems during leaf trichome morphogenesis. *Nature Plants, 1*, 15014

Yeats TH., Rose JKC. (2013). The formation and function of plant cuticles. Plant Physiol. 163, 5–20

Zhang J, Broeckling CD, Blancaflor EB, Sledge MS, Sumner LW, Wang Z (2005) Overexpression of WXP1, a putative Medicago trunculata AP2 domain-containing transcription factor gene, increases cuticular wax accumulation and enhances drought tolerance in transgenic alfalfa (*Medicago sativa*). *The Plant Journal, 42*, 689-707

CHAPTER 7. CHARACTERIZING THE PHENOTYPES OF GENETICALLY MODIFIED PLANT CUTICLES

7.1 Introduction

7.1.1 Characterization of cuticular phenotypes in genetically modified cuticles

The advent of genetic engineering has opened new avenues for studying the role of the cuticle as a barrier between the plant and the environment. In Sections 3.2.2 and 6.2.1 we discussed many of the major biochemical pathways leading towards the development of the plant cuticle and how researchers have induced genetic perturbations to engineer plants with modified cuticles. Using model wax compounds representing the crystallinity of plant cuticles, we found that an abundance of crystalline waxes contributed to decreased diffusion across the cuticle. However, for linking phenotypes to specific genetic modifications in plants, a major limitation remains in quantifying the relationship between chemical composition and permeability, due to the large number of wax components. Deviations in individual wax constituents may result in immeasurable changes in physical properties such as melting behavior or absolute crystallinity. Despite this, various methods to assess the phenotypes of genetically modified cuticles have provided insight into the putative functions of numerous cuticle-associated genes (Kerstiens et al., 2006; Petit et al., 2017).

Here, we assess the cuticle composition and crystallinity of cuticles from transformed *Petunia hybrida* flowers generated from three independent genetic engineering strategies. First, the *Arabidopsis thaliana* transcription factor *AtMYB106* was overexpressed in petunia using the petal-specific promoter *MYB1* identified in Japanese morning glory known to be active during early flower development (Azuma et al., 2016). In Arabidopsis, the knockout of *AtMYB106* resulted in cuticle deficiencies identified by increased organ adhesion during development and a reduction in the crystalline surface morphology (Oshima et al., 2013). Measurement of wax gene transcript levels suggested that *AtMYB106* regulates the expression of the transcription factor WAX INDUCER1/SHINE1 (WIN1/SHN1) which induces the wax and cutin biosynthetic pathways (Aharoni et al., 2004). The second transformant characterized was the down-regulation by RNA interference of the petunia wax exporter *PhABCG12* (Pighin et al., 2004). In Chapter 6, *PhABCG12*-RNAi lines were found to have a decreased cuticle thickness. Finally, cuticle

biosynthesis genes *CYP88A4*, *CYP77A6*, and *GPAT6* encoding for a ω-hydroxylase, a fatty acid midchain hydroxylase, and a glycerol 3-phosphate acyltransferase, respectively, were overexpressed to induce increased cuticle development. Overexpression of *CYP77A6*/*GPAT6* in Arabidopsis resulted in enhanced quantities of crystalline nanoridges on leaf surfaces (Li-Beisson et al., 2009). Using the methods developed for assessing the physicochemical properties of cuticles in Chapters 3 and 6, we identify the major changes that are induced as a result of genetic perturbations.

7.1.2 Motivations and objectives

Genetic modifications of plant cuticles can result in phenotypic changes such as modified surface morphology, increased permeability, or increased organ adhesion during development, all of which are attributed to the chemical composition of the cuticle. Due to large number of wax constituents, determining which compounds contribute to an observed phenotype is difficult to deduce. Connecting plant cuticle-associated traits with specific genes is of great importance for the rational design of plants that can tolerate shifting climate patterns and rapidly evolving ecosystems.

Using GC-MS, the compositions of three wax mutants in petunia flowers were quantified to obtain changes in the distribution of individual wax constituents arising from the genetic modification strategies. Finally, ATR-FTIR and XRD were used to determine the structural characteristics of isolated and reconstituted petal cuticles.

7.2 Materials and methods

7.2.1 Plant materials and growth conditions

Wild-type and transgenic *Petunia hybrida* cv. Mitchell diploid (W115; Ball Seed Co., West Chicago IL) were grown under standard greenhouse conditions with a light period from 6:00 h to 21:00 h. Transgenic constructs were synthesized by Genscript (Piscataway NJ). To ensure that cuticle development is affected during early flower development, all modifications were performed using the petal-specific promoter *MYB1* from Japanese morning glory (*Ipomoea nil*) which displays activity through floral organ development and predominantly in flower limbs (Azuma et al., 2016). Transgene constructs for AtMYB106 overexpression, PhABCG12 silencing

by RNA interference, and CYP88A4/CYP77A6/GPAT6 co-expression (nanoridge inducing – *NANOR*) and the 1023-bp *InMYB1* promoter were inserted into the destination vector R4pGWB5_stop_HSP (Oshima et al., 2011) using the MultiSite Gateway Three-Fragment Vector Construction Kit (Invitrogen, Carlsbad, CA). CYP88A4, CYP77A6, and GPAT6 were linked using the viral self-cleaving 2A linker for co-expression of distinct peptides (Ha et al., 2010). Transgenic *P. hybrida* plants were obtained via *Argobacterium tumefaciens* (strain GV3101 carrying the final *AtMYB106*, *PhABCG12*-RNAi and *NANOR* constructs) leaf disc transformation using a standard transformation protocol (Horsch et al., 1985). Constructs for transgenic lines are given in Fig. 7.1.

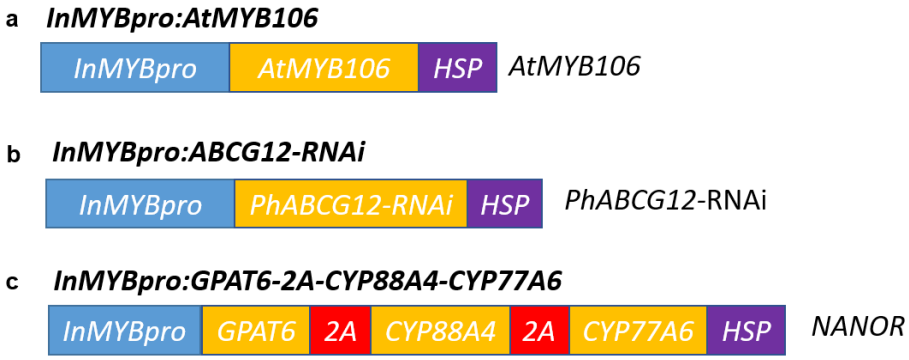

Fig. 7.1 – Gene cassettes for generating transgenic petunia. All modifications were performed using the petal-specific promoter *MYB1* (shown in blue) from *I. nil*, with transgene sequences (shown in orange) inserted into a destination vector R4pGWB5_stop_HSP (shown in purple) (a) Down-regulation of PhABCG12 wax exporter (see Section 6.2.1). (b) Overexpression of the AtMYB106 transcription factor (Oshima et al., 2013). (c) Overexpression of the CYP88A4/CYP77A6/GPAT6 pathway for cutin biosynthesis to induce nanoridge formation on petal surfaces (Li-Beisson et al., 2009). Co-expression of individual peptides was achieved using the viral self-cleaving 2A-linker (shown in red).

7.2.2 Wax extraction and GC-MS analysis

Detailed procedure is presented in Section 3.3.3.

7.3 Fourier-transform infrared spectroscopy

Detailed procedure is presented in Section 3.4.3.

7.3.1 X-ray diffraction

Detailed procedure is presented in Section 3.4.4.

7.3.2 Water loss measurement

Detailed procedure is presented in Section 6.3.8.

7.3.3 Statistical analysis

Multivariate analysis was performed using JMP, Version 14.0 (SAS Institute Inc., Cary NC). Hierarchical clustering analysis was conducted using the relative abundance of individual wax constituents identified and quantified by GC-MS analysis of cuticular wax extracts. The Ward's minimum variance method was used to perform the clustering analysis. Principal Component Analysis (PCA) was applied on mass spectrometry data for dimensionality reduction and exploratory analysis to interpret composition data.

7.4 Results and discussion

7.4.1 Wax chemical analysis of transgenic petunia cuticles

Several independent lines of petunia expressing *PhABCG12* down-regulation by RNAi, overexpression of *AtMYB106*, and overexpression of *CYP77A6*/*GPAT6* (*NANOR*) were generated. For each genotype, three lines expressing the greatest change relative wild-type transcript for their respective genes were selected for wax composition screening (Fig. 6.1). To determine if genetic modifications resulted in a measurable change in cuticle composition, transgenic and wild-type petunia cuticle extracts were profiled for individual wax constituents using GC-MS analysis (Fig. 7.2a). Petunia flowers expressing *PhABCG12*-RNAi were found to have significantly decreased wax content, with *PhABCG12*-RNAi-9 exhibiting a decrease of 43-49% relative to the wild-type control. In contrast, overexpression of *AtMYB106* resulted in increased wax coverage relative to wild-type flowers, with an overall increase of 19-24% total wax content measured in *AtMYB106*-12. *NANOR* petunia lines overexpressing the cutin biosynthetic pathway did not exhibit any increase in total wax content relative to the wild-type control. Despite changes in total wax amount, analysis of wax composition revealed no significant changes across all transgenic petunia relative

to the wild-type control when sorted by total wax compound class (Fig. 7.2b). Despite increases in total primary alcohol quantities for *AtMYB106* overexpression lines (-10, -12) (Fig. 7.2a), the relative fraction of total alcohols in the cuticular waxes remained unchanged.

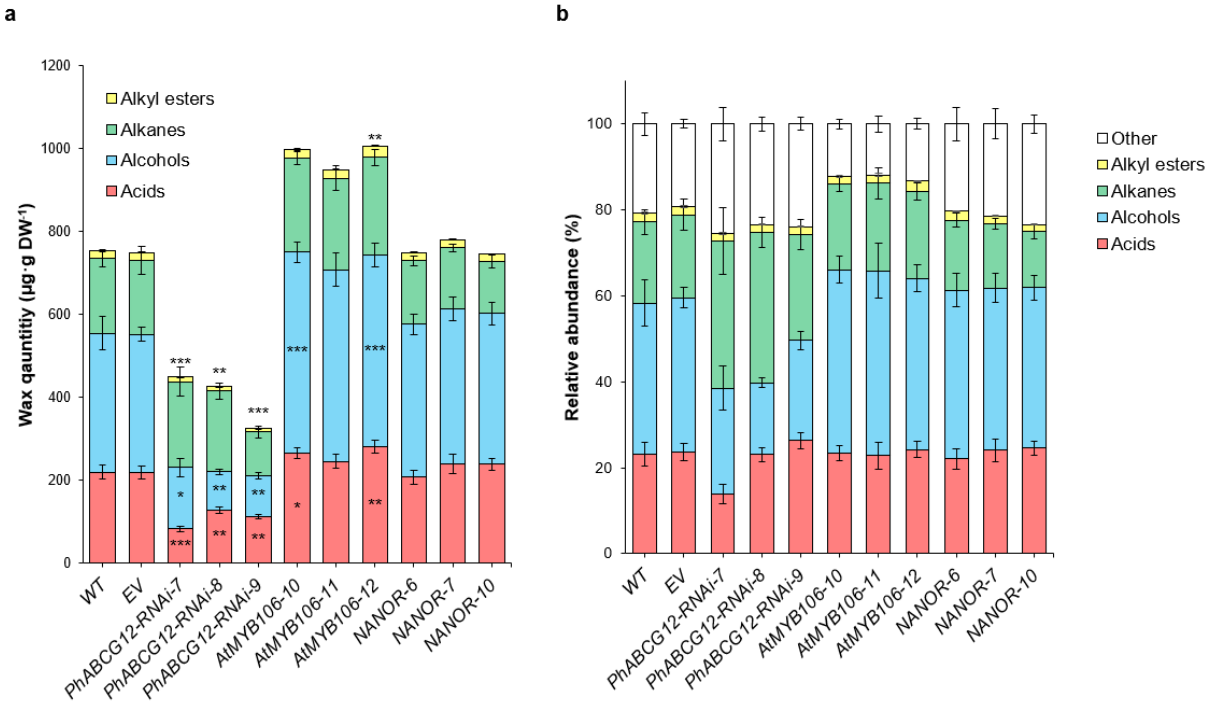

Fig. 7.2 – Effect of genetic modifications on wax amount and cuticle composition in petunia flowers. (a) Total wax abundance in transgenic flowers on day 2 post-anthesis relative to wild-type (WT) and empty vector (EV) control. (b) Wax composition by major constituent classes: fatty acids, primary alcohols, *n*-alkanes, and alkyl esters. Data are means ± S.E. (n = 5 biological replicates). * $P < 0.05$, ** $P < 0.01$, *** $P < 0.001$ represent statistical differences with respect to the empty vector control by Student's *t*-test.

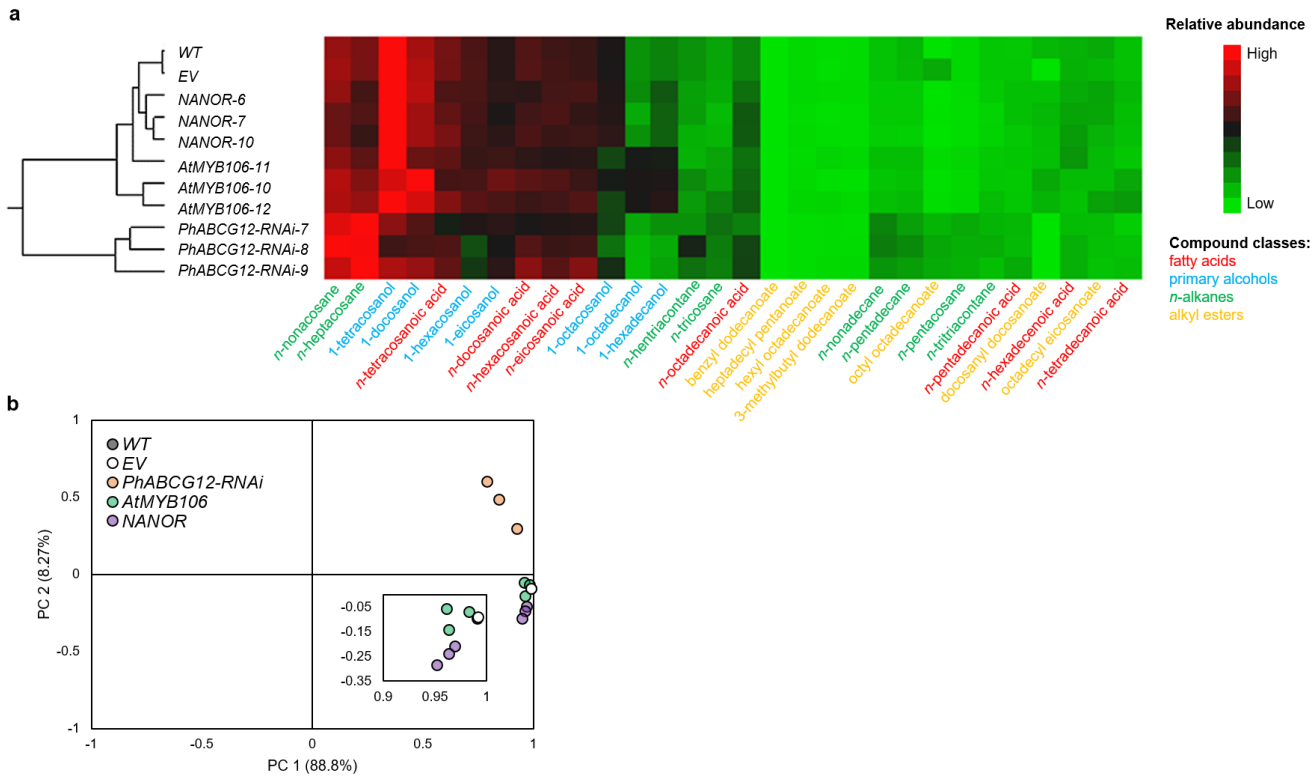

Fig. 7.3 – Effect of genetic modifications on individual wax constituents of petunia petal cuticles. (a) Dendrograms obtained from hierarchical clustering of individual lines profiled for wax composition. (b) Principal component analysis of wax compositions of across the genetic backgrounds.

To identify if individual constituents result in statistically measurable changes in the overall composition, multivariate analysis of the mass spectrometry data was performed. Clustering analysis was performed on the relative abundances of individual wax compounds detected from wax extracts across all transgenic flowers (Fig. 7.3a). In general, the pattern for wax constituent distribution remains largely conserved across all lines profiled, with the exception of a few wax metabolites. For *AtMYB106* lines, abundant alcohols such as 1-octadecanol and 1-hexadecanol are found in higher proportions compared to the other lines. Additionally, 1-hexacosanol was found in lower proportions in *PhABCG12*-RNAi lines compared to all other lines profiled. For the five most abundant wax metabolites, *n*-nonacosane, *n*-heptacosane, 1-tetracosanol, 1-docosanol, and *n*-tetracosanoic acid, their relative abundances remained consistent across all lines profiled. Despite the commonality in compositions, lines with unique genotypes were found clustered in the same branch, with *NANOR* and *AtMYB106* overexpression lines exhibiting the closest wax composition profile with that of wild-type flower cuticles. Indeed, principal

component analysis (PCA) of the abundance data further illustrates the similarity in wax compositional profile between *NANOR*, *AtMYB106*, and wild-type petal cuticles (Fig. 7.3b), suggesting that overexpression of cuticle pathways does little to modify the overall composition. In general, the change in overall wax composition is negligible when considering wax metabolite classes (acids, alcohols, etc.) but measurable changes can be found for individual wax constituents.

7.4.2 Physical characterization of transgenic cuticles

The structural integrity of the cuticle dictates its ability to protect the plant against uncontrolled water loss. Measuring water loss from detached plant tissue is a valid method for assessing this integrity (Isaacson et al., 2009). Two-day post-anthesis transgenic and wild-type petunia petals were detached from their receptacles and total corolla fresh weight was measured incrementally over twelve hours (Fig. 7.4). *PhABCG12*-RNAi lines were found to have both significantly decreased petal dry weight and total water content, suggesting that the decrease in wax amount results in diminished ability to retain water (Fig. 7.4a). Even with decreased total water content, *PhABCG12*-RNAi lines demonstrate enhanced water loss compared to the wild-type control upon detachment (Fig. 7.4b). Conversely, *AtMYB206* flowers are found to have increased water content, but with no difference in their petal dry weight (Fig. 7.4a). Increased wax amount in *AtMYB106* lines (Fig. 7.2a) likely contributes to increased water content, however, there was no measurable improvement in their ability to protect against water loss compared to wild-type petals (Fig. 7.4c). In *NANOR* lines, there was no measured change in water content (Fig. 7.4a) or the rate of water loss (Fig. 7.4d). To determine if the rate of water loss is dependent on the chemical composition, the total rate ($mg \cdot hr^{-1}$) for individual lines was compared to the abundance of individual wax constituents (Fig. 7.5a). In general, no trend was observed between the abundance of individual compound classes (acids, alcohols, *n*-alkanes, alkyl esters). Additionally, no significant trend was observed between wax amount and water permeability across all lines (Fig. 7.5b). While the lack of correlation between permeability and cuticle abundance has been noted in previous studies (Riederer and Schreiber, 2001), it may be that the engineered plants have cuticles with limited variation in composition and amount.

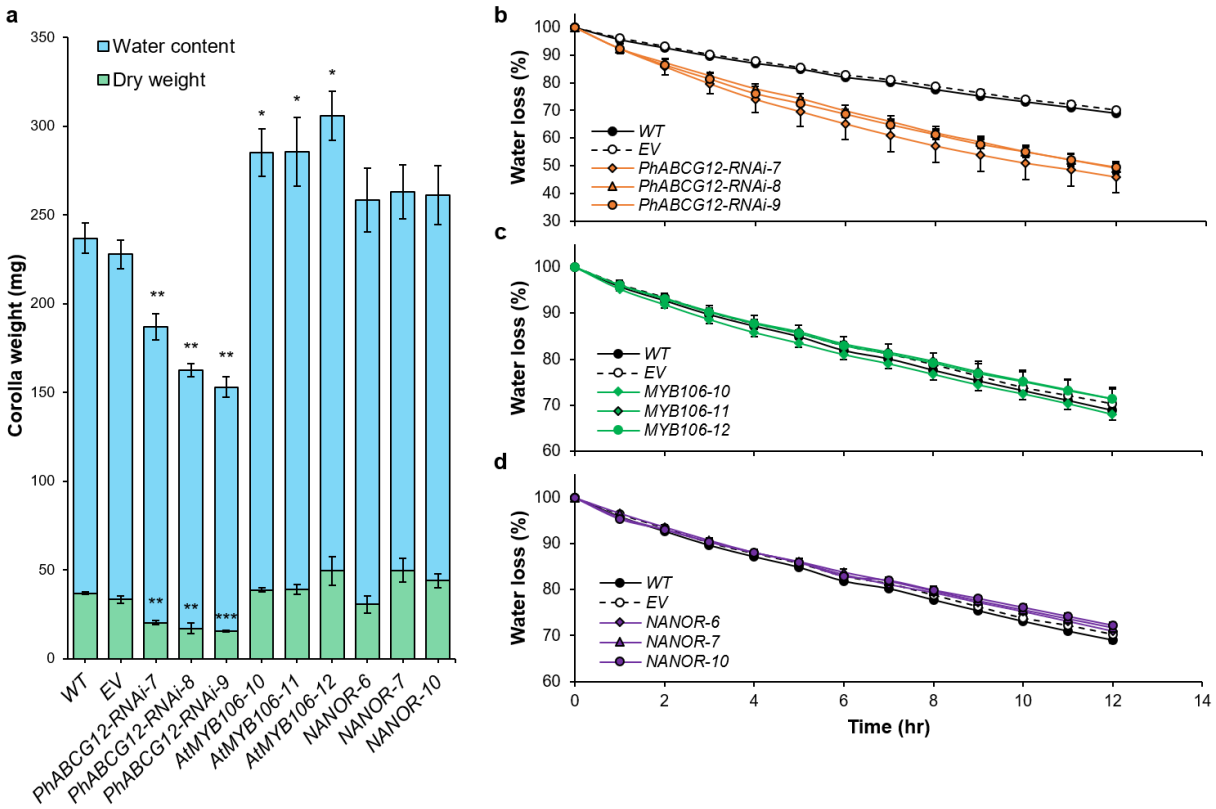

Fig. 7.4 – Water content and rate of water loss in detached transgenic and wild-type petunia petals. (a) Total fresh weight of day 2 post-anthesis petunia flowers detached from their receptacles. Dry weight was obtained upon desiccation in an oven for 2 hr; water content is given by the difference in corolla fresh and dry weight. The water loss rate from detached petals measured over twelve hours for WT, EV, (b) *PhABCG12*-RNAi, (c) *AtMYB106*, and (d) *NANOR* flowers. Data are means ± S.E. (n = 5 biological replicates). * $P < 0.05$, ** $P < 0.01$, *** $P < 0.001$ by Student's *t*-test.

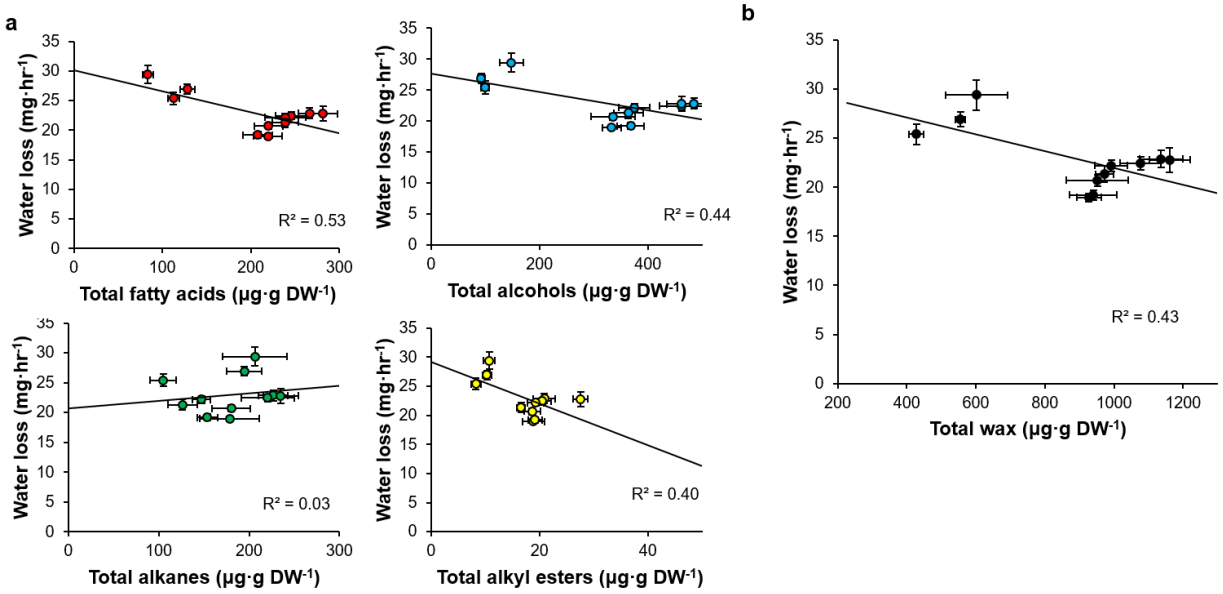

Fig. 7.5 – Effect of wax composition and amount on the rate of water loss in transgenic and wild-type petunia. (a) Effect of wax composition by compound class (fatty acids, primary alcohols, *n*-alkanes, alkyl esters) on the rate of water loss in WT, EV, *PhABCG12*-RNAi (lines 7-9), *AtMYB106* (lines 10-12), and *NANOR* (lines 6, 7, 10). Data are means ± S.E. (n = 5 biological replicates).

ATR-FTIR absorbance spectra collected from freshly harvested day 2 post-anthesis transgenic flowers indicate some changes with respect to the molecular arrangements found in the cuticle (Fig. 7.6a). Petunia expressing down-regulation of *PhABCG12* exhibit decreased peak intensity for wax-associated vibrations relative to wild-type spectra, as seen by the decrease in methylene stretching (at 2920 and 2850 cm^{-1}) and bending (at 1470 cm^{-1}) modes. Additionally, there is a clear increase in intensity for the peak associated with the cell wall (at 1050 cm^{-1}), indicating that the coverage of wax relative to other petal surface components has significantly decreased. For *AtMYB106*-12 petals, there was a slight increase in the methylene stretching and bending peak signals compared to wild-type, likely due to the increased wax coverage. No significant changes were readily apparent between wild-type and *NANOR* lines.

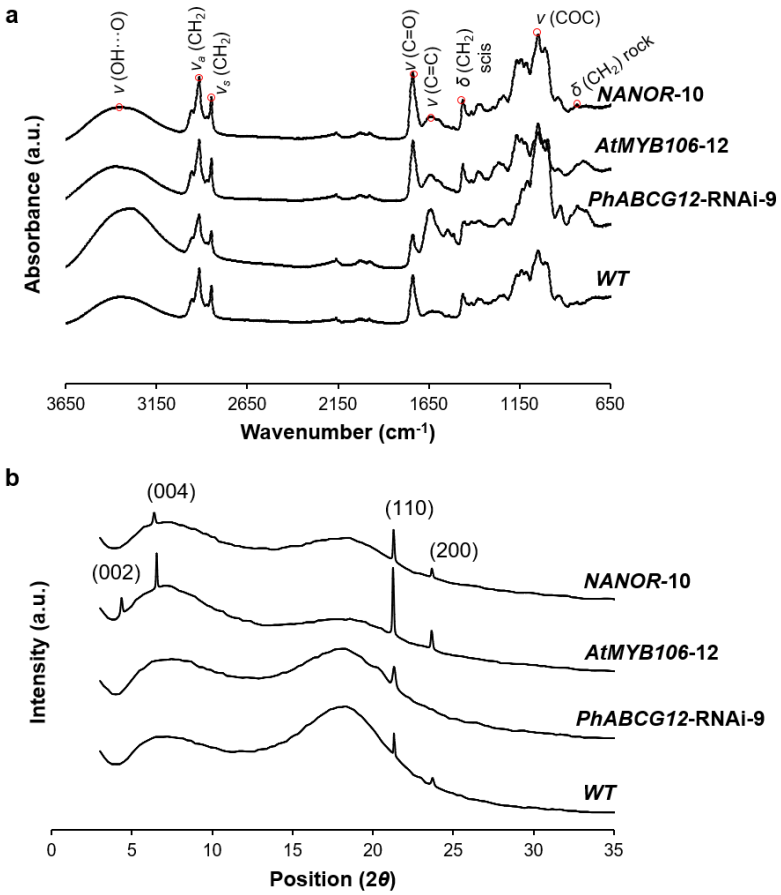

Fig. 7.6 – Effect of genetic modifications on cuticle structure. (a) ATR-FTIR absorbance spectra for two-day old post-anthesis wild-type (*WT*), *PhABCG12*-RNAi-9, *AtMYB106*-12, and *NANOR*-10 petunia petals freshly harvested. (b) XRD patterns obtained for reconstituted cuticles isolated from two-day old post-anthesis *WT*, *PhABCG12*-RNAi-9, *AtMYB106*-12, and *NANOR*-10 petunia petals.

Measurement of the X-ray diffraction patterns of reconstituted cuticles exhibited changes with respect to crystalline symmetry (Fig. 7.6b). *AtMYB106* cuticles were found to have increased layer order based on increases in peak intensity at low diffraction angles. In addition, peaks at high diffraction angles associated with the spacing between crystalline units were significantly increased for *AtMYB106* cuticles when compared to the other cuticles tested. An increase in absolute crystallinity is also observed from the decrease in the amorphous halo centered at 2θ = 19°. While chemical analysis of *AtMYB106* cuticles revealed no significant change in composition relative to wild-type, it is possible that the increase in crystalline wax compounds is coupled with a decrease in amorphous cuticle components (cutin, cyclic compounds, etc.) that were not measured by GC-MS. Despite this increase in cuticle crystallinity, *AtMYB106* flowers did not

demonstrate decreased water permeability relative to wild-type flowers. It may be that changes in cuticle crystallinity result in negligible changes towards water loss, as plant cuticles may already be well adapted towards protection against water loss. However, changes in crystallinity may still contribute to limiting water loss under high temperature stress.

7.4.3 Summary and future directions

Plants produce a diverse array of secondary metabolites with numerous benefits relating to cosmetics, flavoring, medicine, and renewable fuels. Genetic engineering plants to produce high quantities of these desired biochemicals successfully requires *a priori* knowledge of the processes and regulation governing plant secondary metabolism. In this dissertation, we have focused largely on elucidating the role of the cuticle in the emissions of VOCs. In Chapter 3, we formulated a model cuticle that represents the physicochemical properties of petunia flower petals. By varying the proportions of individual wax constituents found in the cuticle, different structural characteristics were observed by X-ray diffraction. In Chapter 4, a model cuticle was simulated using molecular dynamics, and the diffusivities of various volatiles were measured over a broad range of cuticle compositions. Taken together, we concluded that the chemical composition of the waxes directly contributes to the crystallinity of the cuticle, an increase in which can result in decreased flux across the cuticle. Chapter 5 highlighted the effects of varying temperature on the crystalline morphology of the model cuticle as well as the effect on diffusion. While cuticles with different compositions may have similar crystalline content, their thermal phase behavior can be significantly different. Chapters 3-5 primarily serve to illustrate the importance of assessing the integrity of the cuticle as it relates to chemical composition, positing that the distribution of wax compounds serves as the major determinant towards permeability.

In Chapter 6, the effect of a genetically modified petunia petal cuticle on the observed emissions and accumulation of VOCs was investigated. It was discovered that VOCs are localized in high abundance in the cuticle, where they hyper-accumulate to sustain high emission rates. Knock-down of a wax exporter resulted in thinner cuticles that were incapable of storing VOCs to the same extent as wild-type cuticles, resulting in decreased emissions overall. Individual VOCs were found to have different mass transfer resistances in the cuticle where compounds with higher relative volatility experienced negligible resistance. Thus, the cuticle is found to add another level of regulation in the VOC network, controlling the quantity and dynamics of VOC emissions. In

this chapter, we further characterize the effects of other genetic modifications, such as the overexpression of cuticle biosynthetic pathways. Overexpression of AtMYB106 in petunia flowers led to increased wax coverage, while overexpression of the CYP77A6/GPAT6 pathway led to no measurable increase in wax abundance. However, no transgenic line appeared to have a significant change in wax composition, causing insignificant effect of composition on permeability. Nonetheless, phenotypic changes could be observed in these transgenic lines when using physical characterization techniques, suggesting that there are changes in the wax distribution that are not readily identified by GC-MS analysis.

While there has been increased effort into establishing the physicochemical properties of the cuticle with relation to many of its associated functions, the desired properties of an "improved" cuticle remains elusive. As researchers continue phenotyping transgenic variants, there will be increased sampling of cuticle chemical compositions and physical properties. Comprehensive coverage of the literature in time may prove beneficial towards resolving the effects of wax composition on permeability, phase behavior, resistance towards biotic stresses, etc. Deep learning methods are already being implemented to establish relationships for various plant phenotypes with various variables (Ubbens and Stavness, 2017; Namin et al., 2018). Additionally, molecular dynamics simulations can be implemented for multi-component wax systems to study the effect of small changes in chemical composition and to assess the impact of specific gene perturbations. Accurate phenotype characterization and estimation of parameters such as kinetic rate constants and diffusion coefficients will be be able to further progress the field of rational plant engineering for improved crops.

7.5 Acknowledgements

This work was supported by grant IOS-1655438 from the National Science Foundation awarded to Dr. Natalia Dudareva and Dr. John A. Morgan. I would like to thank Dr. Benoît Boachon transformation and screening transgenic *Petunia hybrida* lines (Fig. 7.1). I would like to thank the Research Instrumentation Center in the Department of Chemistry, Purdue University, for training and access to the Thermo Nicolet 6700 FT-IR Spectrophotometer. I would also like to Department of Chemistry, Purdue University, for training and access to the Empyrean Powder X-ray Diffractometer.

7.6 References

Aharoni A., Dixit S., Jetter R., Thoenes E., van Arkel G., Pereira A. (2004) The SHINE clade of AP2 domain transcription factors activates wax biosynthesis, alters cuticle properties, and confers drought tolerance when overexpressed in Arabidopsis. *Plant Cell, 6*, 2463-80

Azuma M., Morimoto R., Hirose M., Morita Y., Hoshino A., Iida S., Oshima Y., Mitsuda N., Ohme-Takagi M., Shiratake K. (2016) A petal-specific InMYB1 promoter from Japanese morning glory: a useful tool for molecular breeding of floricultural crops. *Plant Biotechnology Journal, 14* (1), 354-63

Kerstiens G., Schreiber L., Lendzian KJ. (2006) Quantification of cuticular permeability in genetically modified plants. *Journal of Experimental Botany, 57* (11), 2547-52

Ha SH., Liang YS., Jung H., Ahn MJ., Suh SC., Kweon SJ., Kim DH., Kim YM., Kim JK. (2010) Application of two bicistronic systems involving 2A and IRES sequences to the biosynthesis of carotenoids in rice endosperm. *Plant Biotechnology Journal, 8* (8), 928-38

Horsch RB., Fry J., Hoffmann N., Neidermeyer J., Rogers SG., Fraley RT. (1985) Leaf disc transformation. In: Gelvin S.B., Schilperoort R.A., Verma D.P.S. (eds) Plant Molecular Biology Manual. Springer, Dordrecht

Li-Beisson T., Pollard,M., Sauveplane V., Pinot F., Ohlrogge J., Beisson F. (2009) Nanoridges that characterize the surface morphology of flowers require the synthesis of cutin polyester. *Proceedings in the National Academy of Science USA, 106* (51), 22008-13

Namin ST., Esmaeilzadeh M., Najafi M., Brown TB., Borevitz JO. (2018) Deep phenotyping: deep learning for temporal phenotype/genotype classification. *Plant Methods, 14*, 66

Oshima Y., Shikata M., Koyama T., Ohtsubo N., Mitsuda N., Ohme-Takagi M. (2013) MIXTA-like transcription factors and WAX INDUCER1/SHINE1 coordinately regulate cuticle development in Arabidopsis and Torenia fournieri. *Plant Cell, 25* (5), 1609-24

Petit J., Bres C., Mauxion J-P., Bakan B., Rothan C. (2017) Breeding for cuticle-associated traits in crop species: traits, targets, and strategies. *Journal of Experimental Botany, 68* (19), 5369-87

Pighin JA, Zheng H, Balakshin LJ, Goodman IP, Western TL, Jetter R, Kunst L, Samuels AL (2004) Plant cuticular lipid export requires an ABC transporter. *Science, 306*, 702-4

Riederer M., Schneider, G. (1990). The effect of the environment on the permeability and composition of Citrus leaf cuticles: II. Composition of soluble cuticular lipids and correlation with transport properties. *Planta, 180* (2): 154-65

Ubbens JR., Stevens I. (2017) Deep Plant Phenomics: A Deep Learning Platform for Complex Plant Phenotyping Tasks. *Frontiers in Plant Science, 8*, 1190

Yeats TH., Rose JKC. (2013). The formation and function of plant cuticles. *Plant Physiology. 163*, 5–20

APPENDIX A. CHAPTER 2 SUPPORTING INFORMATION

2-Phenylethanol (2-PE) substrate stoichiometric balance:

$8\ CO_2 + 29\ ATP + 20\ NADPH + NADH + O_2 + 14\ H_2O \longrightarrow$ **2-PE** $+ 29\ ADP + 20\ NADP^+ + NAD^+ + 37\ H^+ + 29\ P_i + H_2O_2$

Lignin substrate stoichiometric balance (H/G/S lignin ratio of 2/66/32%):

$10.118\ CO_2 + 35.59\ ATP + 27.472\ NADPH + 2.118\ O_2 + 15.354\ H_2O \longrightarrow$ **lignin** $+ 33.472\ ADP +$ AMP $+ 1.118$ adenosine $+ 27.472\ NADP^+ + 43.708\ H^+ + 34.59\ P_i + 2.118\ PP_i$

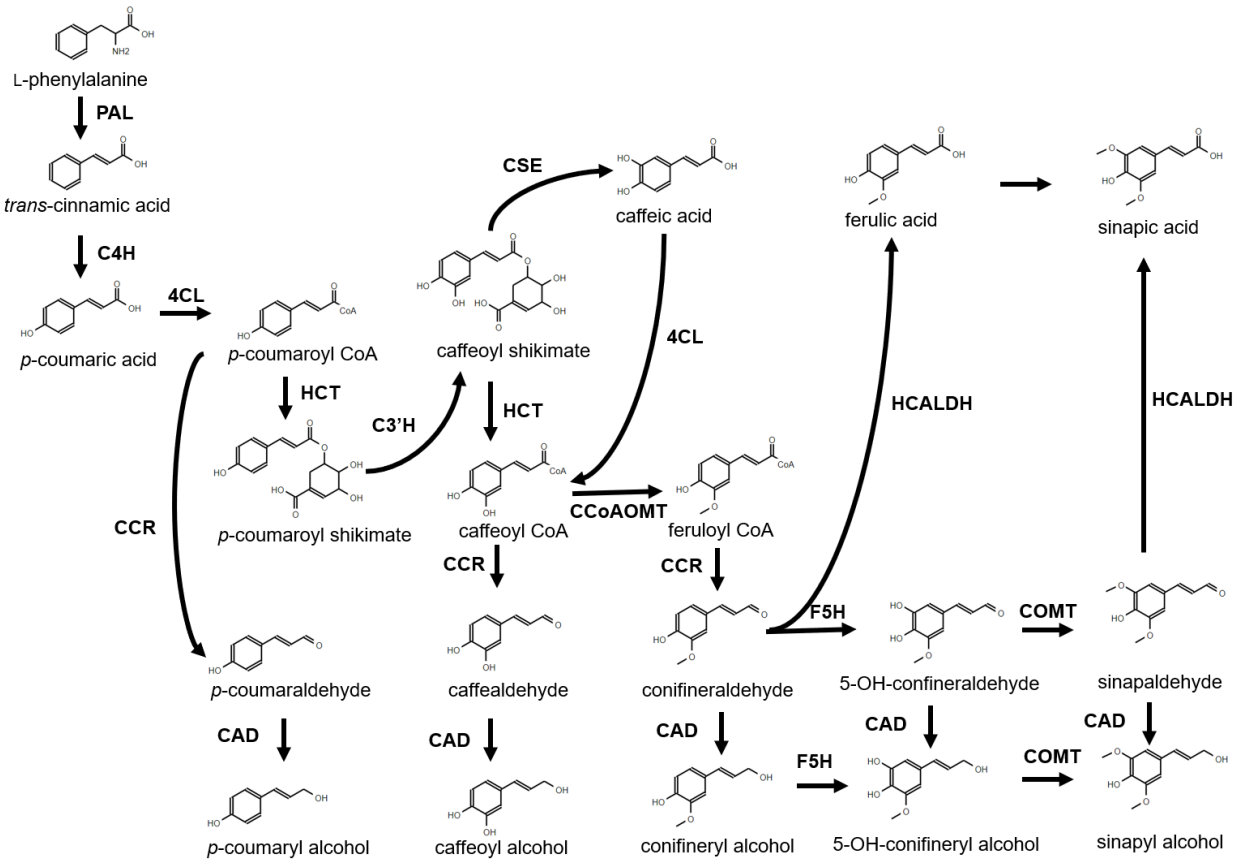

Fig. A1 – The phenylpropanoid pathway in plants. Solid arrows indicate enzymatic steps. 4CL – 4-coumarate:CoA ligase; C3'H – *p*-coumaroyl shikimate 3'-hydroxylase; C4H – cinnamic acid 4-hydroxylase; CAD – cinnamyl alcohol dehydrogenase; CCoAOMT – caffeoyl CoA 3-O-methyltransferase; CCR – cinnamoyl-CoA reductase; COMT – caffeic acid/5-hydroxyferulic acid O-methyltransferase; F5H – ferulate 5-hydroxylase; HCALDH – hydroxycinnamaldehyde dehydrogenase; HCT – hydroxycinnamoyl-coenzyme A shikimate:quinate hydroxycinnamoyl-transferase; PAL – phenylalanine ammonia lyase.

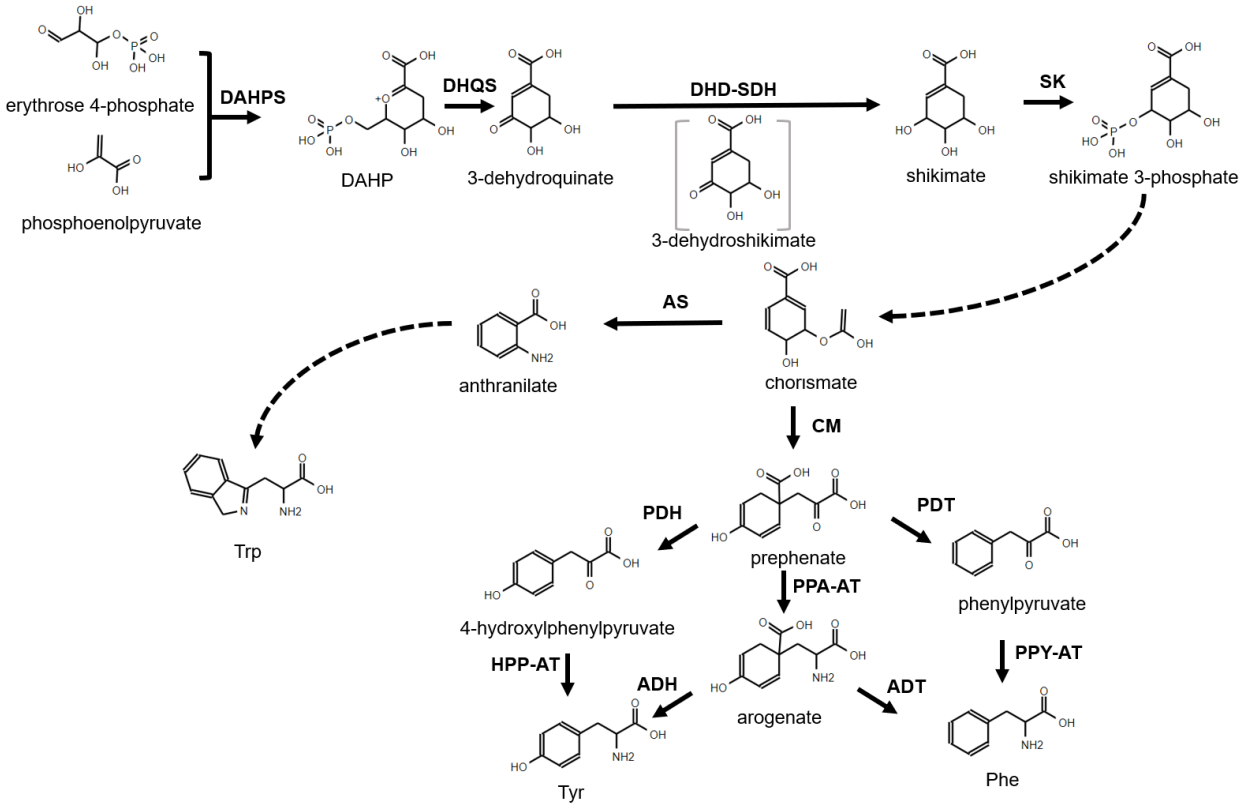

Fig. A2 – The shikimate and aromatic amino acid biosynthesis pathways in plants. Solid arrows indicate enzymatic steps, dashed arrows indicate multiple kinetic steps. Co-factors and co-substrates are not shown in figure. ADH – arogenate dehydrogenase; ADT – arogenate dehydratase; AS – anthranilate synthase; CM – chorismite mutase; DAHPS – 3-deoxy-D-arabino-heptulosonate 7-phosphate synthase; DHD – 3-dehydroquinate dehydratase; DHQS – 3-dehydroquinate synthase; HPP-AT – 4-hydroxyphenylpyruvate aminotransferase; PDH – prephenate dehydrogenase; PDT – prephenate dehydratase; PPA-AT – prephenate aminotransferase; PPY-AT – phenylpyruvate aminotransferase; SDH – shikimate dehydrogenase; SK – shikimate kinase

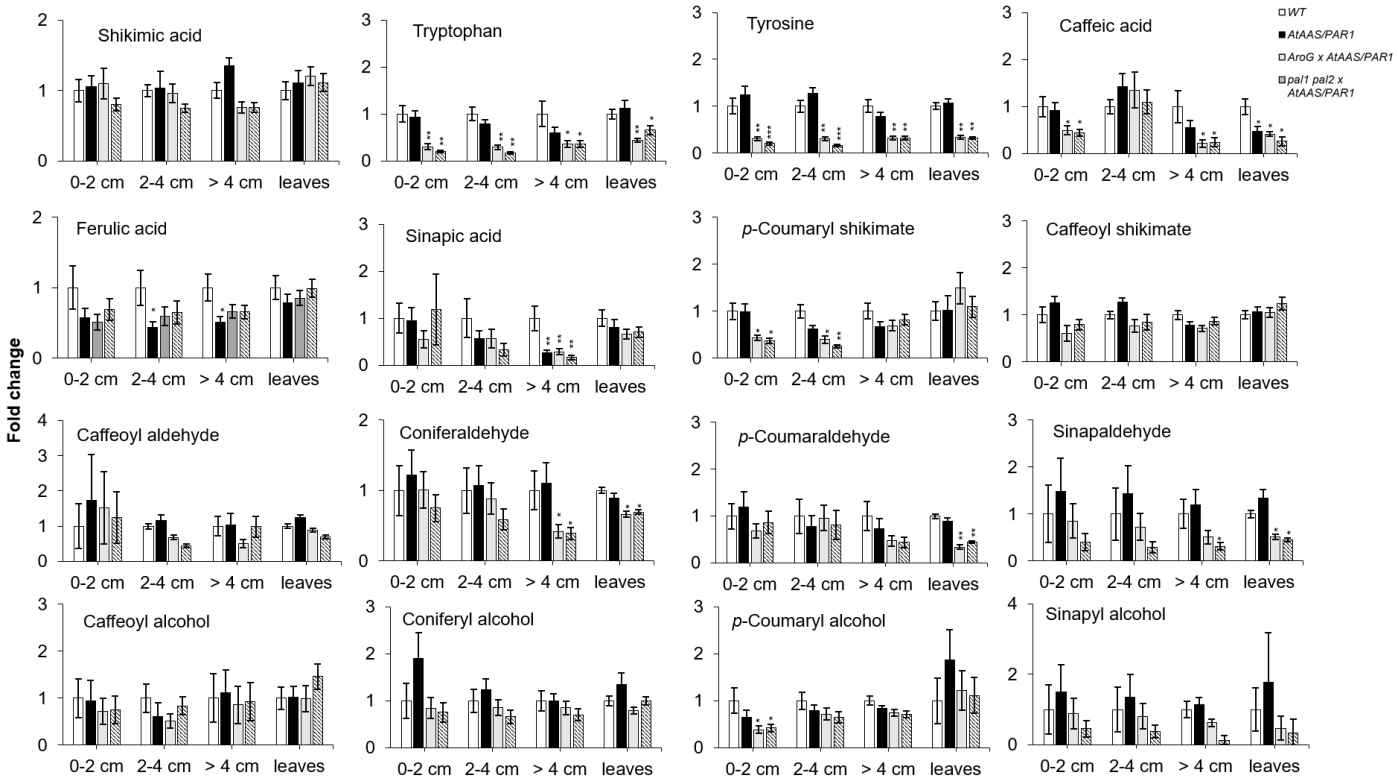

Fig. A3 – Fold change of soluble phenolic compound pools upon subsequent genetic modification. 8-week-old wild-type transgenic Arabidopsis were harvested by segments (0-2 cm stem, 2-4 cm stem, > 4 cm stem, rosette leaves) and profiled for aromatic amino acids and phenylpropanoid metabolites. All fold changes are reported with respect to the wild-type control, *AtAAS*/*PAR1*-53. WT – wild-type; AroG – *AroG* × *AtAAS*/*PAR1*-53; *pal1 pal2* - *pal1 pal2* × *AtAAS*/*PAR1*-53. Data are means ± S.E. (n = 4 biological replicates). * $P < 0.05$, ** $P < 0.01$, *** $P < 0.001$ by Student's *t*-test.

APPENDIX B. CHAPTER 3 SUPPORTING INFORMATION

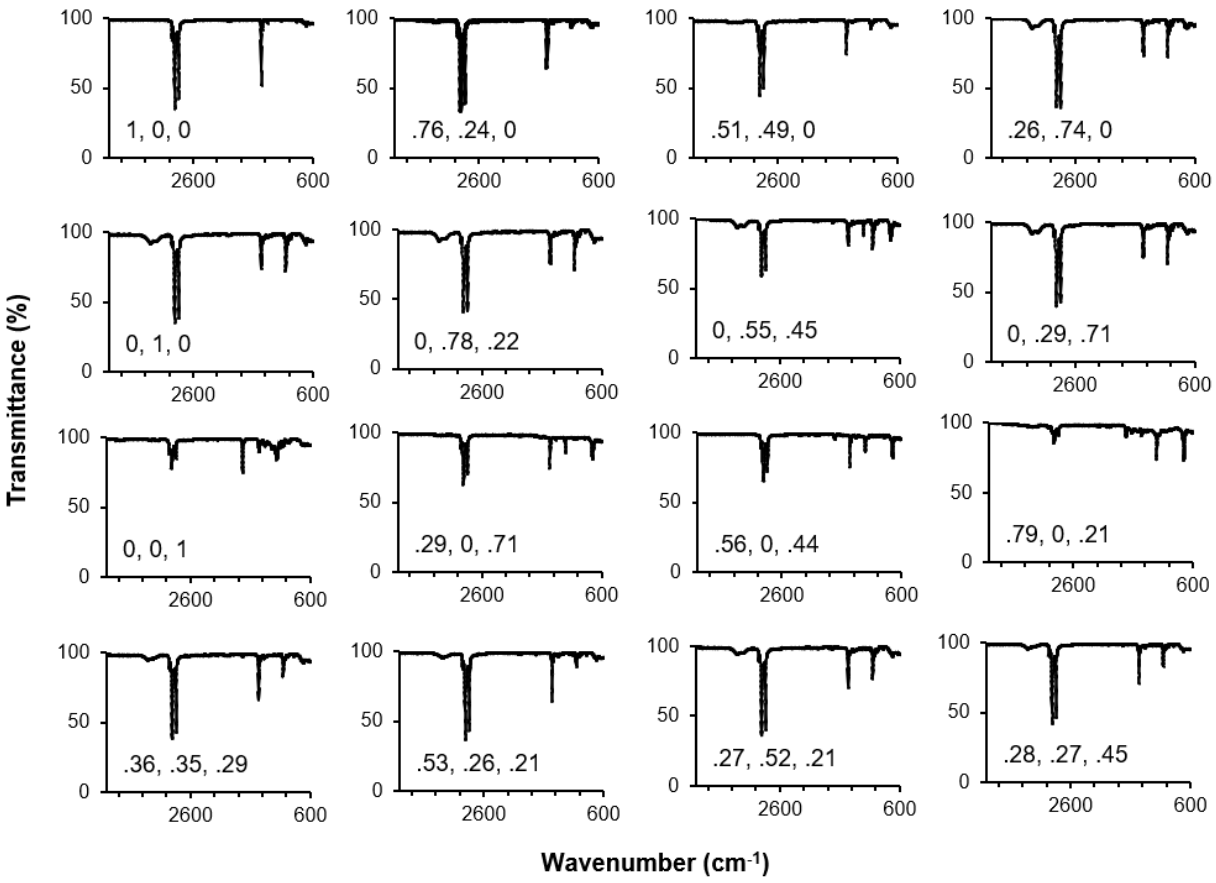

Fig. B1 – ATR-FTIR spectra of wax mixtures. Transmission IR spectra of wax mixtures ($C_{24}H_{50}$, $C_{22}H_{45}OH$, $C_{17}H_{34}O_2$, by wt. frac.).

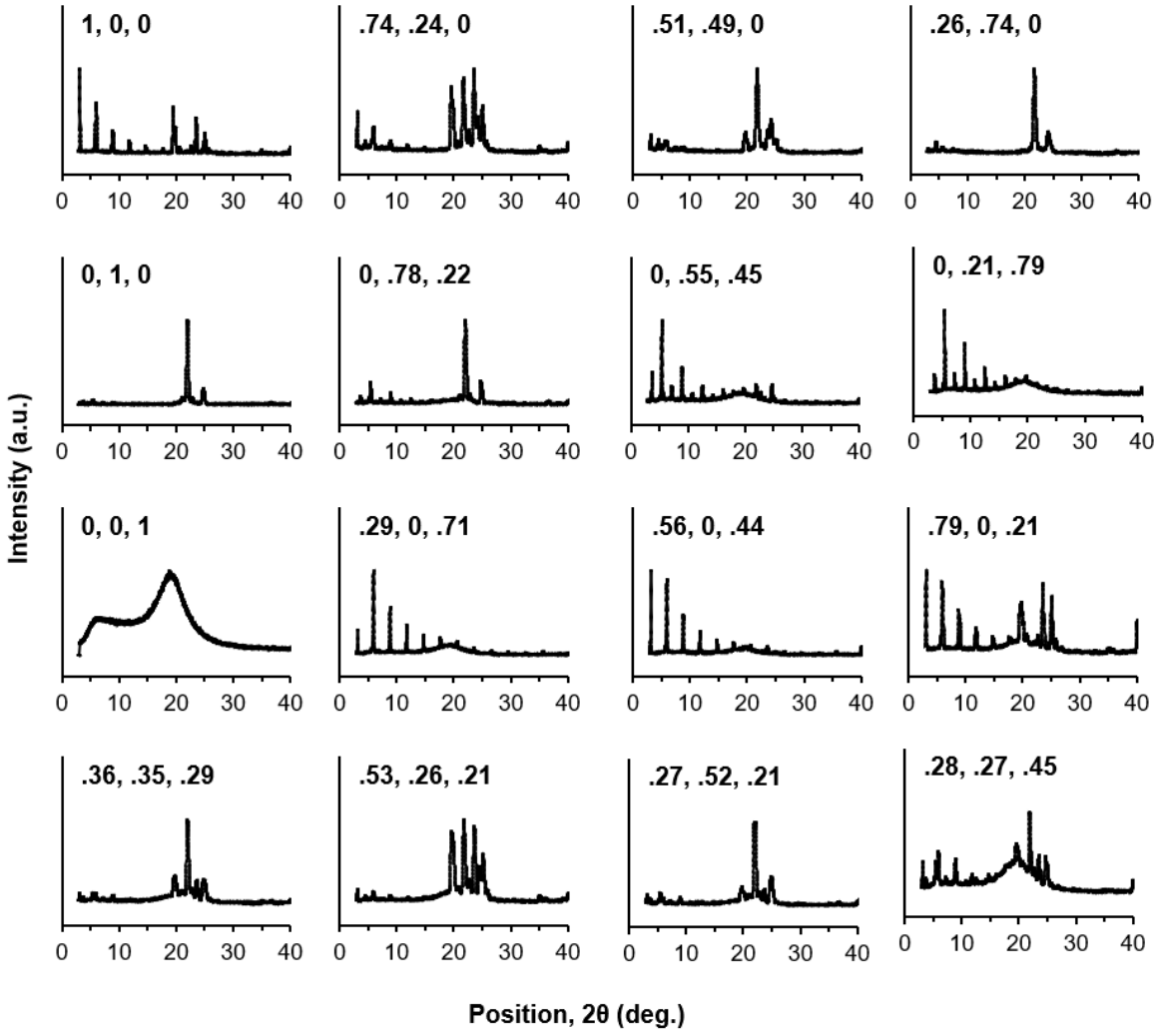

Fig. B2 – XRD patterns for wax mixtures ($C_{24}H_{50}$, $C_{22}H_{45}OH$, $C_{17}H_{34}O_2$ by wt. frac.).

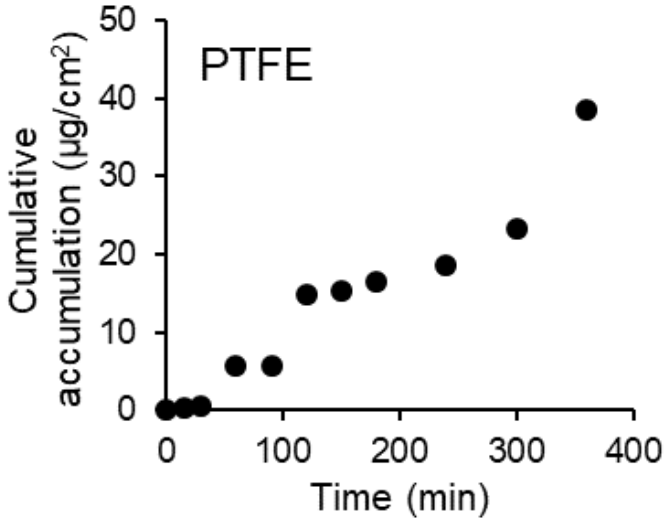

Fig. B3 Methylbenzoate concentration profile obtained from permeability assay through the PTFE substrate.

APPENDIX C. CHAPTER 4 SUPPORTING INFORMATION

Simulation Initialization File

The following script was used in LAMMPS to study the diffusion of volatile organic compounds in the model cuticle as described in Chapter 4. The input file (.init extension) contains information on the simulation conditions (force-field empirical form, minimization procedure, equilibration procedure, operating conditions, etc.). Lines starting with # denote comments.

```
# lammps input file for polymer simulation with dilute ions

# VARIABLES
variable        data_name       index   wax_15_voc-5.data
variable        settings_name   index   wax_15_voc-5.in.settings
variable        log_name        index   wax_15_voc-5.log
variable         nSteps_ramp     index   500000 # number of data
steps   for the ramped anneal
variable        nSteps_equil    index   10000000 # number of data
steps for the ramped anneal
variable        avg_freq        index   1000
variable        coords_freq     index   1000
variable        thermo_freq     index   1000
variable        dump4avg        index   100
variable        vseed           index   74357
variable        ANNEAL_TEMP     index   400.0 # Temperature during
the initial anneal
variable        FINAL_TEMP      index   298.0 # Temperature ramped
to during the final anneal
variable        pressure        index   1.0 # Pressure during the
simulations

# Change the name of the log output #
log ${log_name}
```

```
#============================================================
# GENERAL PROCEDURES
#============================================================
units          real #  g/mol,  angstroms,  fs,  kcal/mol,  K,  atm,
charge*angstrom
dimension 3    # 3 dimensional simulation
newton         off  # use Newton's 3rd law
boundary  p p p     # periodic boundary conditions
atom_style     full    # molecular + charge

#============================================================
# FORCE FIELD DEFINITION
#============================================================
special_bonds  lj   0.0 0.0 0.0  coul 0.0 0.0 0.0     # NO     1-
4 LJ/COUL interactions
pair_style        hybrid  lj/cut/coul/long  14.0  14.0  #  outer_LJ
outer_Coul (cutoff values, see LAMMPS Doc)
kspace_style   pppm 0.0001           # long-range electrostatics
sum method
bond_style     harmonic             # parameters needed: k_bond,
r0
angle_style    harmonic            # parameters needed: k_theta,
theta0
dihedral_style hybrid opls           # parameters needed: V1, V2,
V3, V4
pair_modify     shift  yes  mix  arithmetic         # using Lorenz-
Berthelot mixing rules

#============================================================
# SETUP SIMULATIONS
#============================================================
```

```
# READ IN COEFFICIENTS/COORDINATES/TOPOLOGY
read_data ${data_name}
include ${settings_name}

# SET RUN PARAMETERS
timestep  1.0       # fs
run_style verlet         # Velocity-Verlet integrator
neigh_modify every 1 delay 0 check no one 10000 # More relaxed
rebuild criteria can be used

#============================================================
# RUN CONSTRAINED RELAXATION
#============================================================

# SET OUTPUTS
thermo_style   custom step temp vol density etotal pe ebond eangle
edihed ecoul elong evdwl enthalpy press
thermo_modify   format float %20.10f
thermo ${thermo_freq}

# DECLARE RELEVANT OUTPUT VARIABLES
variable        my_step equal   step
variable        my_temp equal   temp
variable        my_rho  equal   density
variable        my_pe   equal   pe
variable        my_ebon equal   ebond
variable        my_eang equal   eangle
variable        my_edih equal   edihed
variable        my_evdw equal   evdwl
variable        my_eel  equal   (ecoul+elong)
variable        my_ent  equal   enthalpy
```

```
variable        my_P    equal   press
variable        my_vol  equal   vol

fix   averages all ave/time ${dump4avg} $(v_avg_freq/v_dump4avg)
${avg_freq}   v_my_temp   v_my_rho   v_my_vol   v_my_pe   v_my_edih
v_my_evdw v_my_eel v_my_ent v_my_P file thermo.avg

# INITIALIZE VELOCITIES AND CREATE THE CONSTRAINED RELAXATION FIX
velocity        all create ${ANNEAL_TEMP} ${vseed} mom yes rot yes
# DRAW VELOCITIES

fix relax all nve/limit 0.01
run             10000
unfix relax

#=============================================================
# RUN RAMPED ANNEAL
#=============================================================

# REINITIALIZE THE VELOCITIES AND CREATE THE ANNEALING FIX
velocity        all create ${ANNEAL_TEMP} ${vseed} mom yes rot yes
# DRAW VELOCITIES

fix mom all momentum 1000 linear 1 1 1 angular # Zero out system
linear and angular momentum every ps
fix anneal all npt temp ${ANNEAL_TEMP} ${FINAL_TEMP} 100.0 iso
${pressure} ${pressure} 1000.0 # NPT, nose-hoover 100 fs T
relaxation

# CREATE COORDINATE DUMPS FOR ANNEAL
dump anneal all custom ${coords_freq} anneal.lammpstrj id type x
y z
```

```
dump_modify anneal sort id format float %20.10g

# RUN RAMPED ANNEAL
run ${nSteps_ramp}
unfix anneal

# RUN EQUILIBRATION PHASE AT FINAL TEMP
fix anneal all npt temp ${FINAL_TEMP} ${FINAL_TEMP} 100.0 iso
${pressure} ${pressure} 1000.0 # NPT, nose-hoover 100 fs T
relaxation
run ${nSteps_ramp}
unfix anneal
undump anneal

#=============================================================
# RUN EQUILIBRIUM SIM
#=============================================================

# UPDATE REBUILD CRITERIA
neigh_modify every 1 delay 10 check yes one 10000 # More relaxed
rebuild criteria can be used

# UPDATE RUN PARAMETERS AND CREATE FIX
fix equil all npt temp ${FINAL_TEMP} ${FINAL_TEMP} 100.0 iso
${pressure} ${pressure} 1000.0 # NPT, nose-hoover 100 fs T
relaxation

# CREATE COORDINATE DUMPS FOR EQUILIBRIUM
dump equil all custom ${coords_freq} equil.lammpstrj id type x y
z
dump_modify equil sort id format float %20.10g
```

```
# RUN EQUIL
run       ${nSteps_equil}
unfix equil
undump equil

# WRITE RESTART FILES, CLEANUP, AND EXIT
write_restart   wax_15_voc-5.end.restart
write_data      wax_15_voc-5.end.data pair ii
unfix          averages
```